12-2017

GEOPHYSICAL DELINEATION OF MEGAPOROSITY AND FLUID MIGRATION PATHWAYS FOR GEOHAZARD CHARACTERIZATION WITHIN THE DELAWARE BASIN, CULBERSON COUNTY, TEXAS

Jonathan David Woodard
Stephen F. Austin State University, jonathan.d.woodard@gmail.com

Repository Citation

Woodard, Jonathan David, "GEOPHYSICAL DELINEATION OF MEGAPOROSITY AND FLUID MIGRATION PATHWAYS FOR GEOHAZARD CHARACTERIZATION WITHIN THE DELAWARE BASIN, CULBERSON COUNTY, TEXAS" (2017). *Electronic Theses and Dissertations*. 137.
https://scholarworks.sfasu.edu/etds/137

GEOPHYSICAL DELINEATION OF MEGAPOROSITY AND FLUID MIGRATION PATHWAYS FOR GEOHAZARD CHARACTERIZATION WITHIN THE DELAWARE BASIN, CULBERSON COUNTY, TEXAS

GEOPHYSICAL DELINEATION OF MEGAPOROSITY AND FLUID MIGRATION PATHWAYS FOR GEOHAZARD CHARACTERIZATION WITHIN THE DELAWARE BASIN, CULBERSON COUNTY, TEXAS

By

Jonathan D. Woodard, Bachelor of Science

Presented to the Faculty of the Graduate School of
Stephen F. Austin State University
In Partial Fulfillment
Of the requirements

For the Degree of
Master of Science

STEPHEN F. AUSTIN STATE UNIVERSITY

DECEMBER, 2017

GEOPHYSICAL DELINEATION OF MEGAPOROSITY AND FLUID MIGRATION PATHWAYS FOR GEOHAZARD CHARACTERIZATION WITHIN THE DELAWARE BASIN, CULBERSON COUNTY, TEXAS

By

Jonathan D. Woodard, Bachelor of Science

APPROVED:

Dr. Wesley Brown, Thesis Director

Dr. Kevin Stafford, Committee Member

Dr. Melinda Faulkner, Committee Member

Dr. Joseph Musser, Committee Member

Richard Berry, D.M.A
Dean of the Graduate School

ABSTRACT

Differential dissolution of gypsum karst within the Delaware Basin poses a significant threat to infrastructure that society depends on. The study area is located in Culberson County, Texas and traverses a distance of approximately 54 kilometers along RM 652 within the Gypsum Plain which is situated on the northern margin of the Chihuahua Desert and includes outcrops of Castile and Rustler strata that host karst geohazards. Regions of karst geohazard potential have been physically surveyed proximal to the study area in evaporites throughout the Castile Formation outcrop; minimal hazards, in comparison to the Castile Formation, have been documented in the Rustler Formation.

A TR-5 OhmMapper capacitively-coupled resistivity meter was used to acquire resistivity data for geohazard characterization. This study utilized a traditional dipole-dipole array, with an electrode spacing of 2.5 meters between receivers, and a transmitter offset of 2.5 meters. This geometric configuration combined with the medium analyzed, allowed for resistivity readings to be recorded up to approximately 5 meters deep. Data acquisition was recorded with the OhmMapper attached to a vehicle moving at approximately 3 kilometers per hour and transmitting and receiving once per second (approximately three feet per sample). Resistivity data was processed using AGI's EarthImager 2D inversion software. Capacitively-coupled resistivity has shown to be effective in locating karst geohazards in the shallow subsurface.

DEDICATION

I would like to dedicate this research to my beautiful daughter Charlotte Reese Woodard, her mother Hailee Kastine Walker, and my mother Evelyn Gassaway for being my greatest motivations throughout my academic career. I would also like to dedicate this research in loving memory to my paternal grandparents David and Mary Woodard, and to my nephew Max Michael McDonough.

ACKNOWLEDGEMENTS

The completion of this research would not have been possible without the assistance of others. I would like to thank my thesis committee: my thesis advisor Dr. Wesley Brown, Dr. Kevin Stafford, Dr. Melinda Faulkner, and Dr. Joseph Musser for their wisdom, support, and for their time sacrificed to ensure that this project was completed in a punctual manner. I would like to further extend my sincerest appreciation and gratitude to Dr. Wesley Brown and Dr. Kevin Stafford for providing me with the opportunity to work on this project, for playing a vital role in data acquisition, and for their invaluable guidance with data processing and final interpretations.

I am grateful for my friends Cole Hendrickson, Austin Wilkerson, Robert Schoen, Jensen Angelloz, Kaitlin Askelson and Ryan Silberstorf for their friendship and comradery throughout this graduate program.

Finally, I would like to thank my family: my parents Evelyn and William Gassaway; grandparents Susan Gaylord Buxton, Jim and Jane Buxton; my siblings Amanda Davis, Leslie McDonough and husband Matthew, Rachel McPherson and husband Levi, Julia Gassaway, Wyatt Gassaway and wife Laura; niece and nephews Nathan McDonough, Christian McPherson, Lucas McPherson, Blaise Gassaway, Corbin Gassaway, and Azlyn Gassaway for their unwavering support.

TABLE OF CONTENTS

LIST OF FIGURES

LIST OF APPENDIX FIGURES

LIST OF EQUATIONS

LIST OF TABLES

PREFACE

The Gypsum Plain of the Delaware Basin is located in West Texas and southeastern New Mexico. Due to the highly solutional nature of gypsum combined with the complexities of the region's hydrogeologic system, this area has undergone extensive karsting. These phenomena make locating and monitoring karst geohazards difficult without the application of geophysical methods. The following manuscript represents a portion of an interdisciplinary study being conducted by the Geology Department at Stephen F. Austin State University in order to characterize and delineate subsurface karst manifestations and preferential fluid flow associated with roadway degradation. Capacitively-coupled electrical resistivity measurements were taken in order to complete this task in this portion of the larger study project.

The Texas Department of Transportation (TxDOT) contracted Stephen F. Austin State University to conduct land surveys and document surficial karst features that could potentially be responsible for road failure along Ranch to Market (RM) 652 during the summer of 2015. After traditional mapping of surficial features, the decision was made to conduct electrical resistivity surveys along the entire 54 kilometer traverse of the road. The resistivity data acquisition, of the entire traverse, was conducted during the summer of 2016.

The following manuscript highlights areas of more densely populated geophysical anomalies throughout the roadway, not the entire roadway. However, this manuscript is supported by appendices that contain additional data not referenced in the primary manuscript. Appendix A contains a detailed literature review of the geologic history of the study area, and the theory behind electrical resistivity. Appendix B provides a detailed explanation of the methodology utilized for the results of the study. Appendix C includes all data that was collected, processed, and interpreted in the study area.

Geophysical Delineation of Megaporosity and Fluid Migration Pathways for Geohazard Characterization within the Delaware Basin, Culberson County, Texas

Abstract

Differential dissolution of gypsum within the Delaware Basin poses a significant threat to infrastructure that society depends on. The study area is located in Culberson County, Texas and traverses a distance of approximately 54 kilometers along RM 652 within the Gypsum Plain, which is situated on the northern margin of the Chihuahua Desert, and includes outcrops of Castile and Rustler strata that host karst geohazards. Regions of karst geohazard potential have been surveyed proximal to the study area in evaporites throughout the Castile Formation outcrop; minimal hazards, in comparison to the Castile Formation, have been documented in the Rustler Formation.

A TR-5 OhmMapper capacitively-coupled resistivity (CCR) meter was used to acquire resistivity data for geohazard characterization. This study utilized a traditional dipole-dipole array, with an electrode spacing of 2.5 meters between receivers, and a transmitter offset of 2.5 meters. This geometric configuration combined with medium analyzed, allowed for resistivity readings to be recorded up to approximately 5 meters deep. Data acquisition was recorded with the OhmMapper attached to a vehicle moving at approximately 3 kilometers per hour and transmitting and receiving once per second (approximately three feet per sample). Resistivity data was processed using AGI's

EarthImager 2D inversion software. Capacitively-coupled resistivity has shown to be effective in locating karst geohazards in the shallow subsurface.

Introduction

The Delaware Basin of West Texas and southeastern New Mexico is the northern most extension of the Chihuahuan Desert and is often referred to as the Gypsum Plain (Hill, 1996). Throughout the Gypsum Plain, significant karst geohazard manifestations have proven to be detrimental for infrastructure maintenance. The research area, RM 652, is a 54 kilometer section of roadway located on the northeastern edge of Culberson County, Texas (Figure 1). The dominant outcrop within the study area is the evaporitic Castile Formation with moderate outcrop exposures Rustler Formation in the eastern portion of the study area (Figure 2). Significant amounts of surficial karst phenomena commonly develop throughout the evaporite Castile Formation. Subsequent geohazards form from karsting, often characterized as sinkholes, solution conduits, and subsidence features (Stafford et. al., 2008).

Karst features that have substantial cover may not be easily identified by traditional mapping techniques, satellite imagery, or aerial photos (Neukum et. al., 2010). Due to the length of the study area, a non-invasive, capacitively-coupled resistivity technique was used to locate the shallow karst phenomena without surficial expressions. This method has been proven in numerous studies to be a reliable technique in locating near surface karst manifestations, with similar studies being conducted in Florida and Europe (e.g. Garman and Purcell, 2004; Vadillo et al., 2012; Samyn et. al., 2014).

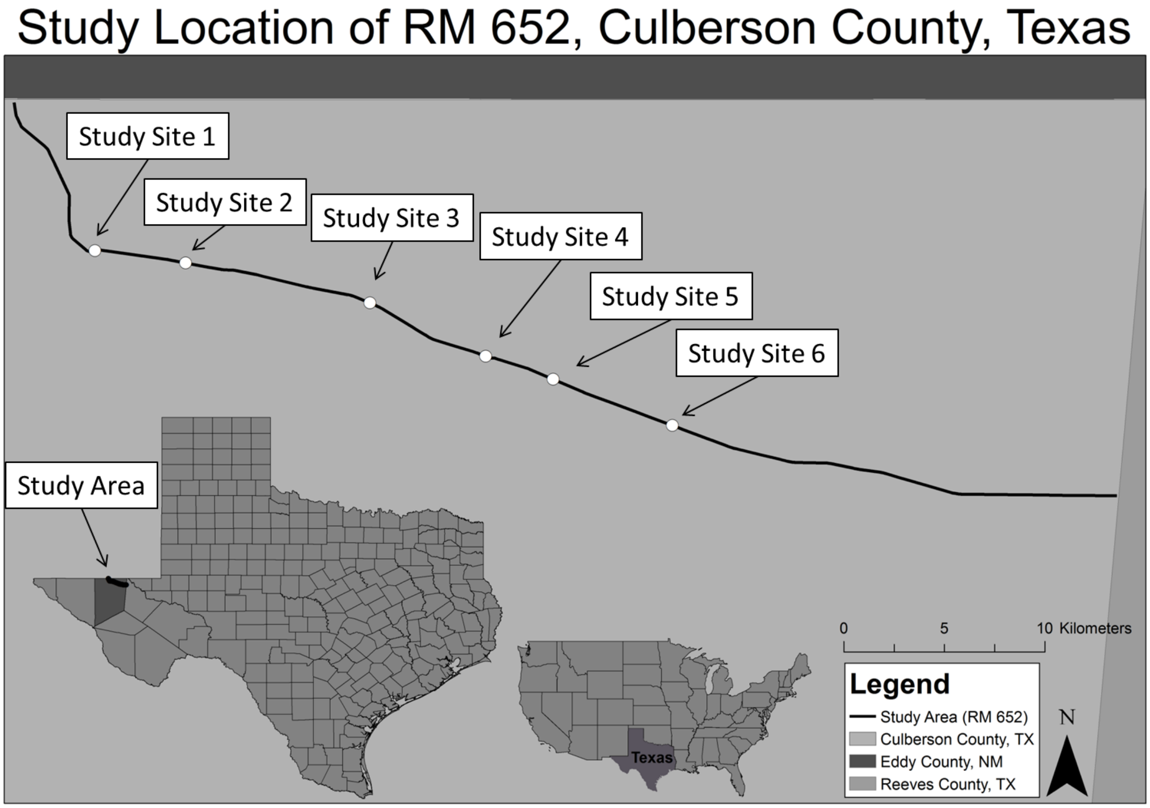

Figure 1. Geographic location of the study area, RM 652 in thickened black line stretches across the northeastern corner of Culberson County, Texas.

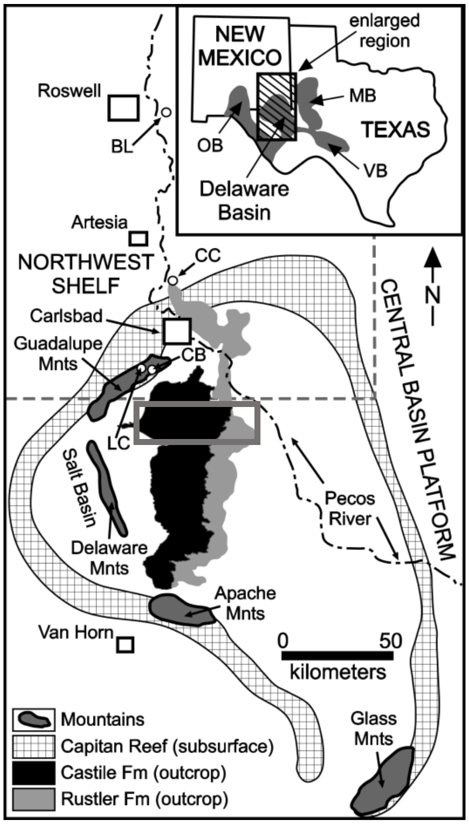

Figure 2. Map showing geographic orientation of the Delaware Basin with respect to Texas. The general study area is identified by the grey box, and primary geologic features of the region are outlined (modified after Stafford et. al., 2008).

Known areas of significant road failure, and the abundance of karst geohazard surface expressions, have justified imaging this section of roadway in Culberson County, Texas. A continuous electrical resistivity survey was conducted for approximately 54 kilometers on the westbound and eastbound lanes of RM 652. Six sites where geophysical anomalies were verified through excavation are presented in this manuscript to attest to the practicality and efficiency of using a continuous, Alternating Current (AC), resistivity method to image near surface karst phenomena.

Geologic Setting

The Delaware Basin of West Texas and New Mexico is a restricted evaporite intracratonic basin outlined by a 600-700 kilometer reef complex (Hill, 1996). During Late Mississippian and Early Permian time, the convergence of Laurasia and Gondwana resulted in the formation of Pangea. Subsequent block faulting along Precambrian zones of weakness formed the Permian Basin, which is structurally subdivided into the Midland Basin, Central Basin Platform, and Delaware Basin. Increased sediment loading aided in further separating the Delaware Basin from the Central Basin Platform (Adams, 1962). Subsidence in the Pennsylvanian-Early Permian dominated the depositional environment throughout the Permian which caused the Delaware Basin to experience deep water deposition until the end of Guadalupian time (Ross, 1981). During Guadalupian time, carbonates formed the rim of the Delaware Basin margin and early silicicalstic material was deposited into the deep basin. Extensive reef growth encircled the Delaware Basin during Ochoan time which restricted flow of open marine waters, by closure of the Hovey Channel, creating a deep saline lake and conditions conducive for late evaporite deposition. While the Castile Formation is restricted to the Delaware Basin, subsequent deposition of Salado and Rustler formations capped the entire region, including surrounding basins (Scholle et al., 2004).

Throughout the Early Mesozoic, the Delaware Basin was tectonically inactive and relatively stable. This tectonic quiescence would come to an end during Late Mesozoic when the Laramide Orogeny caused regional uplift and tilting of the basin strata approximately 3-5° to the east-northeast. Following the Laramide Orogeny, a change from compression to extension occurred within the region, leading to the Basin and Range Phase which is subdivided into three stages that affected the Delaware Basin; Transition Stage, Main Uplift Stage, and Quaternary Stage. Block faulting on the western side of the Delaware Basin during the Transition Stage is responsible for the down-drop of the Salt Basin (Hill, 1996; Figure 2). During the Main Uplift Stage, a shift of maximum stress from east-northeast to west-northwest, formed northeast trending graben-boundary faults in the basin (Hentz and Henry, 1989). Throughout the Quaternary Stage, border faults continued to be active with continued movement along the Salt Basin Quaternary faults (Hill, 1996).

Climate change within the Delaware Basin has had a profound impact on the modern geomorphic nature of the Gypsum Plain as the climate shifted from cool and wet to dry and arid. Today the average precipitation ranges from 20-40 cm with an average annual temperature of 24°C and average summertime high of 40°C. Rainfall typically occurs between May and October, however over half falls between July and September as short-duration, monsoonal-type storm events (Sares, 1984).

Karst Development

The Delaware Basin is one of the most renowned developments of gypsum karst in North America. Sinkholes, caves, and underground drainage systems are typical throughout the landscape (Hill, 1996). Gypsum outcrops generally only survive in arid climates, thus sinking stream patterns in gypsum karst tend to be small, dry arroyos that terminate into swallow holes or open caves (White, 1988).The highly soluble nature of evaporite rocks of the Castile Formation is primarily responsible for the abundance of karst throughout the Gypsum Plain. Karst expressions occur to a lesser degree in the carbonate Rustler strata because they are slightly more resilient to dissolution effects. The former widespread, halite-rich Salado Formation has undergone extensive surficial weathering and erosion in outcrop, and it has been mostly dissolved in the shallow subsurface by intrastratal dissolution thereby creating a solutional contact between the Castile and Rustler formations (Stafford et. al., 2008). Throughout the Gypsum Plain, hypergene processes dominate the surficial geomorphic evolution of surface rocks while hypogene processes seem to control the diagenetic alteration, and speleogenetic evolution (Stafford et. al., 2016).

Sinkholes, solution fractures, and caves are abundant throughout the study area forming under the influences of dissolution and suffosion. Sinkholes formed by descending water typically exhibit more lateral development and will have a series of dendritic arroyos that converge and drain into the sink while collapse sinkholes generally have steeper sides, and are normally near-circular in shape (Stafford et. al., 2008). Individual caves that have been researched throughout the Castile Formation show an intricate speleogenetic history that includes hypergene and hypogene origins (Stafford et. al., 2016). Hypergene caves form from meteoric processes near the surface and are frequently found throughout the Gypsum Plain; however, they are usually expressed as isolated features with collapsed and filled sinkholes. Hypergene caves also have a tendency to form in areas where surficial gypsic soil comes into contact with gypsum bedrock. Usually, these hypergene “gypsite” caves are either filled with soil or rapidly decrease in size away from the entrance area, limiting field surveys to within a few tens of meters. However, in some cases these gypsic caves will connect to caves that formed in gypsum bedrock which suggests that the gypsic caves provide a preferential flow path for water to drain (Stafford et. al., 2008). Hypogene caves do not have a direct connection with surface environment activity and meteoric waters at the time of formation, and thus form from dissolution caused by rising fluids in confined systems (Stafford et. al., 2008). Differences in hydraulic pressure gradients drive dissolution through convection; fluids from lower, pressurized aquifers will flow upwards to areas of a lower hydraulic pressure regime, which is often the regional base level (Toth, 1999).

Electrical Resistivity Methods

The G858 OhmMapper resistivity system, by Geometrics Inc., TR-5 configuration with a traditional dipole-dipole array was used to collect continuous resistivity data along the 54 kilometer traverse of RM 652 on the east- and west-bound lanes, of which six locations, each approximately 160 meters long, are presented. The TR-5 configuration dipole-dipole array uses one pair of current emitting electrodes (*transmitter*), and five pairs of potential electrodes (*receivers*), connected by a non-conductive tow-link cable.

The resistivity meter was attached to a vehicle and towed at a pace of ~3 km/h while simultaneously collecting GPS data with an average geometric resolution of approximately 50 cm. A 5m operator isolator cable, 2.5m dipole cables, and a 2.5m non-conductive tow-link rope configuration was used (Figure 3). This electrode geometry enabled recordings to be taken at an effective depth of penetration of approximately five meters at a resolution of approximately one sample at five different depth per meter. The OhmMapper system utilizes a working frequency of approximately 16.5 Khz that is transmitted and received through the dipole cables (Geometrics, 2016). Remote and arid location factors of the Gypsum Plain reduced concern of bad data quality normally caused by shallow skin depth and cultural noise.

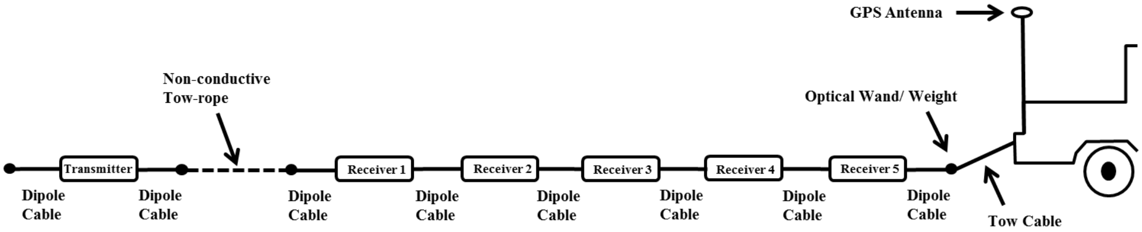

Figure 3. *Diagram of OhmMapper TR-5 resistivity meter configuration used and electrode geometries. This image shows a TR5 configuration, with a transmitter (Tx) and five receivers (Rx) that allow for five depths of investigation while continuously collecting resistivity data along a single traverse.*

Resistivity recordings and GPS data points were quality checked in MagMap2000, a pre-inversion software program by Geometrics, before importing data into the inversion program (Geometrics, 2001). Data inversion was executed in EarthImager 2D, a product of Advanced Geosciences Incorporated (AGI). A smooth model inversion was chosen because of its dependability and ability to generate clear resistivity boundaries (AGI, 2007). The six resistivity profiles rendered by inversion were terrain corrected against data extracted from a digital elevation model, which was constructed from LiDAR data and processed in ArcGIS. LiDAR data was acquired with a horizontal resolution at 0.3-0.4 meters with 10 centimeters vertical resolution (Ehrhart, 2016).

Study Sites and Characterization

Study Site 1 (160 meter segment)

Study Site 1 was chosen due to significant anomalous patterns found within the profile (Figure 4A, 5A). Road failure and water ponding commonly occur above areas indicated to be collapse and/or void features; deeper resistivity surveys were required to further characterize collapse features. However, interpretations of “Cave 1” were confirmed through field check excavation, and other anomalous signatures that corresponded to its pattern were interpreted to be similar features (Figure 6A). Traditionally, caves are defined by their ability to allow for human entry. However, this study extends the definition of caves to include features large enough to allow the passage of a substantial amount of sediment and fluid. This “Cave 1” feature was approximately 30 cm tall, two meters wide and partially filled with water saturated soil and void space traversing directly under the roadway. Surface runoff at the site flows to the northeast; surface expressions on the southern road margin collect runoff and sediment transporting it under the roadway.

Study Site 2 (Approximately 160 meter segment)

Study Site 2 was selected for excavation in order to confirm anomalous patterns seen in profile (Figure 4B) and significant water ponding during the monsoonal season. Differential dissolution of gypsic soil, used as original road base material during construction, resulted in filled sink features and preferential soil piping under and along the survey path (Figure 5B). Through field excavations, interpretations of this filled sink were verified, along with many soil piping features (Figure 6B). This resistivity method was able to uncover many filled sink geohazards that do not have surficial expression connecting directly to subsurface conduits that would otherwise reveal their presence. These sites represent areas of preferential ponding and increased infiltration leading to increased dissolution of the gypsic soil road base.

Study *Site 3 (Approximately 160 meter segment)*

Study Site 3 was selected for field evaluations so that anthropogenic enhancement effects could be included in characterization. The resistivity profile along this segment indicated significant void space (Figure 4C). This anomaly occurred proximal to a “toe wall” (i.e. concrete-reinforced vertical barrier at the margin of the road) that was designed to direct water away from the roadway and to maintain infrastructure stability, which site excavation verified (Figure 5C). A large conduit approximately 11 cm in diameter was uncovered at an approximate depth of 1.5 m in the trench (Figure 6C). During excavation, substantial water and sediment drained through this solution conduit in the gypsum bedrock as field excavations were underway indicating an extensive dissolution network beneath the road at depth. Anomalous patterns, such as the ones identified at *Study Site 3*, were seen on resistivity profiles in areas associated with "toe walls" and drainage retention berms throughout the study.

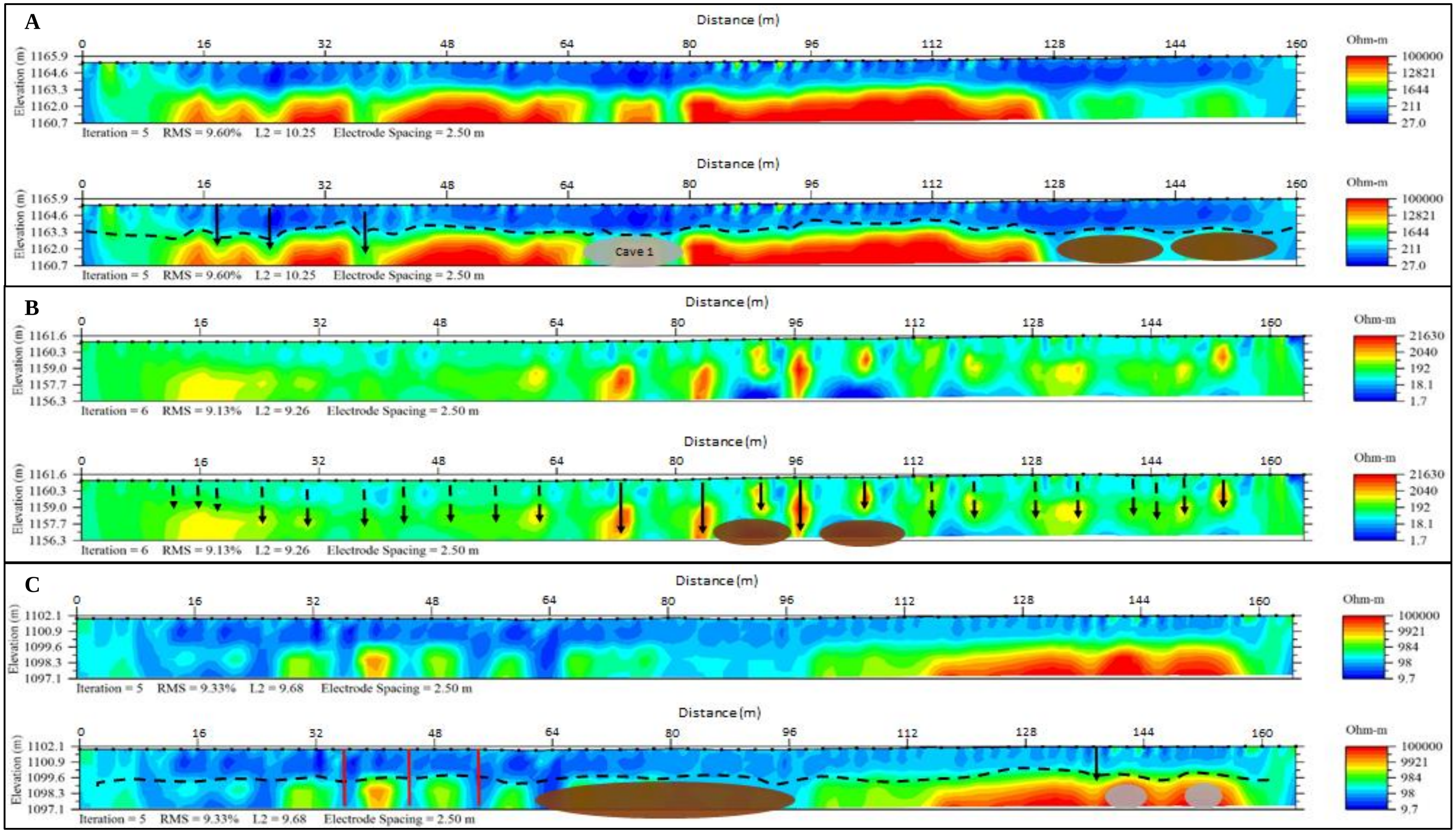

Figure 4. All profiles are displayed at a 2:1 vertical to horizontal scale ***A)*** *Site 1* inverted and interpreted section. RMS error = 9.60%, iteration = 5. The black dashed line = soil-rock contact, black arrows = solution conduits, brown polygon = leached zones, grey polygon = Cave 1; ***B)*** *Site 2* inverted and interpreted section. RMS error = 9.13%, iteration = 6. Black arrow = solution conduits, black dashed arrows = soil piping, brown polygon = filled sinks; ***C)*** *Site 3* inverted and interpreted section. RMS error = 9.33%, iteration = 5. Black dashed line = soil-rock contact, black arrows = solution conduits, red lines= fractured rock, brown polygon = filled sink, grey polygon = cave locations.

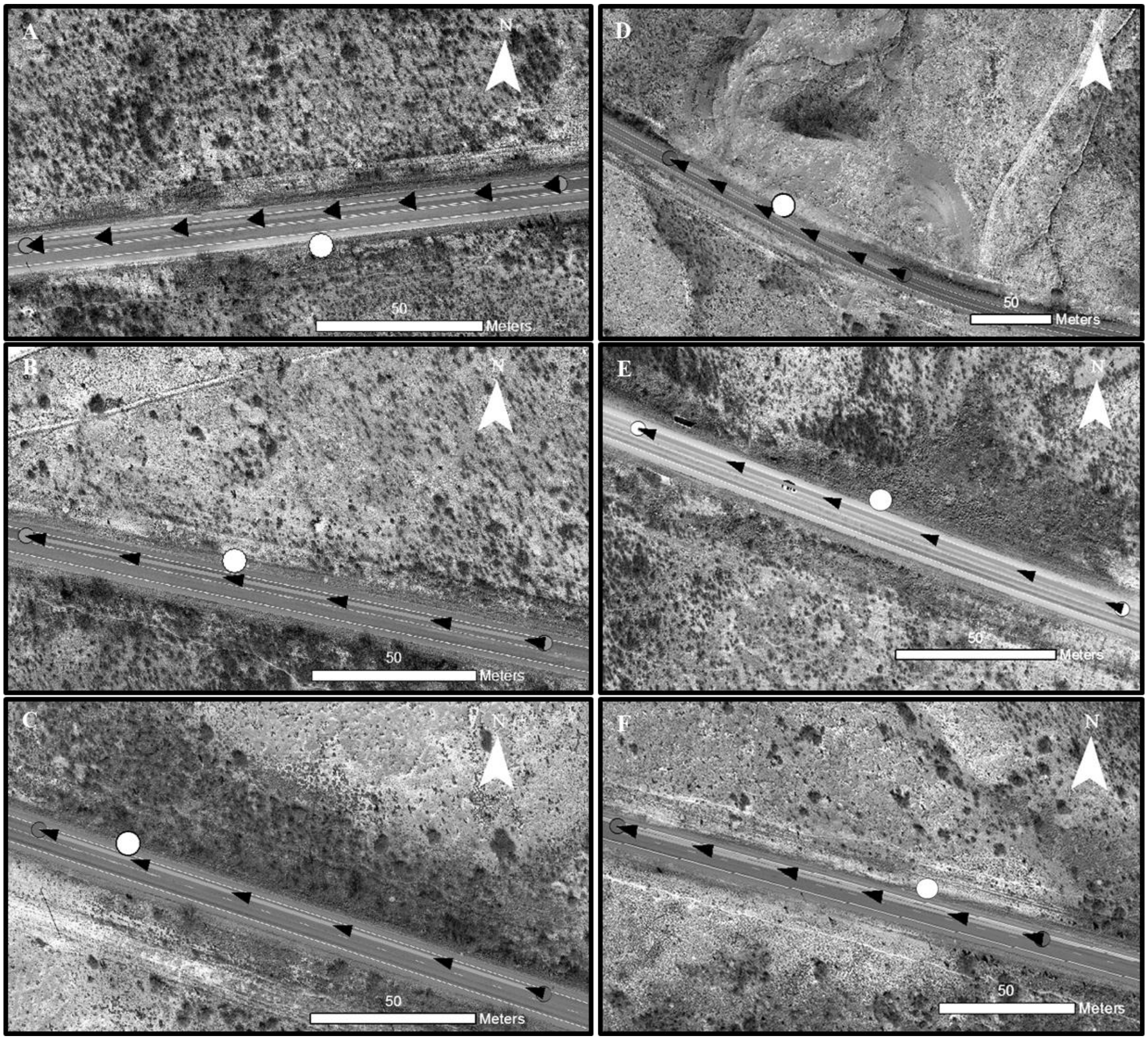

Figure 5. Excavation locations are marked by the circle, survey path is marked by black arrows which indicate survey direction, and the scale bars represent 50 meters on the surface. ***A)*** *Study Site 1* ***B)*** *Study Site 2* ***C)*** *Study Site 3* ***D)*** *Study Site 4* ***E)*** *Study Site 5* ***F)*** *Study Site 6.*

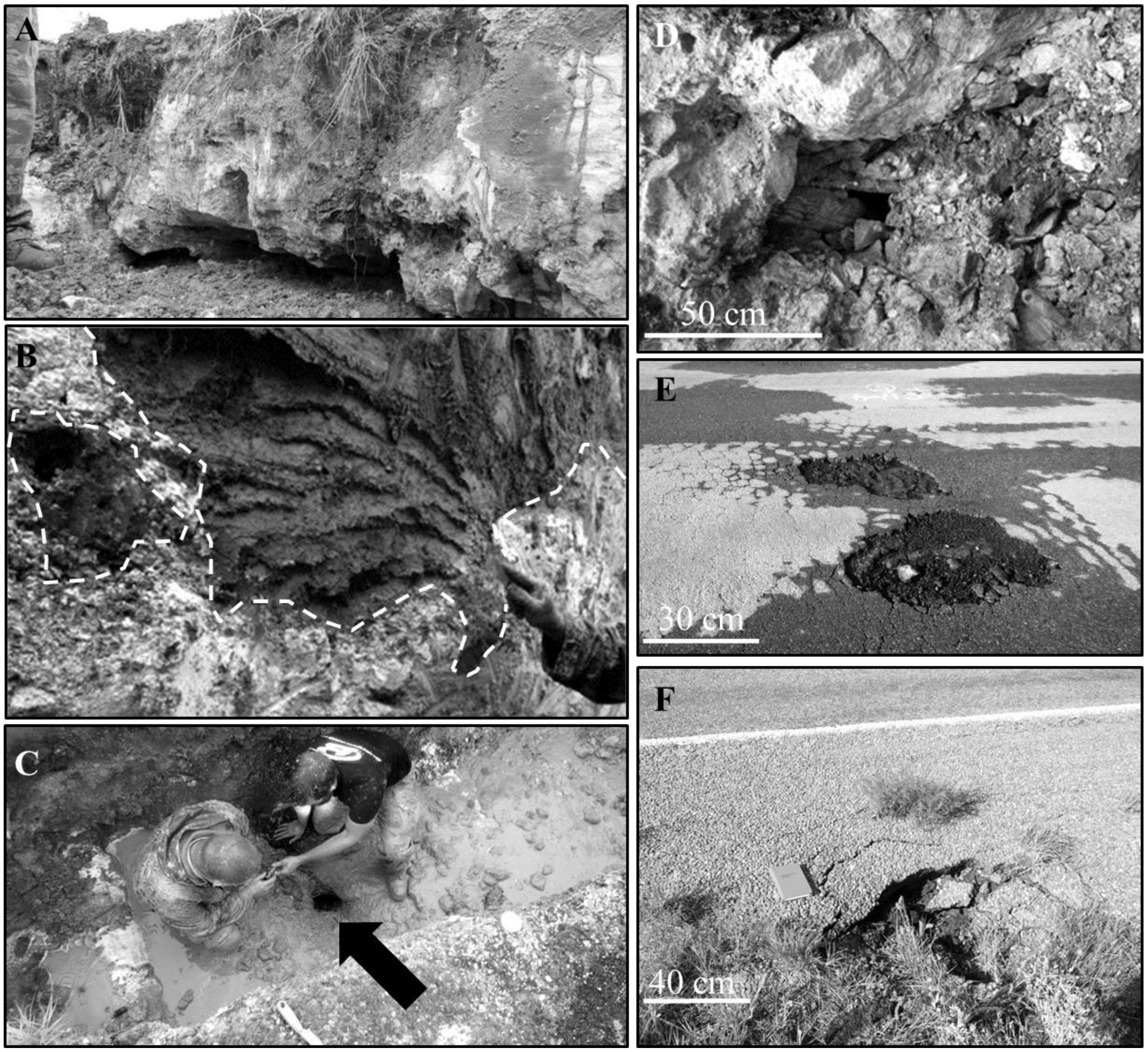

Figure 6. A) Photo of “Cave 1” at *Study Site 1* partially filled with soil and extending directly beneath RM 652; ***B)*** Photo of filled sink feature along with preferential soil piping at *Study Site 2* outlined by the white dashed lines; ***C)*** Photo of solution conduit likely enhanced by anthropogenic structures is indicated by the black arrow at *Study Site 3* ***D)*** Photo of brecciation at Study *Site 4* exhibiting pathways of preferential fluid flow throughout collapse feature; ***E)*** Photo of roadway failure along survey path induced by soluble nature of gypsic road-base at Study *Site 5*; ***F)*** Photo of a solution conduit expressed at Study *Site 6;* features such as this express themselves along the roadway as a result of dissolution and suffosion.

Study Site 4 (Approximately 160 meter segment)

Brecciation is common within the Castile Formation and resistivity profiles at Study Site 4 show significant anomalous patterns where analyses pass through a roadcut within a breccia pipe (Figure 5D; Figure 7A). This study site was located on a topographic high and descended down slope perpendicular to the margin of the exposed breccia pipe which likely extends through the entire thickness of the Castile Formation (Hill, 1996). These features are generally re-cemented after a collapse and most often exhibit low permeability conditions within the breccia core, but frequently possess higher permeability characteristics on their outer margins (Figure 6D). Brecciation within the study area seems to be a result of intrastratal dissolution of evaporites by hypogenic speleogenesis, where a void formed at depth and stoped upward (Stafford et. al., 2008; Figure 9A).

Study Site 5 (Approximately 160 meter segment)

Study Site 5 exhibited a resistivity profile that contained significant soil piping anomalous patterns that matched previously excavated locations (Figure 5E; Figure 7B). Since the roadway was elevated substantially in this location during construction, the resistivity profile does not penetrate deep enough to identify a soil/rock contact, but it does indicate areas of soil piping and water retention. The differential dissolution of gypsic soil used in the original road base construction exhibits preferential soil piping.

This piping enhances degradation of RM 652 and can lead to a higher soil moisture retention, which promotes disaggregation of asphalt at the surface (Figure 6E).

Study Site 6 (Approximately 160 meter segment)

Study Site 6 was chosen because of a trend of anomalous patterns observed in previous excavations that matched solution conduits, fractured rock, filled sinks, and cave locations (Figure 5F; Figure 7C). Surface expressions of solution conduits populated this road segment and are indicated in the resistivity profile below. These surficial karst features allow for suffosion processes to remove surface sediments, and in this case, the road itself (Figure 6F).

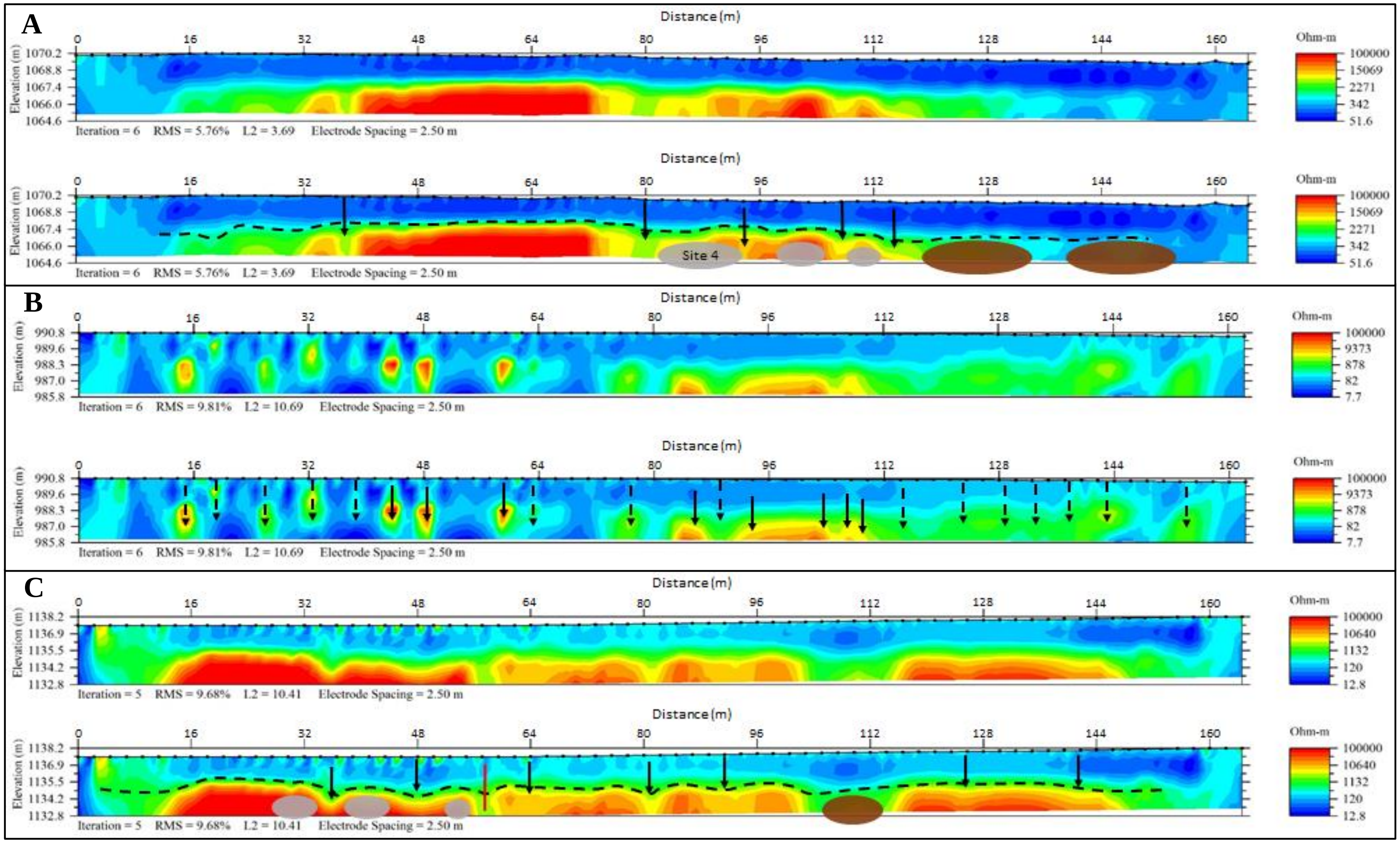

Figure 7. All profiles are displayed at a 2:1 vertical to horizontal scale ***A)*** *Site 4* inverted and interpreted section. RMS error = 5.76%, iteration = 6. The black dashed line = soil-rock contact, black arrows = solution conduits, brown polygon = road fill, grey polygon = Brecciation; ***B)*** *Site 5* inverted and interpreted section. RMS error = 9.81%, iteration = 6. Black arrows = solution conduits, black dashed arrows = soil piping; ***C)*** *Site 6* inverted and interpreted section. RMS error= 9.68%, iteration = 5. Black dashed line = soil-rock

Karst Phenomena Discussion

Karst topography throughout the Gypsum Plain develops through natural processes that can be intensified by anthropogenic structures. Karst terrains commonly display complex systems that communicate between geomorphological, hydrogeological and stratal diagenesis (Stafford et. al., 2008). Suffosion processes dominate regions of dense karst geohazard potential, and are most likely connected to deeper karst features that allow fluid and sediment transport. During monsoon seasons, heavy rain events dissolve highly susceptible evaporite rocks and widen solution fractures in gypsum bedrock. This solutional widening leads to greater suffosion piping rates of gypsic soil and induces failures, along with subsidence, under the margins and traverse path of the road within the study area.

Anthropogenically-enhanced karst features are due largely to traditional road construction techniques during infrastructure development and subsequent maintenance stages. In areas along the road, complex resistivity profiles correlated well with areas containing a concrete "toe wall” and retention berm emplacement despite their purpose to redirect flow away from the thoroughfare. Instead of maintaining roadway integrity, these practices caused water to infiltrate into the highly soluble gypsic road-base materials, dissolving the high gypsic content, allowing for preferential flow paths to form and increasing permeability. This gradual increase in flow, coupled with heavy traffic can accelerate dissolution of gypsum bedrock, causing void geohazards to manifest, leading to collapse and road failure.

In survey locations such as Study *Site 2* and Study *Site 5* where the road has been elevated with gypsic soil, the soil-rock contact is not seen in the resistivity profiles. However, significant piping and frequent sinks can be found in areas where gypsic roadbase is abundant. These features lead to an increase in subsidence that can be visibly seen on the surface, especially in rain events when water ponding occurs. Profiles containing more gypsic soil than bedrock tend to have lower resistivity readings, but that is most likely due to soil water retention, which continues to weaken the road above it.

Surveys containing soil-rock contact horizons show signs of significant dissolution and degradation of gypsum bedrock. Study *Sites 1, 3,* and *6* contain signature anomalies that match surface expressions of fractured gypsum bedrock that are solutionally widening slowly. These fractures enable greater fluid migration, contributing to suffusion processes and formation of caves under the roadway. At Study *Site 1,* the excavation location was across the road from the interpreted resistivity profile, which was chosen to illustrate feature communication under the road through a network of passageways.

Zones of brecciation are common throughout the Castile Formation; however, they vary in their origin. Blanket breccias frequently occur laterally over wide regions as thin layers, while breccia pipes are vertically extensive but laterally-limited (Stafford et.

al., 2008). A roadcut at Study *Site 4* exposes a breccia pipe that is represented as a topographic high with abrupt changes in resistivity occurring along the margins of the roadcut. While the cores of these features appear well-cemented, high permeability seems to be dominant along the margin of breccia pipes. Further dissolution and collapse of brecciated zones will lead to increased piping and fracturing allowing for a perpetuating cycle of increased dissolution under RM 652.

The karst density distribution along the study area varies according to geologic properties of shallow rocks and anthropogenic enhancements perpetuating suffusion and dissolution. These destructive geologic features predominate the western side of the study area where the Castile Formation outcrops (Figure 10). Individual geohazards delineated through "CCR" methods are most likely underestimated compared to the total amount of existing features. Therefore, a statistical analysis was executed based on hazard density in order to achieve an accurate representation of geohazard occurrences. Karst development typically suggests a fractal pattern where positioning of large-scale phenomena perpetually repeats at smaller scales (Stafford et. al., 2016).

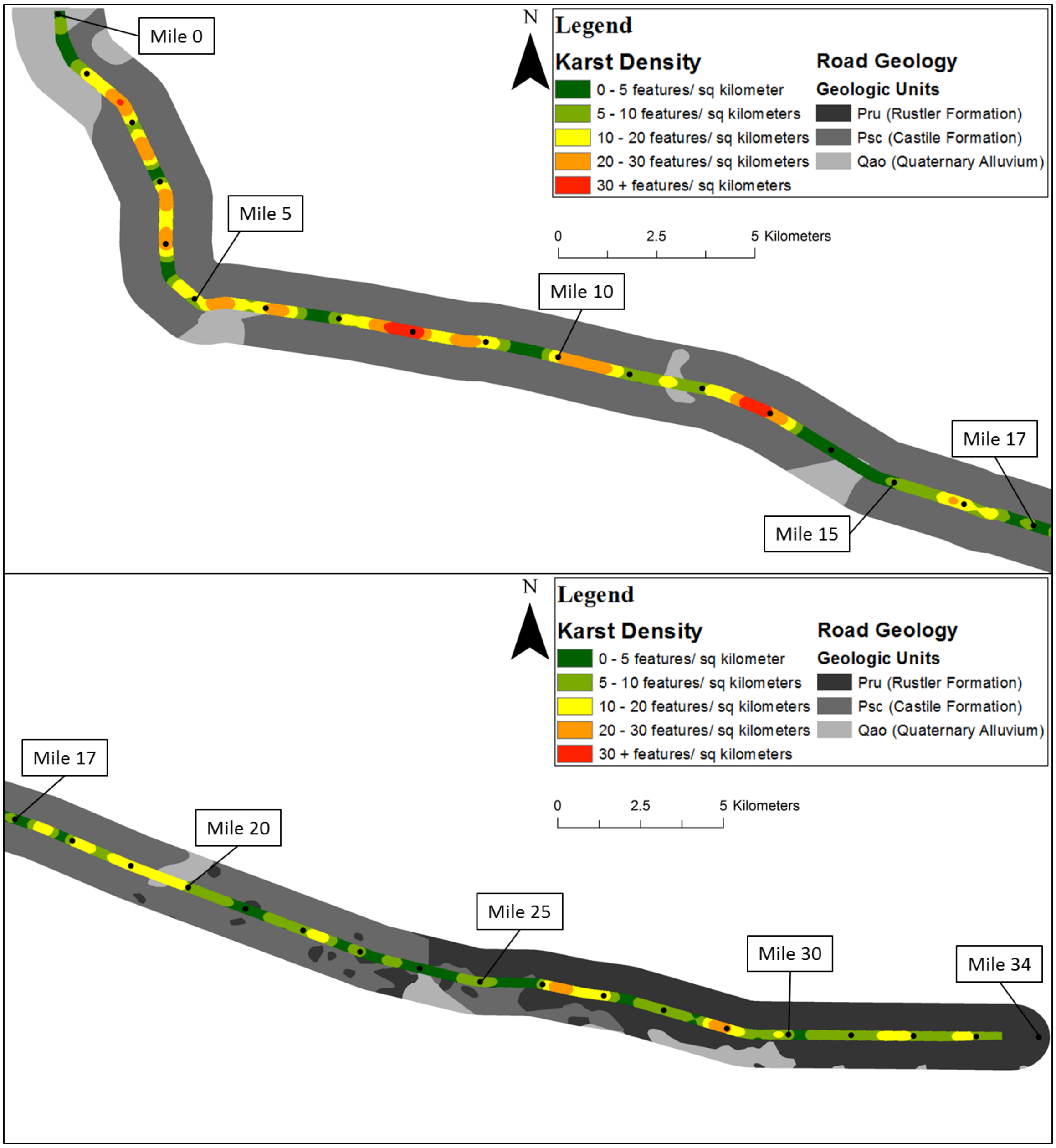

Figure 8. Maps of the study area illustrating the spatial density of karst phenomena delineated by “CCR” methods, and the geologic formations associated with karsting. The density was measured by calculating the occurrence of individual geohazards against square kilometers, **Top)** Contains the beginning of the study area where RM 652 intersects US highway 62/180 and ends at mile marker 17, **Bottom)** begins with mile marker 17 and ends at mile marker 34.

Conclusion

Karst features pose a significant threat to infrastructure within the Delaware Basin. The 54 kilometer long segment of RM 652 that traverses Culberson County is experiencing severe degradation due to differential compaction and dissolution of soluble soil/rock in the subsurface, preferential piping of road base material and general suffosion processes. Furthermore, traditional engineering techniques used to control surface water drainage have enhanced formation of karst manifestations in the study area. Numerous karst surface expressions have been surveyed along the study area, and in adjacent private properties (Ehrhart, 2016). Large sinks, solutional fractures, and caves are forming a network of conduits throughout the study area, which enhance subsurface fluid flow along with road failure. Field excavations confirm capacitively-coupled resistivity to be a successful non-invasive method in locating significant karst features, while being a cost effective and time efficient method over long distances. These 2D resistivity surveys, along with hydrogeologic knowledge of the area, were crucial in interpretation and characterization of the study area.

The use of non-invasive, geophysical methods to characterize subsurface phenomena, such as karst, should be utilized to aid in development and maintenance of infrastructure. This method can provide insight into significant problems beneath the subsurface, that could otherwise remain undetected and cause catastrophic failure and financial burden.

Acknowledgements

This research was partially funded by the Texas Department of Transportation (TxDOT) with support from the Department of Geology at Stephen F. Austin State University. The authors are thankful for the generous field assistance of individuals that made this work possible: Aaron Eaves, Adam Majzoub, and Niko Welch.

References

Adams, J. E., 1962, Foreland Pennsylvanian rocks of Texas and eastern New Mexico; in Branson, C. C. (ed.), Pennsylvanian system in the United States: American Association of Petroleum Geology, Tulsa, OK, pp. 372-384.

AGI, 2007, Instruction Manual for EarthImager 2D Resistivity and IP Inversion Software: Austin, TX, Advanced Geosciences, Inc., 139pp.

Ehrhart, Jon T., 2016, "Speleogenesis and Delineation of Megaporosity and Karst Geohazards Through Geologic Cave Mapping and LiDAR Analyses Associated with Infrastructure in Culberson County, Texas" (2016). *Electronic Theses and Dissertations*. 66.

Garman, K. M., and Purcell, S. F., 2004, Applications for Capacitively Coupled Resistivity Surveys in Florida; The Leading Edge, v. 23, no. 7, pp. 697-698.

Geometrics, 2001, Geometrics Operation Manual: OhmMapper TR1, 29005-01, Rev. F. 134 pp.

Geometrics, 2016, OhmMapper: <http://www.geometrics.com/geometrics-products/geometrics- electro-magnetic-products/ohm-mapper>. Accessed December 13, 2016.

Hentz T.F., and Henry C.D., 1989, Evaporite-hosted native sulfur in Trans-Pecos Texas: relation to late-phase Basin and Range deformation. Geology 17:400-403.

Hill, C.A., 1996, Geology of the Delaware Basin, Guadalupe, Apache and Glass Mountains: New Mexico and West Texas. Permian Basin Section – SEPM, Midland, TX, 480 p.

Neukum, C., Grutzner, C., Azzam, R., and Reicherter, K., 2010, Mapping buried karst features with capacitive-coupled resistivity system (CCR) and ground penetrating radar (GPR). *Advances in Research in Karst Media* (2010): p. 429-434.

Ross, C. A., 1981, Pennsylvanian and Early Permian history of the Marathon Basin, West Texas; in Pearson, B. T. (field trip leader), Marathon-Marfa region of West Texas: Soc. Econ. Paleontol. Mineral., Permian Basin section, Guidebook Publ. 81-20, pp. 135-144.

Samyn, K., Mathieu, F., Bitri, A., Nachbaur, A., Closset, L., 2014, Integrated geophysical approach in assessing karst presence and sinkhole susceptibility along flood-protection dykes of the Loire River, Orléans, France; Engineering Geology, v. 183, pp170-194.

Sares, S. W., 1984, Hydrologic and geomorphic development of a low relief evaporite karts drainage basin, southeast New Mexico; MS Thesis, Albuquerque, University of New Mexico, 123 pp.

Scholle, P.A., Goldstein, R.H., and Ulmer-Scholle, D.S., 2004, Classic Upper Paleozoic Reefs and Bioherms of West Texas and New Mexico. New Mexico Institute of Mining and Technology, Socorro, NM, 166p.

Stafford, K., Nance, R., Rosales-Lagarde, L., and Boston, P., 2008, Epigene and hypogene gypsum karst manifestations of the Castile Formation: Eddy County, New Mexico and Culberson County, Texas, USA: International Journal of Speleology IJS, v. 37, pp. 83–98.

Stafford, K. W., Brown, W., Ehrhart, J., Majzoub, A., Woodard, J., 2016, 2016 Karst Geohazard Characterization of RM 652: Phase Two of Karst Development and Geohazards Associated with RM 652 in Culberson County, Texas

Toth J., 1999, Groundwater as a geologic agent and overview of the causes, processes, and manifestations. Hydrogeology Journal, 7: 1-14.

Vadillo, I., Benavente, J., Neukum, C., Grutzner, C., Carrasco, F., Azzam, R., Liñán, C., Reicherter, K., 2012, Surface geophysics and borehole inspection as an aid to characterizing karst voids and vadose ventilation patterns (Nerja research site, S. Spain); Journal of Applied Geophysics, doi: 10.1016/j.jappgeo.2012.03.006.

White, W. B., 1988, Geomorphology and Hydrology of karst terrains: Oxford Univ.Press, New York, 464 pp.

APPENDIX A

LITERATURE REVIEW

Introduction

The Permian Basin formed as Laurasia and Gondwana collided to create the supercontinent Pangea. Due to compression from plate suturing, associated block-faulting took place and further divided the ancestral Permian Basin into the following components: the Delaware Basin in the west, the Central Basin Platform, the Midland Basin to the east, and the Val Verde Basin to the southeast as the Central Basin Platform became a structural high (Figure A1). The basins were eventually filled with clastic, carbonate, and evaporate facies during Permian time. Carbonates rimmed the Delaware Basin margin, while early clastic material filled the deep basin, culminating in late evaporite formations capping off the basin (Hill, 1996). The later evaporate deposits provided for karst development in the region. Karst development throughout the Delaware Basin is widespread, and the Castile Formation contains the largest concentration of karst features. This karst development is causing the integrity of RM 652 in Culberson County, Texas, to degrade. This failure is initiated by fluids migrating through megaporosity, or conduits, causing karst geohazards to form in the subsurface (Stafford, 2015).

The Delaware Basin is a proven economic resource for the oil and gas industry. This stretch of road in particular experiences a large amount of commercial traffic and the transportation of heavy equipment to support the expansion and continuation of the industry. Due to the combination of heavy traffic, heavy rain events, and the nature of soluble rock, zones of weakness have developed along the road.

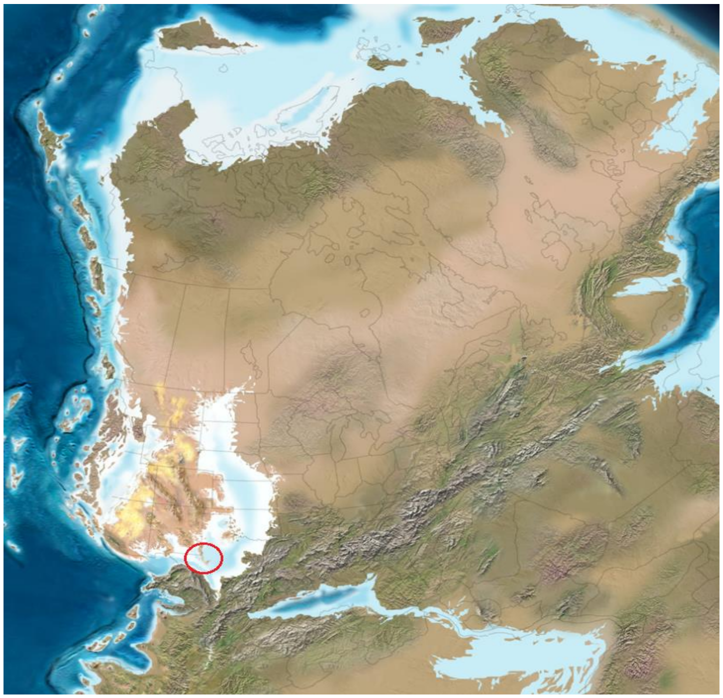

Figure A1. *Early Permian time showing the formation of Pangea and development of the Permian Basin. Permian Basin indicated by the red circle (modified from Blakey, 2016).*

The study area, RM 652, is located in Culberson County, Texas (Figure A2). It is positioned on the northern end of the Chihuahua Desert, and is focused on strata of the Castile and Rustler formations that outcrop in the Gypsum Plain within the Delaware Basin. This region is typically characterized as having an arid to semiarid continental climate with average precipitation ranging from 20-40 cm, an average annual temperature of 24°C and average summertime high of 40°C. Rainfall typically occurs between May and October; however, over half falls between July and September (Hill, 1996).

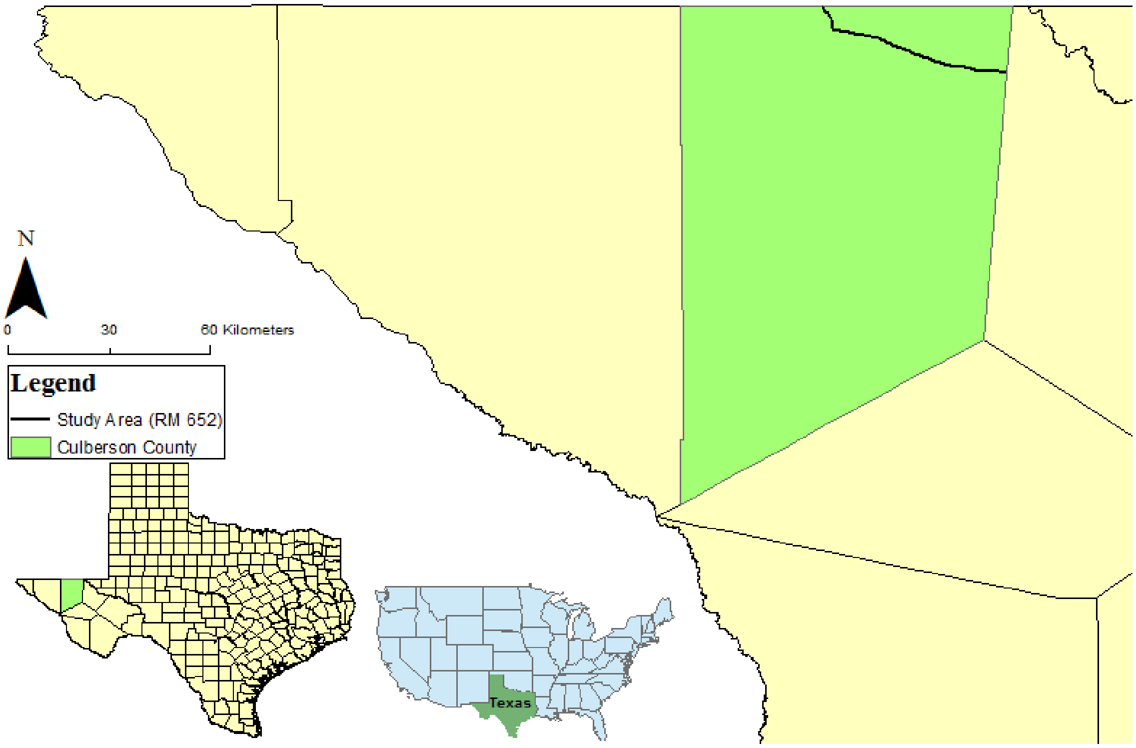

Figure A2. *Map showing the location of the 54 kilometer long study area, RM 652, in Culberson County, Texas.*

The Gypsum Plain is situated in the west to central part of the Delaware Basin. It is an area of low relief, approximately 12-40 km wide and about 90 km long. It is bordered to the west by a graveled plain at the foot of the Delaware Mountains and on the east by the Rustler Hills. It stretches northward from the Apache Mountains to Carlsbad, New Mexico (Figure A3). The Gypsum Plain is rife with caves, sinkholes, and other dissolution features.

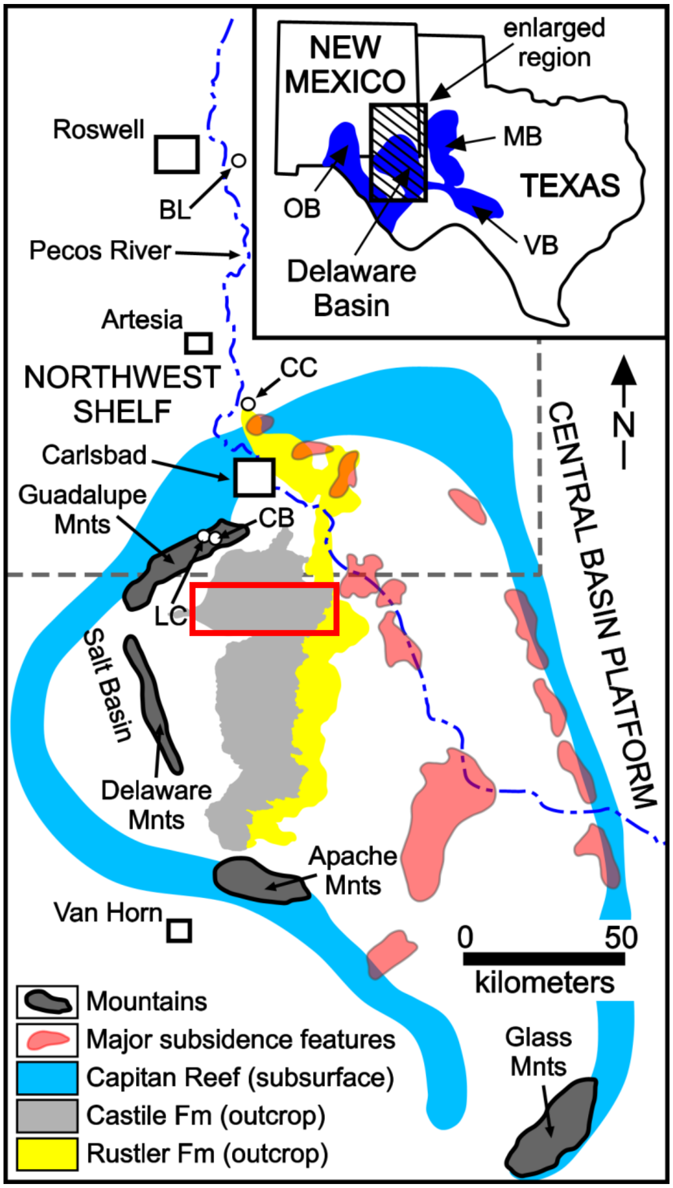

Figure A3. *General location of the study area, outlined by the red box, within the Gypsum Plain showing outcrops of the Castile and Rustler formations, and locations of prominent features such as the Guadalupe Mountains, the Capitan Reef Complex, the Apache Mountains, and the city of Carlsbad, New Mexico (modified from Stafford et al., 2008c).*

Due to the significant surficial karst manifestations along the roadway, electrical resistivity readings were conducted along the 54 kilometer segment of RM 652, on the east and westbound lanes. A TR-5 OhmMapper capacitively-coupled resistivity meter, designed by Geometrics Inc., was used to collect resistivity data. The OhmMapper was used for several reasons; it is a non-invasive tool making it environmentally friendly, it is cost effective by allowing data acquisition to take place in a shorter amount of time than traditional instrumentation using galvanic stakes, and this tool is able to image anomalies as deep as five meters. These attributes allow for shallow resistivity investigations to occur at larger scales.

Structural Evolution of the Delaware Basin

Precambrian – Cambrian

The tectonic evolution of the Delaware Basin can be divided into eight phases which were inspired by, and since modified from, Horak (1985b). During the late Proterozoic the North American craton was situated on the supercontinent Rodinia (Dickinson, 1981). The tectonic events, of the Delaware Basin area, at this time are vague, but the trends that were established in response to the Grenville Orogeny appear to be the earliest that can be interpreted (Horak, 1985b). The Grenville Orogeny can be characterized as a widespread and ubiquitous tectonic event, during which time caused crustal shortening and thrust faulting associated with compressional tectonics, causing regional metamorphism (Hill, 1996). The later Precambrian has been interpreted as being a time of crustal extension, and rifting (Figure A4). This caused north-northwest trending, high-angle faults within the Delaware Basin. Both of these tectonic events, along with associated tectonic fabrics, are considered to have an influence on later structural events that would impact the basin. This time frame is considered to be the Precambrian Phase, of the basin.

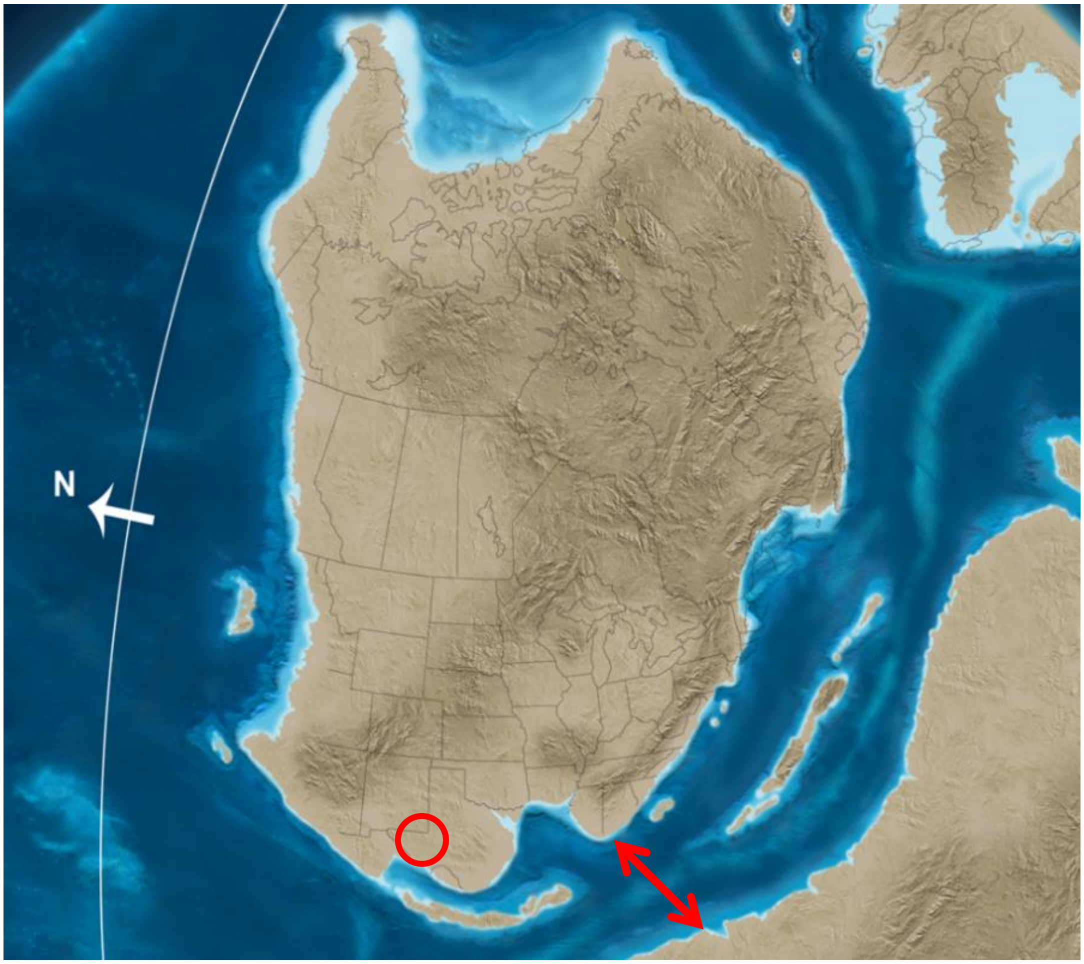

Figure A4. *Paleogeography of the Delaware Basin during Late Precambrian time. The red circle indicates the general area of interest, and the red arrow indicates extension and rifting (modified from Blakey, 2016).*

Cambrian – Late Mississippian

From the Late Precambrian to the Late Mississippian, the Delaware Basin was part of a larger basin known as the Tabosa Basin. Throughout this time, passive continental margins flanked both sides of the North American Craton, and passive subsidence allowed for successions of shelf sediment to accumulate across broad belts of North America (Hill, 1996). The Tabosa Basin formed in the Cambrian due to the rifting of a continental block inland from a continental margin of the North American craton (Dickinson, 1981). Afterwards, a shallow sea advanced over the southeastern New Mexico and west Texas areas, this deposition continued almost uninterrupted for 300 million years, drowning the basin, with the exception of minor periods of exposure (Figure A5). This long period of passive sedimentation, with no major episodes of tectonism, is known as either the "sedimentation phase" (Hills, 1985) or the "passive margin phase" (Horak, 1985b). Minor tectonic activity may have interrupted the early Paleozoic stable platform-basin setting during the Early Ordovician and Late Devonian-Mississippian (Hill, 1996). Block faulting was produced from weak extension in the Early Ordovician, and a western compressive stress from the Antler Orogeny, in the Late Devonian-Mississippian, produced broad arching over most of New Mexico and Northern Texas. Throughout this time, the Tabosa Basin was a prominent sag in the southern area of this transcontinental basement arch (Figure A6). This sag is representative of a long period of slow crustal warping and sagging (Horak, 1975).

Figure A5. *Paleogeography of the Tabosa Basin from the Cambrian to Late Mississippian indicated by the red circle (modified from Blakey, 2016)*

Figure A6. *Westward compression, causing the Tabosa Basin to sag and broad arching across New Mexico and portions of Texas during Late Devonian time (modified from Blakey, 2016).*

Late Mississippian – Early Permian

During this time period, a major tectonic episode occurred in the Delaware Basin, and it was the product of the continents Laurasia and Gondwana colliding to form the supercontinent Pangea (Figure A1). This major collision not only produced the Ouachita Orogeny in the Marathon-Delaware Basin area, but it was also responsible for the creation of the Appalachian Mountains. The Ouachita Orogeny had an approximate directed stress of N35˚W which propagated into the foreland and caused a reactivation of the PreCambrian block faulting. This caused the Central Basin Platform to rise and the Delaware and Midland Basins to sink, marking the end of the Tabosa Basin and manifestation of the Permian Basin (Figure A7). The basement block faulting within the Delaware Basin created the north-northwest trending Haupache, West Platform, and Central Delaware Basin fault zones (Hill, 1996). Thermal doming of the lithosphere in Pennsylvanian time caused the development of a triple junction rift system that aided in the formation of the Delaware, Val Verde, and Marfa Basins (Elam, 1984). Local melting related to high heat is interpreted within the upper continental crust and this is believed to have created anticlines in Pennsylvanian rock that are now some of the main structural trapping mechanisms for oil and gas in the Delaware Basin (Hill, 1996). Throughout the Pennsylvanian, the Delaware Basin subsided rapidly due to increased compression from the Ouachita orogenic front. The orogenic uplift of the Marathon-Glass Mountains region was followed by subsequent erosion of the uplifted highs. This eroded sediment filled in the newly formed Delaware Basin, and due to sediment loading, began to further separate the Delaware Basin from the Central Basin Platform (Adams, 1962). Subsidence in the Pennsylvanian-Early Permian was the controlling factor of the depositional environment throughout most of the remaining time left in the Permian; this caused the Delaware Basin to stay a deep-water basin until the end of Guadalupian time (Ross, 1981). Towards the end of this sedimentation process, shallow marine shelves were progressively thrust over one another due to northwestward growth by tectonic influences (Hill, 1996). Folding and faulting were effectively completed by the end of Leonardian time within the Delaware Basin (Ross, 1978a).

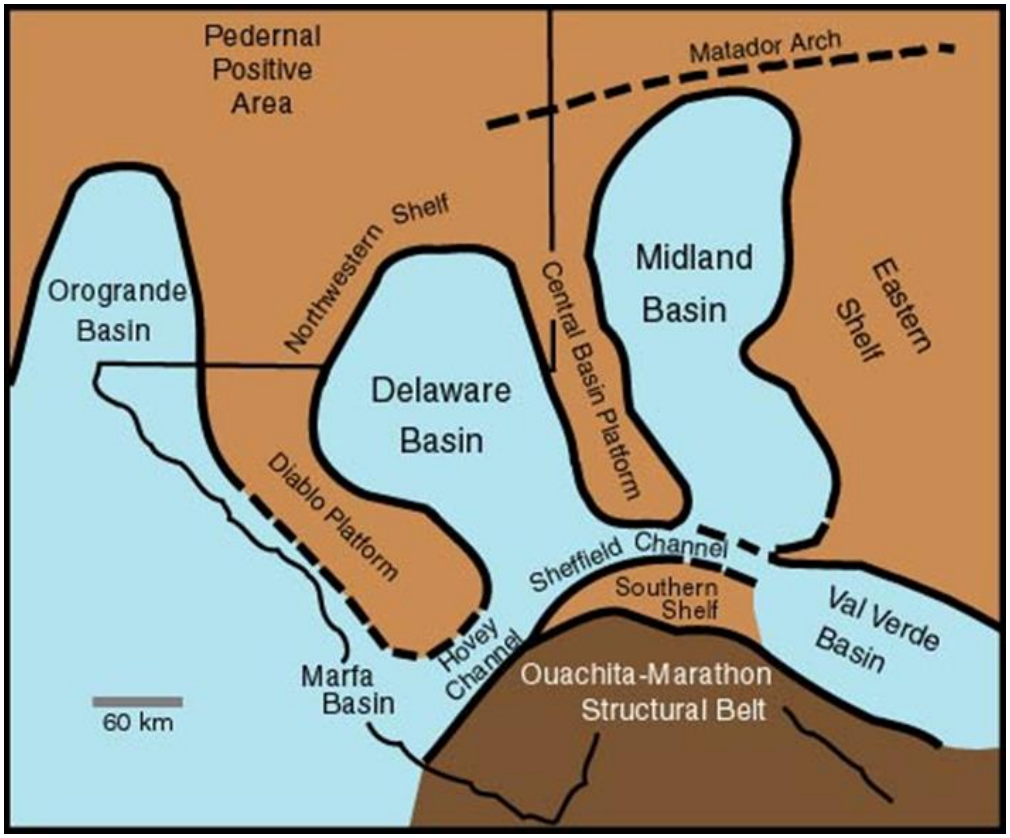

Figure A7. *Diagram showing the divisions of the Permian Basin (modified after Hill, 1996).*

Permian

The Delaware Basin was positioned along the western edge of Pangea at approximately 5-10˚N latitude during Permian time (Burdett, 1985). The Permian time was tectonically quiet throughout the Delaware Basin area. Subsidence that began in the Pennsylvanian continued into the later Permian due to increased load of sediment supplied dominantly by the Padernal landmass to the northwest and the Ouachita Uplift to the south (Hill, 1996). Approximately 2 km accumulated on the shelf of the Delaware Basin throughout this time (King, 1942, 1948). This time-span of tectonic quiescence was termed the Permian Phase by Horak (1985b), and stretches from the Wolfcampian to Ochoan. During the Permian, this region continued to be divided into the Delaware Basin, Midland Basin, and Central Basin Platform (Figure A8). The Delaware Basin was the most long-lived center for subsidence within the Permian Basin (Hill, 1996). The most rapid subsidence occurred in the Wolfcampian in the southern Delaware Basin; between the Marathon thrust sheets and the Fort Stockton Uplift due, most likely, to flexural subsidence (Ewing, 1993). Even though the majority of Permian time is identified as tectonically passive, several authors have concurred that the Delaware Basin was uplifted on its western end during the Late Permian-Triassic. While the evidence provided seems to support such an uplift, it is not clear what the mechanism of this uplift were, nor is there an indication of the magnitude of this upward movement (Hill, 1996).

Figure A8. *Paleogeography of the Delaware Basin throughout the Permian. Red circle indicates the Permian basin (modified after Blakey, 2016).*

Triassic – Late Cretaceous

Throughout the Triassic and Jurassic, the Delaware Basin experienced subaerial exposure and was dominated by clastic sedimentation. Rifting along the Mojave-Sonora megashear in the Late Triassic-Late Jurassic-Early Cretaceous separated North and South America. This situation reflected global patterns of sea floor spreading that accompanied the breakup of Pangea (Figure A9). Rifting and spreading related to the modern Atlantic, formed the Gulf of Mexico as the Yucatan rifted apart from Texas (Hill, 1996). As time progressed, the rifted margin of the Gulf of Mexico subsided further and transgression of the Western Interior Seaway spread shelf sediments across Texas (Figure A10). During the later portion of this evolutionary phase, the Farallon plate began its collision with the North American plate. Back-arc deformation from the convergence included the Chihuahua Trough of Late Jurassic to mid-Cretaceous ages. Marine waters migrated slowly up this trough in the Early Cretaceous and stretched as far inland as the Delaware Basin, covering the Glass Mountains, Apache Mountains, and at least the northeastern portion of the Guadalupe Mountains (Hill, 1996).

Figure A9. *Rifting North America from South America, and the breakup of Pangea throughout Jurassic time (modified from Blakey, 2016).*

Figure A10. *Illustration of the rifted margin of the Gulf of Mexico, subsequent subsidence, and the advancement of the Western Interior Seaway (modified from Blakey, 2016).*

Late Cretaceous – Eocene

The long period of tectonic stability during the Mesozoic was ended by uplifting and tilting brought on by the Laramide Orogeny (Figure A11). During this time, the convergence of the Farallon and North American plates was rapid, produced a low-angle subduction and east to northeast directed compressive stresses, which caused the uplift of the Rocky Mountain region from New Mexico to Wyoming (Dickerson, 1985). Even though the deformation from the Laramide Orogeny is not as obvious in the Delaware

Basin as it is in Colorado and Wyoming, this event did have an impact. It uplifted the entire Permian Basin above sea level permanently; subsequent erosion and alluvium deposition followed and began to dominate the evolution of topography in the area (Horak, 1985b). The Delaware Basin was also tilted eastward, approximately 3-5 degrees (Dickenson, 1981; Hentz and Henry, 1989).

Figure A11. *Paleogeography of the Delaware Basin throughout the Eocene showing Laramide significant deformation from New Mexico to Wyoming (modified from Blakey, 2016).*

Late Eocene – Late Oligocene

During what is termed the volcanic phase within the basin, volcanism increased not only in the Trans-Pecos, Delaware Basin region, but it also extended into Mexico and western New Mexico (Henry et. al., 1989; Kelley et. al., 1992). This phase took place during a change in the tectonic environment, and marked the beginning of a transition from subduction and compression to extension and crustal thinning. This controversial time in the basin's history could be attributed to steepening of the subducted Farallon slab as a remnant influence from Laramide aged compression (Keith, 1978), or to an "extensional orogenic" event in which a detached piece of the subducting slab sinks, causing back-arc extension along with Basin and Range block faulting (Elston, 1984). Either of these theories would ultimately lead to the Basin and Range phase within the basin. During the volcanic phase all of the domes, intrusives, and extrusives in the Glass Mountains, and all of the intrusives and extrusives in the Davis-Barrilla Mountains were produced, along with the intrusive dikes in the basin (Hill, 1996).

Late Oligocene – Present

The Basin and Range phase, which is characterized by regional, crustal extension and thinning, high heat flow, rifting (Horak, 1985b; Figure A12), and represents events beginning with this regional extension to present day conditions. The transition from Laramide compressional phase to Basin and Range extension was nearly completed by Late Oligocene. Extension throughout this time produced conjugate joint and fault sets that are oriented approximately N75˚E and approximately N15˚W throughout the basins. The graben development in the western region of the Delaware Basin created the Salt Basin by dropping the western margin of the basin into the subsurface (Nance, 1993). As lithospheric thinning occurred beneath the basin, the heat regime evolved from intrusive magmatism to an increased temperature gradient and convective heat flow. Basin and Range effects on the basin decreased, as did the geothermal gradient by Quaternary time with the exception of episodic seismic activity and normal faulting throughout the region (Hill, 1996).

Figure A12. *Paleogeography during the Oligocene, showing the effects of Basin and Range extension to the west of the Delaware Basin (modified from Blakey, 2016).*

Stratigraphic Succession

Wolfcampian - Leonardian

There is more known about Permian-aged rocks than all of the pre-Permian rocks combined, due to the fact that approximately 95% of all outcrops in the Delaware Basin date from this period (Hill, 1996). Permian rocks, within the basin, are divided into four series: the Wolfcampian, Leonardian, Guadalupian, and the Ochoan (Adams et. al., 1939). In the beginning of Wolfcampian time, the Central Basin Platform, Diablo Platform, Padernal Massif, and Marathon-Ouachita belt were active and uplifted areas that supplied the subsiding Delaware Basin. The majority of this sediment came from the Marathon-Ouachita Mountains and thick deposits accumulated in the southern region of the basin. The Wolfcampian series is made up of the Hueco Limestone from the Guadalupe Mountains and within the basin, and the Neal Ranch Formation followed subsequently by the Lenox Hills Formation of the Glass Mountains (Hill, 1996). When the Leonardian was being deposited, the Delaware Basin continued to subside, however, not as quickly as it did throughout the Wolfcampian. The basin continued to fill with fine-grained clastic sediment and limestone, and by the end of the Leonardian, the seas had retreated, leaving the Wolfcampian rocks buried to depths of more than 900 meters (Hills, 1942, 1948a). The Leonardian was a time when the general sequence of backreef-reef-basin facies was established in the Delaware Basin. The Leonardian Series contains the Yeso Formation, Victorio Peak Limestone, Cathedral Mountain, Skinner Ranch Formation, Bone Spring Limestone, and the Road Canyon Formation.

Guadalupian Series

The Delaware Mountain Group is named for the Delaware Mountains where this group makes up most of the range, and consists of three formations, in ascending order within the basin: the Brushy Canyon, Cherry Canyon, and Bell Canyon (Figure A13). The divisions of the formations and members within this group are not clear contacts, but they were established primarily on the basis of divisions in time-correlative reef and shelf facies. For example, the Cherry Canyon-Bell Canyon basin-facies contact corresponds in position to the Goat Seep-Capitan reef-facies contact (Hill, 1996). The Brushy Canyon, Cherry Canyon, and Bell Canyon were named for drainage courses that cut across broad belts of outcrop in the Delaware Mountains, members were named for specific geographic features, such as springs or buildings. In the Delaware Group, the Cherry Canyon Formation merges into the Goat Seep which is equivalent to the Queen Formation of the Artesia Group, and it is characterized by marginal carbonate members.

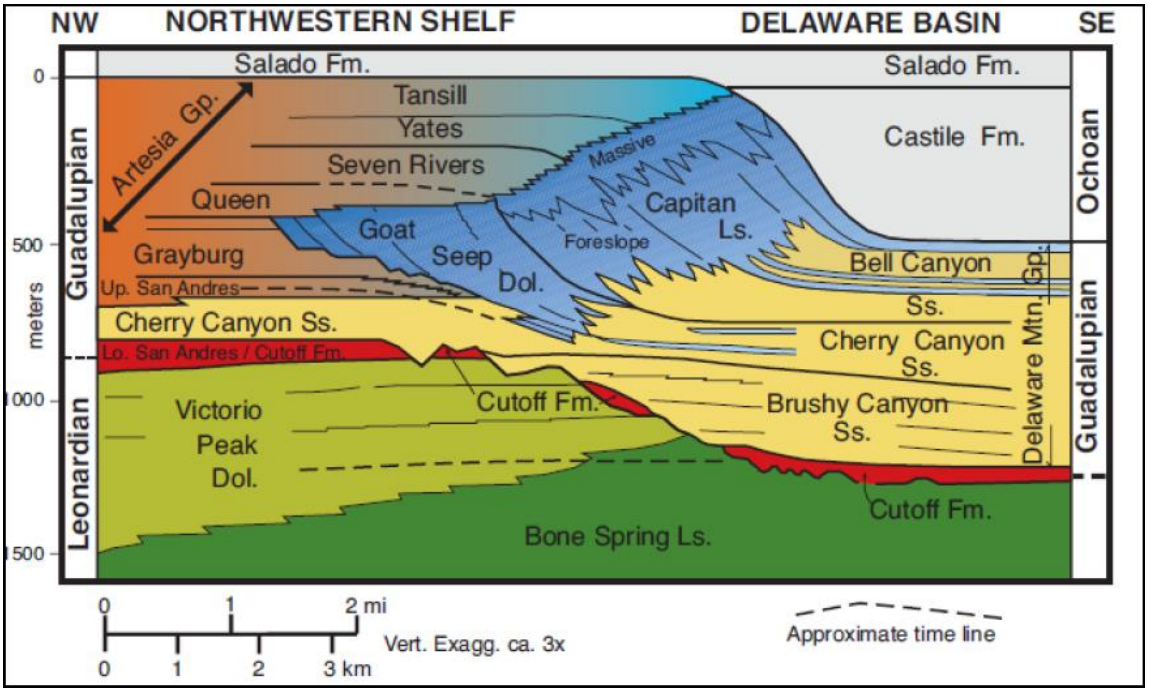

Figure A13. *Cross-section of the Delaware Basin including lithologic units (from Scholle et. al., 2004).*

These carbonate members represent periods of an increase in mass-wasting and contain boulders and smaller debris that extended long distances into the basin (Hill, 1996). The Delaware Mountain Group is known for being a uniform, well-sorted, coarse-grained siltstone to fine-grained sandstone that contains minor clay. Sand grains are noted as being rounded to well-rounded and silt grains are noted for being sub-angular to sub-rounded (Hull, 1957). The Delaware Mountain Group siliciclastics exhibit numerous sedimentary structures, from laminations and cross-laminations, to scour-and-fill structures, and ripple marks, to completely structureless units. There is an absence of shallow-water sedimentary features such as oscillation ripples, barrier islands, and beach sands (Beck, 1967). Sandstone channels are the largest and most prominent feature of the Delaware Mountain Group (Hill, 1996).

The Cherry Canyon Formation is the middle formation of the Delaware Mountain Group and was named for Cherry Canyon which is a shallow gorge that drains eastward from Pine Spring (King, 1942). The Cherry Canyon Formation forms the upper half of slope below Capitan Limestone cliffs near Guadalupe Peak at the southern end of the Guadalupe Mountains; here the formation is between 300-400 meters thick. It consists mostly of thin-bedded, finely-laminated, fine-grained sandstone and siltstone (Hill, 1996). The Cherry Canyon is a unit that displays cyclic sedimentation. Sixteen separate cycles were identified in 145 meter of rock: shaley sandstone is followed by thin-bedded sandstone, and then by lenticular or nodular limestone, after which, the cycle is repeated. These cycles seem to appear in intervals of approximately 3-6 meters. The thinner sandstone beds are all marked by light and dark laminae of which there are usually 10-20 every 2-3 centimeters (Snider, 1966). The Cherry Canyon differs from the underlying brushy Canyon because it contains tongues of limestone that can be correlated to reef and shelf rocks. Siliciclastics of the basin gradually thin out towards the margins as limestone members gradually thicken and merge with the forereef bed of the Goat Seep Dolomite. In the Guadalupe Mountains, the Cherry Canyon persists as a sandstone tongue a few kilometers shelfward. Above this sandstone tongue are the carbonate members of the Cherry Canyon: the Getaway, South Wells, and Manzanita members (Hill, 1996). Submarine canyons were the main mechanism of transport for siliciclastics within the basin. These canyons explain the linear orientation of sandstone channels inside the basin. During the time of deposition for the Cherry Canyon Formation, the Last Chance-Sitting Bull submarine canyon was the primary way in which siliciclastics poured into the basin. The origin of this siliciclastic material is believed to be from the Ancestral Rocky Mountains (Cromwell, 1984).

The Bell Canyon Formation is the upper unit of the Delaware Mountain Group and it was named for Bell Canyon (King, 1942). The formation varies in thickness from about 200-300 meters (Hendrickson and Jones, 1952). The Bell Canyon Formation is lithologically similar to the Cherry Canyon and contains mostly fine-grained sandstone, and coarse-grained siltstone with some interbedded thin limestone. It is characterized by extremely well-sorted, fine-grained quartz sand that only slightly varies in grain size and composition throughout the basin (Hill, 1996). Much like the Cherry Canyon, carbonate tongues of the Bell Canyon interfinger with sandstone units along the edges of the basin. The carbonate tongues thicken as they move towards the reef and merge with the Capitan Limestone. There are five formally-named carbonate members of the marginal facies of the Bell Canyon Formation: Hegler, Pinery, Rader, McCombs, and Lamar. With the exception of the Hegler, they are all very calcitic when compared to the tongues of the Cherry Canyon, which are mainly dolomitic (Hampton, 1989).

Ochoan Series

At the end of the Guadalupian, open marine circulation had essentially been cut off through the Hovey Channel by Capitan reef growth, which caused the area to become a restricted evaporitic basin during the Ochoan (Scholle et al., 2004). This shift from widespread carbonate shelf deposition to evaporite deposition occurred in basins around the world, leading to the extinction events of the Late Permian. After Ochoan time, the Delaware Basin was uplifted and exposed to erosion, except for a brief time period during the Cretaceous. The Ochoan Series consists of the Castile, Salado, Rustler, and Dewey Lake formations (Figure A14). These formations have a combined thickness of 1200-1500 meters (Hill, 1996). The Castile Formation is composed dominantly of anhydrite and is restricted to the Delaware Basin. The remaining three formations stretch the expanse of the Delaware Basin, Central Basin Platform, Northwest Shelf, and the Midland Basin. The Salado Formation is primarily made up of Halite, the Rustler of dolomite and anhydrite, and the Dewey Lake of continental red beds (Hill, 1996). During the Ochoan, the West Texas-eastern New Mexico area was an interior continental desert on the supercontinent Pangea (Scholle et. al., 1992).

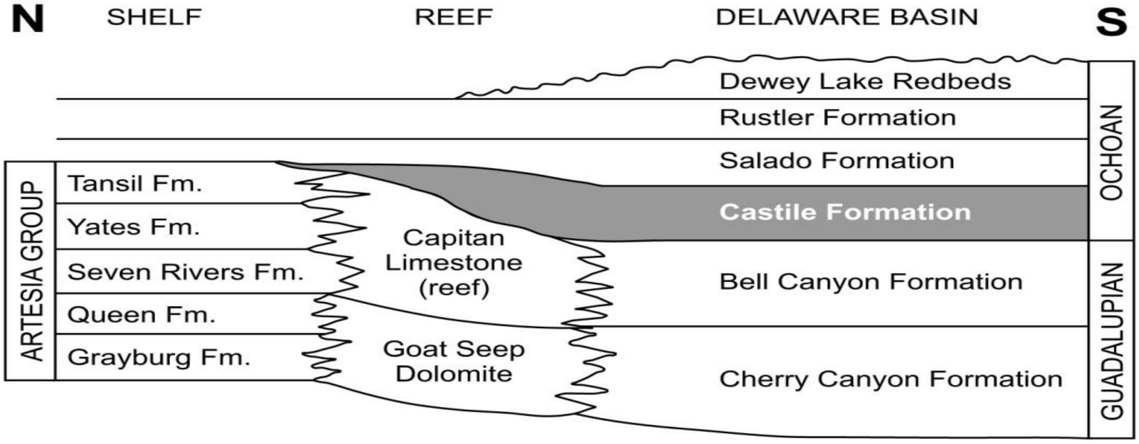

Figure A14. *Formations of the Ochoan series within the Delaware Basin. Highlighted is the formation where most karst manifestations occur (adapted from Scholle et. al., 2004).*

Density-stratified brines developed within the Delaware Basin and cycle deposits of the Castile Formation filled the Delaware Basin with anhydrite and calcite couplets in the western area of the basin, which grade into interbedded anhydrite and halite in the eastern area of the basin where the water depths were the deepest (Dietrich et. al., 1995). The thickness of the Castile Formation varies depending both on depositional and dissolutional characteristics. It is not clear as to which of these factors was the most influential in deciding the current extent of this unit. The original distribution of this unit has been, without a doubt, altered by subsequent dissolution. This is because of uplift and tilting of the basin at the end of Castile time, during the Jurassic and Tertiary, which cause pronounced erosion and dissolution of Castile evaporites (Hill, 1996). The Castile marks an abrupt transition between itself and the Bell Canyon Formation, and it is overlain by an unconformable Salado Formation. The Castile Formation has been subdivided into eight informal members: the Basal Limestone Member, Anhydrite 1 Member, Halite 1 Member, Anhydrite 2 Member, Halite 2 Member, Anhydrite 3 Member, Halite 3 Member, Anhydrite 4 Member, and the Painthorse Member (Anderson et. al., 1972). It contains cyclothems, occurring from large to small in scale. As indicated by the laminations, major anhydrite-halite alterations occur in the Castile between 30,000-70,000 years (Snider, 1966). This supports the concept of a transgressive-regressive cycling of the Castile Sea. Laminated textures are common in the Castile Formation, and not unusual, in that all of the lower-lying Delaware Mountain Group units have laminated sequences. However, the siltstone-limestone laminations of the Bell

Canyon Formation abruptly change to anhydrite-limestone laminations at the contact between the Castile and Bell Canyons formations (Hill, 1996). Laminations within the Castile Formation often exhibit microfolding with varying characteristics. Microfolding has been attributed to several causes: hydration/dehydration of anhydrite/ gypsum, density differences between anhydrite and carbonate laminae, and tectonic factors. Nodular anhydrite ranges in size from a few millimeters to more than 5 cm and they are common within the Castile Formation (Hill, 1996). Nodular anhydrite is characterized by a loss of carbonate laminae in the nodular zone; nodules of anhydrite vary widely in density and arrangement, and normally occur in the middle of a salinity sequence, above the anhydrite and below the halite. Stylolites in the Castile Formation are seen along the bases of carbonate laminae. It is unclear if stylolitic texture in the Castile Formation is caused by deposition, or is a result of diagenetic processes, representing either early diagenesis or deep-burial. Brecciated anhydrite is also common in the Castile Formation; breccia units at the Culberson mine can be correlated eastward with halite beds, which suggests that they formed as a result of collapse, due to the dissolution of halite beds (Hill, 1996).

The thickness of the Salado Formation varies greatly due to a combination of deposition and subsequent dissolution. Thicknesses ranging between 500-600 m are often measured in the basin, while decreasing to approximately 300 m, or less, where the salt overlies the Tansill on the shelf, beyond the margins of the basin (Hill, 1996). The Salado Formation is dominated by chloride minerals followed by secondary sulfate minerals and minor siliclastics (Stafford, 2015). The halite of the Salado Formation is less pure than halite found in the Castile Formation and sand and silt beds are found in many parts of the Salado. The halite is often laminated with anhydrite, but there are no bituminous calcite laminae as found in the Castile Formation. The Salado Formation is made up of three informal members; the Lower Member, middle McNutt Member, and the Upper Member (Hill, 1996). This formation was deposited over the extent of the Permian Basin with sediment of the Salado Formation changing from limestone in the south, to mostly anhydrite and halite in the Delaware Basin, and then to halite and potash in the north. The Salado Saline Sea extended far beyond the backreef than the previous Castile Sea which is why the Salado is not restricted to the Delaware Basin. The Salado Formation is known to be a shallow-water, saline to mudflat, lagoon deposit (Hill, 1996).

After Salado time, a marine sea advanced while the extent of the saline sea declined. There are large-scale cycles in the Rustler Formation that are on the order of 20,000 years (Snider, 1966). These cycles show the alteration between transgressions and regressions of the Rustler Sea with simultaneous deepening and shallowing of the basin, respectively. The Rustler records at least two advances of the sea as indicated by its two dolomite members, the Culebra and the Magneta. Major transgressive events ended at the beginning of the last Rustler cycle, which includes the lower portion of the Dewey Lake Red Beds. As with the Salado, the Rustler was deposited in the basin and on the shelf, and is made up of dolomite, siltstone, anhydrite, and halite (Mercer and Gonzales, 1981). The Rustler and Salado formations are lithologically similar, except that the Rustler contains significantly more dolomite (Hentz et. al., 1989). In unleached zones, the Rustler is made up of mostly halite, followed by sulfates, clastics, and lastly by dolomite and limestone (Barrows et. al., 1983). Fossils found within the dolomite members are large and varied; mollusks, brachiopods, and other expected marine fossils characterize the dolomite members of the Rustler, and they suggest a calcareous mud-bottom habitat (Walter, 1953). In the anhydrite zones, molluscan fauna are found, however no brachiopods have been found. The Rustler Formation members from oldest to youngest are the Virginia Draw, Culebra, Tamarisk, Magenta, and the Forty-Niner. The dolomite members, Culebra and Megneta, maintain their general characteristics with little change in thickness over thousands of square kilometers (Bachman, 1987c). However, the clastic and evaporite members show significant variation in thickness and facies due to the depositional environment and subsequent dissolution of evaporites (Hill, 1996).

At the end of Rustler time, the sea retreated and the Dewey Lake Red Beds were deposited, marking the last advance of the Permian Sea. Throughout Ochoan time, the Delaware Basin was uplifted and tilted to the east, which is marked by an angular unconformity between the Dewey Lake Red Beds and the overlying Triassic aged Chinle Group, while the contact between the Rustler and the Dewey Lake is mostly believed to be conformable. During most of the Permian, this region had an arid climate which contributed to these iron-oxidized continental red-beds. The Dewey Lake is made up of poorly-indurated, earthy, well-laminated, thin-bedded, reddish-brown to reddish-orange siltstone, claystone and lenticular fine-grained spots, and no fossils. There have been a variety of depositional environments proposed for the Dewey Lake Formation from lagoonal marine to sabkha to continental delta-eolian, or a combination of these (Hill, 1996). A north to northwest paleo-current direction in the Dewey Lake indicates a sediment origin to the south-southeast of the Delaware Basin. The silt and fine-grained sands of the Dewey Lake were from an uplift in the south-southeast encompassing the Pennsylvanian Marathon-Ouachita thrust belt and foredeep basins (Schiel, 1994). This uplift is believed to be responsible for an alluvial plain that extends throughout the southwestern United States (Hill, 1996).

Regional Karst and Dissolution

Karst features throughout the Delaware Basin are widespread due to the soluble nature of the rocks located within the basin and on the basin margins. The largest numbers of reported karst features are from the Castile Formation outcrops, and to a lesser degree, the Rustler and Salado formations (Stafford, 2015; Figure A15). Hypergene and hypogene karst processes worked together throughout geologic time to affect the Delaware Basin. Hypergene processes dominate the geomorphic evolution of the surface rocks cropping out throughout the basin, and hypogene processes seem to dominate the diagenetic alteration, and speleogenetic evolution, throughout the basin (Stafford, 2015).

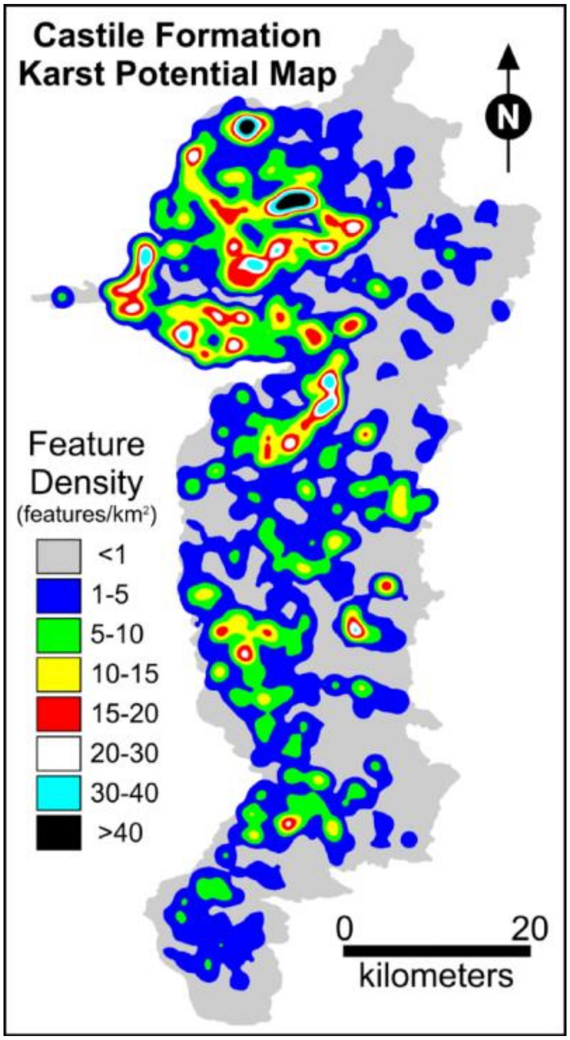

Figure A15. *Density map illustrating the distribution of karst features from the Castile Formation in the study area (from Stafford et. al., 2008b).*

Gypsum Karst

The Delaware Basin represents one of the most prominent developments of gypsum karst in North America. The term "Gypsum Karst" simply refers to the karst forming in gypsum rather than carbonate rocks. Sinkholes, caves, and underground drainage systems are typical throughout this type of topography with dissolution and suffosion being perpetrators of the karst evolution (Figure A16). Surficial karst and caves in gypsum within the Delaware Basin occur in three primary locations: the Burton Flat, Nash Draw, and the Gypsum Plain (Hill, 1996). Since gypsum outcrops only survive in arid climates, sinking stream patterns in gypsum karst tend to be small, dry arroyos that terminate into swallow holes or open caves (White, 1988).

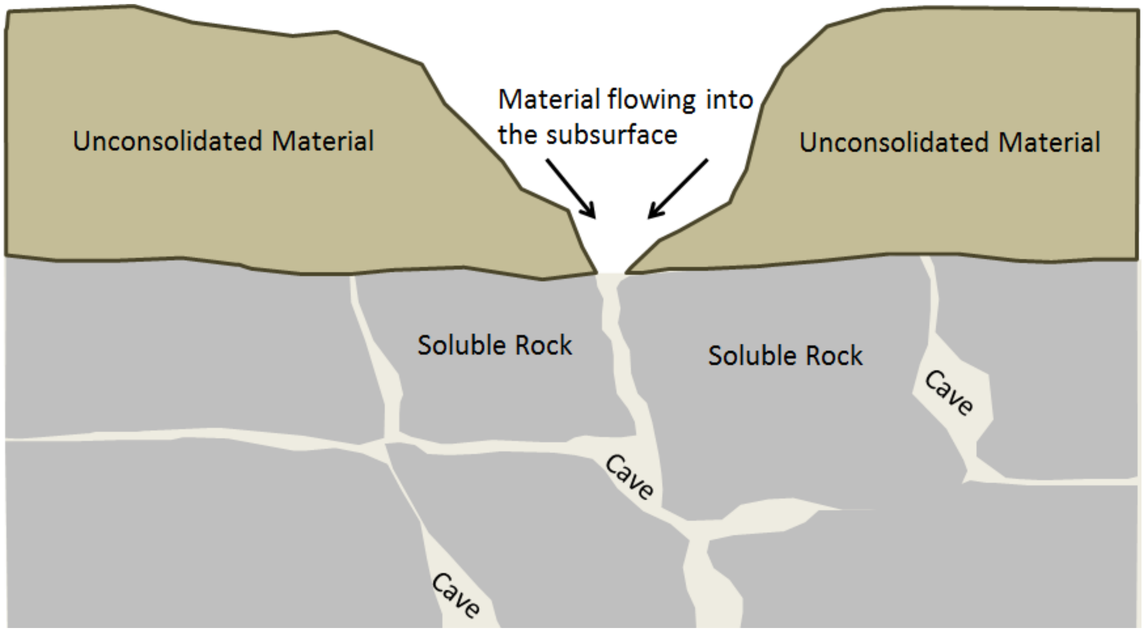

Figure A16. *Generalized diagram illustrating how dissolution and suffosion processes create karst topography in soluble rock.*

Surface Karst

Sinkholes are surficial dissolution features that usually develop due to the collapse of rocks into an underground void that formed from percolating meteoric groundwater or as a solutional feature from descending water. Those formed by descending water tend to be more developed laterally and they will have a series of arroyos that converge and drain into the sink. Collapse sinkholes generally have steeper sides and are normally near-circular in shape (Stafford et. al., 2008a). Sinkholes will either be active or inactive and they are abundant throughout the Castile Formation outcrop region. During times of surface runoff, active sinkholes will work as swallow holes or stream sinks, while inactive sinkholes will form playa lakes (Hill, 1996). Sinkholes are identified in the three primary gypsum karst regions and along the Pecos River drainage system, where they number in the hundreds (Bachman, 1986). Solutional karren is prominent in the study area where gypsum rock is exposed at the surface, with a wide variety of morphological forms. Rillenkarren is formed on near-vertical surfaces and is expressed by deep incisions in the rock; moderately sloping surfaces generally have shorter and shallower solution flutes that converge to create a dendritic-style drainage pattern and nearly horizontal surfaces will form karst pinnacles and shallow depressions that are often floored by microbial mats. In areas where a significant amount of selenite is exposed, blade-like karren and microkarren will form, due to preferred dissolution of the individual crystals within the selenite (Stafford et. al., 2008a).

Hypergene Caves

Caves are an identifying feature of the Gypsum Plain and the Burton Flat areas. The caves within the Gypsum Plain are developed throughout the Castile Formation (Hill, 1996). Individual cave and karst features that have been researched throughout the

Castile Formation show an intricate speleogenetic history that includes hypergene and hypogene beginnings (Stafford, 2015). Caves display a repeated orientation of ~N40˚W with secondary orientations of ~N10˚W and ~N45˚E. The complexity of cave passages, mainly along jointing, indicates that endokinetic fissuring is most likely the main cause for the local variations in brittle deformation that provide the preferential flow route of fluid migration and dissolution (Stafford et. al., 2008b). Because of the soluble nature of calcium sulfate, dissolution has the potential to occur quickly with the changing environment. In places throughout the Gypsum Plain where dissolution has been going on long enough to form caves, they tend to be limited in their lateral evolution and form shallow recharge areas. In these specific instances, the effects of dissolution are greatest at the surface and within the first few tens meters of the subsurface (Stafford et. al., 2008a). In some instances, hypergene caves will form shallow subsurface networks that connect points of differing elevations at the surface without exhibiting the usual decrease in passage dimensions (Stafford et. al., 2006). Hypergene caves also have a tendency to form in areas where surficial gypsic soil comes into contact with gypsum bedrock. Most hypergene caves that form in this environment appear to be small, have a limited lateral extent, and are largely ephemeral. In most cases, these hypergene “gypsite” caves are either filled with soil or have an entrance that decreases in size inward, limiting exploration to within a few tens of meters. However, in some cases these gypsic caves will connect to caves that formed in gypsum bedrock which suggests that the gypsic caves provide a preferential flow path for water to drain (Stafford et. al., 2008a). The strictly hypergene caves exhibit strong solutional control by joints, while the hypogene show a lesser relation to structural controls, but greater correlation to a change in lithology and ductile deformation (Stafford, 2015).

Hypogene Caves

Unlike hypergene caves and surficial karst features, hypogene caves do not have a direct connection with surface environment activity and meteoric waters and thus form from dissolution caused by rising fluids (Stafford et. al., 2008). Forced and free convection processes are required components with regards to hypogene systems (Klimchouk, 2000c, 2007; Anderson and Kirkland, 1980; Kohout et. al., 1988). Differences in hydraulic pressure are what drive forced convection throughout the region. The fluids from lower, pressurized aquifers will flow upwards to areas of a lower hydraulic pressure regime, which is often the base level of a region (Toth, 1999). In order for aquifers to become pressurized, they must be confined by an impermeable or semi-impermeable layer in order for the required pressure regime to develop (Klimchouk, 2007). In the study area, the Castile Formation acts as the confining layer above the lower clastic Bell Canyon Formation (Lee and Williams, 2000). However, fractures within the Castile Formation allow for fluid to flow vertically. These fractures do not usually cross the entire formation; instead, they terminate within the formation and limit cross-formational activity (Hill, 1996). In free convection, waters are continuously delivered to the area of active dissolution by the simultaneous rising of less dense, under-saturated fluids and the descent of more dense, saturated fluids (Anderson and Kirkland, 1980; Klimchouk, 2007). Rising fluids come from the lower pressurized zones, while the saturated fluids are removed downward through the same lower aquifer. Speleogenesis is seen in any type of soluble rock, but it is profound in calcium sulfate rocks because the highly soluble nature allows for a steep density gradient to form through free convection (Klimchouk, 2007; Anderson and Kirkland, 1980). Many caves in the study area show an origin of hypogenetic processes; however, many of these caves contain hypergenetic overprinting because surface denudation has reached them and allowed for human entry and study. The morphology of these caves, with the exception of the entrances, generally exhibit extensive and complex cave patterns, and contain an abundance of speleogenetic features that align with a hypogene origin (Stafford et. al., 2008a).

Intrastratal Breccia

Brecciation is common throughout the Castile Formation. Extensive breccia pipe structures are found throughout the Castile Formation and can pass through its entire thickness (Figure A17). Unlike vertical breccia structures, blanket breccias occur over wide regions and they are laterally extensive (Figure A18). Breccia pipes and blanket breccias are formed as solution subsidence valleys, dissolution troughs, and collapse pits. This means that all breccia occurrences are a result of intrastratal dissolution of evaporites by hypogenetic speleogenesis where a void formed in the subsurface was followed by a collapse (Stafford et. al., 2008a). Large breccia pipes are found along the northern and eastern boundaries of the Delaware Basin, above the Capitan Reef descending through the Castile and Salado formations. Throughout the Castile outcrop, vertical breccia pipes and blanket breccias are common; however, this region is not overlying the Capitan Reef Aquifer as in the northern and eastern Delaware Basin. The evaporites of the outcrop region overly the clastic Bell Canyon Aquifer which supplies the fluids needed to produce hypogenetic dissolution features, and that also form the brecciated zones (Lee and Williams, 2000).

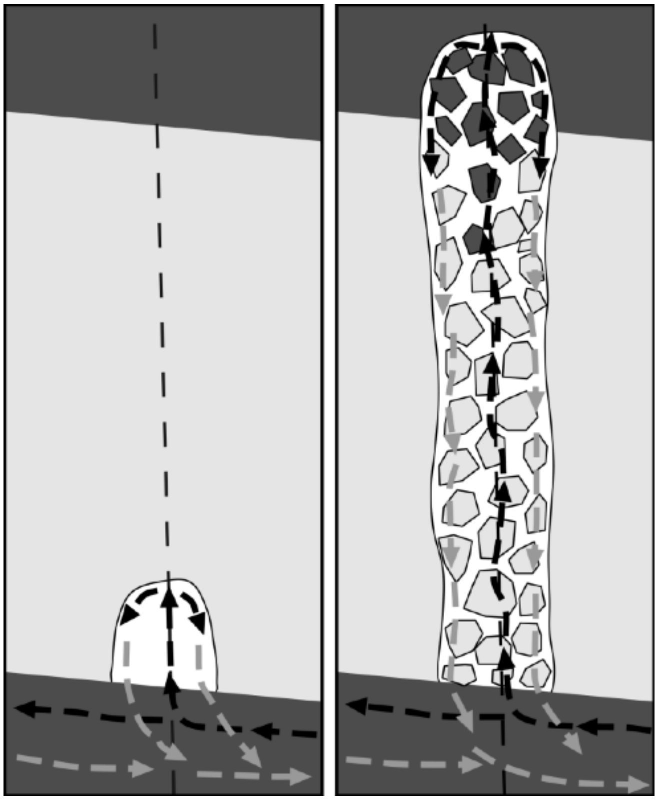

Figure A17. *Illustration of how breccia pipes form. Dark arrows represent the upward movement of low density under-saturated fluids, while the light colored arrows represent the descending high density oversaturated fluids (from Stafford et. al., 2015).*

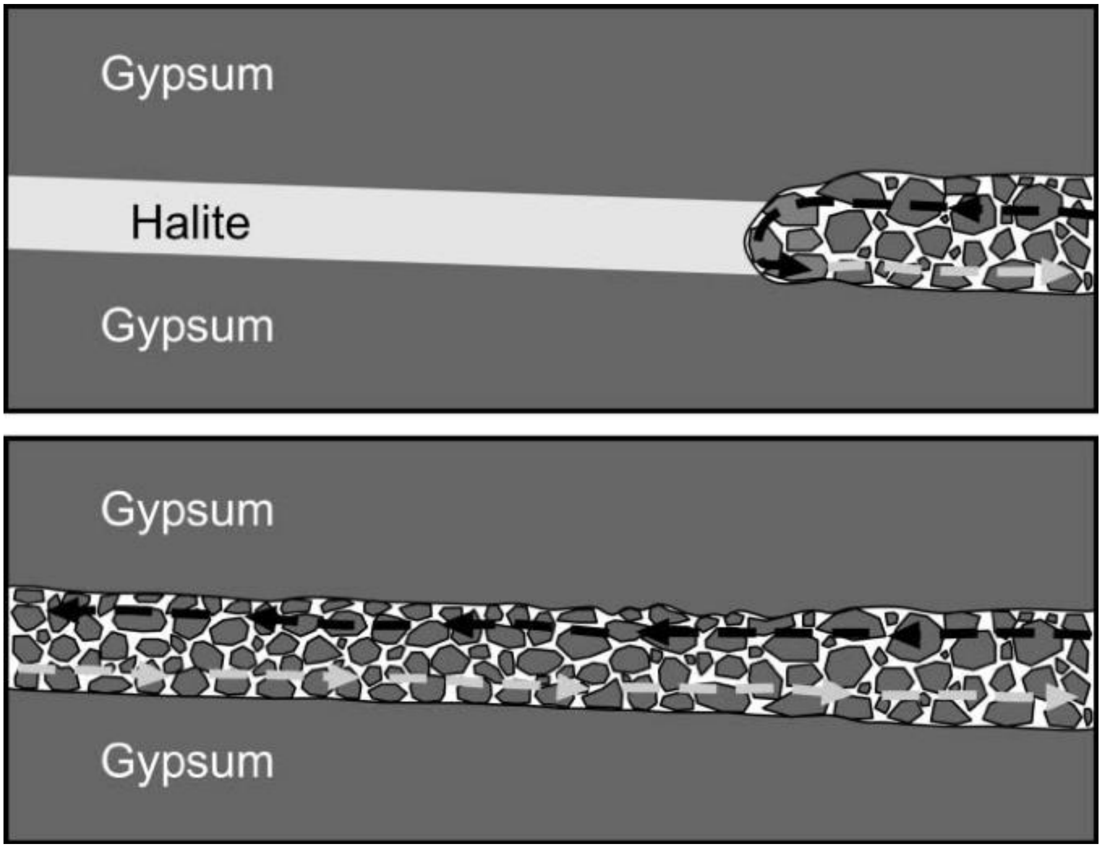

Figure A18. *Illustration of the formation of blanket breccia zones through intrastratal dissolution of halite layers (Stafford et al., 2015).*

Evaporite Calcitization

Evaporite calcitization occurs through three main processes; Bacterial Sulfate Reduction (BSR), Thermochemical Sulfate Reduction (TSR), and by meteoric calcitization. Meteoric calcitization is typically associated with dolomite being converted into calcite. In this process, the dissolution of dolomite and precipitation of calcite happens simultaneously (Back et. al., 1983). In contrast, BSR and TSR need to have sulfate rocks and an organic carbon source. Hydrogen sulfide and calcite saturated fluids are formed once the sulfate is reduced, which will either simultaneously or subsequently produce native sulfur and secondary gypsum. BSR takes place in a variety of low temperatures and sedimentary environments, but it is limited because it relies on sulfate reducing bacteria to supply a catalyst for sulfate reduction. TSR can take place as long as sulfate and organic compounds are present, but it does not require microbial organisms to play an active role. This means that TSR can take place in confined environments, without having to completely remove hydrogen sulfide byproducts that would otherwise become toxic for sulfur reducing bacteria (Machel, 1992). Native sulfur bodies are often associated with calcitized masses within the Ochoan-aged evaporites of the Delaware Basin. The extensive distribution of calcitization within the Castile Formation suggests that hypogenetic speleogenesis has significantly impacted the diagenetic evolution of the area. A significant amount of the hydrogen sulfide produced during calcitization appears to have been partially oxidized to native sulfur or oxidized to sulfuric acid, which would eventually turn limestone to secondary gypsum within the region (Stafford et al., 2008c).

Theory of Resistivity

The history of electrical resistivity dates back to the 1800's, when Robert W. Fox experimented with natural currents associated with sulfide ore deposits at Cornwall, England. In the 1900's, Conrad Schlumberger in France and Frank Wenner in the United States applied current to the ground and measured the resulting potential differences. In the United States, O.H. Gish and W.J. Rooney first studied telluric currents in the 1920's. Nearly all early work involving electrical resistivity methods was centered on ore deposits and their exploration. Since earlier studies, progress has been made to refine instrumentation, develop a theoretical base, and improve upon interpretation methods, which is mostly possible due to advancements in computer technology (Burger et al., 1992).

Basic Properties of Electricity

In electrical resistivity methods, a direct current (DC) or an alternating current (AC) is applied at the ground surface, and the potential difference is measured between two points. The differences in resistance to current flow at depth will cause distinct variations in the potential difference measurements, which will provide insight on subsurface composition and structure. In figure A19, a basic electrical circuit containing a battery, connecting wires and a resistor is illustrated. The battery maintains a potential difference between two points: its positive and negative terminals. This means that the battery is working as the source of power, moving charges through the circuit.

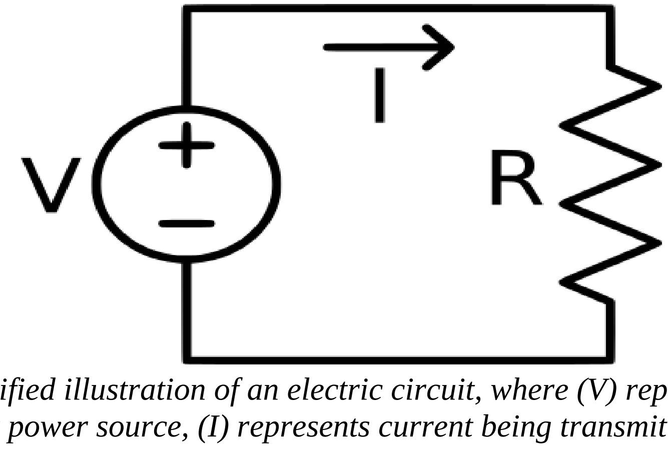

Figure A19. *Simplified illustration of an electric circuit, where (V) represents voltage from the battery or power source, (I) represents current being transmitted through the wire, and (R) represents the resistor.*

In order to define the current flow as the movement of positive charges, the battery must move positive charges from a high potential at the positive terminal to low potential at the negative terminal. The work done in this potential change needs a force to be applied, which is known as electromotive force or *emf*, and the unit of emf is the *volt*. The movement of charges through the conducting wire is termed *current*, and is measured in *amperes*. Current (i) can be calculated by dividing the charge (q) in coulombs, by time (t) in seconds. Another important aspect of electrical resistivity is the current density. Current density (j) is defined as the current (i) divided by the cross-sectional area (A) of the material through which the current is flowing (Figure A20).

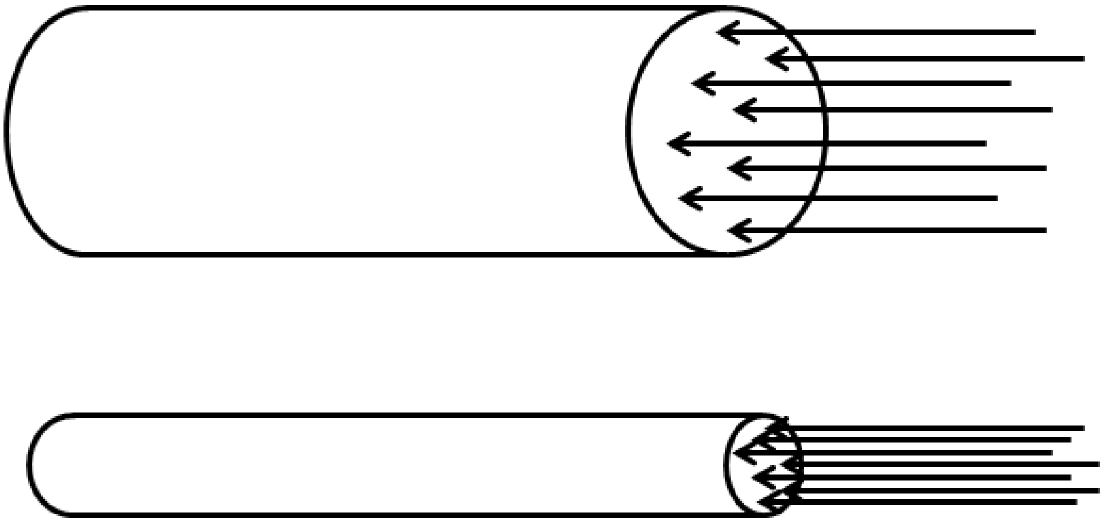

Figure A20. *Diagram showing the relationship between current density (j) and cross-sectional area. Current flow is indicated by arrows (after Burger et al., 1992).*

One thing recognized through the study of electrical resistivity, is that different mediums pose varying resistances to the flow of an electrical current. For example, copper has a very low resistance, and rubber has a very high resistance. This knowledge can be quantified by saying that one ohm of resistance allows a current of one ampere to flow when one volt of *emf* is applied (Burger et al., 1992). The fundamental theory of resistivity measurement is based on Ohm's Law, which states that current is directly proportional to voltage (*V*) and inversely proportional to resistance (*R*), which was introduced by physicist Georg Simon Ohm (Geometrics, 2016: Eq. A1). Resistance will not only vary because different geologic materials have varying resistances to current flow, but it will also vary with the dimensions of the geologic material in the subsurface. Resistors made of the same material, but of different dimensions, will not possess the same resistance to current flow. For example, current flow would be more restricted in a long, thin wire as opposed to a shorter wire with a larger cross-sectional area, composed of the same material (Figure A20; Eq. A2). This behavior indicates that the resistance of a resistor is dependent on its length, cross-sectional area, and on a fundamental property of the components used in its assemblage, which is termed resistivity (ρ) (Eq. A3).

$$\frac{\text{Potential or voltage difference (volts)}}{\text{current (amps)}} = \frac{V}{I} = \text{resistance } R \text{ (ohms } \Omega) \qquad \text{[Eq. A1]}$$

$$\text{resistance, } R = \text{resistivity } (\rho) \times \frac{\text{length}}{\text{area of cross−section}} \qquad \text{[Eq. A2]}$$

$$\text{resistivity, } \rho = \text{resistance} \times \frac{\text{area of cross−section}}{\text{length}} \qquad \text{[Eq. A3]}$$

The primary objective of collecting resistivity data is to record a relative distribution of resistivity points. Controls on resistivity values include the type of soil, mineralogy, amount of water saturation, and the amount of porosity in the subsurface being surveyed. Resistivity surveys measure a current injected into the ground by transmitting electrodes and recording the potential difference between two receiving electrodes. The measured current and electrode geometry together can be converted to find the apparent resistivity. Apparent resistivity is an Ohm's Law ratio of measured voltage to applied current, multiplied by a geometric constant (k) which depends on the electrode array. The OhmMapper is similar to traditional galvanic resistivity in this respect because it also has a geometric factor, also known as the "K factor", for conversion (Figure A21). This geometric factor is resistance normalized to resistivity by a factor for the array type. However, the factor between point source (DC resistivity) and line source (OhmMapper) is significantly different (Groom, 2004). In order to find the "true resistivity" from "apparent resistivity" the data must be processed through an inversion program. Inversion is defined as the process of determining the estimations of the model parameter based on the data and type of model. Inversions remake the subsurface resistivity distribution from the measured voltage and current data (AGI, 2009).

$$\rho = K \cdot \Delta V / I$$

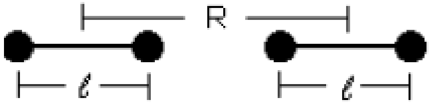

$$\frac{1}{K} = \frac{\Delta V}{\rho_{\omega} I} = \frac{1}{\pi} \int_0^{l_1} \int_0^{l_2} \frac{I(L_1)}{I_{(L_1=0)}} \frac{I(L_2)}{I_{(L_2=0)}} \frac{dL_1 dL_2}{R^3}$$

$$K = \frac{l\pi}{\ln\left[\left(\frac{b^2}{b^2-1} \right)^{2b} \left(\frac{b^2+2b}{(b+1)^2} \right)^{(b+2)} \left(\frac{b^2-2b}{(b-1)^2} \right)^{(b-2)} \right]} \qquad \text{where} \qquad b = 2R/l$$

Figure A21. *Geometric "K-Factor" for a capacitive, AC, line-source, dipole-dipole resistivity measurement (Geometrics, 2001).*

Electrode Geometries

The electrode arrays that are generally used in resistivity surveys are the Wenner, Schlumberger, or dipole-dipole. The Wenner electrode array is illustrated in (Figure A22A). The spacing between electrodes is equal and conventionally is represented by the letter (*a*). When conducting an expanding-spread Wenner survey, all electrodes are moved along a straight line after every reading so that the electrode spacing remains equal and retains preselected values. The Wenner electrode array has been the primary geometry used in North America for resistivity surveys. One advantage of the Wenner array is that the larger potential electrode spacing demands less of the instrument sensitivity, and a second advantage would be the simplicity of calculating apparent resistivity because the electrode spacing is equally spaced. Some disadvantages with using the Wenner array is that all electrodes must be moved for each reading which leads to longer field time, and it is more sensitive to local, near-surface lateral variations. Most European resistivity surveys use the Schlumberger array. When using the Schlumberger array (Figure A22B), the current and potential electrodes are moved symmetrically outward from a central point, but the potential electrodes are spaced more closely than the current electrodes. The spacing of electrodes is selected to maintain the relationship $2L>5MN$, and to also follow the same numbering scheme as the Wenner array. Some advantages of the Schlumberger array are that there are fewer electrodes to move between each survey, and it requires shorter cables for the potentials. Some disadvantages are that it requires more sensitive equipment, and requires longer cables for the current electrodes. The last common electrode geometry is the dipole-dipole array (Figure A22C). In this array the potential electrodes and current electrodes function independently. Both sets usually have a close spacing with a significant distance between each set. Since the cable lengths between the electrodes are short, it is easier to place the potential electrodes at longer distances from the current electrodes which will facilitate a deeper investigation. However, with deeper resistivity investigations, the current must be stronger in order to reach the proper depth. An advantage for this array is that deeper soundings can be achieved with shorter cables. The disadvantages, however, are that a larger current is required for deep soundings, and it needs more sensitive instrumentation (Burger et. al., 1992).

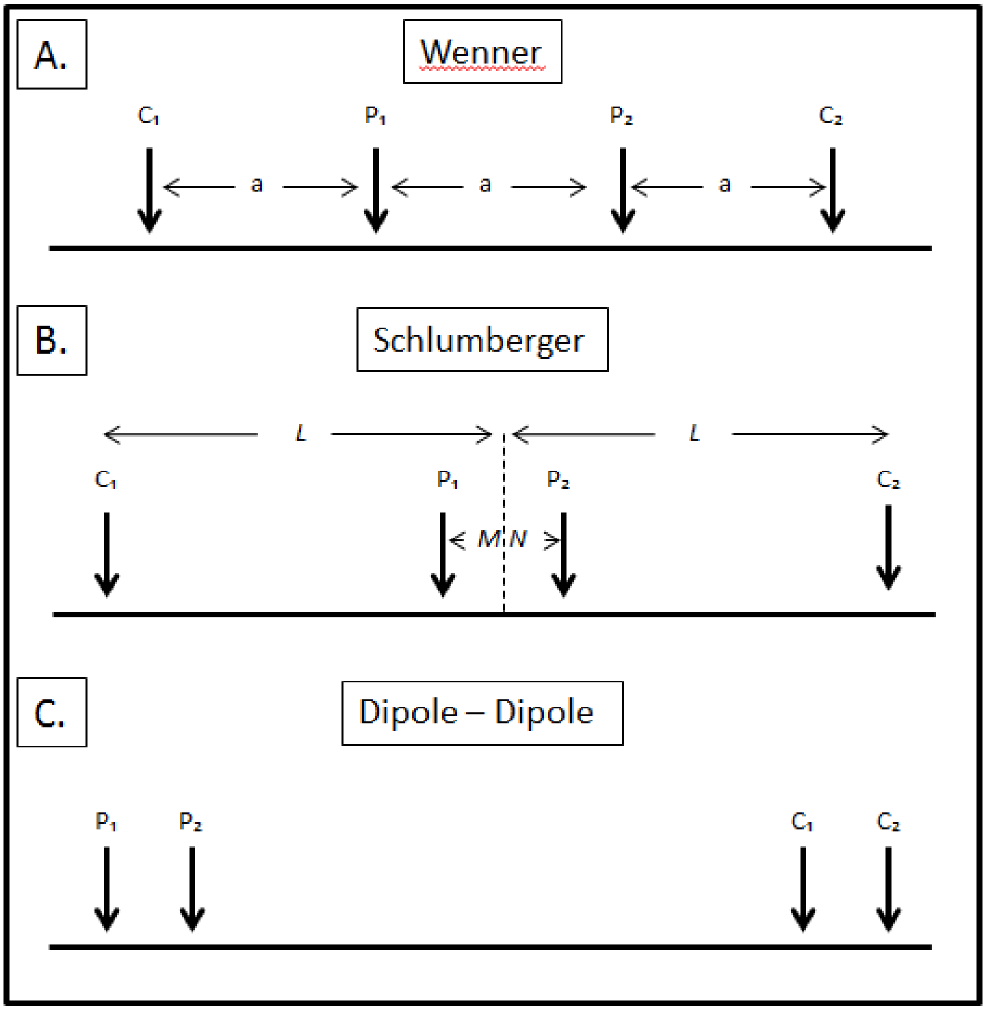

Figure A22. *Diagram of the different types of electrode geometries (modified after Burger et. al., 1992).*

Capacitively-Coupled Resistivity

In a capacitively-coupled resistivity system the transmitter uses the capacitance of an antenna to couple an AC signal into the ground (Geometrics, 2016). This procedure of measuring resistivity is not only possible because of Ohm's Law, but also because of the discoveries made independently by a German cleric named Ewald Georg von Kleist and a Dutch scientist named Pieter van Musschenbroek of Leiden. Together they independently invented a device that is now called the "Leyden Jar" or a modern-day "capacitor" which is used to store an electric charge around the same time. The jar was made of an ordinary glass jar half-filled with water, foil wrapping the bottom with metal on the outside, and foil coating the bottom of the inside with metal, and a wire was hung from the lid to the inside of the jar (Figure A23). It was soon realized that larger capacitors would store a greater charge than smaller capacitors, assuming the voltage was the same (Encycloædia Britannica, 2013). This property of a capacitor would be known as its capacitance. Modern day capacitors are not made of glass; instead, they are made of other nonconductive material, sandwiched between two conductors. Once a capacitor is charged, it maintains the same voltage as the power source. A natural example for capacitive-coupling would be a lightning strike. One plate of the capacitor would be the cloud, the other plate of the capacitor would be the ground, and the lightning would be the charge released between these to "plates." If a charge is applied on one plate of a capacitor and then removed, electrons on the other plate will be repelled only during the time the charge is on the first plate. Therefore, if alternating between applying the charge and removing it, an equal charge will flow in and out of the other plate. This method will apply an AC "alternating current" voltage to one plate of a capacitor and appear on the other plate. The ability to cause a charge to move in and out of one plate by applying an alternating voltage to a nearby plate is known as "Capacitive Coupling." The OhmMapper resistivity unit uses this method in two places, to induce a current into the Earth from the transmitter, and again to record the resulting voltage from the Earth into the receiver (Figure A24).

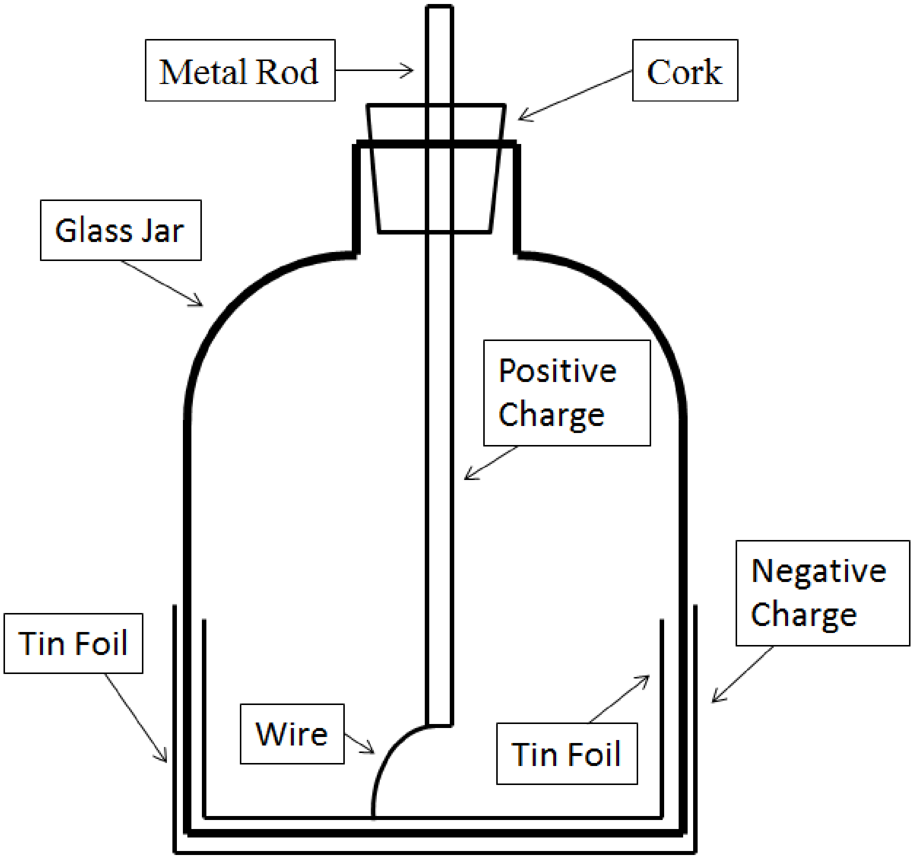

Figure A23. *Simple diagram of a Leyden Jar or modern day capacitor.*

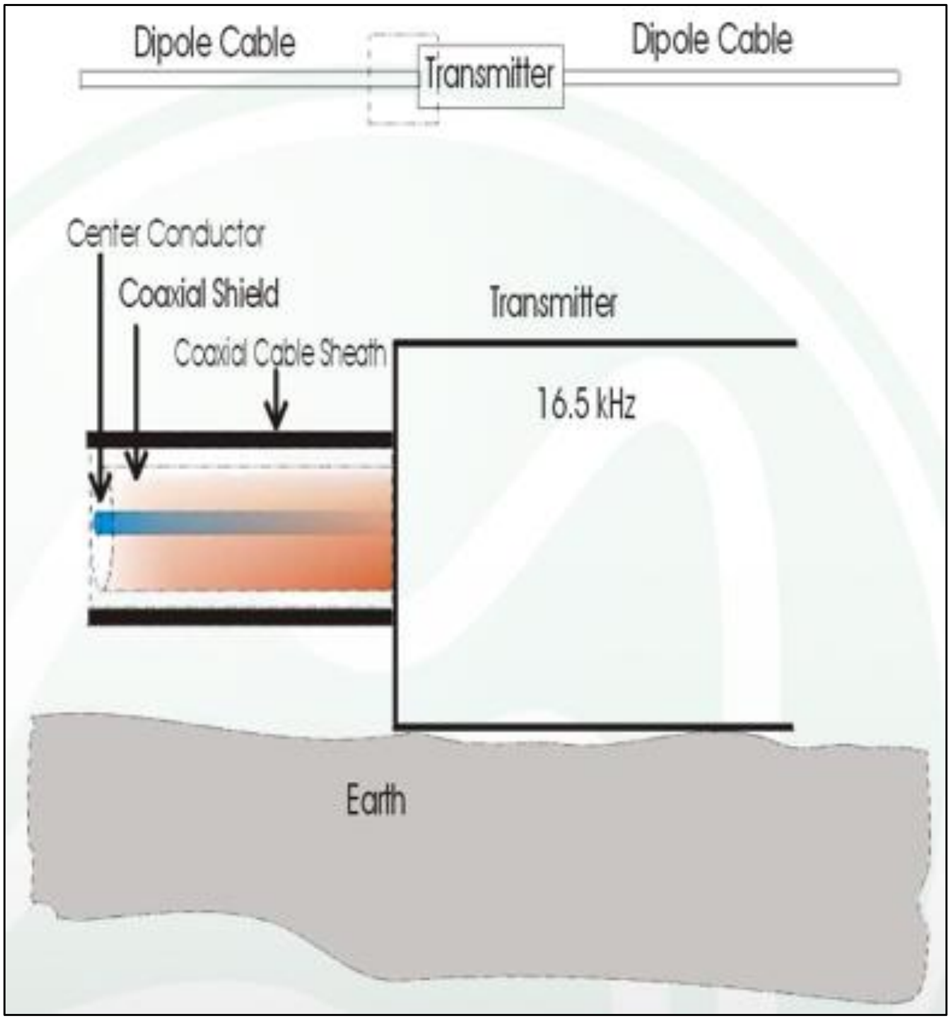

Figure A24. *Illustration of the OhmMapper transmitter electrode, the Earth, and how they form the two plates of a capacitor. The transmitter labeled above will charge the cable, and thus capacitive-coupling is achieved (Geometrics, 2016).*

Skin Depth Effect and Electromagnetism

What makes the OhmMapper a viable, non-invasive tool is its innate ability to detect resistivity changes within the subsurface without the need to dig or drill. This method, however, comes at a cost with how deep the OhmMapper system can investigate.

This depth can change between different locations, and this change is dependent on the maximum separation between the transmitter and receiver at which the transmitted signal can be reliably detected and decoded. This separation is determined by the resistivity or conductivity of the survey site (Geometrics, 2001). Signal attenuation is approximately 1/distance^3 as it travels from the transmitting electrode to the receiving electrode, which means that if the transmitter-receiver space is increased, the receiver signal will be reduced from its original strength and will continue to be reduced as the spacing increases. This is why the maximum depth of investigation will change based off of survey site resistivity properties. Ohm's Law dictates that for a given current, if the ground resistance is high, the voltage generated is also high. In contrast, if ground resistance is low the resulting voltage is low, which would make the resistivity measurement more difficult. Signal attenuation is rapid in both resistive and conductive environments, however, the signal dissipates much faster in conductive ground which means the separation between transmitter and electrode can be much greater in resistive ground allowing for a greater maximum depth of investigation (Geometrics, 2001).

For an alternating current (AC) signal, the maximum transmitter-receiver separation for a conductive survey environment is a function of skin depth. If the separation between transmitter and receiver are outside of skin depth, there will normally not be enough of a detectable signal for the receiver to record (Geometrics, 2001). In order to further understand skin depth, Faraday's Law of Induction and Lenz's Law must be introduced. Michael Faraday discovered that if he moved a magnet past a wire, it produced an *emf* (voltage) in the wire, and the faster he moved the magnet the greater the voltage that was produced. This basic law of electromagnetism is known as Faraday's Law of Induction. Lenz's Law was conceptualized by a physicist known as Heinrich Friedrich Lenz, and his experiments used Michael Faraday's observations, along with the knowledge that electric currents create magnetic fields, to form his experiments. His tests showed that changing the electric current in a wire caused a voltage to appear on the wire. The direction of the induced *emf* on a wire by a changing magnetic field, due to Faraday's Law of Induction, will create a magnetic field that opposes the change that produced it. The propensity of a change in current to create voltage is termed inductance. This idea becomes more complex when you replace the wire, with the ground, because the AC current is flowing in and all throughout the soil and underlying rocks. The magnetic field produced by an AC current spreading throughout the ground will create voltages in other parts of the ground surface. Current flowing in the very shallow surface will create a voltage that typically impedes the current from flowing into the deeper subsurface. In more resistive mediums, much like the ones throughout the study area, the voltage produced by current flowing in the resistance of the soil will be greater in comparison to the voltage produced by the inductance of the soil. In these instances, the skin depth effect is not a significant problem; however, the opposite is true for very conductive mediums (Geometrics, 2001).

Under prescribed operating conditions the OhmMapper is not regarded as an electromagnetic device, instead it is a resistivity meter that measures electric fields only. This doesn’t mean that electromagnetic phenomena don’t influence the measurements of the OhmMapper; voltages caused by the inductance offset OhmMapper recordings, but not by a significant amount (Groom, 2004). The reason for its insignificance is that the voltage caused by inductance and the voltage associated with the resistance are not in sync with each other. The voltage associated with resistance is generated when the current flows, while voltage from inductance is generated when the current changes. Its peak happens at the moment the current has stopped and changes directions (Geometrics, 2001).

References

Adams, J. E., Cheney, M. G., DeFord, R. K., Dickey, R. I., Dunbar, C. O., Hills, J. M., King, R. E., Lloyd, E. R., Miller, A. K., and Needham, C. E., 1939, Standard Permian of North America: Am. Assoc. Petroleum Geol., Bull., v. 23, no. 11, pp/ 1673-1681.

Adams, J. E., 1962, Foreland Pennsylvanian rocks of Texas and eastern New Mexico; in Branson, C. C. (ed.), Pennsylvanian system in the United States: American Association of Petroleum Geology, Tulsa, OK, pp. 372-384.

AGI: Advanced Geosciences Incorporated, 2009, Austin, Texas. <http://www.agiusa.com>. Accessed December 13, 2016.

Anderson, R. Y., Dean, W. E., Kirkland, D. W., and Snider, H. I., 1972, Permian Castile varved evaporate sequence, West Texas and New Mexico: Geol. Soc. Am., Bull., v. 83., pp. 59- 86.

Anderson R. Y., and Kirkland D. W., 1980, Dissolution of salt deposits by brine density flow. Geology, 8: p. 66-69.

Bachman, G. O., 1986, Stratigraphy and dissolution of the Rustler Formation; in Chaturvedi, L. (ed.), The Rustler Formation at the WIPP site: Environ. Eval. Gp., Albuquerque, NM, EEG-34, pp. 16-25.

Bachman, G. O., 1987c, Stratigraphy and dissolution of the Rustler Formation; in Chaturvedi, L. (ed.), Rustler Formation at the WIPP site: Environ. Eval. Gp., Albuquerque, NM, EEG-34, pp. 16-25.

Back W., W., Hanshaw, B. B., Plummer, L. N., Rahn, P. H., Rightmire, G. T., and Rubin, M., 1983, Process and rate of dedolomitization: mass transfer and C^{14} dating in a regional carbonate aquifer: Geological Society of America Bulletin, v. 94, p. 1415- 1429.

Barrows, L. J., Shaffer, S. E., Miller, W. B., and Felt, J. D., 1983, Waste Isolation Pilot Plant (WIPP) site gravity survey and interpretation: Sandia Natl. Labs., Albuquerque, NM, SAND82-2922, 113pp.

Beck, R. H., 1967, Depositional mechanics of the Cherry Canyon Formation, Delaware Basin, Texas: Unpubl. MS thesis, Texas Technological College, 107 p.

Blakey, R., 2016, Paleogeography and Geologic Evolution of North America: www.jan.ucc.nau.edu/rcb7/nam.html. Accessed December 13, 2016.

Burdett, J. W., 1985, Stable carbon and oxygen isotopes and organic carbon, carbonate, and anhydrite accumulation rate records through laminated evaporite cycles, Permian Castile Formation, Delaware Basin, Texas and New Mexico: Unpubl. MS thesis, Univ. South Carolina, 76 pp.

Burger, H. R., Sheehan, A. F., and Jones, C. H., 1992, Introduction to Applied Geophysics: Exploring the Shallow Subsurface.

Canter, K. L., Wheeler, D. M., and Giesaman, R. C., 1992, Sequence stratigraphy and depositional facies of the Siluro-Devonian interval of the northern Permian Basin; in Candelaria, M. P., and Reed, C. L. (eds.), Paleokarst, karst-related diagenesis and reservoir development – examples from Ordovician-Devonian age strata of West Texas and the mid-continent: Soc. Econ. Paleontol. Mineral., Permian Basin section, Guidebook Publ. 92-33, pp. 93-109.

Cromwell, D. W., 1984, The upper Delaware Mountain Group, Permian (Guadalupian), southeast New Mexico and West Texas; in Mazzullo, S. J. (chairman), The geologic evolution of the Permian Basin: Soc. Econ. Paleontol. Mineral., Permian Basin section, Symp., Midland, TX, pp. 32-34.

Dickerson, P. W., 1985, Evidence for Late Cretaceous- early Tertiary transpression in Trans- Pecos Texas and adjacent Mexico; in Dickerson, P. W. and Muehlberger, W. R. (eds.), Structure and tectonics of Trans-Pecos Texas, West Texas Geol. Soc., Guidebook Publ. 85-81, pp. 185-194.

Dickinson, W. R., 1981, Plate tectonic evolution of the southern Cordillera; in Dickinson, W. R., and Payne, W. D., (eds.), Relations of tectonic to ore deposits in southern Cordillera: Arizona Geol. Soc. Digest, v. 14, pp. 113-135.

Dietrich, J. W., Owen, D. E., Shelby, C. A., and Barnes, V. E., 1995, Geologic atlas of Texas: Van Horn-El Paso Sheet. University of Texas Bureau of Economic Geology, Austin, Texas, 1 sheet.

The Editors of Encyclopædia Britannica, 2013, Leyden jar: Encyclopædia Britannica, Inc.; https://www.britannica.com/technology/Leyden-jar (Accessed September 25, 2017).

Elam, J. G., 1984, Structural systems in the Permian Basin: West Texas Geol. Soc., Bull., v. 24, no. 1, pp. 7-10.

Elston, W. E., 1984, Subduction of young oceanic lithosphere and extensional orogeny in southwestern North America during mid-Tertiary time: Tectonic, v. 3, no. 2. pp. 229-250.

Ewing, T. E., 1993, Erosional margins and patterns of subsidence in the Late Paleozoic West Texas Basin and New Mexico; in Love, et al., (eds.), Carlsbad region, New Mexico and West Texas; New Mexico Geol. Soc., Guidebook, 44th Ann. Field Conf., pp. 115-166.

Ford, D. C., and Williams, P. W., 1989, Geomorphology and Hydrology, Unwin Hman, London, 601 pp.

Ford, D. C., and Williams, P. W., 2007, Karst Hydrology and Geomorphology, West Sussex, England: John Wiley & Sons Ltd, Print.

Galley, J. E., 1958, Oil and geology in the Permian Basin of Texas and New Mexico; in Weeks, L. G. (ed), Habitat of oil: Am. Assoc. Petroleum Geol., pp. 395-446.

Galley, J. E., 1984, Geologic evolution of the Permian Basin of Texas and New Mexico; in Mazzullo, S. J. (chairman), The geologic evolution of the Permian Basin: Soc. Econ. Paleontol. Mineral., Permian Basin section, Symp. Proc., Midland, TX, pp. 6-8.

Gardiner, Wayne B., 1990, Structural Subprovinces of the Central Basin Platform, West Texas, Strike-Slip Bounded Crustal Blocks. West Texas Geological Society, v. 90-87, p.15-27.

Grant, P. R., and Foster, R. W., 1989, Future petroleum provinces in New Mexico – discovering new reserves: New Mexico Bur. Mines Mineral Resources, 94 pp.

Groom, D., 2008, Common misconceptions about capacitively-coupled resistivity (CCR) what it is and how it works: SAGEEP 2008, 6p.

Geometrics, 2001, Geometrics Operation Manual: OhmMapper TR1, 29005-01, Rev. F. 134 pp.

Geometrics, 2016, OhmMapper: <http://www.geometrics.com/geometrics-products/geometrics- electro-magnetic-products/ohm-mapper>. Accessed December 13, 2016.

Hampton, B. D., 1989, Carbonate sedimentology of the Manzanita Member of the Cherry Canyon Formation; in Harris, P. M., and Grover, G. A. (eds.), Subsurface and outcrop examination of the Capitan shelf margin, northern Delaware Basin: Soc. Econ. Paleontol. Mineral., Core Workshop no. 13, San Antonio, TX, pp. 431- 439.

Hayes, P. T., 1964, Geology of the Guadalupe Mountains, New Mexico: U.S. Geological Society, Prof. Paper 446, 69 pp.

Hendrickson, G. E., and Jones, R. S., 1952, Geology and groundwater resources of Eddy County, New Mexico: New Mexico Bur. Mines mineral Resource, Groundwater Rept. 3, 109 pp.

Henry, C. D., Price, J. G., Parker, D. F., and Wolff, J. A., 1989, Excursion 9A: Mid-Tertiary silicic alkali magmatism of Trans-Pecos Texas – rheomorphic tuffs and extensive silicic lavas, in Chapin, C. E. and Zidek, J. (eds.), Field excursions to volcanic terranes in the western United States, v. 1, southern Rocky Mountain region: New Mexico Bur. Mines mineral Resources, Mem. 46, pp. 231-274.

Hentz, T. F., and Henry, C. D, 1989, Evaporite-hosted native sulfur in Trans-Pecos Texas: relation to late phase Basin and Range deformation. Geology, v. 17, pp. 400-403.

Hentz, T. F., Price, J. G., and Gutierrez, G. N., 1989, Geologic Occurrence and regional assessment of evaporite-hosted native sulfur, Trans Pecos Texas: Bur. Econ. Geol., Univ. Texas Austin, Rept. Invest. 184, 70pp.

Hill, C. A., 1996, Geology of the Delaware Basin, Guadalupe, Apache and Glass Mountains: New Mexico and West Texas. Permian Basin Section – SEPM, Midland, Texas, 480 p.

Hills, J. M., 1942, Rhythm of Permian seas – a paleogeographic study: Am. Assoc. Petroleum Geol., Bull., v. 26, no. 2, pp. 217-255.

Hills, J. M., 1970, Late Paleozoic structural directions in southern Permian Basin, West Texas and southeastern New Mexico: American Association of Petroleum Geology, Bull., v. 54, no. 10, pp. 1809-1827.

Hills, J. M., 1984a, Sedimentation, tectonism, and hydrocarbon generation in the Delaware Basin, West Texas and southeastern New Mexico: Am. Assoc. Petroleum Geol., Bull., v. 68, no. 3, pp. 250-267.

Hills, J. M., 1985, Structural evolution of the Permian Basin of West Texas and New Mexico; in Dickerson, P. W. and Muehlberger, W. R. (eds.), Structure and tectonics of Trans-Pecos Texas: West Texas Geol. Soc., Guidebook Publ. 85-81, pp. 89-99.

Holt, R. M., and Powers, D. W., 1990a, Geologic mapping of the air intake shaft at the Waste Isolation Pilot Plant: Dept. Energy, Rept. DOE/WIPP-90-051, inconseq. pgs.

Holt, R. M., and Powers, D. W., 1990c, The Late Permian Dewey Lake Formation at the Waste Isolation Pilot Plant (WIPP); in Powers et. al., (field trip leaders), Geological and Hydrological studies of evaporites in the northern Delaware Basin for the Waste Isolation Pilot Plant (WIPP), New Mexico: Geol. Soc. Am., Field Trip no. 14, pp. 107-129

.

Horak, R. L., 1975, Tectonic relationship of the Permian Basin to the Basin and Range Province; in Hills, J. M., (ed.), Exploration from the mountains to the basin: Am. Assoc. Petroleum Geol., Southwest section-Soc-. Paleontol. Mineral., Permian Basin section, El Paso Geol. Soc., Trans., pp. 61-94.

Horak, R. L., 1985b, Trans-Pecos tectonism and its effect on the Permian Basin; in Dickerson, P. W., and Muehlberger, W. R. (eds.), Structure and tectonics of Trans- Pecos, Texas: West Texas Geol. Soc., Guidebook Publ. 85-81, Marine Minerals, Short Course, pp. 81-87.

Hull, J. P., 1957, Petrogenesis of Permian Delaware Mountain sandstone, Texas and New Mexico: Am Assoc. Petroleum Geol., Bull., v. 41, no. 2, pp. 278-307.

James, A. D., 1985, Producing characteristics and depositional environments of Lower Pennsylvanian reservoirs, Parkway-Empire south area, Eddy County, New Mexico: Am. Assoc. Petroleum Geol., Bull., v. 69, no. 7, pp. 1043-1063.

Keith, S. B., 1978, Paleosubduction geometries inferred from Cretaceous and Tertiary magmatic patterns in southwestern North America: Geology, v. 6, pp. 516-521.

Kelley, S. A., Chapin, C. E., and Corrigan, J., 1992, Let Mesozoic to Cenozoic cooling histories of the flanks of the northern and central Rio Grande rift, Colorado and New Mexico: New Mexico Bur. Mines Mineral Resources, Bull. 145, 39 pp.

King, P. B., 1942, Permian of West Texas and southeastern New Mexico: Am. Assoc. Petroleum Geol., Bull., v. 26, no. 4, pp. 535-763.

King, P. B., 1948, Geology of the Southern Guadalupe Mountains, Texas: U.S. Geological Survey, Prof. Paper 215, 183 pp.

Kilmchouk, A., 2000c, Speleogenesis under deep-seated and confined conditions. In: Klimchouk A., Ford D. C., Palmer A. N., and Dreybrodt W. (eds.) – Speleogenesis: evolution of karst aquifers. Huntsville, National Speleological Society: 244-260.

Klimchouk A., 2007, Hypogene speleogenesis: hydrogeological and morphometric perspective. Carlsbad, National Cave and Karst Research Institute: 106pp.

Kohout F. A., Meisler H., Meyer F., Johnston R., Leve G., and Wait R., 1988, Hydrogeology of the Atlantic Continental Margin. In: Sheridan R. and Grow J. (eds.) – The geology of North America, the Atlantic Continental Margin. Boulder, Geological Society of America: p. 463-480.

Lee M. K., and Williams D. D., 2000, Paleohydrology of the Delaware Basin, western Texas: overpressure development, hydrocarbon migration, and ore genesis. Bulletin of the American Association of Petroleum Geologists, vol. 84, no. 7, pp 961-974.

Machel, H. G., 1992, Low-temperature and high-temperature origins of elemental sulfur in diagenetic environments, in G. R. Wessel and B. H. Wimberly (eds.), Native Sulfer: Developments in Geology and Exploration. Society of Mining, Metallurgy, and Exploration, Inc., Littleton, CO, p. 3-22.

Markello, J.R., Sarg, J.F., 1996, Phanerozoic Tectono-Stratagraphic Evolution of the Trans-Pecos and Permian Basin Regions (Mexico, Texas, New Mexico) Using Landsat Imagery, Subsurface and Outcrop Data, Eleventh Thematic Conference on Applied Geologic Remote Sensing, Las Vegas, Nevada, 27-29 February 1996.

Melim, L. A., 1991, The origin of dolomite in the Permian (Guadalupian) Capitan Formation, Delaware Basin, West Texas and New Mexico – implications for dolomitization models: Unpubl. PhD dissert., Southern Methodist Univ., 200 pp.

Mercer, J. W., and Gonzalez, D. D., 1981, Geohydrology of the proposed Waste Isolation Pilot Plant site in southeastern New Mexico; in Wells, S. G. and Lambert, W. (eds.), Environmental geology and hydrology in New Mexico: New Mexico Geol. Soc., Spec. Publ. 10, pp. 123-131.

Nance, R., 1993, Application of the standard tablet method to a study of denudation in gypsum karst, Chosa Draw, southeastern New Mexico, MS Thesis, University of Northern Colorado, Greely Colorado, 82p.

Netherland, D., Sewell, P., and Associates, 1974, Evaluation of hydrocarbon potential, AEC study area, Southeast New Mexico: Oak Ridge Natl. Labs., Oak Ridge, TN, ORNL78X-38284V, 23 pp.

Ross, C. A., 1978a, Late Pennsylvanian and Early Permian sedimentary rocks and tectonic settingof the Marathon geosyncline; in Mazzullo, S. J., Tectonics and Paleozoic facies of the Marathon geosyncline, West Texas: Soc. Econ. Paleontol. Mineral., Permian Basin section, Pub. 78-17, pp. 89-93.

Ross, C. A., 1981, Pennsylvanian and Early Permian history of the Marathon Basin, West Texas; in Pearson, B. T. (field trip leader), Marathon-Marfa region of West Texas: Soc. Econ. Paleontol. Mineral., Permian Basin section, Guidebook Publ. 81-20, pp. 135-144.

Schiel, K. A., 1994, A new look at the age, depositional environment, and paleogeographic setting of the Dewey Lake Formation: West Texas Geol. Soc., Bull., v. 33, no. 9, pp. 5-13.

Scholle, P. A., Ulmer, D. S., and Melim, L. A., 1992, Late-stage calcites in the Permian Capitan Formation and its equivalents, Delaware Basin margin, West Texas and New Mexico – evidence for replacement of precursor evaporites: Sedimentology, v. 39., pp. 207-234.

Scholle, P.A., Goldstein, R. H., and Ulmer-Scholle, D.S., 2004, Classic upper Paleozoic reefs and bioherms of west Texas and New Mexico. New Mexico Institute of Mining and Technology Socorro, New Mexico, 166 p.

Snider, H. I., 1966, Stratigraphy and associated tectonics of the upper Permian Castile-Salado-Rustler evaporate complex, Delaware Basin, West Texas and southeast New Mexico: Unpubl. PhD. Dissert., Univ. New Mexico, 140 pp.

Stafford, K. W., Klimchouk, A., and Boston, P. J., 2006, Polygenetic evaporite karst of the Castile Formation of the western Delaware Basin. Abstracts and Program. Geological Society of America, 38 (7): 289.

Stafford, K.W., Nance, R., Rosales-Lagarde, L., and Boston, P., 2008a - Epigene and hypogene karst manifestations of the Castile Formation: Eddy County, New Mexico and Culberson County, Texas. International Journal of Speleology, v. 37, no. 2, p. 83-98.

Stafford, K.W., Rosales-Lagarde, L., and Boston, P.J., 2008b - Castile evaporite karst potential map of the Gypsum Plain, Eddy County, New Mexico and Culberson County, Texas: A GIS methodological comparison. Journal of Cave and Karst Studies, v. 70, no. 1, p. 35-46.

Stafford, K.W., Ulmer-Scholle, D., and Rosales-Lagarde, L., 2008c - Hypogene calcitization: evaporite diagenesis in the western Delaware Basin. Carbonates and Evaporites, v. 23, no. 2, p. 89-103.

Stafford, K. W., 2015 - Evaluation of existing geologic conditions along RM 652: Initial characterization of karst geohazards associated with RM 652 in Culberson County, Texas.

Toth J., 1999 – Groundwater as a geologic agent and overview of the causes, processes, and manifestations. Hydrogeology Journal, 7: 1-14.

Walter, J. C., 1953 - Paleontology of Rustler Formation, Culberson County, Texas: Jour. Paleontology, v. 27, no. 5, pp. 679-702.

White, W. B., 1988 - Geomorphology and Hydrology of karst terrains: Oxford Univ.Press, New York, 464 pp.

Wilcox, R. E., 1989 – Evidence for an early Cretaceous age for the Bissett Formation, western Glass Mountains, Brewster and Pecos Counties, West Texas – implications for regional stratigraphy, paleogeography, and tectonics: Unpubl. MS thesis, Sul Ross State University, 253 pp.

APPENDIX B

METHODOLOGY

Project Methodology

Resistivity data was collected along the entire traverse of RM 652 in Culberson County, Texas. The geophysical instrumentation that was used in this study is the Geometrics OhmMapper G858 resistivity system, which uses the dipole-dipole, TR-5 configuration. This type of configuration uses one pair of current emitting electrodes (transmitter), and five pairs of potential electrodes (receivers) (Figure B1). The OhmMapper G858 resistivity meter simultaneously recorded resistivity data in conjunction with a GPS (Global Positioning System) unit, a Trimble Nomad 900 series logger connected to a Pathfinder Pro receiver and Zephyr antennae with a horizontal accuracy of less than 20 inches or 50 cm, which outlined the path where readings were taken (Figure B2). Because of the arid and dusty nature of the survey environment, all system connections were routinely cleaned in order to avoid poor connections that had the potential to cause errors in the data. Electrodes were encased in plastic sheaths designed by Geometrics Inc., and were used in this survey in order to protect the equipment from the roadway and the high temperatures of the asphalt within the study area (Figure B3)

.

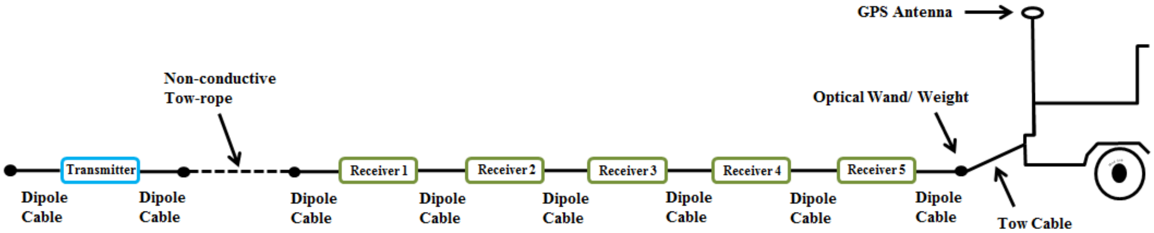

Figure B1. *Diagram of OhmMapper use and electrode geometries. This image shows a TR5 configuration, with a transmitter and five receivers that allow for five depths of investigation while continuously collecting resistivity data along a single traverse (modified from Geometrics, 2016).*

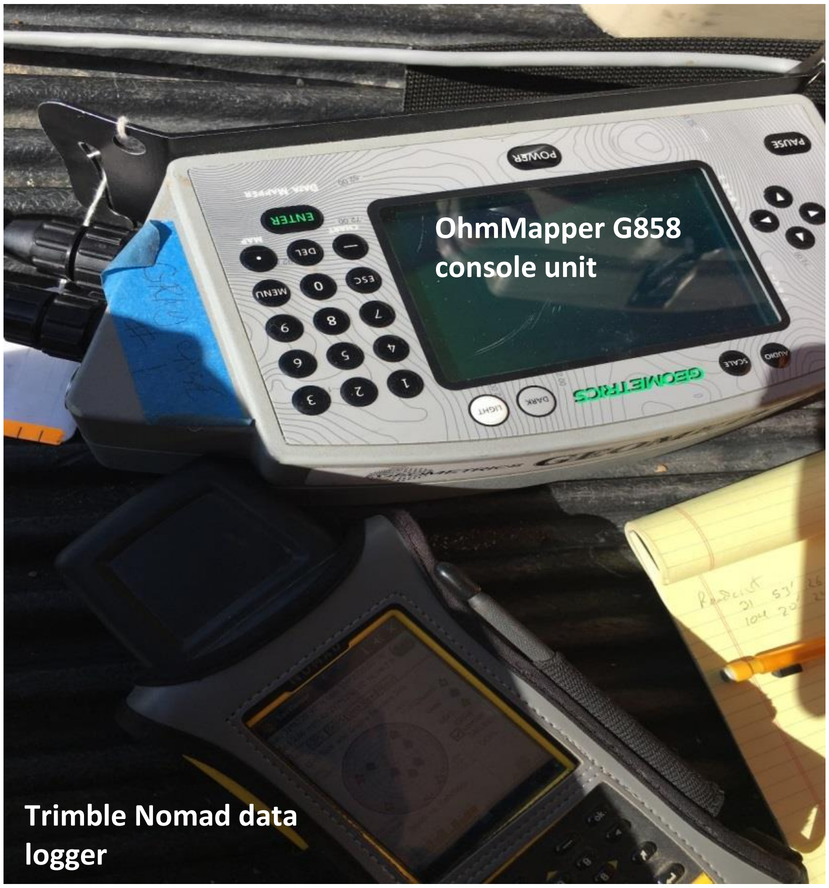

Figure B2. *Image of the OhmMapper G858 resistivity meter on the top portion of the photo, and the Trimble Nomad 900 Series GPS data logger in the bottom portion of the photo.*

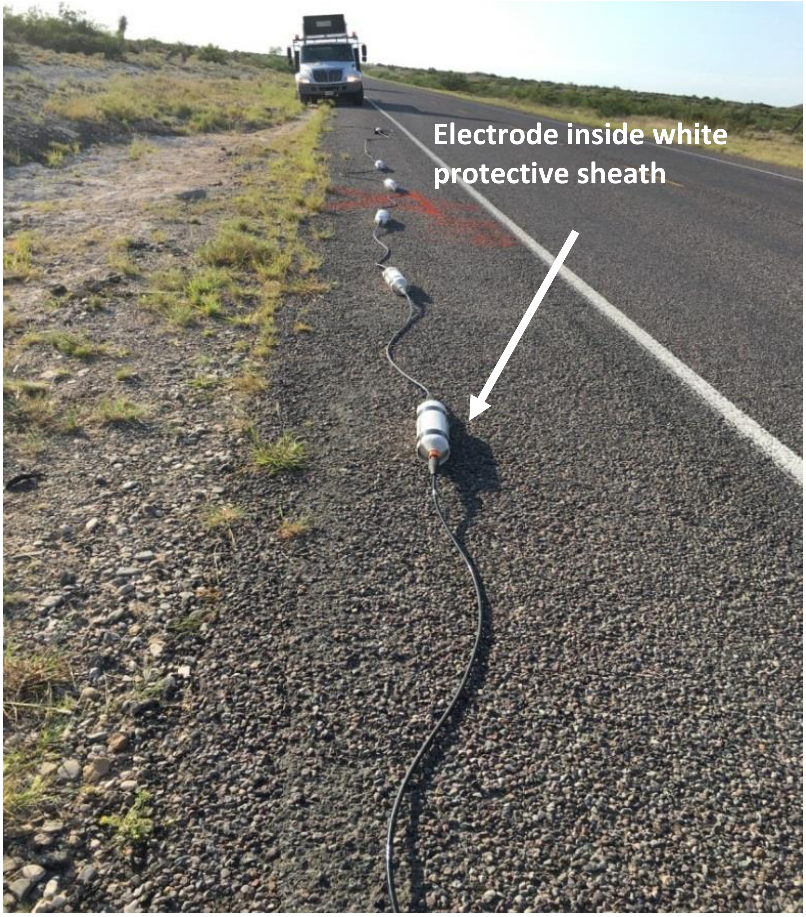

Figure B3. *Photo showing the white sheaths, designed by Geometrics, used to protect the equipment from the high temperatures and abrasive roadway.*

Survey Parameters

Before the survey could be conducted, survey parameters were set in the G858 console unit; this included the electrode geometry and ensuring that the G858 console and GPS unit were communicating. The 2.5 meter dipole cables were used, equaling to 5 meter dipoles throughout the survey, and the non-conductive rope was set to 2.5 meters (Figure B4). The transmitter dipole length, and the receiver dipole length, must

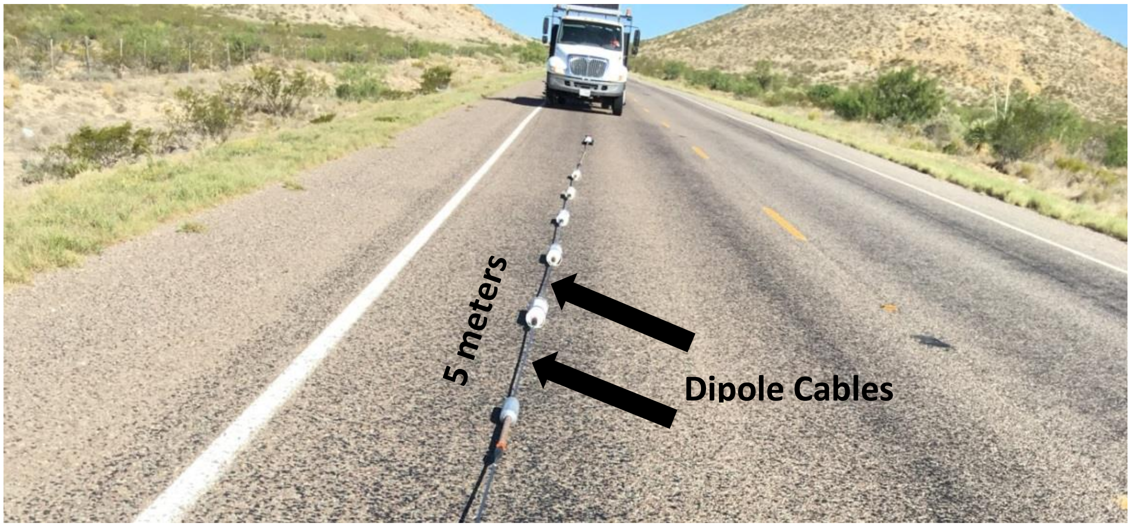

Figure B4. *Photo showing individual 2.5 meter dipole cables indicated by the black arrows, completing a 5 meter dipole* ***.***

be equal because the dipole-dipole array was used. The operator offset cable, that connected to the G858 console at the quick disconnect, was 5 meters and its length must be entered into the survey parameters (Figure B5). While collecting data, an AC current couples the ground to the dipoles with the aid of a weighted optical wand, which is positioned between the first dipole cable and the operator offset cable.(Figure B6). The weight allows for continuous ground contact of the receivers and transmitters while the instrument produces a vertical continuous resistivity profile of known depth (Geometrics, 2016). The optical wand that is connected to the weight contains integrated electrical-to-optical and optical-to-electrical converters, which allows the console to read data from the receivers. During data collection, the OhmMapper was towed behind the SFASU geology department truck along the 34 mile long road segment at 2 mph. A minimum crew size of three people is recommended for this task, one person to operate the tow vehicle, a survey manager to operate and monitor the G858 console, and another member to ensure the electrodes stay on path.

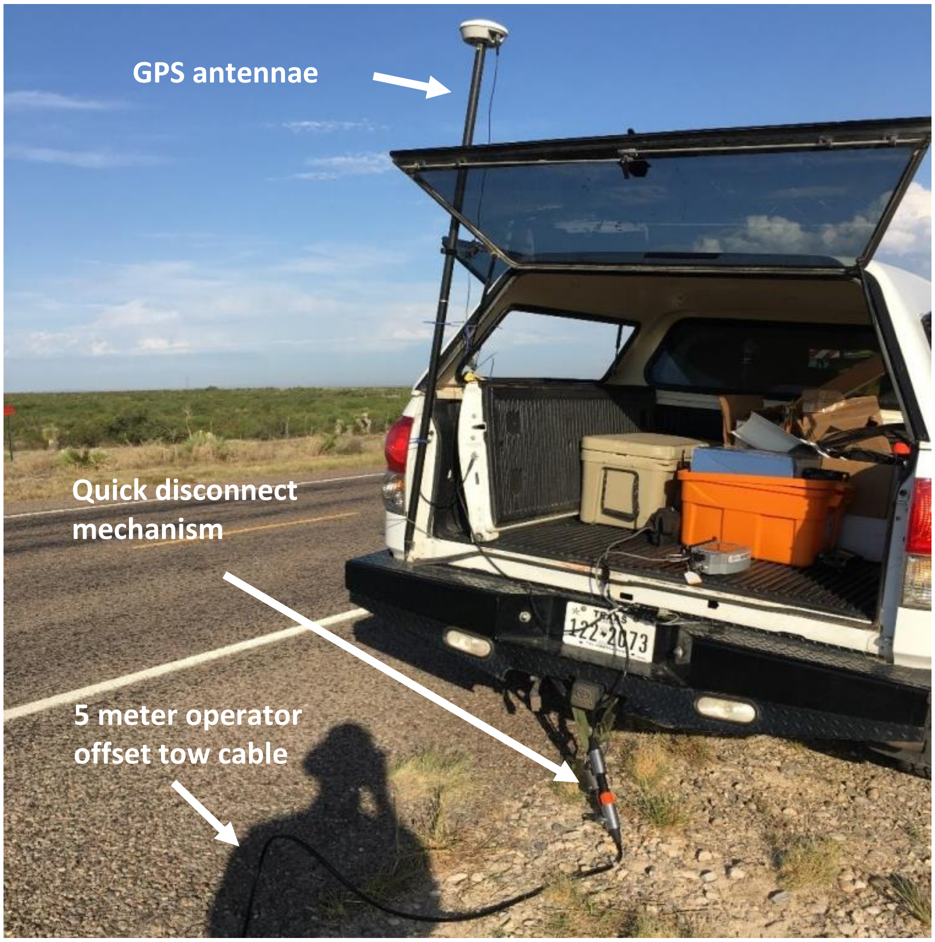

Figure B5. *Image of the 5 meter operator offset tow cable, the quick disconnect mechanism where it connects to the G858 console unit, and the GPS antenna.*

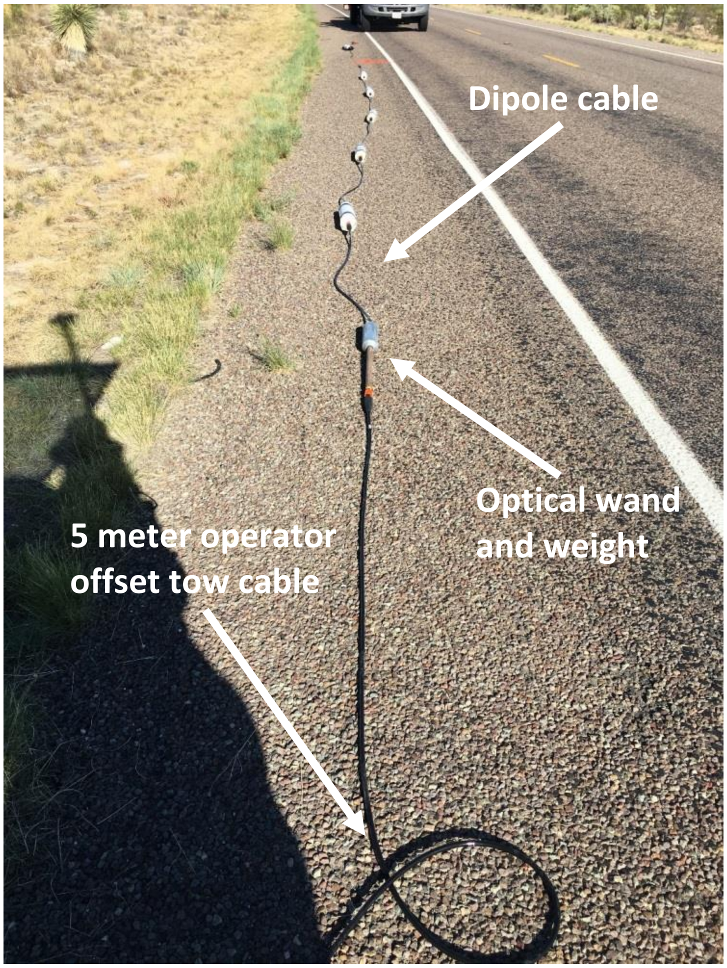

Figure B6. *Photo showing the position of the fiber optic communication wand and the weight that helps keep the system close to the ground.*

Data Processing

Resistivity data was recorded as raw binary data (.bin) files along the entire 54 kilometer study area, and were imported from the console unit into the pre-inversion software, Magmap2000, which was used to assess data quality and consistency between collected data points (Geometrics, 2016). After the data was imported into MagMap2000, a GPS map of collected data points was drawn, and then set to display true map latitude and longitude coordinates (Figure B7 and Figure B8). The map was then converted into UTM coordinates, which is required to export pseudosections, and the road was divided into manageable sections, six ~160 meter sections and the rest of the road into ~322 meter sections. This is achieved by deleting unwanted selected GPS positions (*blue squares*), and moving the line markers (*green and red boxes for the beginning and end of a line respectively*) to the correct GPS coordinates (Figure B9). Once the desired number of GPS positions (*blue squares*) remained, to represent the ~160 meter or ~322 meter section due for processing, the quality of OhmMapper readings for all five receivers was checked to verify that none of the receivers lost the signal connection to the transmitter during that section of the traverse. This step should have a colored line for each receiver (Figure B10). Once readings were verified, a despiking filter was used to smooth data by removing exaggerated and artificial readings, seen as single spike events, by applying a peak threshold to the data (Figure B11). The individual resistivity lines should have gradual ascending and descending curves that more accurately represents the gradual change of resistive properties as the medium gradually changes throughout the survey. Therefore, a single, abrupt increase in resistivity is interpreted to be erroneous data.

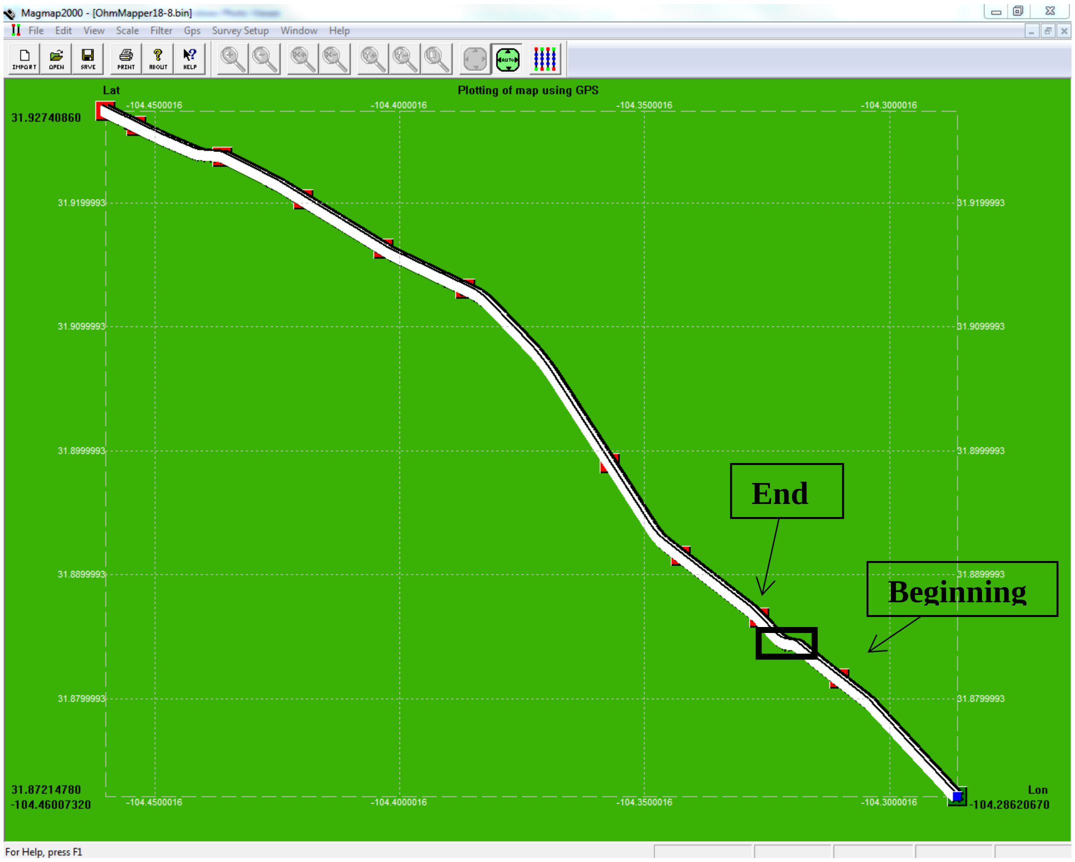

Figure B7. *Screenshot of collected resistivity data points representing 10 miles that correspond to latitude and longitude coordinates collected by GPS. Black box indicates a section of interest. Green and red boxes indicate the beginning and end line points respectively. Note, the green beginning box in this photo is under a red end of line box, but is indicated by an arrow. (Image created in Geometrics' MagMap2000, 2016).*

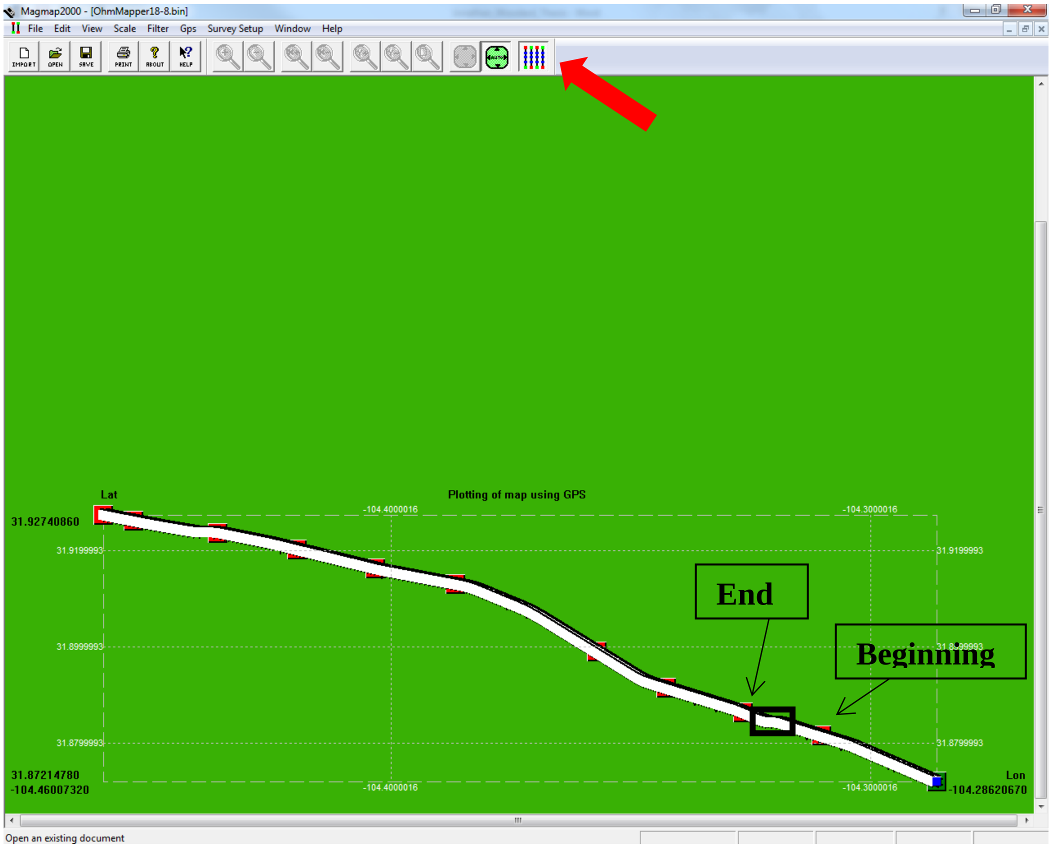

Figure B8. *Screenshot of the 10 mile segment adjusted to true coordinates. Black box indicates a section of interest and the red arrow indicates where to convert to true map coordinates. Green and red boxes indicate the beginning and end line points, respectively. Note, the green beginning box in this photo is under a red end of line box, but is indicated by an arrow. (Image created in Geometrics' MagMap2000, 2016).*

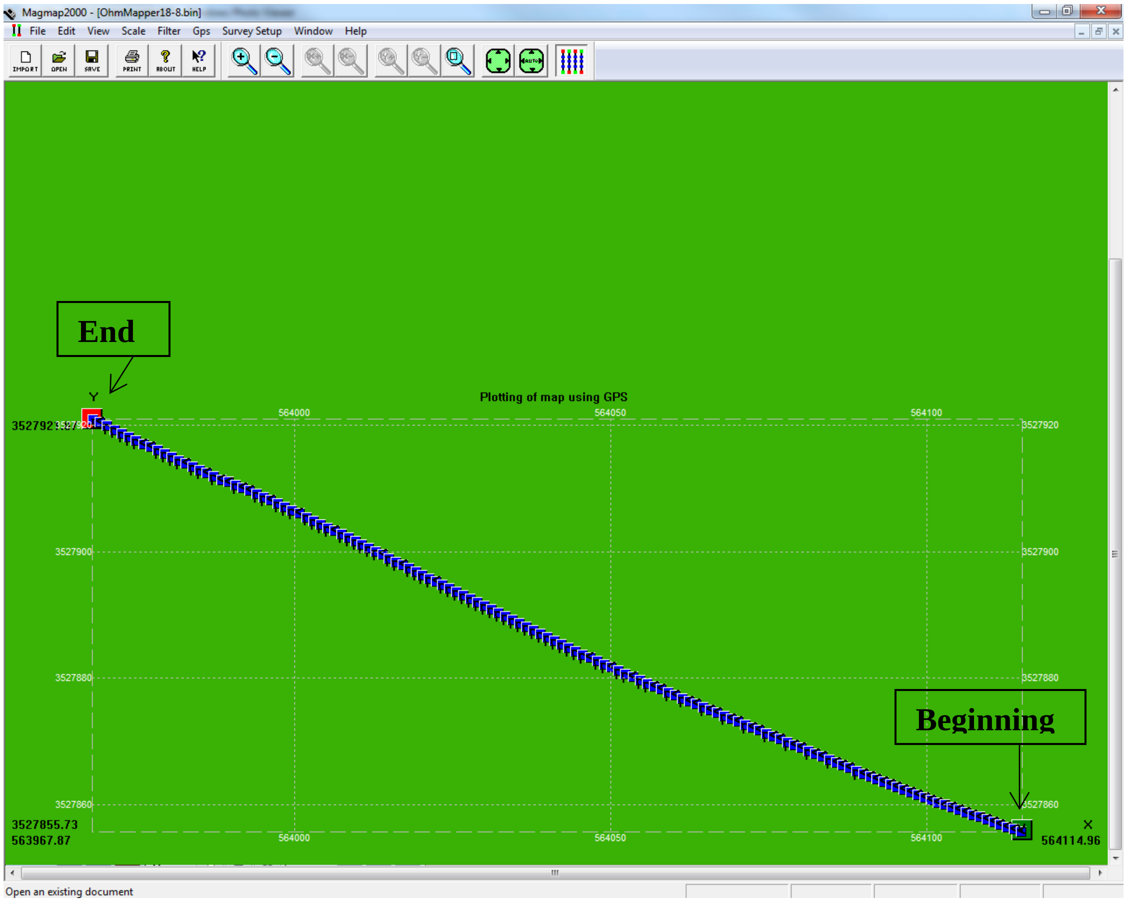

Figure B9. *Screenshot of the desired segment. The green and red box indicate the beginning and end points of the line respectively. GPS and resistivity recordings are indicated by the blue squares. The coordinate system is in UTM (Image created in Geometrics' MagMap2000, 2016).*

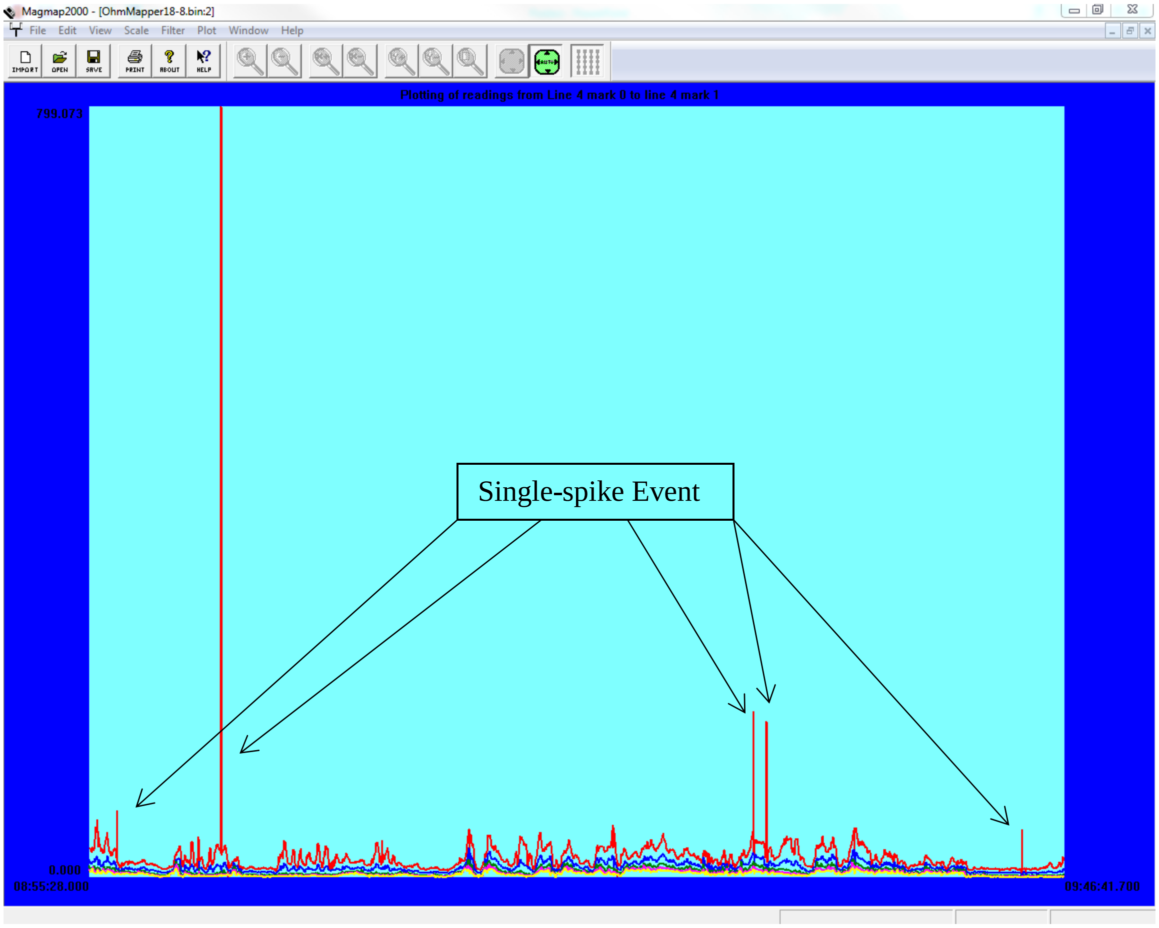

Figure B10. *Screenshot of the section resistivity readings before the despiking filter was applied. This feature removed the large single-spike events that represent erroneous data points. This is also where signal quality is checked by making sure all lines exist across the survey. The Y axis represents resistivity and it is plotted against time on the X axis. Each receiver is represented by a different color line; Red = Rx1, Blue = Rx2, Green = Rx3, Pink = Rx4, Yellow = Rx5 (Image created in Geometrics' MagMap2000, 2016).*

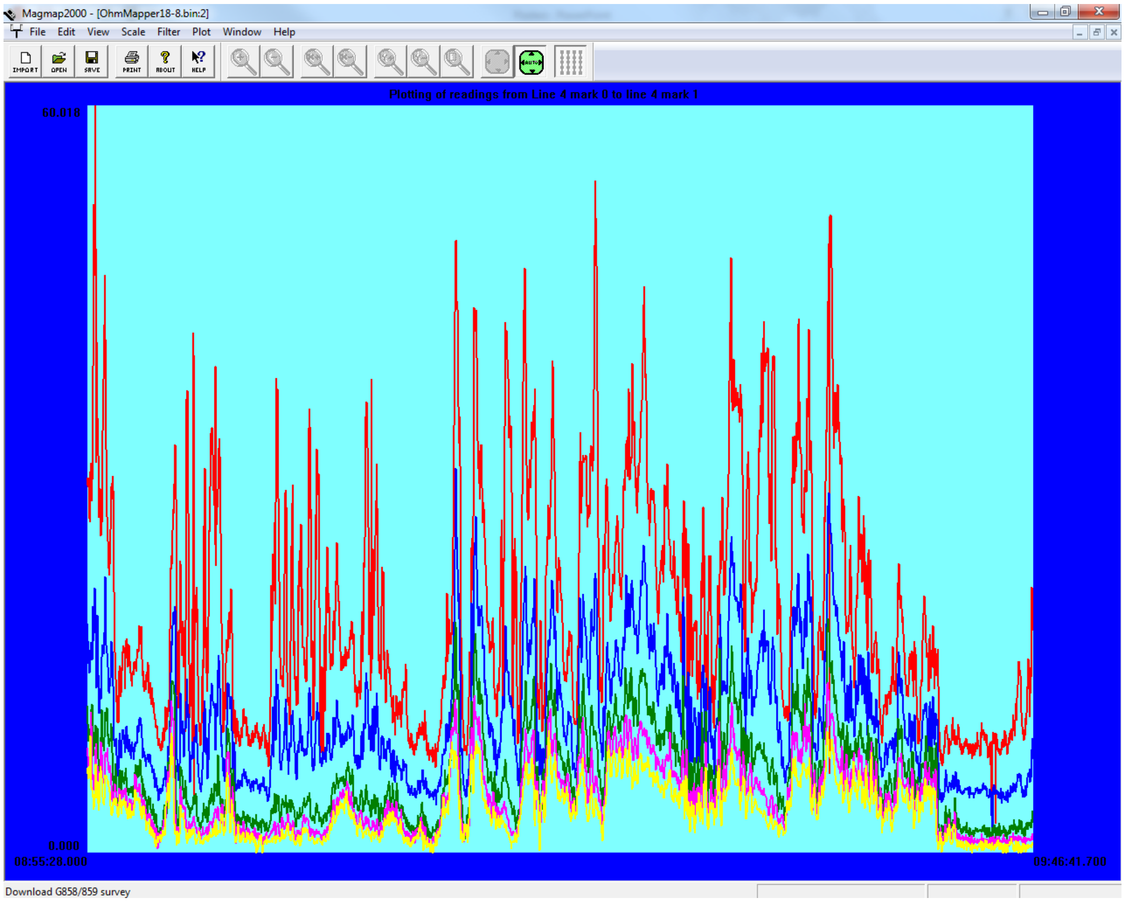

Figure B11. *Screenshot of the section resistivity readings after the despiking filter was applied. The large single spike events seen before have been removed by applying a peak threshold. Now the curves have gradual changes instead of abrupt increases. The Y axis represents resistivity and it is plotted against time on the X axis. Each receiver is represented by a different color line; Red = Rx1, Blue = Rx2, Green = Rx3, Pink = Rx4, Yellow = Rx5 (Image created in Geometrics' MagMap2000, 2016).*

Pseudosections, 2D profiles of apparent resistivity, were generated in MagMap2000 showing resistivity changes with depth, for individual segments throughout the entire 54 kilometer long traverse (Figure B12). The color scale for pseudosections was selected so that high resistivity values were indicated by red and low resistivity values were indicated by blue. Pseudosections were exported from MagMap2000 as data (.dat) files for inversion processing.

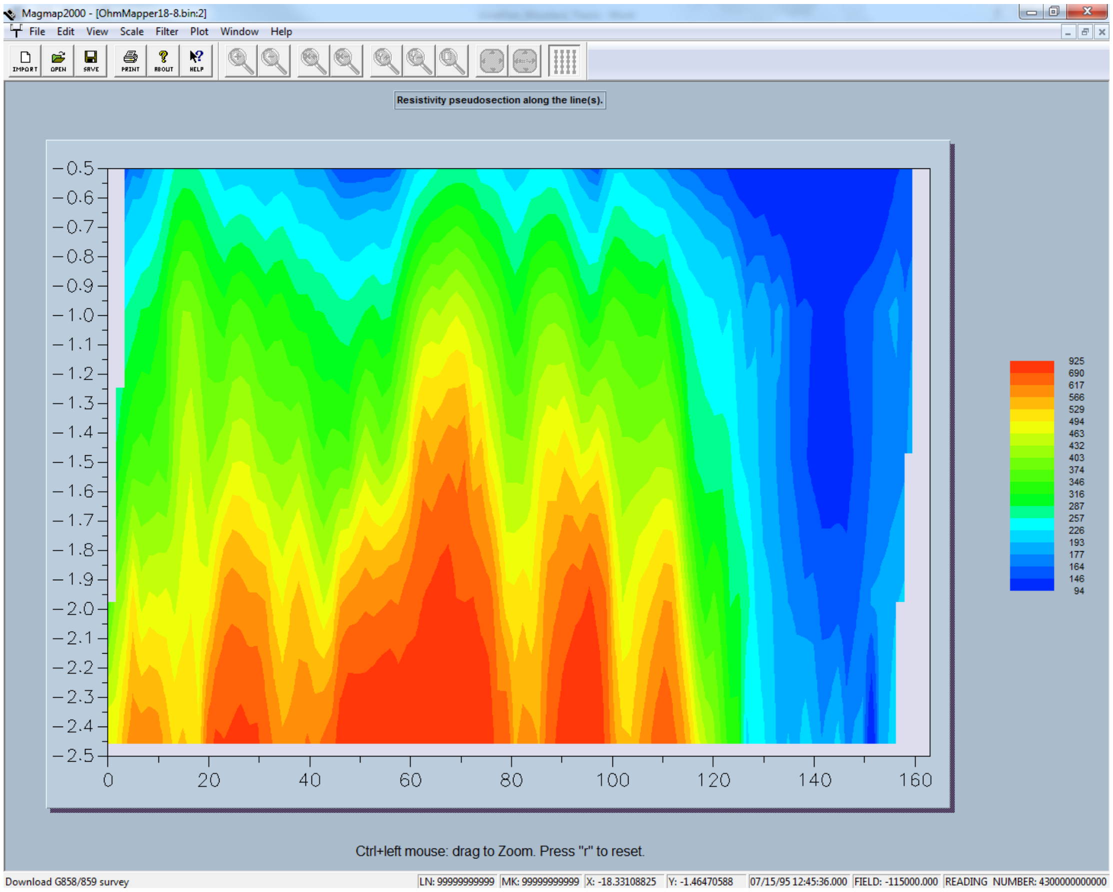

Figure B12. *Screenshot of the apparent resistivity pseudosection for the segment previously mentioned. The Y axis represents n-space (ratio of dipole length to distance between dipoles) and the X axis shows the distance in meters from the beginning of the selected segment to the end (Image created in Geometrics' MagMap2000, 2016).*

2D pseudosections (.dat files) were imported into an inversion software, (AGI's EarthImager 2D) which was used to generate 2D inverted resistivity profiles. Advanced Geosciences Inc.'s (AGI) EarthImager 2D is a computer based, two-dimensional, data interpretation software program that is used in resistivity studies. This program offers an ease of processing resistivity data including, but not limited to, survey planning, surface data inversion, time-lapse inversion, continuous resistivity profiling (CRP), and correction for terrain variability (AGI, 2009). Resistivity data along the 54 kilometer long study area traverse was processed using the *Surface* settings which default to the smooth model inversion and associated resistivity settings (Figure B13 and Figure B14). This inversion method averaged resistivity values every 1.25 m and projecte these values in a cross-sectional model to find the smoothest fit for the resistivity data points. When a completed inversion rendered a resistivity model with a high root-mean squared (RMS) error, noisy data points would be removed using the *Data Misfit Histogram*, which is automatically generated after the inversion (Figure B15). The noisy data points (outliers) were removed in increments, after each inversion, until a model with less than 20% RMS error could be achieved in order to protect data integrity. The accuracy of an inverted model could be verified by viewing the data misfit cross-plot, which is automatically generated after each inversion. The misfit cross-plot is a graphical representation of the collected data (apparent resistivity) values against the predicted values (AGI, 2009; Figure B16).

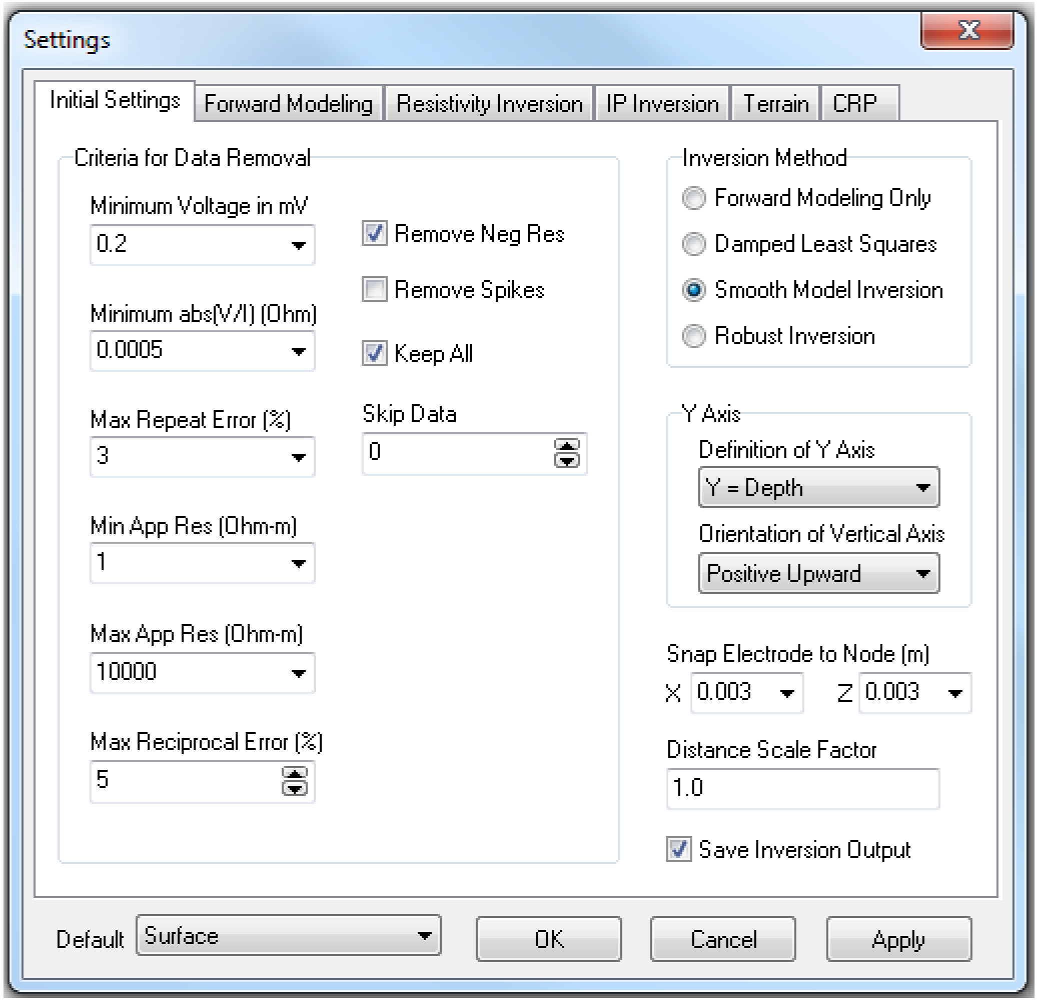

Criteria for Data Removal

Minimum Voltage in mV: 0.2

Minimum abs(V/I) (Ohm): 0.0005

Max Repeat Error (%): 3

Min App Res (Ohm-m): 1

Max App Res (Ohm-m): 10000

Max Reciprocal Error (%): 5

☑ Remove Neg Res

☐ Remove Spikes

☑ Keep All

Skip Data: 0

Inversion Method

○ Forward Modeling Only

○ Damped Least Squares

● Smooth Model Inversion

○ Robust Inversion

Y Axis

Definition of Y Axis: Y = Depth

Orientation of Vertical Axis: Positive Upward

Snap Electrode to Node (m): X 0.003 Z 0.003

Distance Scale Factor: 1.0

☑ Save Inversion Output

Default: Surface

Figure B13. *Screenshot of the initial settings for the segment. All inversion parameters are set to default "Surface" settings that is recommended for most resistivity surveys. This screen shows that a smooth model inversion was ran, and that "Remove Spikes" is not selected so that the user has control over which data points to remove (Image created in AGI's EarthImager 2D, 2016).*

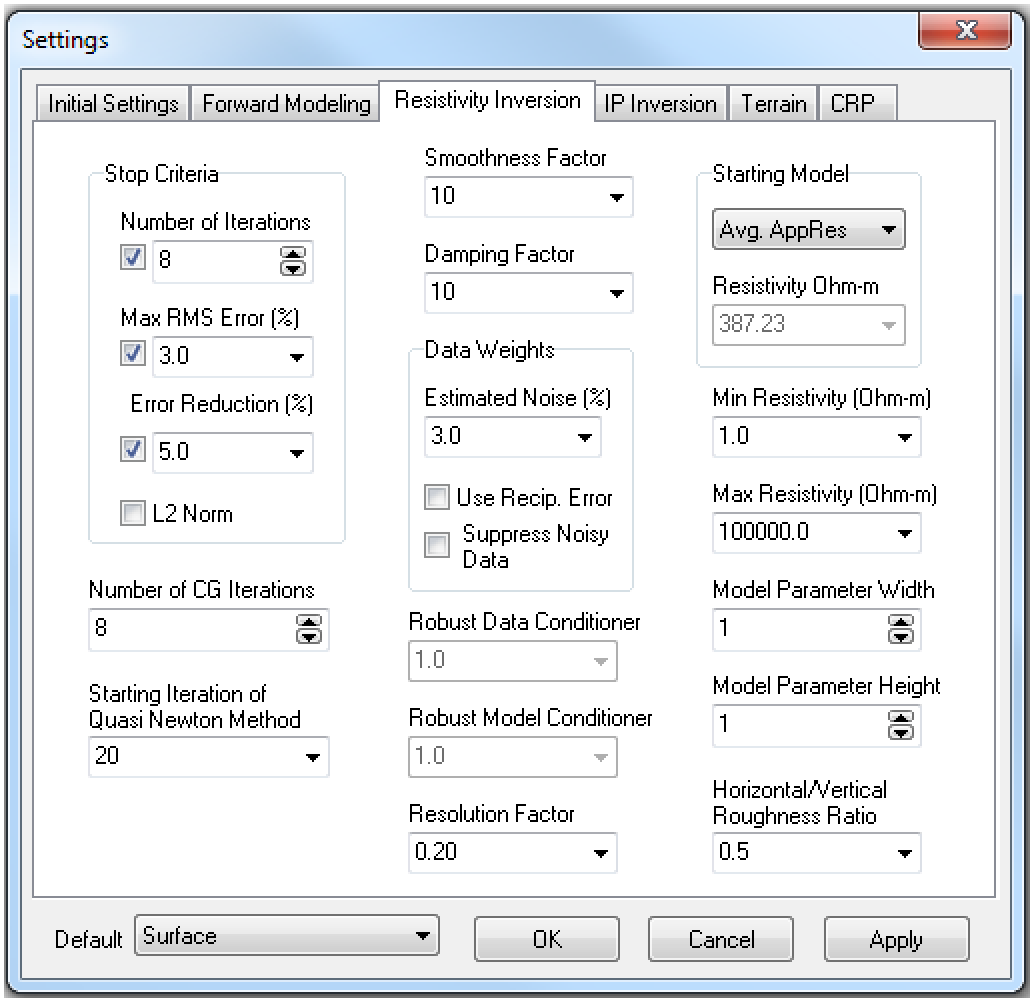

Stop Criteria

Number of Iterations: ☑ 8

Max RMS Error (%): ☑ 3.0

Error Reduction (%): ☑ 5.0

☐ L2 Norm

Number of CG Iterations: 8

Starting Iteration of Quasi Newton Method: 20

Smoothness Factor: 10

Damping Factor: 10

Data Weights

Estimated Noise (%): 3.0

☐ Use Recip. Error

☐ Suppress Noisy Data

Robust Data Conditioner: 1.0

Robust Model Conditioner: 1.0

Resolution Factor: 0.20

Starting Model: Avg. AppRes

Resistivity Ohm-m: 387.23

Min Resistivity (Ohm-m): 1.0

Max Resistivity (Ohm-m): 100000.0

Model Parameter Width: 1

Model Parameter Height: 1

Horizontal/Vertical Roughness Ratio: 0.5

Default: Surface

Figure B14. *Screenshot of the resistivity inversion parameters for the segment. All criteria are default "Surface" settings (Image created in AGI's EarthImager 2D, 2016).*

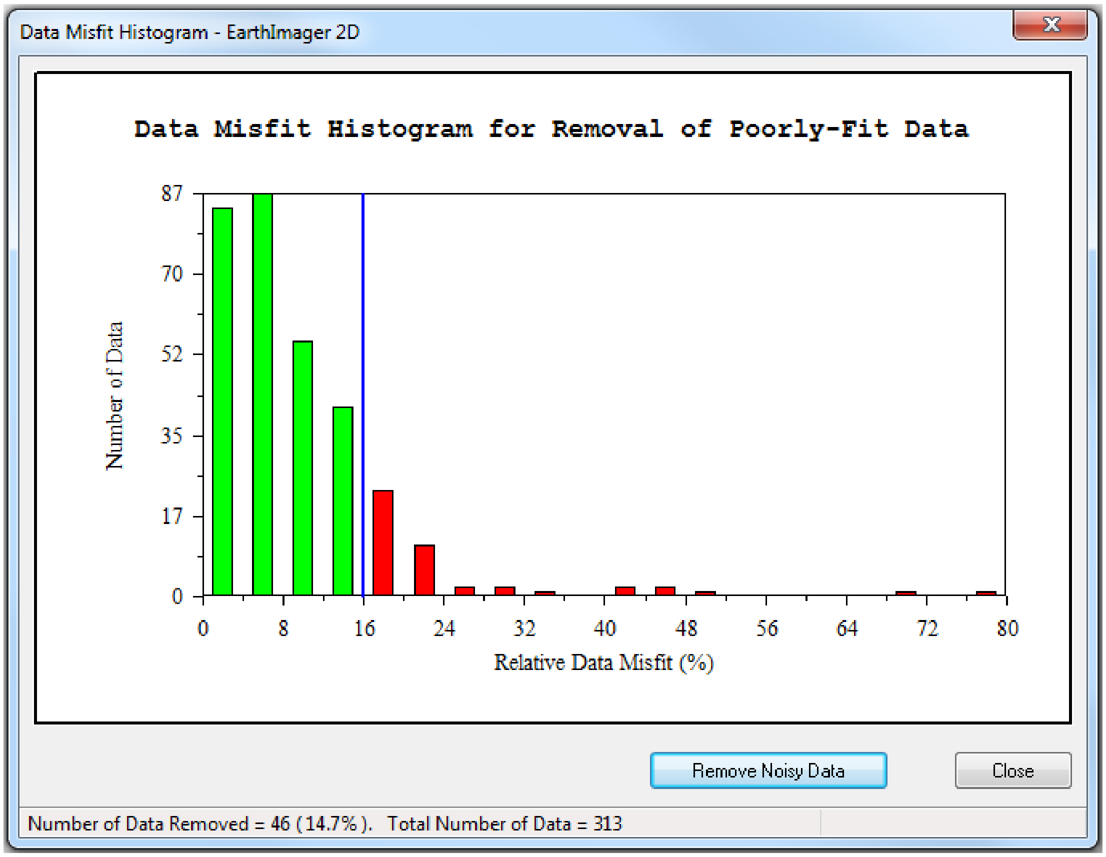

Number of Data Removed = 46 (14.7%). Total Number of Data = 313

Figure B15. *Screenshot of the data misfit histogram for the segment. Outliers were removed by moving the blue line over to the right with the arrow keys. Data preserved would be in green and data to be removed will be in red, and then click remove noisy data. At this screen one or two data points can be removed at a time which can be tracked at the bottom of the image (Image created in AGI's EarthImager 2D, 2016).*

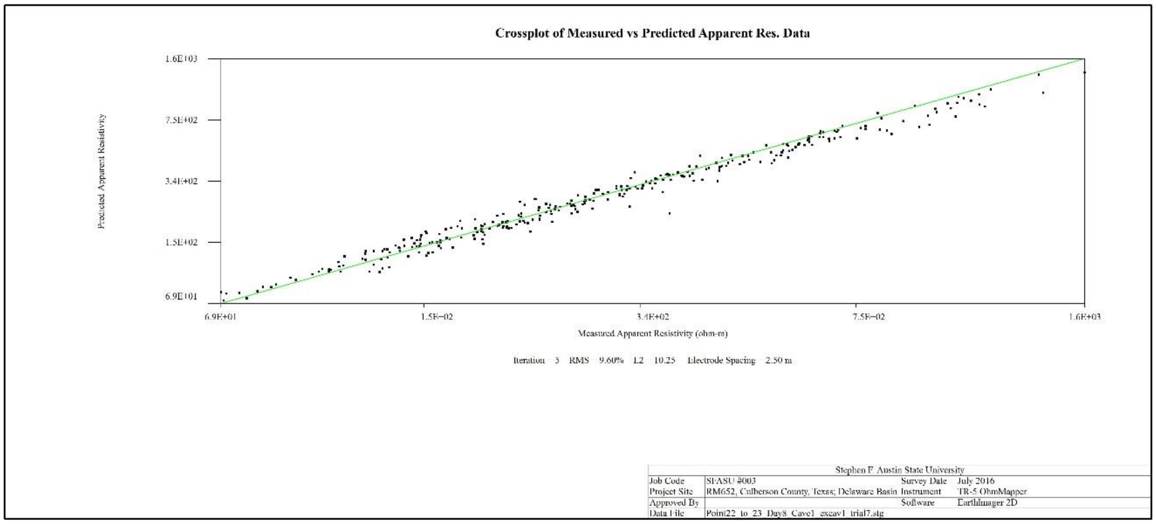

Iteration 5 RMS 9.60% L2 10.25 Electrode Spacing 2.50 m

Stephen F. Austin State University			
Job Code	SFASU #003	Survey Date	July 2016
Project Site	RM652, Culberson County, Texas; Delaware Basin	Instrument	TR-5 OhmMapper
Approved By		Software	EarthImager 2D
Data File	Point22_to_23_Day8_Cave1_excav1_trial7.stg		

Figure B16. *Screenshot of the data misfit cross-plot for the segment. Data points are plotted along a trend line which is the predicted apparent resistivity "Y axis" against the measured apparent resistivity "X axis" (Image created in AGI's EarthImager 2D, 2016).*

Terrain corrections were applied in order to more accurately interpret the resistivity profiles of the six ~160 meter sections. GPS locations that were simultaneously collected with resistivity values were extracted from MagMap2000, imported into ArcGIS and overlain on top of a high-resolution photo of the study area. Elevation values were extracted from a digital elevation model (DEM) that was produced from LIDAR data collected over the study area. The DEM was layered with the GPS points and aerial photo in order to extract elevation values into a comma-delimited excel worksheet with the associated GPS coordinate. This excel file was then imported into *Microsoft Notepad* and formatted in accordance with the terrain file format used by the inversion program (Figure B17). The terrain file is read and applied to the pseudosection data file prior to completing an inversion.

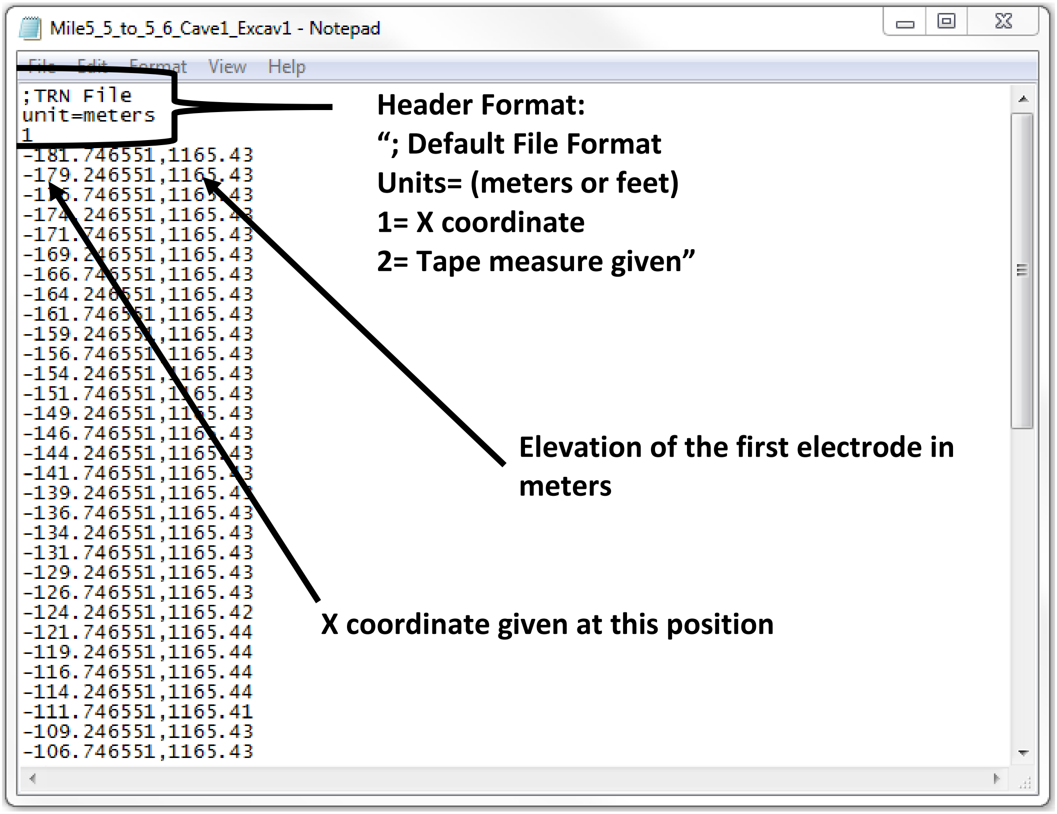

```
;TRN File
unit=meters
1
-181.746551,1165.43
-179.246551,1165.43
-176.746551,1165.43
-174.246551,1165.43
-171.746551,1165.43
-169.246551,1165.43
-166.746551,1165.43
-164.246551,1165.43
-161.746551,1165.43
-159.246551,1165.43
-156.746551,1165.43
-154.246551,1165.43
-151.746551,1165.43
-149.246551,1165.43
-146.746551,1165.43
-144.246551,1165.43
-141.746551,1165.43
-139.246551,1165.43
-136.746551,1165.43
-134.246551,1165.43
-131.746551,1165.43
-129.246551,1165.43
-126.746551,1165.43
-124.246551,1165.42
-121.746551,1165.44
-119.246551,1165.44
-116.746551,1165.44
-114.246551,1165.44
-111.746551,1165.41
-109.246551,1165.43
-106.746551,1165.43
```

Header Format:
“; Default File Format
Units= (meters or feet)
1= X coordinate
2= Tape measure given”

Elevation of the first electrode in meters

X coordinate given at this position

Figure B17. *Terrain file example for the segment. Elevation data was extracted from a DEM of the study area in ArcGIS.*

References

AGI: Advanced Geosciences Incorporated, 2007 – EarthImager 2D Resistivity and IP Inversion Software Instruction Manual: Austin, TX, 139 p.

Geometrics, 2016 – MagMapper2000/DataMap OhmMapper User Guide: <ftp://geom.geometrics.com/pub/GeoElectric/Manuals/DATMAPM.PDF>.

Accessed December 13, 2016.

Geometrics, 2016 – OhmMapper: <http://www.geometrics.com/geometrics-products/geometrics-electro-magnetic-products/ohm-mapper>.

Accessed December 13, 2016.

APPENDIX C

RESULTS

Preface

Descriptions of each anomaly throughout the study area are presented in the following tables in order to provide clarity to subsequent GIS maps and inverted resistivity sections. The resistivity results of the 34 mile traverse are presented in this appendix in one mile sections; first a GIS map will be shown for each mile, and the following inverted resistivity profiles will represent the data recorded for that mile. This sequence serves the reader by offering an orientation for subsequent resistivity profiles, while the profiles show the extensive impact of the anomalies. Units presented in this appendix are from the imperial system because these units are used by the contracting party (TxDOT). Following all results, a conclusion will be provided in order to summarize the results within this appendix. The conclusions will be supported by two graphs, which show a rolling average of individual anomalies per mile, along with a rolling average of karst density within each mile.

Table 1. List of anomaly details along the 34 mile long segment.

Mile Number	**Distance (Mile)**	**Anomaly Number**	**Geohazard Description**	**Length (Feet)**
0-1	0.07	1	Lateral Piping	70
0-1	0.28	2	Vertical Piping	30
0-1	0.36	3	Vertical Piping	70
0-1	0.42	4	Vertical Piping	75
0-1	0.78	5	Lateral Piping	70
0-1	0.89	6	Lateral Piping	60
0-1	0.93	7	Lateral Piping	60
0-1	0.98	8	Lateral Piping	150
1-2	1.07	9	Lateral Piping	30
1-2	1.11	10	Lateral Piping	30
1-2	1.15	11	Lateral Piping	130
1-2	1.18	12	Lateral Piping	30
1-2	1.31	13	Lateral Piping/ Fill	60
1-2	1.41	14	Lateral Piping	45
1-2	1.42	15	Lateral Piping	45
1-2	1.44	16	Vertical Piping	135
1-2	1.61	17	Solution Fractures	40

Table 2. List of anomaly details along the 34 mile long segment.

Mile Number	Distance (Mile)	Anomaly Number	Geohazard Description	Length (Feet)
1-2	1.63	18	Filled Sink	260
1-2	1.70	19	Solution Fractures	85
1-2	1.74	20	Sinkhole Fill	125
1-2	1.78	21	Lateral Piping	30
1-2	1.81	22	Filled Sink/ Arroyo	30
1-2	1.82	23	Solution fracture	30
1-2	1.83	24	Solution Fractures	30
1-2	1.84	25	Solution Fracture/ Void	45
1-2	1.85	26	Solution Fracture	25
1-2	1.91	27	Solution Fractures	35
1-2	1.97	28	Solution Fractures	140
2-3	2.06	29	Valley Fill	300
2-3	2.17	30	Fill (Adjacent to Sink)	230
2-3	2.25	31	Filled Arroyo	75
2-3	2.28	32	Lateral Piping	210
2-3	2.57	33	Lateral Piping	70
2-3	2.61	34	Vertical Piping (Berm)	15

Table 3. List of anomaly details along the 34 mile long segment.

Mile Number	**Distance (Mile)**	**Anomaly Number**	**Geohazard Description**	**Length (Feet)**
2-3	2.62	35	Vertical Piping	20
2-3	2.63	36	Vertical Piping	20
2-3	2.66	37	Solution Fractures	160
2-3	2.68	38	Solution Fractures	45
2-3	2.71	39	Solution Fractures	45
2-3	2.74	40	Leached Zone	165
2-3	2.77	41	Solution Fracture	20
2-3	2.81	42	Solution Fracture	45
2-3	2.97	43	Soil Piping	105
3-4	3.08	44	Increased Piping	265
3-4	3.12	45	Filled Sink	240
3-4	3.25	46	Solutional Piping	40
3-4	3.26	47	Fractured Rock	30
3-4	3.28	48	Solutional Piping	30
3-4	3.29	49	Solutional Piping	30
3-4	3.33	50	Increased Piping	30
3-4	3.34	51	Increased Piping	45

Table 4. List of anomaly details along the 34 mile long segment.

Mile Number	Distance (Mile)	Anomaly Number	Geohazard Description	Length (Feet)
3-4	3.42	52	Fractured Rock	15
3-4	3.42	53	Fractured Rock	20
3-4	3.43	54	Fractured Rock	20
3-4	3.49	55	Fracture/ Gravel Fill	40
3-4	3.51	56	Fracture/ Gravel Fill	30
3-4	3.53	57	Fracture/ Gravel Fill	75
3-4	3.57	58	Solutional Piping	30
3-4	3.61	59	Lateral Piping/Ponding	355
3-4	3.78	60	Lateral Piping/Ponding	50
3-4	3.86	61	Lateral Piping	140
3-4	3.92	62	Arroyo Fill	95
4-5	4.01	63	Solutional Piping	175
4-5	4.06	64	Arroyo Fill	55
4-5	4.13	65	Arroyo Fill	295
4-5	4.17	66	Gravel Fill/ High Perm.	60
4-5	4.22	67	Gravel Fill/ High Perm.	135
4-5	4.51	68	Gravel Fill/ High Perm	50

Table 5. List of anomaly details along the 34 mile long segment.

Mile Number	Distance (Mile)	Anomaly Number	Geohazard Description	Length (Feet)
4-5	4.55	69	Gravel Fill/ High Perm.	60
4-5	4.56	70	Gravel Fill/ High Perm.	60
4-5	4.67	71	Gravel Fill/ Piping/Ponding	240
4-5	4.83	72	Gravel Fill	125
4-5	4.91	73	Gravel Fill/ Ponding	150
4-5	4.98	74	Gravel Fill/ Ponding	230
5-6	5.31	75	Bedrock High	145
5-6	5.41	76	Solutional Fractures	20
5-6	5.44	77	Cave	50
5-6	5.45	78	Solutional Fractures	25
5-6	5.51	79	Solutional Fractures	25
5-6	5.52	80	Cave	30
5-6	5.52	81	Cave	30
5-6	5.56	82	Cave	25
5-6	5.58	83	Solutional Fractures	15
5-6	5.62	84	Increased piping	130
5-6	5.69	85	Solutional Fractures	30

Table 6. List of anomaly details along the 34 mile long segment.

Mile Number	Distance (Mile)	Anomaly Number	Geohazard Description	Length (Feet)
5-6	5.71	86	Solutional Fractures	115
5-6	5.72	87	Cave/ Fractures	105
5-6	5.81	88	Gravel Fill	25
5-6	5.83	89	Gravel Fill	195
5-6	5.91	90	Solutional Fractures	50
6-7	6.01	91	Vertical Piping	30
6-7	6.02	92	Vertical Piping	30
6-7	6.02	93	Vertical Piping	45
6-7	6.05	94	Vertical Piping	45
6-7	6.08	95	Lateral Piping	100
6-7	6.31	96	Cave	40
6-7	6.32	97	Solutional Fracture	35
6-7	6.36	98	Solutional Frcature	35
6-7	6.36	99	Cave	20
6-7	6.48	100	Soil Piping	860
6-7	6.96	101	Increased Piping	365
7-8	7.05	102	Solutional Piping	30

Table 7. List of anomaly details along the 34 mile long segment.

Mile Number	Distance (Mile)	Anomaly Number	Geohazard Description	Length (Feet)
7-8	7.09	103	Solutional Piping	45
7-8	7.13	104	Solutional Piping	165
7-8	7.15	105	Piping at Toewall	30
7-8	7.27	106	Increased piping	170
7-8	7.35	107	Lateral Piping	185
7-8	7.41	108	Vertical Piping	30
7-8	7.42	109	Vertical Piping	30
7-8	7.43	110	Vertical Piping	55
7-8	7.44	111	Vertical Piping	45
7-8	7.56	112	Increased Vertical Piping	345
7-8	7.61	113	Gravel/ High Perm.	230
7-8	7.71	114	Increased Vertical Piping	130
7-8	7.78	115	Soil Piping/ Toewall	30
7-8	7.78	116	Soil Piping/ Toewall	30
7-8	7.82	117	Paleo-Gravel Bar	255
7-8	7.95	118	Lateral Piping	30
7-8	7.95	119	Lateral Piping	30

Table 8. List of anomaly details along the 34 mile long segment.

Mile Number	Distance (Mile)	Anomaly Number	Geohazard Description	Length (Feet)
7-8	7.96	120	Lateral Piping	35
7-8	7.97	121	Lateral Piping	35
7-8	7.97	122	Lateral Piping	35
7-8	7.98	123	Lateral Piping	35
7-8	7.99	124	Lateral Piping	35
7-8	7.99	125	Lateral Piping	35
8-9	8.01	126	Solutional Piping	165
8-9	8.07	127	Solutional Piping	175
8-9	8.09	128	Solutional Piping	45
8-9	8.12	129	Solutional Piping	45
8-9	8.13	130	Solutional Piping	45
8-9	8.14	131	Solutional Piping	45
8-9	8.27	132	Solutional Conduits	255
8-9	8.35	133	Solutional Piping	135
8-9	8.46	134	Solutional Piping	95
8-9	8.49	135	Solutional Piping	115
8-9	8.54	136	Solutional Piping	120

Table 9. List of anomaly details along the 34 mile long segment.

Mile Number	Distance (Mile)	Anomaly Number	Geohazard Description	Length (Feet)
8-9	8.56	137	Solutional Piping	120
8-9	8.58	138	Solutional Piping	125
8-9	8.73	139	Lateral Piping	125
8-9	8.78	140	Lateral Piping	195
8-9	8.85	141	Vertical Piping	100
8-9	8.91	142	Leached Zone	125
8-9	8.92	143	Vertical Piping	40
8-9	8.96	144	Lateral Piping	40
9-10	9.11	145	Lateral Piping	185
9-10	9.18	146	Soil Cave	85
9-10	9.38	147	Soil Cave	50
9-10	9.53	148	Soil Piping	175
9-10	9.87	149	Lateral Piping	205
9-10	9.94	150	Lateral Piping	130
9-10	9.98	151	Lateral Piping	135
10-11	10.05	152	Fill	50
10-11	10.08	153	Fill	50

Table 10. List of anomaly details along the 34 mile long segment.

Mile Number	Distance (Mile)	Anomaly Number	Geohazard Description	Length (Feet)
10-11	10.11	154	Fill	50
10-11	10.15	155	Fill	50
10-11	10.25	156	Breccia Margin	35
10-11	10.27	157	Fill	40
10-11	10.34	158	Fill	80
10-11	10.38	159	Fill	50
10-11	10.41	160	Lateral Piping/ Fill	25
10-11	10.42	161	Filled Sink	50
10-11	10.43	162	Solutional Piping	45
10-11	10.44	163	Solutional Piping	45
10-11	10.50	164	High Perm. Breccia	35
10-11	10.59	165	High Perm. Breccia	50
10-11	10.67	166	High Perm. Breccia	35
10-11	10.71	167	Solutional Piping	35
10-11	10.72	168	Solutional Piping	50
10-11	10.74	169	Solutional Piping	50
10-11	10.82	170	Solutional Piping	35

Table 11. List of anomaly details along the 34 mile long segment.

Mile Number	Distance (Mile)	Anomaly Number	Geohazard Description	Length (Feet)
10-11	10.83	171	Cave	60
10-11	10.84	172	Cave	50
10-11	10.92	173	Soil Piping	80
10-11	10.95	174	Soil Piping	125
11-12	11.08	175	Significant Soil Piping	150
11-12	11.26	176	Soil Piping/ Fill	50
11-12	11.44	177	Soil Piping/ Fill	65
11-12	11.66	178	Leached Zone	35
11-12	11.69	179	Leached Zone	50
11-12	11.82	180	Solutional Fracture	70
11-12	11.85	181	Fracture Zone	80
11-12	11.88	182	Solutional Piping	35
11-12	11.97	183	Enhanced Soil Piping	250
12-13	12.03	184	Thick Fill	75
12-13	12.15	185	Piping/ Thick Fill	155
12-13	12.21	186	Piping/ Culvert Associated	90
12-13	12.31	187	Soil Piping	55

Table 12. List of anomaly details along the 34 mile long segment.

Mile Number	Distance (Mile)	Anomaly Number	Geohazard Description	Length (Feet)
12-13	12.33	188	Soil Piping	55
12-13	12.41	189	Soil Piping	140
12-13	12.49	190	Soil Piping	50
12-13	12.55	191	Soil Piping	50
12-13	12.67	192	Soil Piping	95
12-13	12.71	193	Soil Piping	50
12-13	12.73	194	Soil Piping	40
12-13	12.73	195	Soil Piping	40
12-13	12.74	196	Soil Piping	40
12-13	12.77	197	Soil Piping	65
12-13	12.81	198	Soil Piping	40
12-13	12.83	199	Soil Piping	35
12-13	12.87	200	Soil Piping	35
12-13	12.87	201	Soil Piping	40
12-13	12.88	202	Soil Piping	40
12-13	12.90	203	Soil Piping	40
12-13	12.93	204	Soil Piping	125

Table 13. List of anomaly details along the 34 mile long segment.

Mile Number	Distance (Mile)	Anomaly Number	Geohazard Description	Length (Feet)
12-13	12.94	205	Soil Cave	30
12-13	12.95	206	Soil Piping	80
12-13	12.97	207	Soil Piping	80
12-13	12.98	208	Soil Piping	35
13-14	13.01	209	Fractured Rock	50
13-14	13.02	210	Fractured Rock	40
13-14	13.6	211	Moisture Flux	200
13-14	13.11	212	Rock Fracture	35
13-14	13.21	213	Rock Fracture	35
13-14	13.24	214	Rock Fracture	90
13-14	13.28	215	Leached Zone	245
13-14	13.34	216	Rock Fracture/ Edge of Patch	50
13-14	13.51	217	Cave	35
13-14	13.52	218	Rock Fracture	35
13-14	13.53	219	Rock Fracture/ Leached Zone	35
13-14	13.56	220	Rock Fracture/ Leached Zone	35
13-14	13.77	221	Leached Zone/ Piping	145

Table 14. List of anomaly details along the 34 mile long segment.

Mile Number	Distance (Mile)	Anomaly Number	Geohazard Description	Length (Feet)
13-14	13.88	222	Leached Zone	145
13-14	13.96	223	Leached Zone/ Piping	380
14-15	14.01	224	Leached Zone	240
14-15	14.44	225	Subsidence/ Fracturing	310
14-15	14.67	226	Heavily Leached/ Fill	365
14-15	14.76	227	Heavily Leached/ Fill	375
15-16	15.01	228	Thick Fill	30
15-16	15.11	229	Enhanced Piping	155
15-16	15.28	230	Soil Piping	30
15-16	15.34	231	Soil Piping	125
15-16	15.35	232	Soil Piping	30
15-16	15.51	233	Fill	30
15-16	15.57	234	Fill/ Buried Utilities	30
15-16	15.57	235	Fill/ Buried Utilities	30
15-16	15.63	236	Indurated Soil/ Rock Fractures	140
15-16	15.77	237	Indurated Soil/ Rock Fractures	55
15-16	15.85	238	Indurated Soil/ Rock Fractures	125

Table 15. List of anomaly details along the 34 mile long segment.

Mile Number	Distance (Mile)	Anomaly Number	Geohazard Description	Length (Feet)
15-16	15.90	239	Indurated Soil/ Rock Fractures	205
15-16	15.94	240	Indurated Soil/ Rock Fractures	45
15-16	15.98	241	Indurated Soil/ Rock Fractures	45
16-17	16.14	242	Rock Fracture	40
16-17	16.17	243	Thick Fill	125
16-17	16.31	244	Thick Fill/ Piping	135
16-17	16.44	245	Breccia Margin	55
16-17	16.47	246	Breccia Margin	55
16-17	16.55	247	Rock Fracture	40
16-17	16.71	248	Breccia Margin	40
16-17	16.87	249	Soil Piping	260
16-17	16.95	250	Soil Piping	75
17-18	17.58	251	Soil Cave/ Fractures	55
17-18	17.61	252	Soil Cave	55
17-18	17.66	253	Soil Cave	55
17-18	17.68	254	Soil Cave/ Fractures	55
17-18	17.71	255	Soil Cave/ Fractures	55

Table 16. List of anomaly details along the 34 mile long segment.

Mile Number	Distance (Mile)	Anomaly Number	Geohazard Description	Length (Feet)
17-18	17.74	256	Soil Cave/ Fractures	55
17-18	17.77	257	Soil Cave/ Fractures	55
17-18	17.91	258	Lateral Piping	145
17-18	17.95	259	Lateral Piping	205
18-19	18.03	260	Vertical Piping	40
18-19	18.15	261	Soil Cave	60
18-19	18.15	262	Lateral Piping	60
18-19	18.23	263	Cave/ Lateral Piping	110
18-19	18.28	264	Extensive Lateral Piping	145
18-19	18.33	265	Lateral Piping/ Buried Cable	195
18-19	18.61	266	Soil Cave/ Lateral Piping	95
18-19	18.62	267	Lateral Piping	80
18-19	18.62	268	Lateral Piping	75
18-19	18.69	269	Lateral Piping	70
18-19	18.78	270	Lateral Piping	85
18-19	18.81	271	Lateral Piping	70
18-19	18.82	272	Lateral Piping	70

Table 17. List of anomaly details along the 34 mile long segment.

Mile Number	Distance (Mile)	Anomaly Number	Geohazard Description	Length (Feet)
18-19	18.88	273	Lateral Piping	60
18-19	18.98	274	Vertical Piping/Fracture	55
19-20	19.01	275	Lateral Piping	110
19-20	19.07	276	Lateral Piping	30
19-20	19.10	277	Soil Piping/ Berm	50
19-20	19.14	278	Soil Piping/ Berm	30
19-20	19.21	279	Soil Piping	45
19-20	19.27	280	Soil Piping	65
19-20	19.31	281	Soil Piping	125
19-20	19.41	282	Soil Piping	40
19-20	19.46	283	Soil Piping/ Cave	45
19-20	19.54	284	Soil Piping	40
19-20	19.63	285	Soil Piping	30
19-20	19.78	286	Soil Piping	40
19-20	19.82	287	Soil Piping	50
19-20	19.86	288	Valley Fill/ Lateral Piping	175
20-21	20.04	289	Extensive Lateral Piping	365

Table 18. List of anomaly details along the 34 mile long segment.

Mile Number	**Distance (Mile)**	**Anomaly Number**	**Geohazard Description**	**Length (Feet)**
20-21	20.16	290	Soil Piping	55
20-21	20.17	291	Soil Piping	35
20-21	20.31	292	Extensive Piping/ Fill	230
20-21	20.52	293	Soil piping	40
20-21	20.58	294	Fill	35
20-21	20.62	295	Fill/ Culvert	35
20-21	20.97	296	Extensive Lateral Piping	200
21-22	21.06	297	Lateral Piping/ Fill	645
21-22	21.22	298	Lateral Piping/ Fill	180
21-22	21.29	299	Fill/ Soil Piping	120
21-22	21.48	300	Fill/ Secondary Gypsum	120
21-22	21.75	301	Soil piping/ Berm	330
21-22	21.88	302	Soil Piping/ Berm	110
22-23	22.05	303	Lateral Piping/ Fill/ Arroyo	90
22-23	22.06	304	Lateral Piping/ Fill	65
22-23	22.19	305	Lateral Piping	160
22-23	22.26	306	Lateral Piping/ Fill	95

Table 19. List of anomaly details along the 34 mile long segment.

Mile Number	Distance (Mile)	Anomaly Number	Geohazard Description	Length (Feet)
22-23	22.28	307	Lateral Piping/ Fill	120
22-23	22.33	308	Lateral Piping	30
22-23	22.34	309	Lateral Piping	30
22-23	22.45	310	Lateral Piping/ Buried Cable	40
22-23	22.62	311	Lateral Piping/ Fill/ Berm	125
22-23	22.65	312	Lateral Piping/ Fill/ Berm	80
22-23	22.93	313	Moisture Flux	50
22-23	22.95	314	Moisture Flux	65
23-24	23.01	315	Lateral Piping/ Fill	30
23-24	23.02	316	Lateral Piping/ Fill	30
23-24	23.15	317	Lateral Piping/ Fill	275
23-24	23.31	318	Secondary Gypsum	120
23-24	23.32	319	Lateral Piping/ Fill	30
23-24	23.33	320	Lateral Piping/ Fill	55
23-24	23.35	321	Lateral Piping/ Fill	30
23-24	23.46	322	Soil Piping	140
23-24	23.51	323	Secondary Gypsum	200

Table 20. List of anomaly details along the 34 mile long segment.

Mile Number	Distance (Mile)	Anomaly Number	Geohazard Description	Length (Feet)
23-24	23.58	324	Soil Piping	115
23-24	23.67	325	Lateral Piping	40
23-24	23.68	326	Lateral Piping	90
23-24	23.94	327	Lateral Piping	525
24-25	24.24	328	Lateral Piping	70
24-25	24.39	329	Lateral Piping	30
24-25	24.41	330	Lateral Piping/ Berm	160
24-25	24.44	331	Lateral Piping/ Berm	80
24-25	24.49	332	Lateral Piping	75
24-25	24.51	333	Lateral Piping	90
24-25	24.55	334	Lateral Piping	95
24-25	24.59	335	Lateral Piping	80
24-25	24.63	336	Secondary Gypsum/ Patch	180
24-25	24.65	337	High Perm/ Patch Edge	95
24-25	24.70	338	Lateral Piping	15
24-25	24.84	349	High Perm	30
24-25	24.92	340	Lateral Piping	40

Table 21. List of anomaly details along the 34 mile long segment.

Mile Number	Distance (Mile)	Anomaly Number	Geohazard Description	Length (Feet)
24-25	24.96	341	Soil Piping	90
25-26	25.08	342	Lateral Piping/ Patch	180
25-26	25.25	343	Lateral Piping/ Fill	250
25-26	25.33	344	Lateral Piping/ Fill	95
25-26	25.45	345	Soil Piping	175
25-26	24.55	346	Soil Piping	50
25-26	25.72	347	Increased Lateral Piping	175
25-26	25.98	348	Increased Lateral piping	170
26-27	26.05	349	Salado Gypsum	200
26-27	26.11	350	Salado Gypsum	190
26-27	26.18	351	Rustler Colluvium	115
26-27	26.26	352	Fill/ Berms	100
26-27	26.28	353	Fill	10
26-27	26.30	354	Fill	10
26-27	26.31	355	Fill	60
26-27	26.35	356	Fill	60
26-27	26.48	357	Lateral Piping/ Culvert	20

Table 22. List of anomaly details along the 34 mile long segment.

Mile Number	Distance (Mile)	Anomaly Number	Geohazard Description	Length (Feet)
26-27	26.50	358	Lateral Piping	20
26-27	26.55	359	Lateral Piping	30
26-27	26.56	360	Lateral Piping	45
26-27	26.59	361	Lateral Piping	10
26-27	26.71	362	Lateral Piping	15
26-27	26.76	363	Lateral Piping	10
26-27	26.78	364	Lateral Piping	25
26-27	26.81	365	Lateral Piping/ Fill	40
26-27	26.83	366	Lateral Piping/ Rustler Edge	75
26-27	26.86	367	Lateral Piping/ Fill	35
26-27	26.96	368	Rustler Colluvium	200
27-28	27.05	369	Lateral piping/ Fill	80
27-28	27.08	370	Lateral Piping/ Fill	15
27-28	27.17	371	Moisture Flux	190
27-28	27.44	372	Fractured Rustler	220
27-28	27.65	373	Lateral Piping	100
27-28	27.76	374	Fractured Salado	240

Table 23. List of anomaly details along the 34 mile long segment.

Mile Number	Distance (Mile)	Anomaly Number	Geohazard Description	Length (Feet)
27-28	27.82	375	Soil Piping	40
27-28	27.89	376	Soil Piping/ Fill/ Ponding	40
27-28	27.98	377	Soil Piping/ Ponding	40
28-29	28.10	378	Piping/ Culvert	190
28-29	28.18	379	Rustler Colluvium	100
28-29	28.38	380	Colluvium/ Piping/ Fill	80
28-29	28.40	381	Colluvium/ Piping	35
28-29	28.42	382	High Perm.	85
28-29	28.50	383	High Perm.	30
28-29	28.54	384	Vertical Piping	40
28-29	28.58	385	Fill/ Culvert	40
28-29	28.60	386	Fill/ Culvert	30
28-29	28.66	387	High Perm.	30
28-29	28.70	388	High Perm.	55
28-29	28.74	389	Ponding/ High Perm.	90
28-29	28.88	390	Moisture Flux	160
28-29	28.96	391	High Perm.	70

Table 24. List of anomaly details along the 34 mile long segment.

Mile Number	Distance (Mile)	Anomaly Number	Geohazard Description	Length (Feet)
29-30	29.03	392	Moisture Flux	40
29-30	29.13	393	Fill/ High Perm.	90
29-30	29.18	394	Fill/ High Perm.	60
29-30	29.23	395	Extensive Piping	130
29-30	29.31	396	Fill/ Culvert/ Piping	120
29-30	29.38	397	Piping	85
29-30	29.48	398	Ponding/ Fill	80
29-30	29.52	399	Fill/ Culvert	80
29-30	29.56	400	Piping	60
29-30	29.66	401	Moisture Flux	55
29-30	29.68	402	Moisture Flux	45
29-30	29.75	403	Moisture Flux/ Piping	90
29-30	29.83	404	Moisture Flux	100
30-31	30.05	405	Lateral Piping/ Fill	150
30-31	30.18	406	Moisture Flux	15
30-31	30.26	407	Fill/ Culvert/ Piping	100
30-31	30.38	408	Lateral Piping	50

Table 25. List of anomaly details along the 34 mile long segment.

Mile Number	Distance (Mile)	Anomaly Number	Geohazard Description	Length (Feet)
30-31	30.45	409	Roadcut Margin/ Piping	85
30-31	30.51	410	Moisture Flux	95
30-31	30.67	411	Roadcut Margin/ piping	85
30-31	30.75	412	Ponding/ Piping	110
30-31	30.89	413	Fill/ Extensive Piping	300
31-32	31.01	414	Soil Piping	20
31-32	31.05	415	Vertical Piping	95
31-32	31.15	416	Piping/ Culvert	65
31-32	31.39	417	Moisture Flux/ Berm	10
31-32	31.41	418	Moisture Flux/ Berm	20
31-32	31.47	419	Moisture Flux/ Berm/ Fill	30
31-32	31.55	420	Moisture Flux	30
31-32	31.64	421	Moisture Flux	180
31-32	31.68	422	Soil Piping	15
31-32	31.79	423	Soil Piping	10
31-32	31.82	424	Solutional Piping	145
31-32	31.89	425	Moisture Flux	145

Table 26. List of anomaly details along the 34 mile long segment.

Mile Number	Distance (Mile)	Anomaly Number	Geohazard Description	Length (Feet)
31-32	31.96	426	Solutional Piping	140
32-33	32.03	427	Fractured Gypsum	20
32-33	32.10	428	Solution Conduits	30
32-33	32.15	429	Solution Conduits	95
32-33	32.22	430	Gravel/ High Perm.	110
32-33	32.28	431	Ponding/ High Perm.	20
32-33	32.30	432	Ponding/ High Perm.	20
32-33	32.33	433	Ponding/ High Perm.	20
32-33	32.42	434	Moisture Flux	105
32-33	32.49	435	Moisture Flux	25
32-33	32.51	436	Moisture Flux	25
32-33	32.58	437	Ponding/ High Perm.	85
32-33	32.65	438	Ponding/ High Perm.	70
32-33	32.76	439	Moisture Flux	100
32-33	32.84	440	Gypsum/ Piping	175
33-34	33.07	441	Ponding/ High Perm.	90
33-34	33.23	442	Buried Cable/ Piping	20

Table 27. List of anomaly details along the 34 mile long segment.

Mile Number	**Distance (Mile)**	**Anomaly Number**	**Geohazard Description**	**Length (Feet)**
33-34	32.26	443	Buried Cable/ Piping	20
33-34	32.28	444	Gravel/ High Perm.	55
33-34	32.46	445	Ponding/ Berm	80
33-34	32.67	446	Piping/ Ponding/ Berm	400

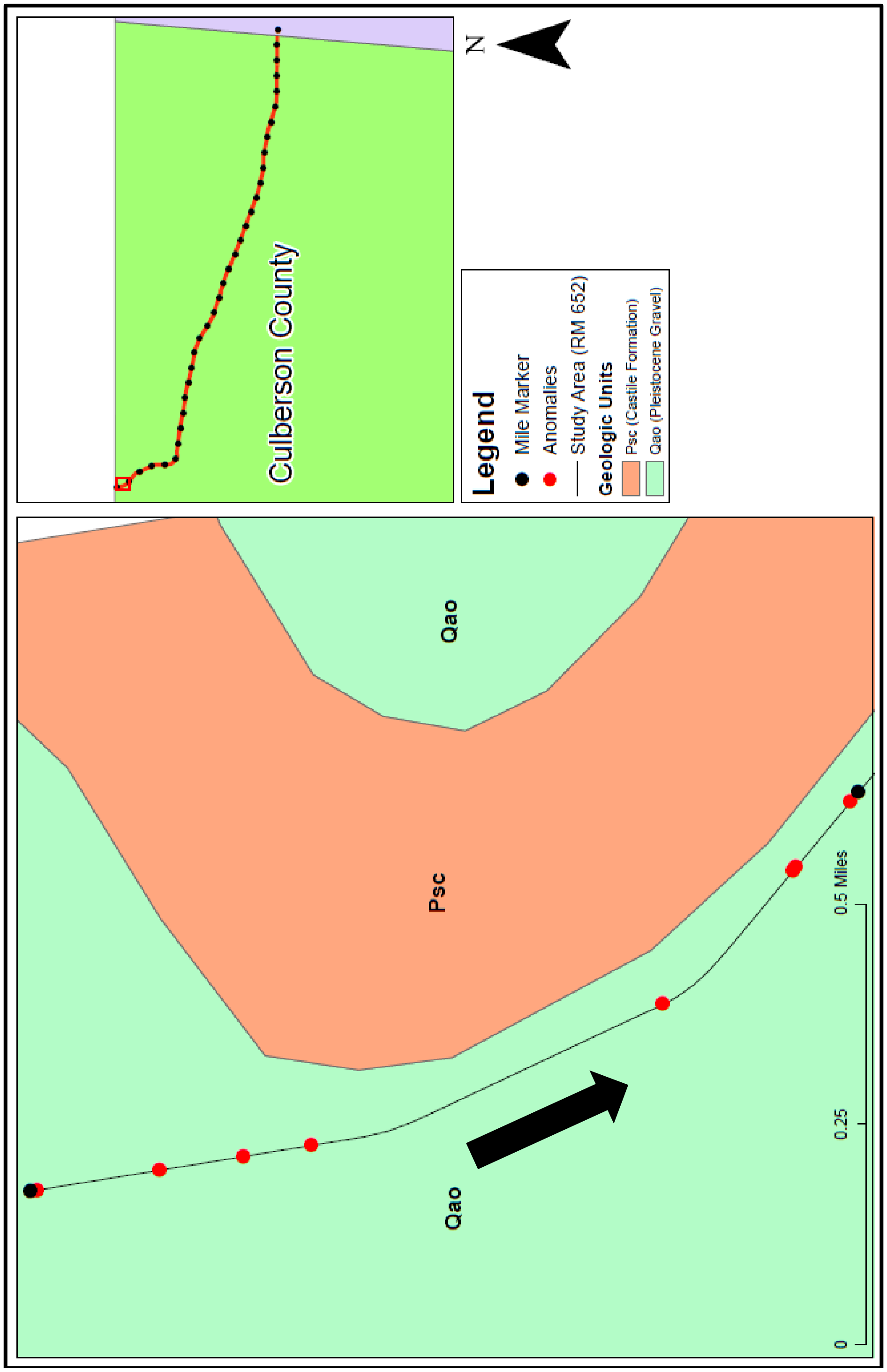

Figure C1. *Map indicating the location of Mile 0-1 resistivity profiles, along with anomalies. The black arrow indicates the profile direction.*

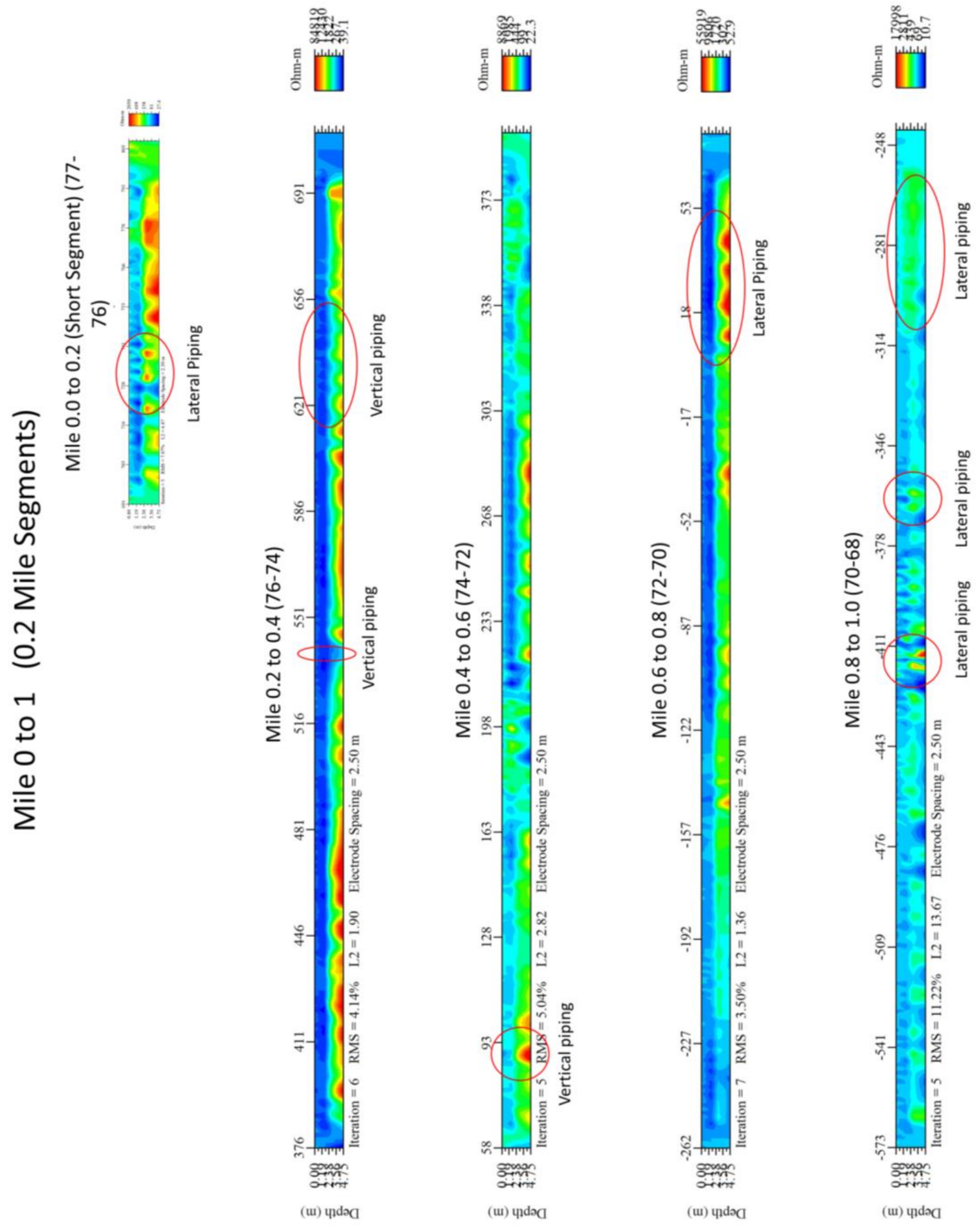

Figure C2. *Resistivity profiles of Mile 0-1 with anomalies marked and interpreted.*

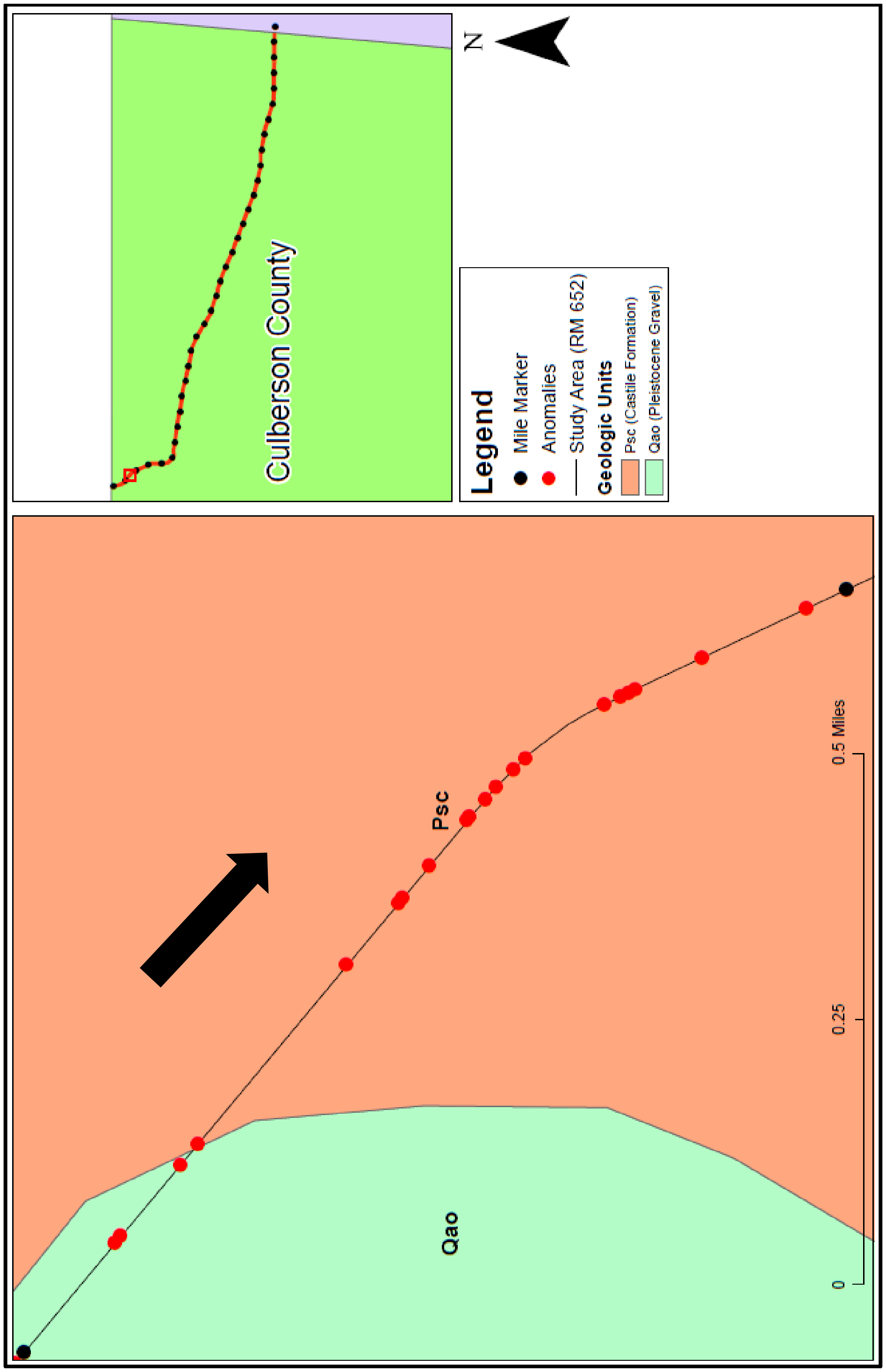

Figure C3. *Map indicating the location of Mile 1-2 resistivity profiles, along with anomalies. The black arrow indicates profile direction.*

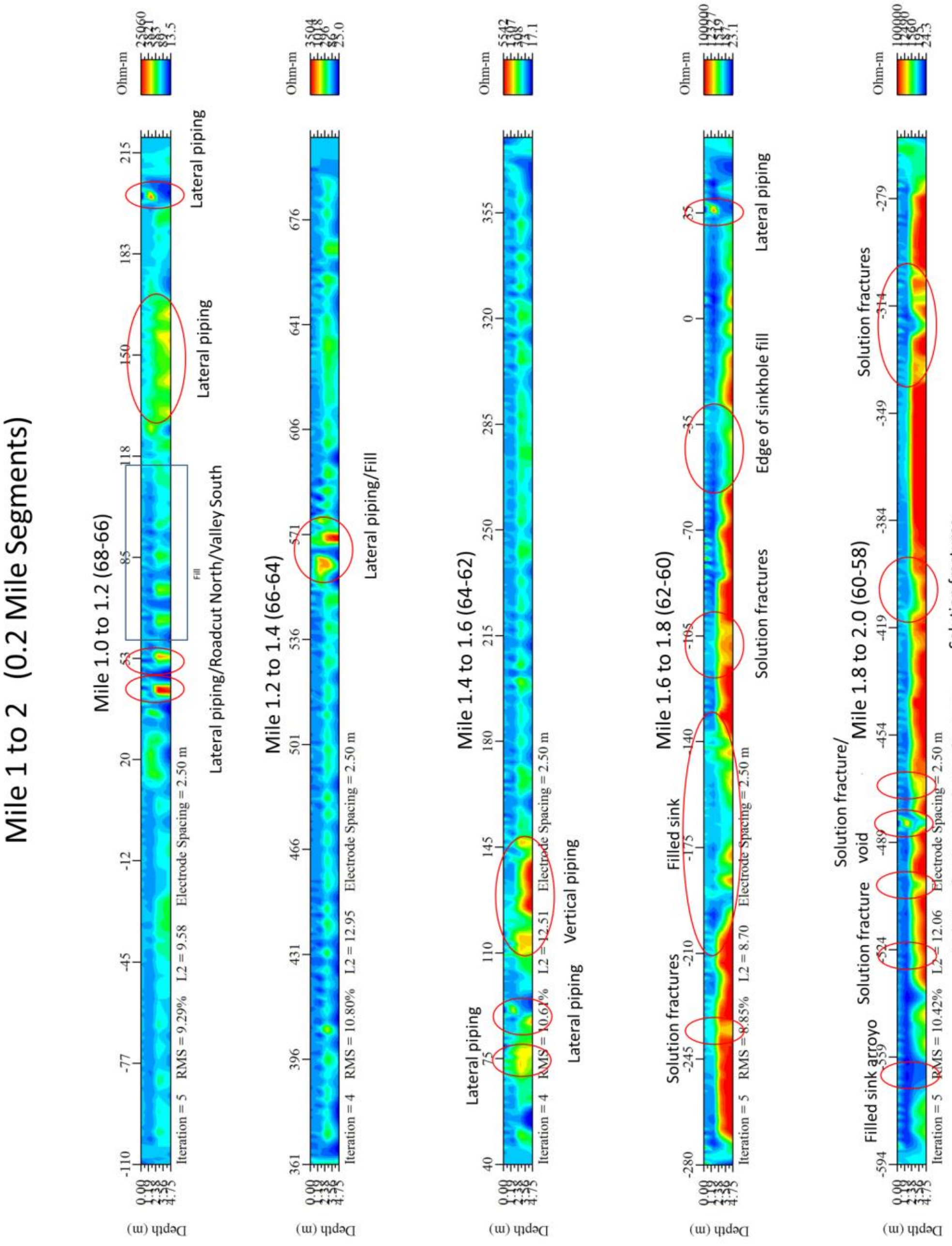

Figure C4. *Resistivity profiles of Mile 1-2 with anomalies marked and interpreted.*

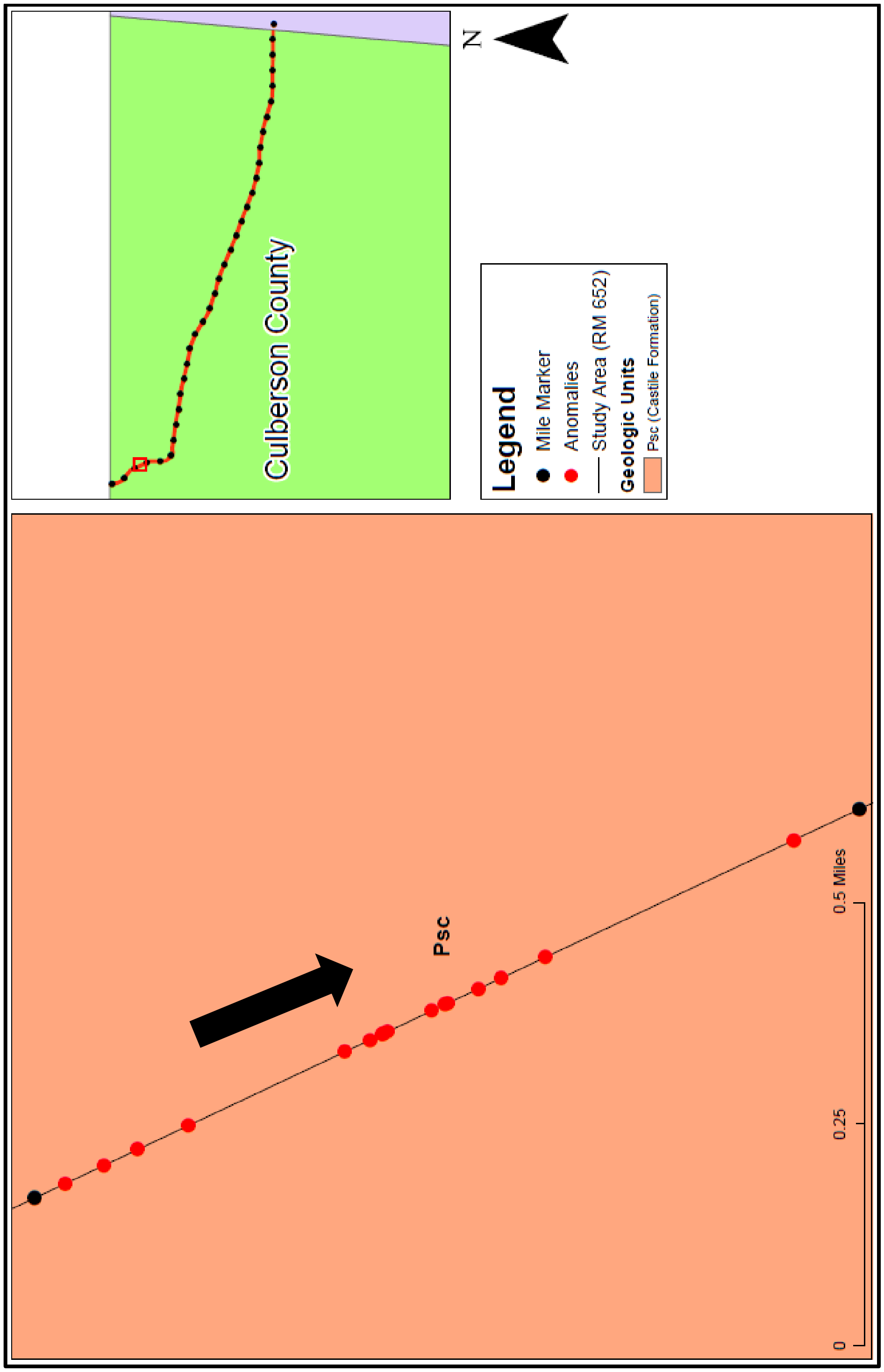

Figure C5. *Map indicating the location of Mile 2-3 resistivity profiles, along with anomalies. The black arrow indicates profile direction.*

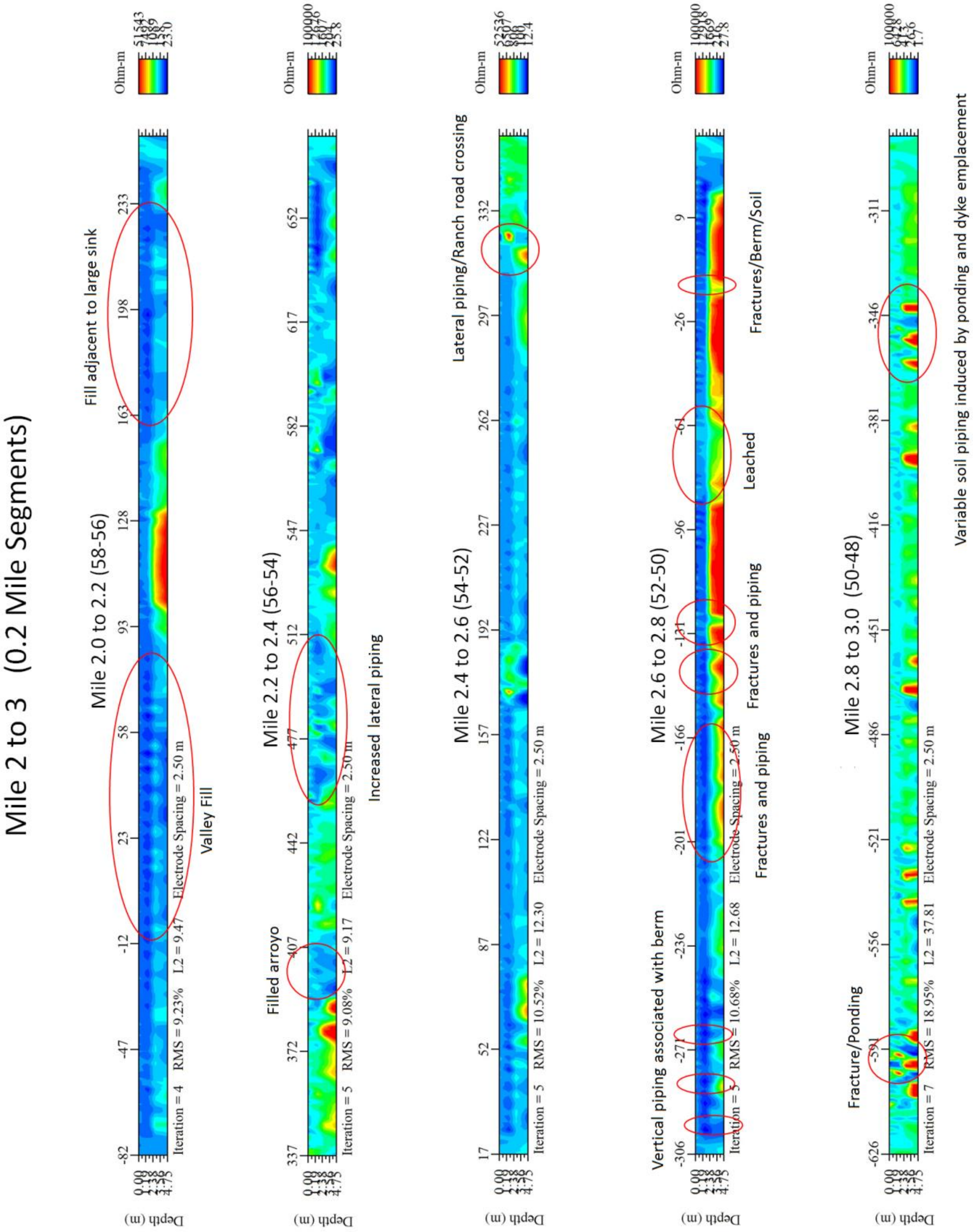

Figure C6. *Resistivity profiles of Mile 2-3 with anomalies marked and interpreted.*

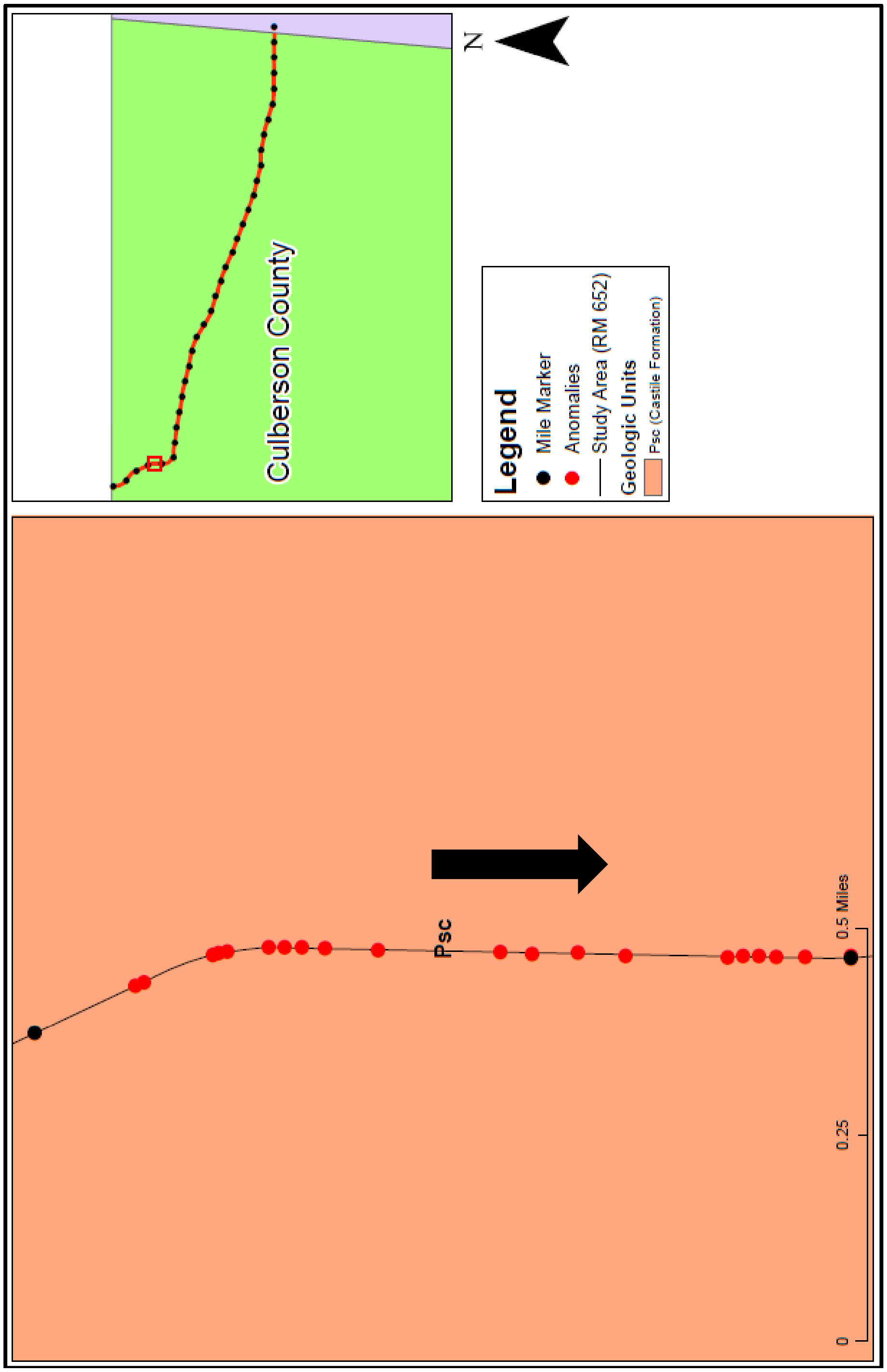

Figure C7. *Map indicating the location of Mile 3-4 resistivity profiles, along with anomalies. The black arrow indicates profile direction.*

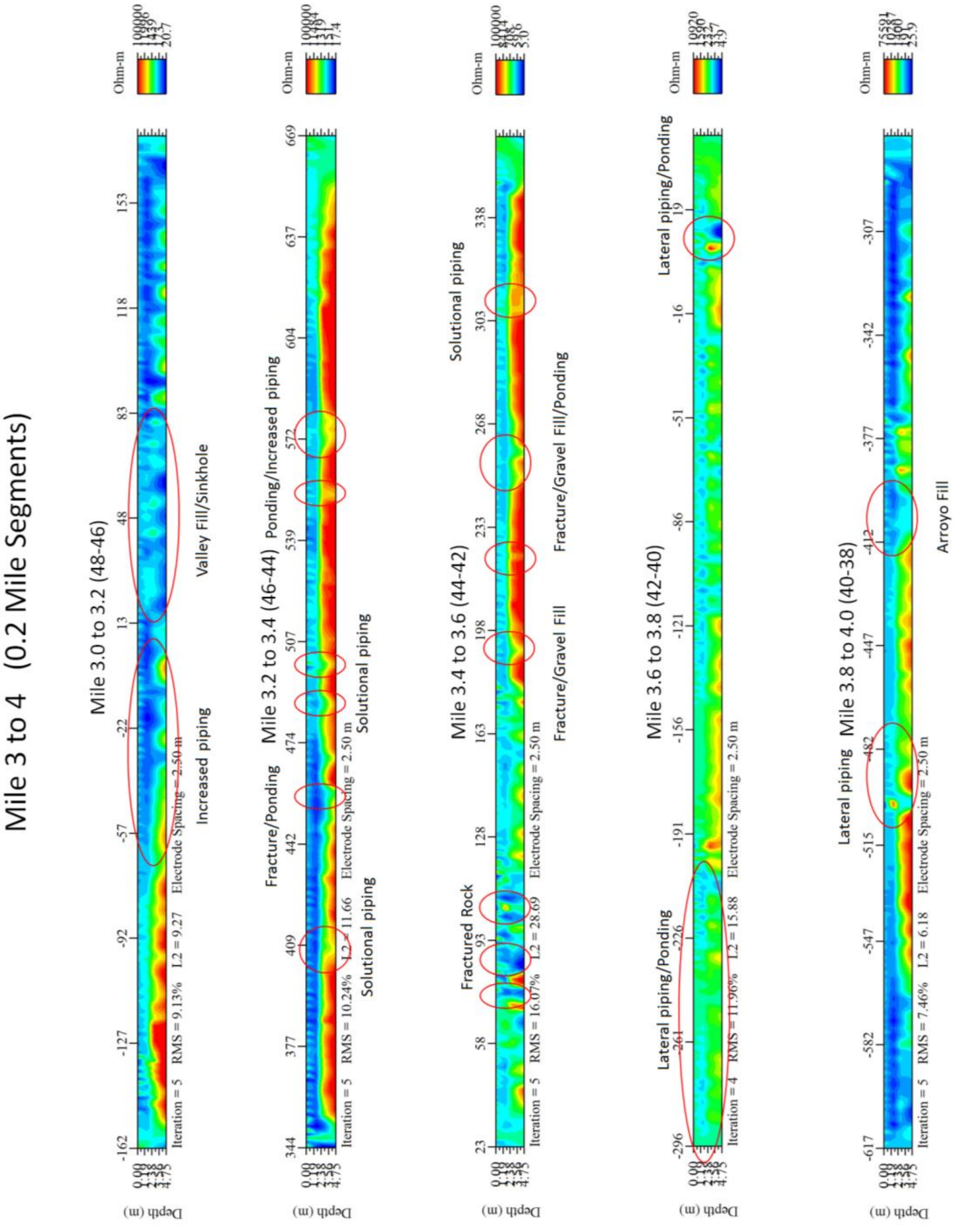

Figure C8. *Resistivity profiles of Mile 3-4 with anomalies marked and interpreted.*

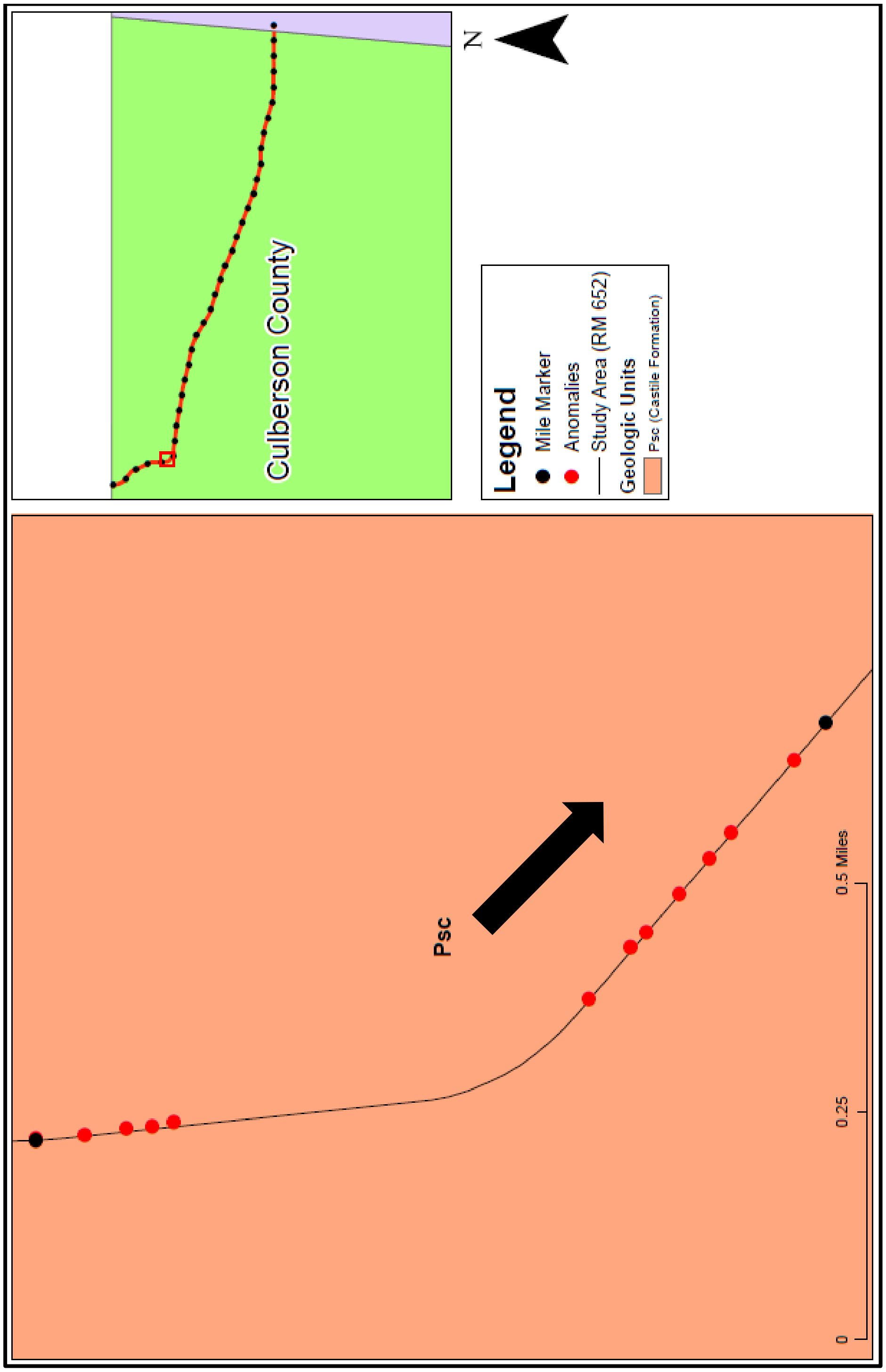

Figure C9. *Map indicating the location of Mile 4-5 resistivity profiles, along with anomalies. The black arrow indicates profile direction.*

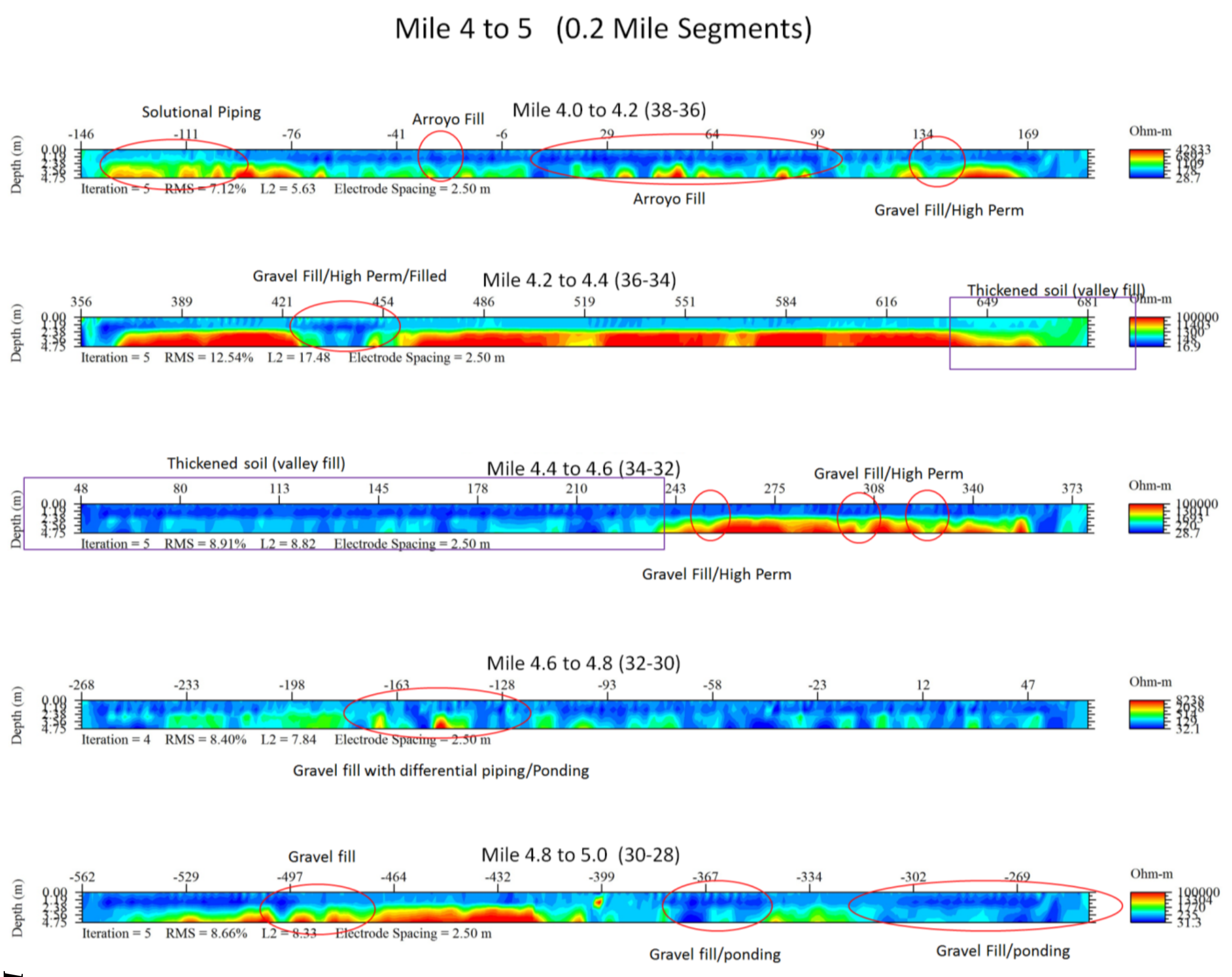

Figure C10. *Resistivity profiles of Mile 4-5 with anomalies marked and interpreted.*

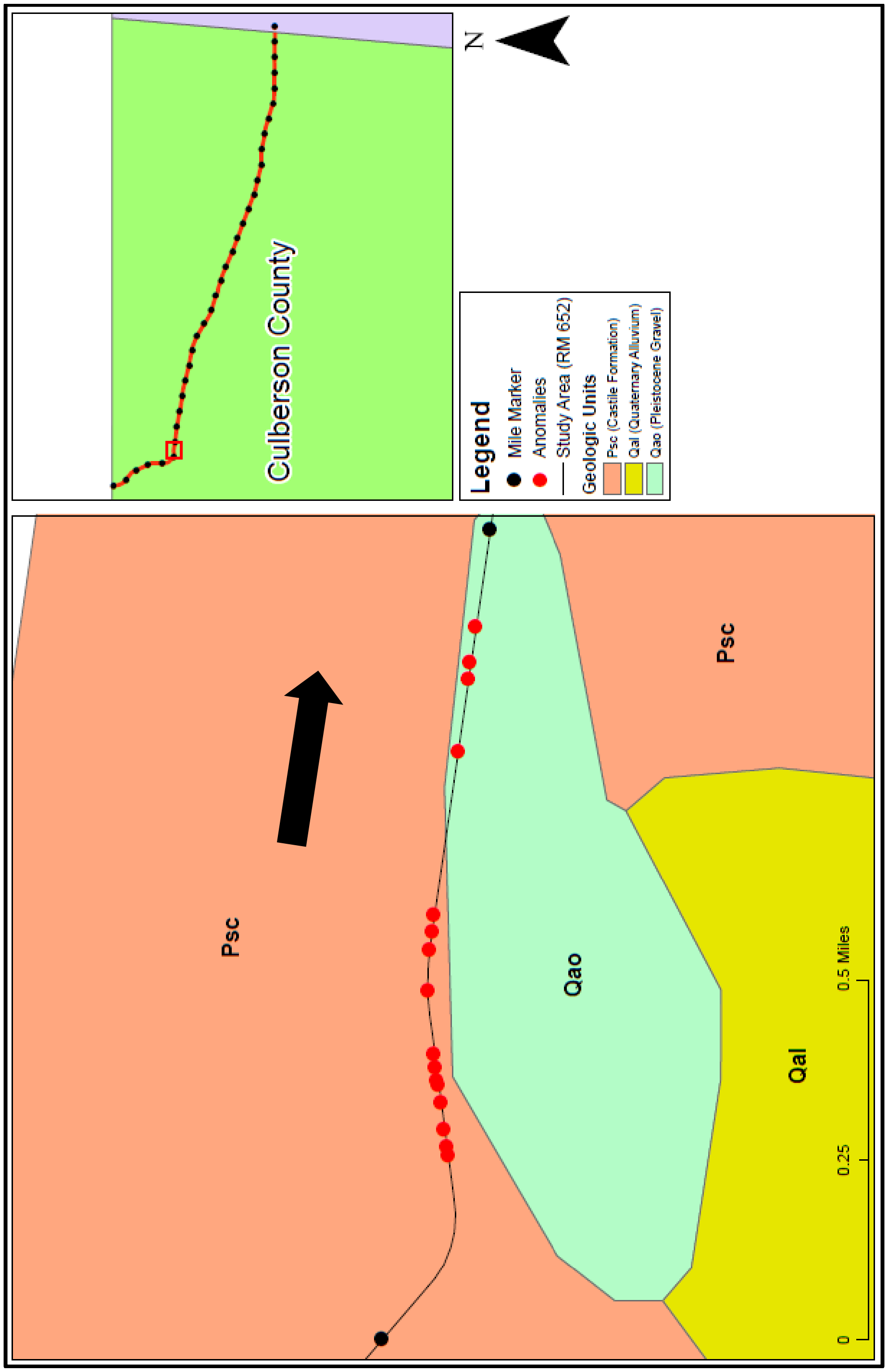

Figure C11. *Map indicating the location of Mile 5-6 resistivity profiles, along with anomalies. The black arrow indicates profile direction.*

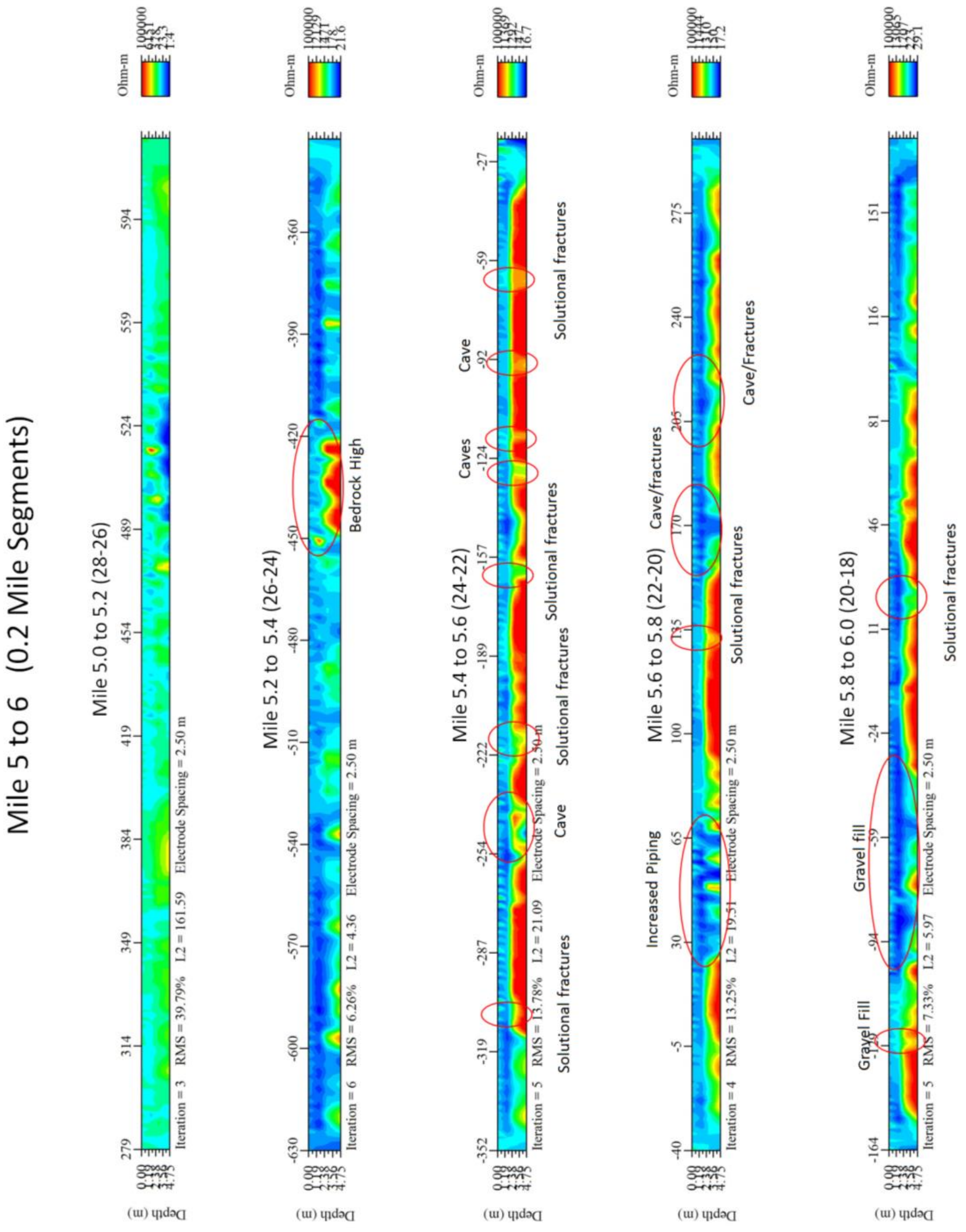

Figure C12. *Resistivity profiles of Mile 5-6 with anomalies marked and interpreted.*

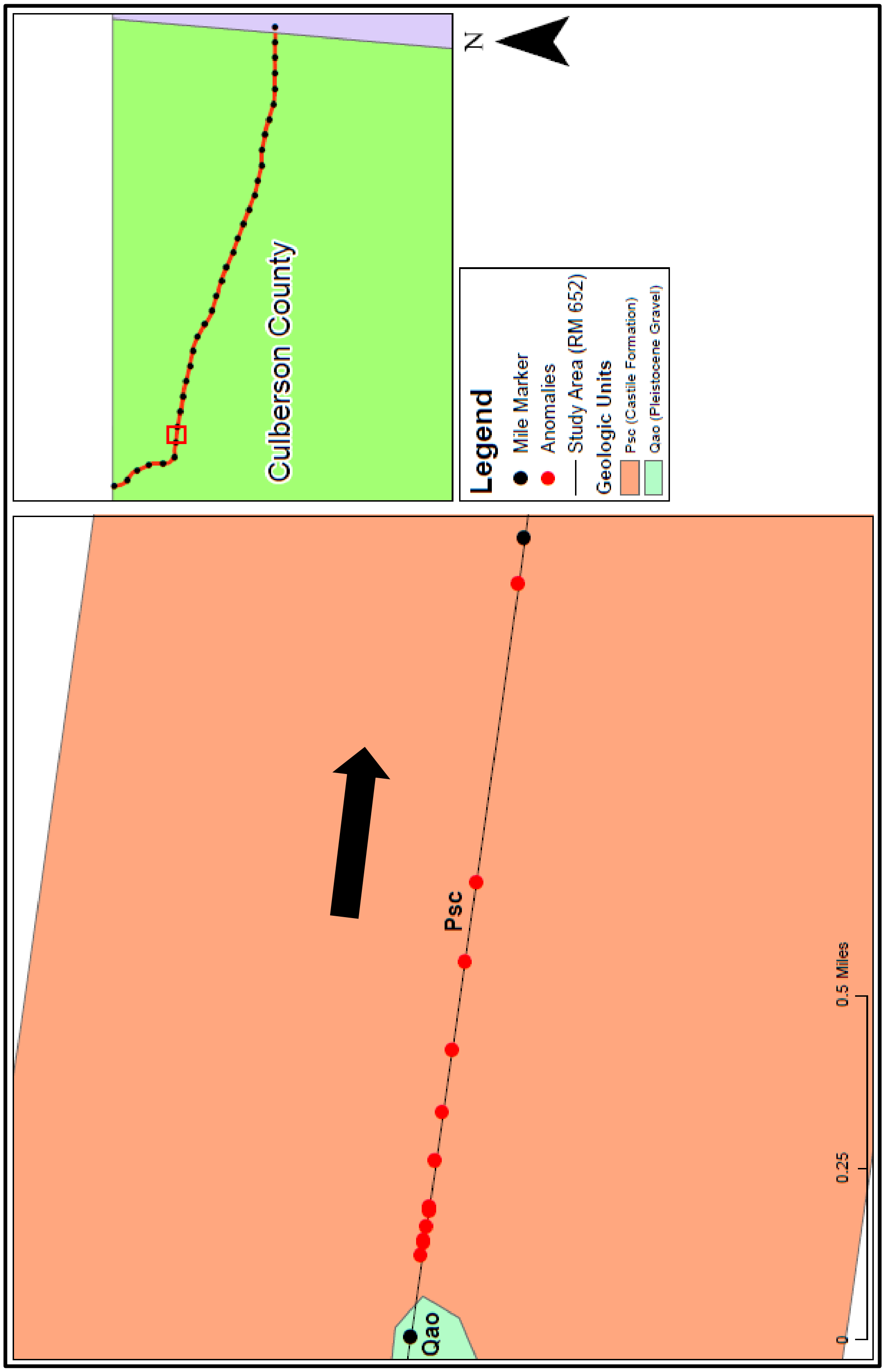

Figure C13. *Map indicating the location of Mile 6-7 resistivity profiles, along with anomalies. The black arrow indicates profile direction.*

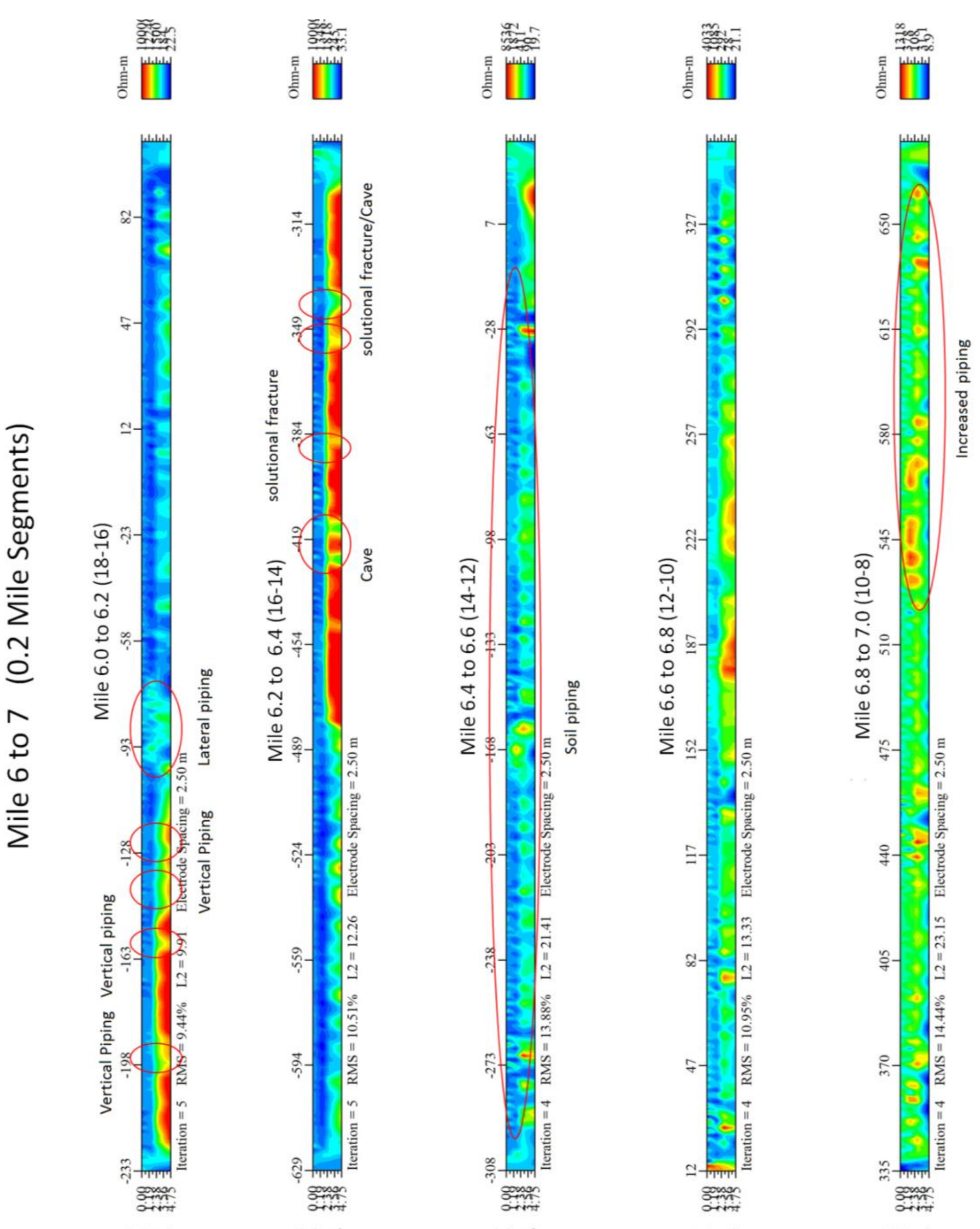

Figure C14. *Resistivity profiles of Mile 6-7 with anomalies marked and interpreted.*

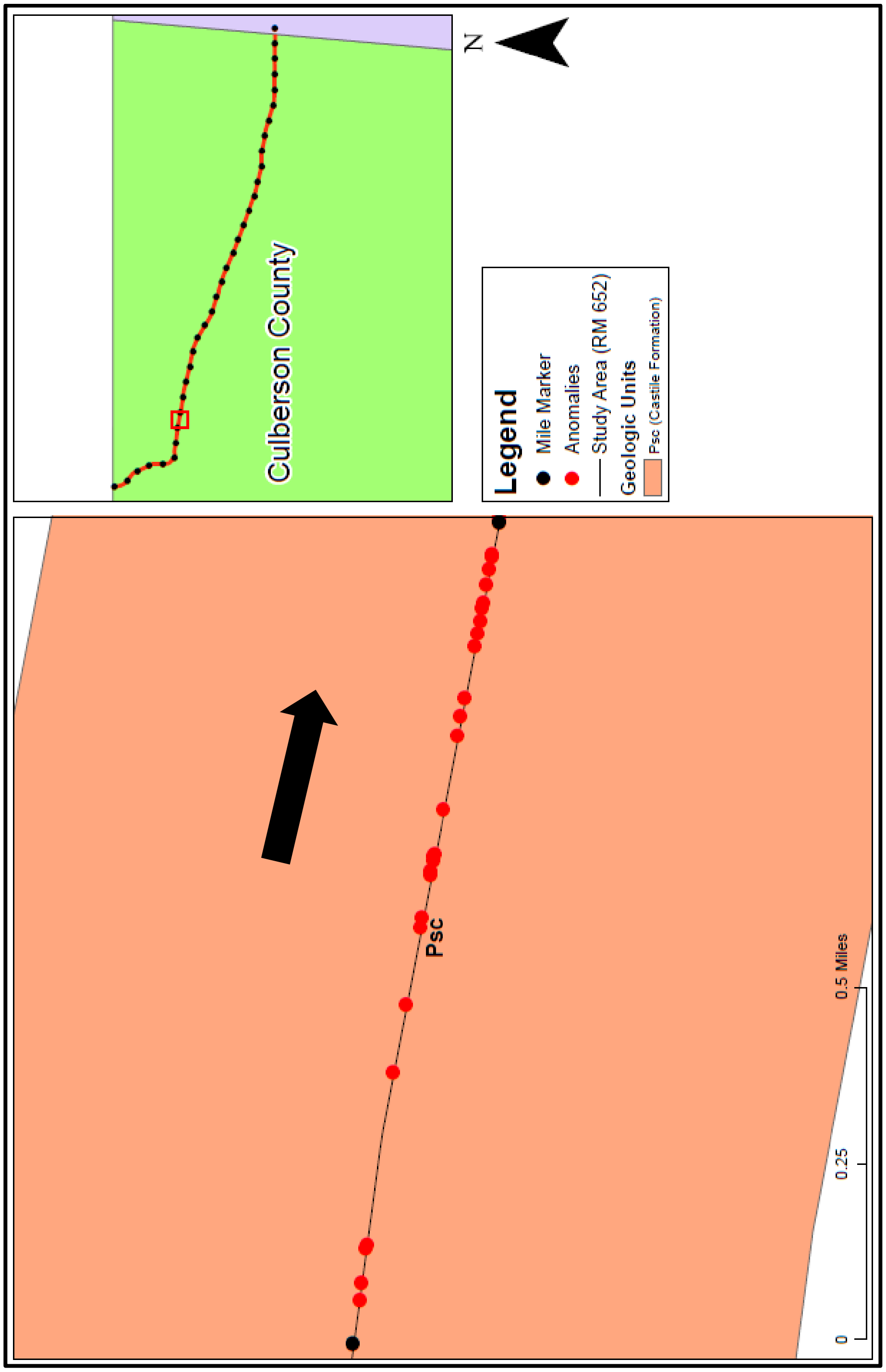

Figure C15. *Map indicating the location of Mile 7-8 resistivity profiles, along with anomalies. The black arrow indicates profile direction.*

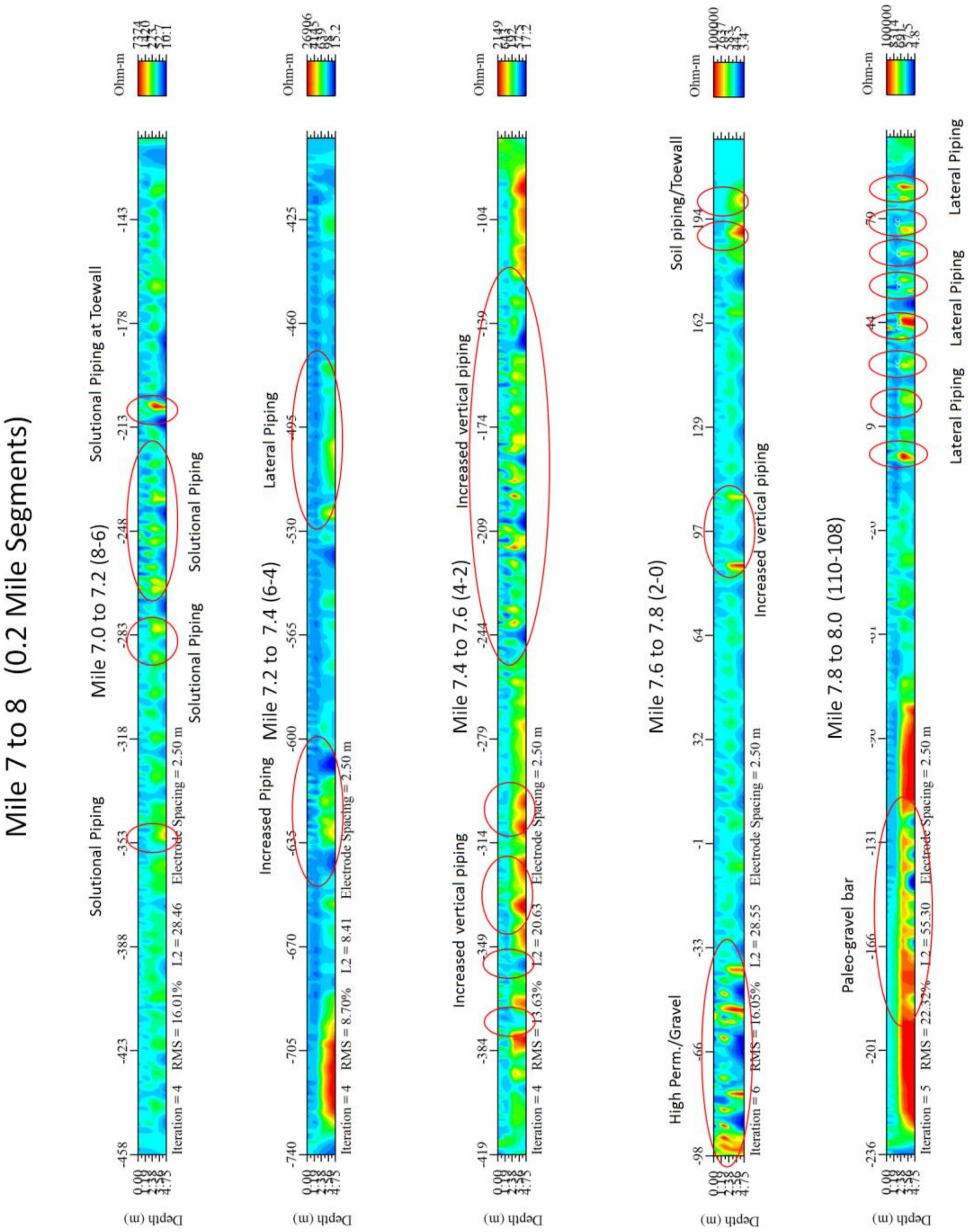

Figure C16. *Resistivity profiles of Mile 7-8 with anomalies marked and interpreted.*

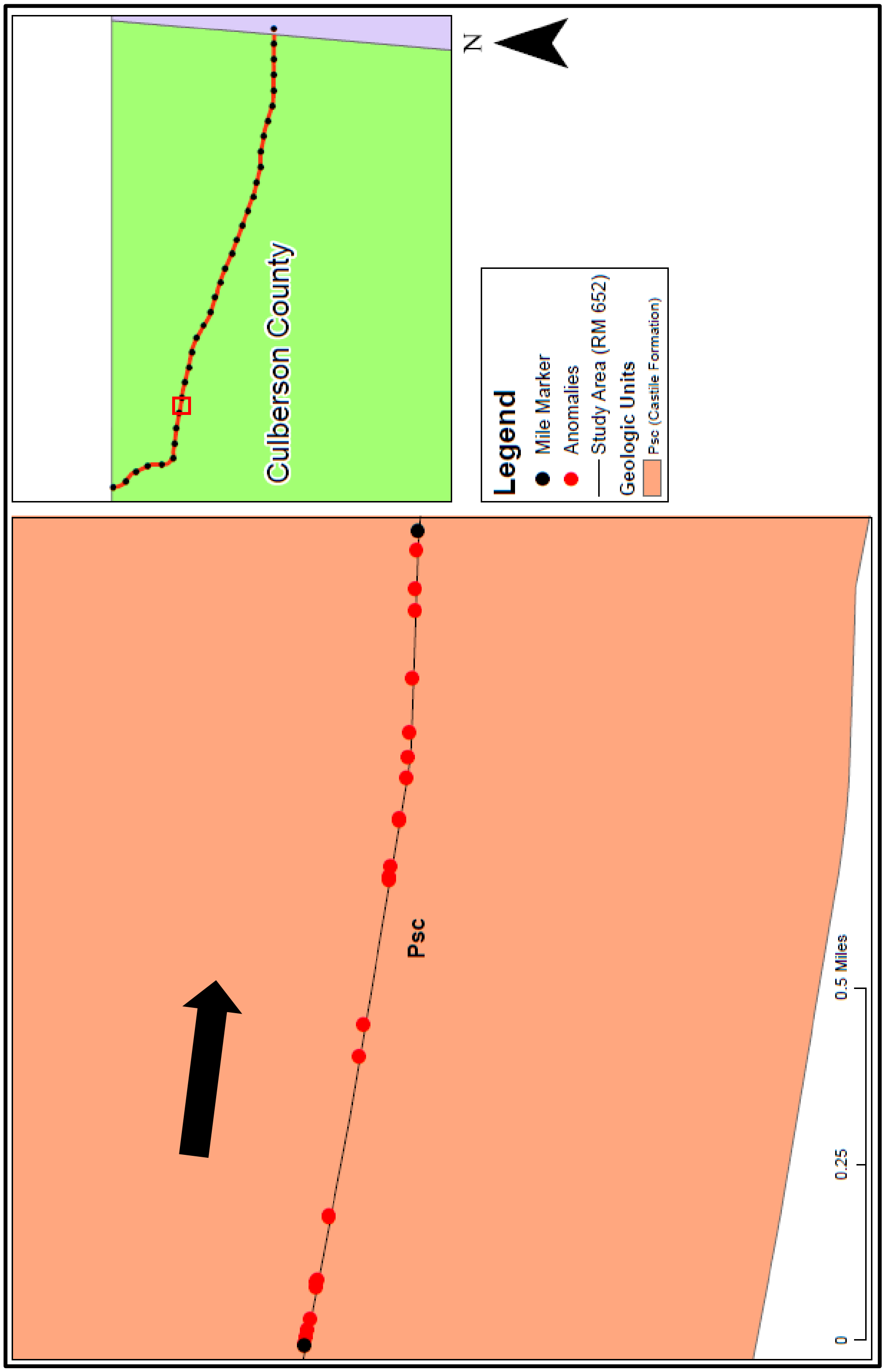

Figure C17. *Map indicating the location of Mile 8-9 resistivity profiles, along with anomalies. The black arrow indicates profile direction.*

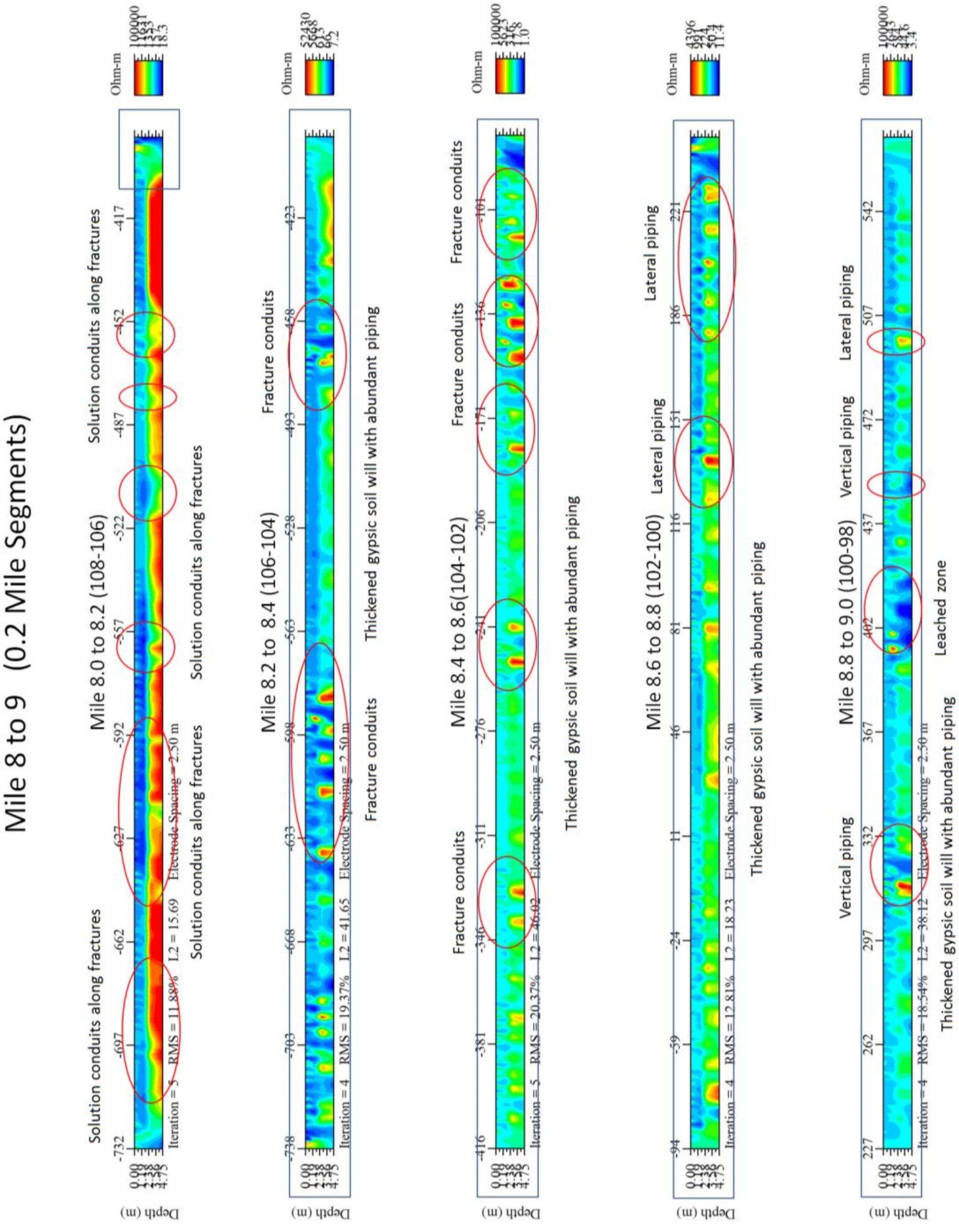

Figure C18. *Resistivity profiles of Mile 8-9 with anomalies marked and interpreted.*

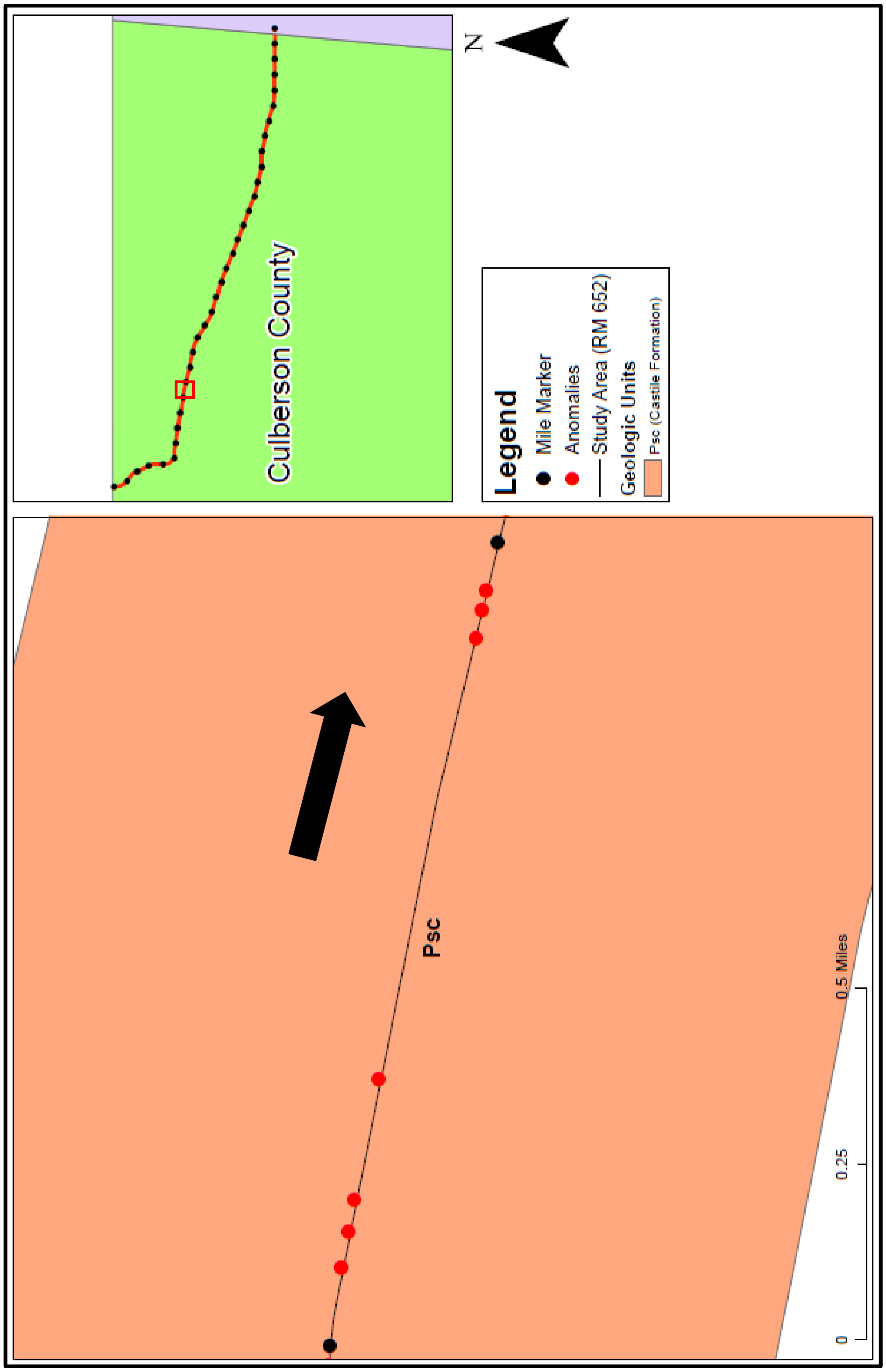

Figure C19. *Map indicating the location of Mile 9-10 resistivity profiles, along with anomalies. The black arrow indicates profile direction.*

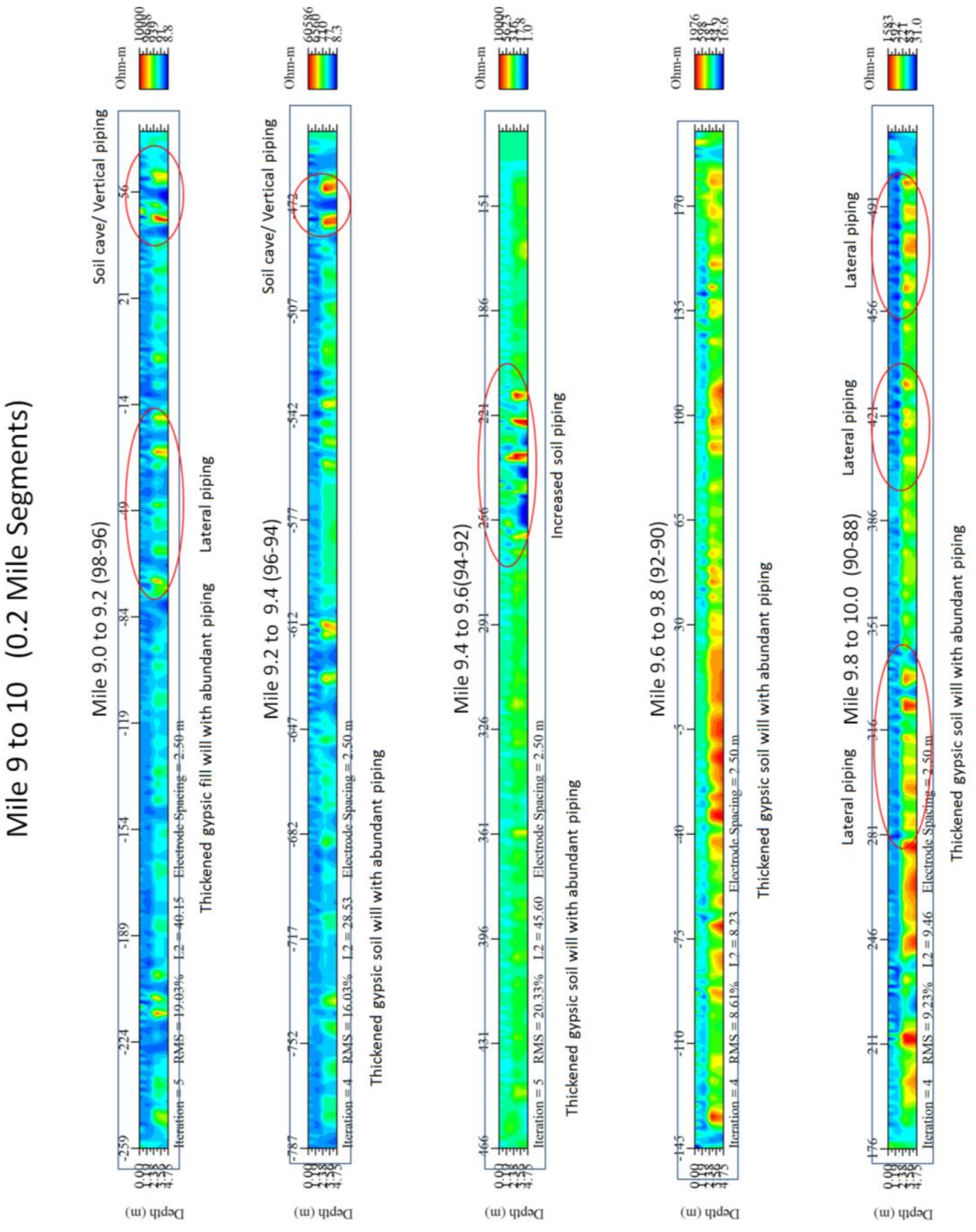

Figure C20. *Resistivity profiles of Mile 9-10 with anomalies marked and interpreted.*

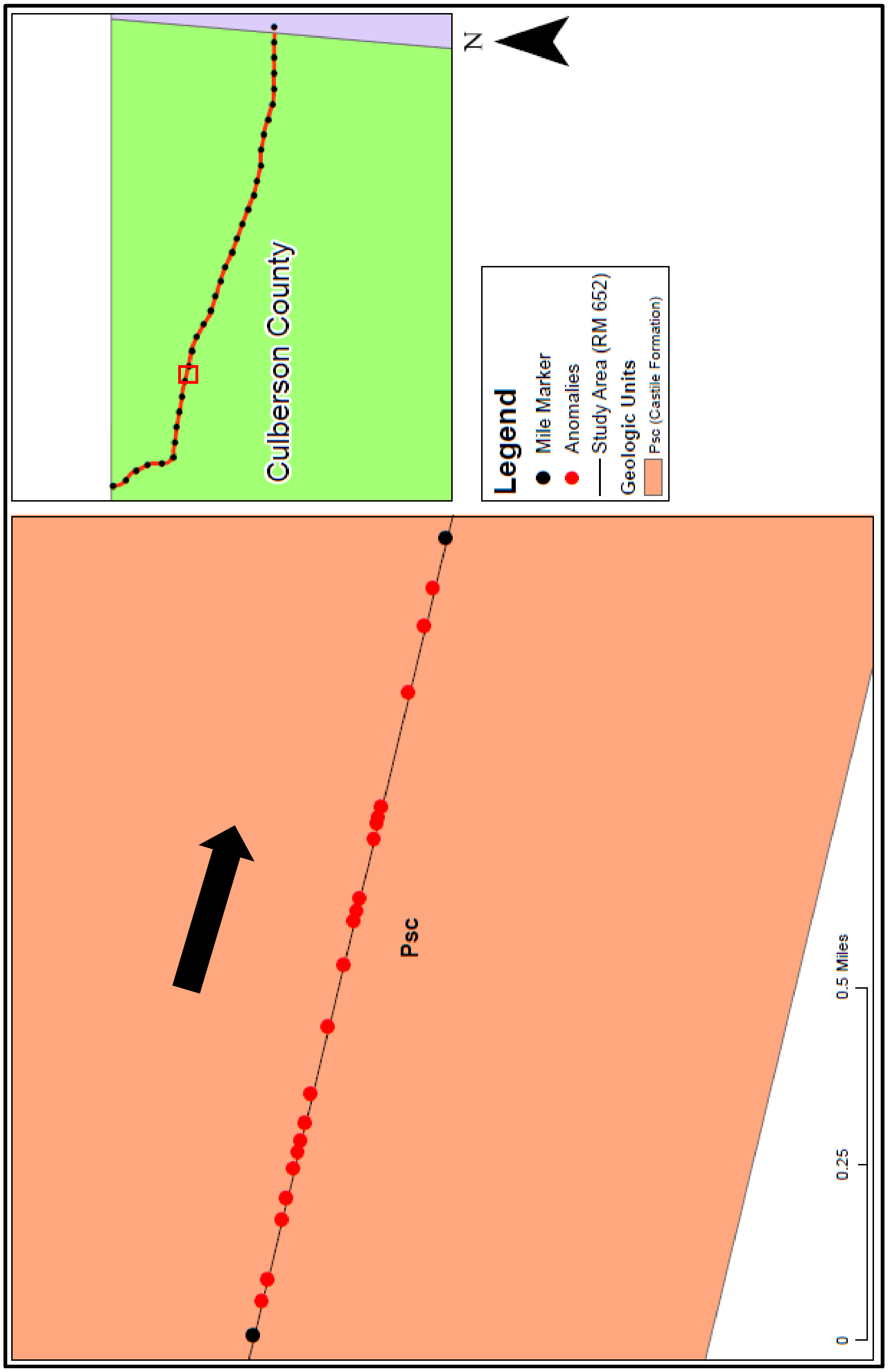

Figure C21. *Map indicating the location of Mile 10-11 resistivity profiles, along with anomalies. The black arrow indicates profile direction.*

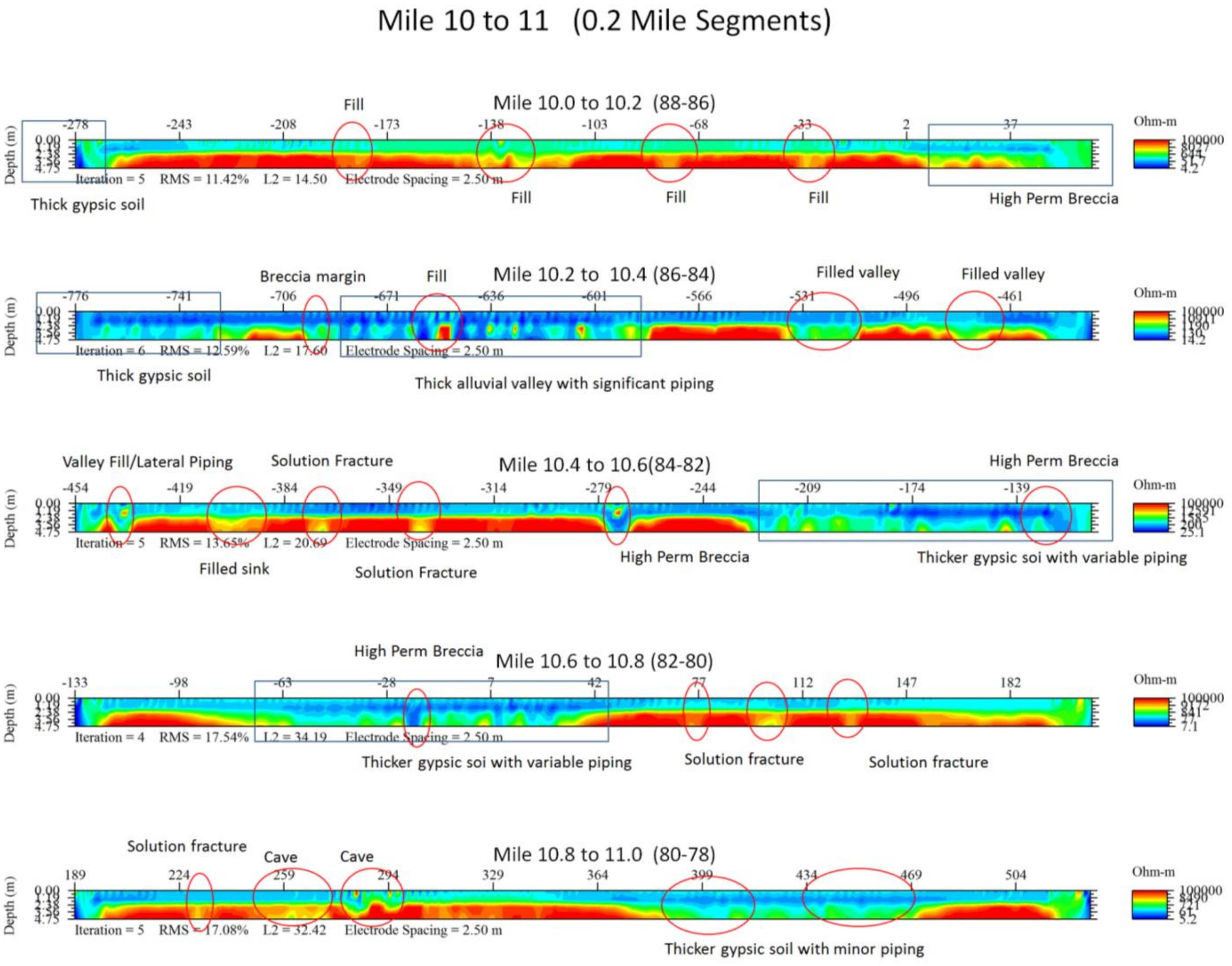

Figure C22. *Resistivity profiles of Mile 10-11 with anomalies marked and interpreted.*

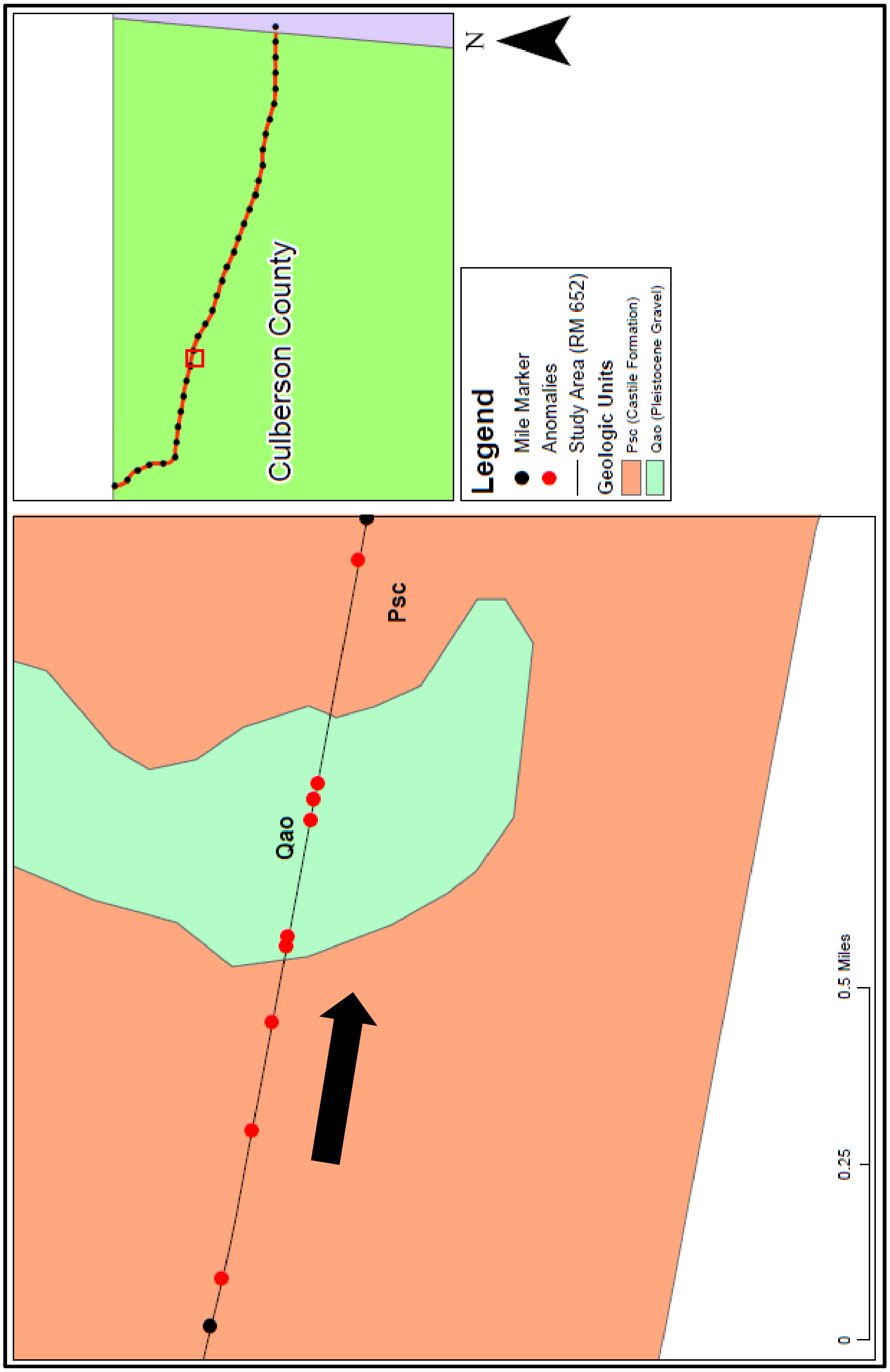

Figure C23. *Map indicating the location of Mile 11-12 resistivity profiles, along with anomalies. The black arrow indicates profile direction.*

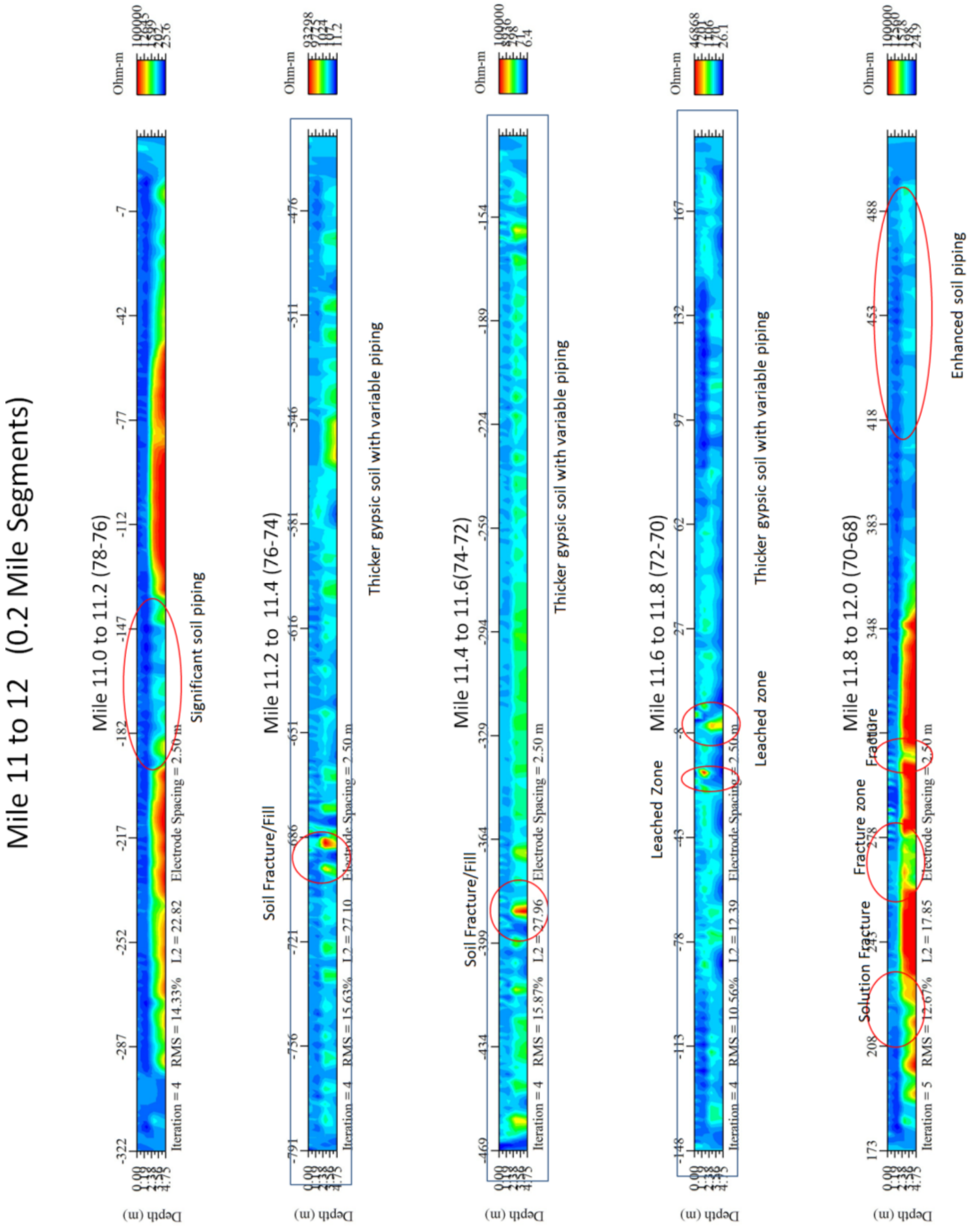

Figure C24. *Resistivity profiles of Mile 11-12 with anomalies marked and interpreted.*

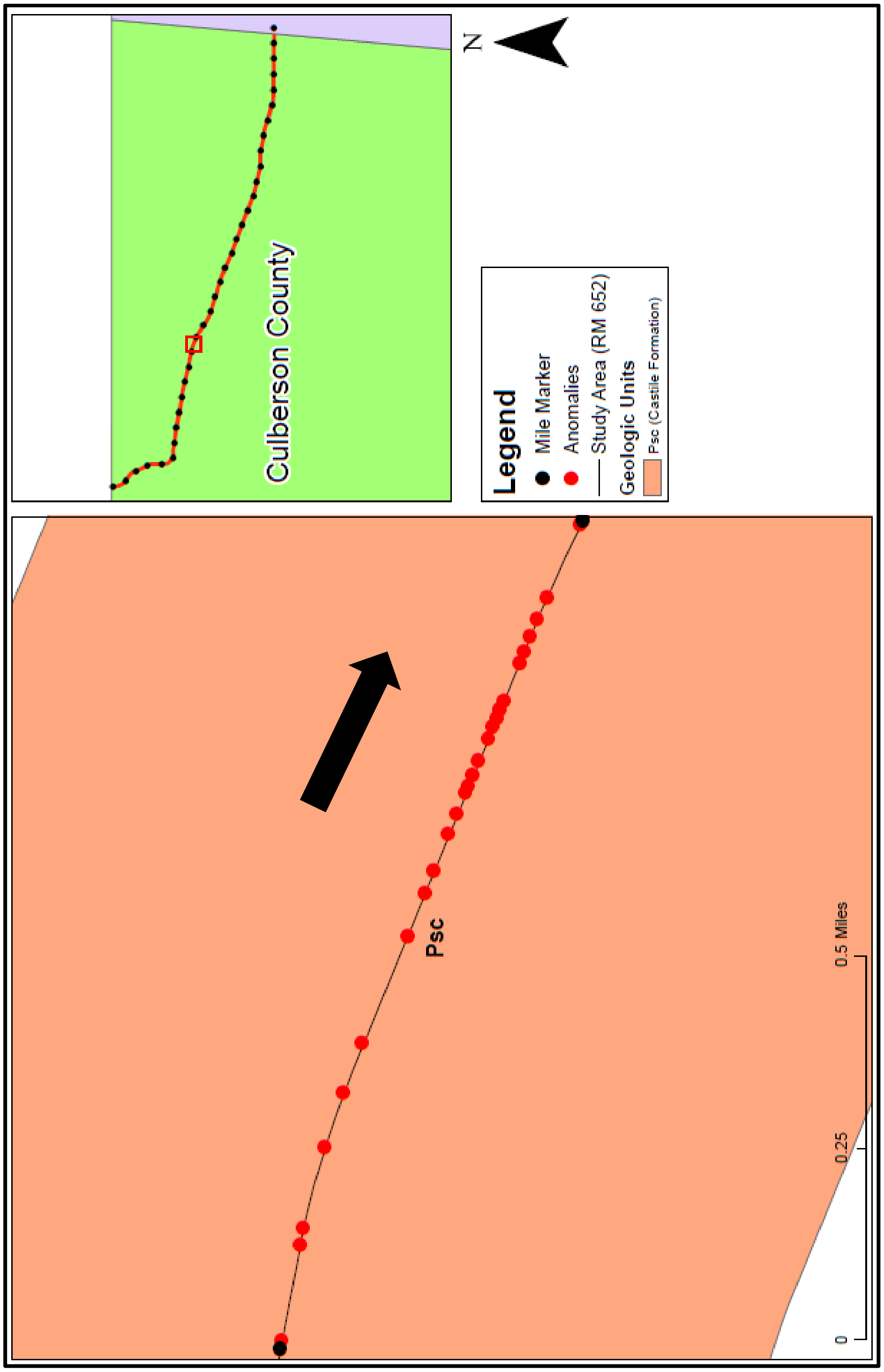

Figure C25. *Map indicating the location of Mile 12-13 resistivity profiles, along with anomalies. The black arrow indicates profile direction.*

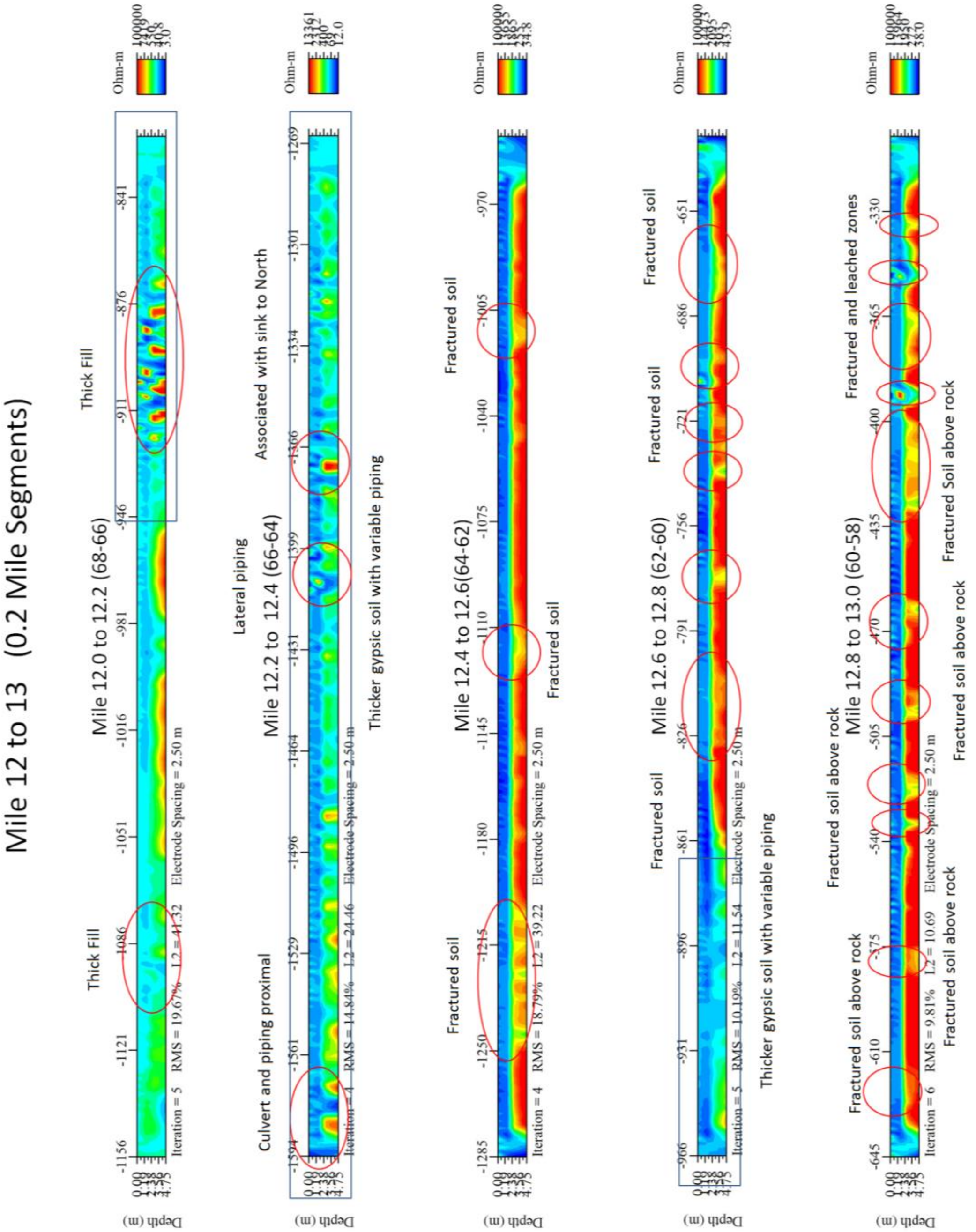

Figure C26. *Resistivity profiles of Mile 12-13 with anomalies marked and interpreted.*

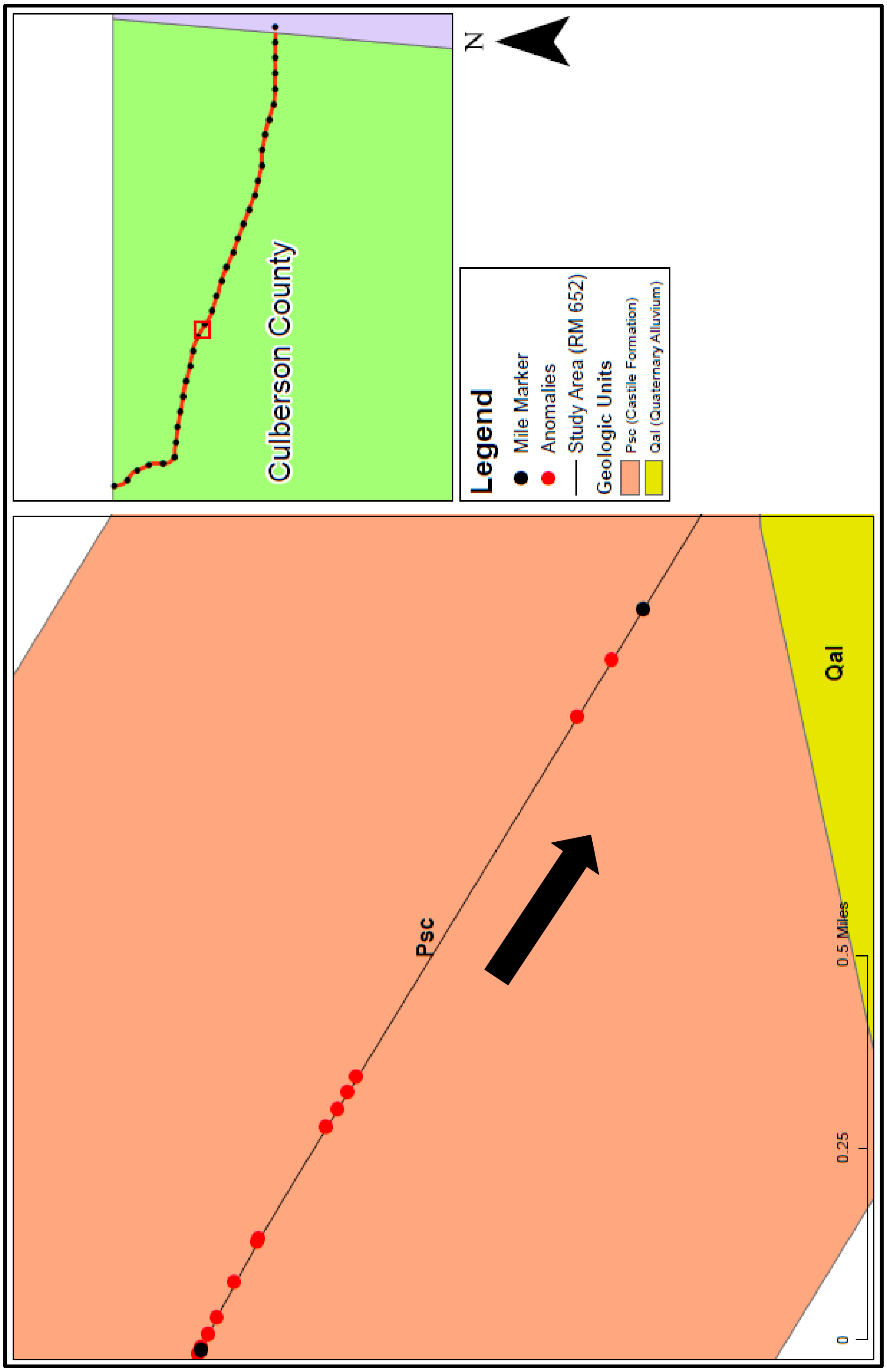

Figure C27. *Map indicating the location of Mile 13-14 resistivity profiles, along with anomalies. The black arrow indicates profile direction.*

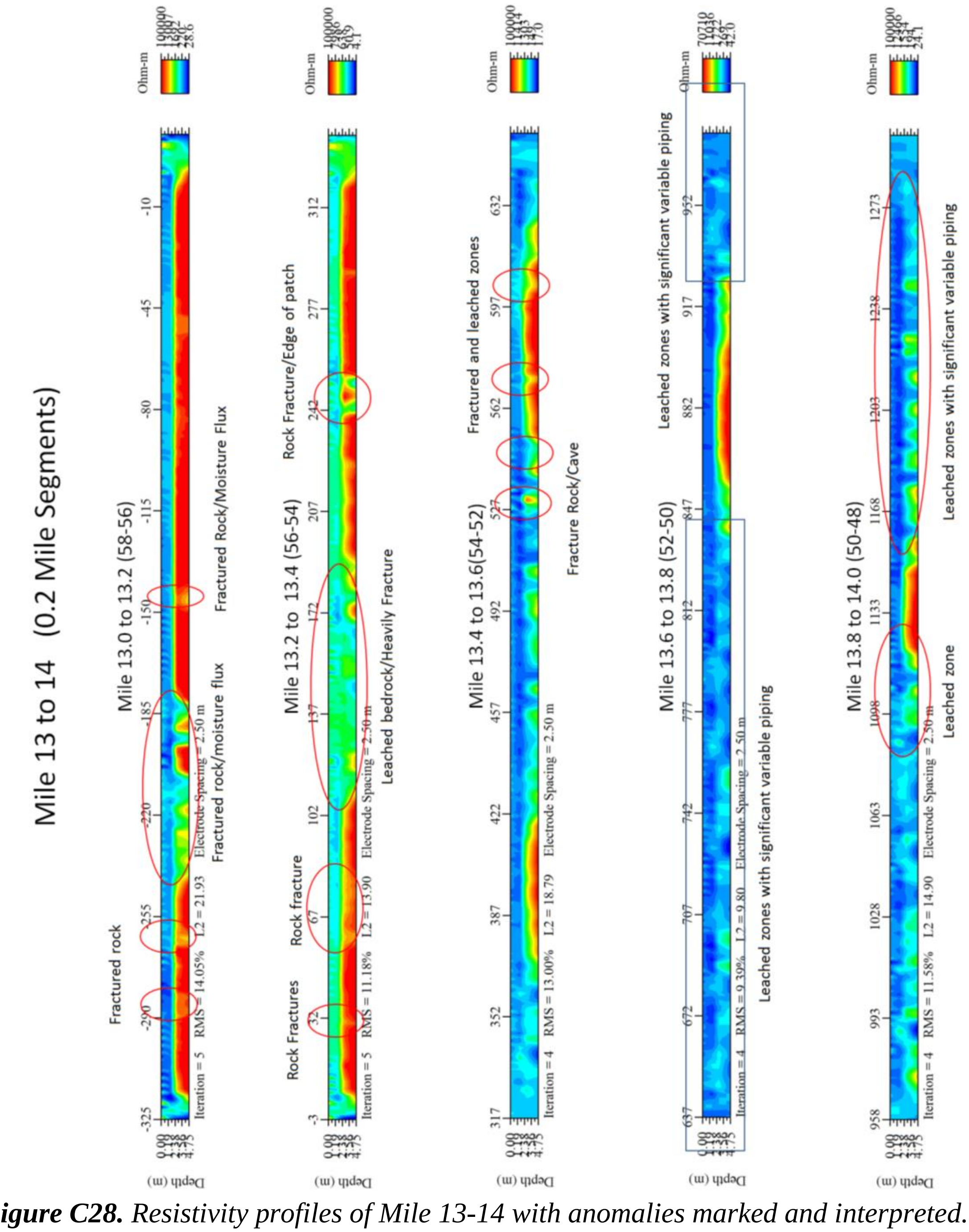

Figure C28. *Resistivity profiles of Mile 13-14 with anomalies marked and interpreted.*

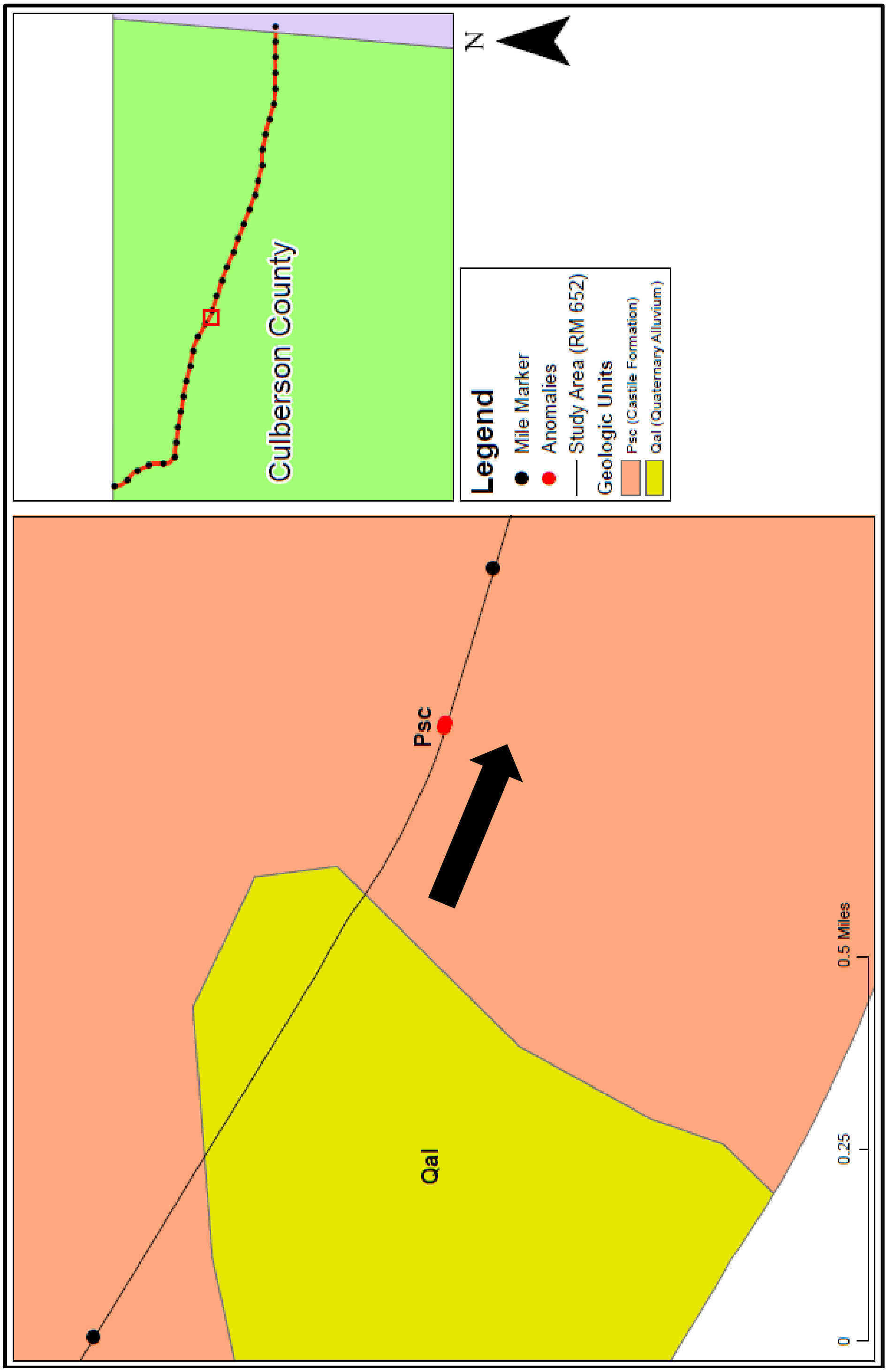

Figure C29. *Map indicating the location of Mile 14-15 resistivity profiles, along with anomalies. The black arrow indicates profile direction.*

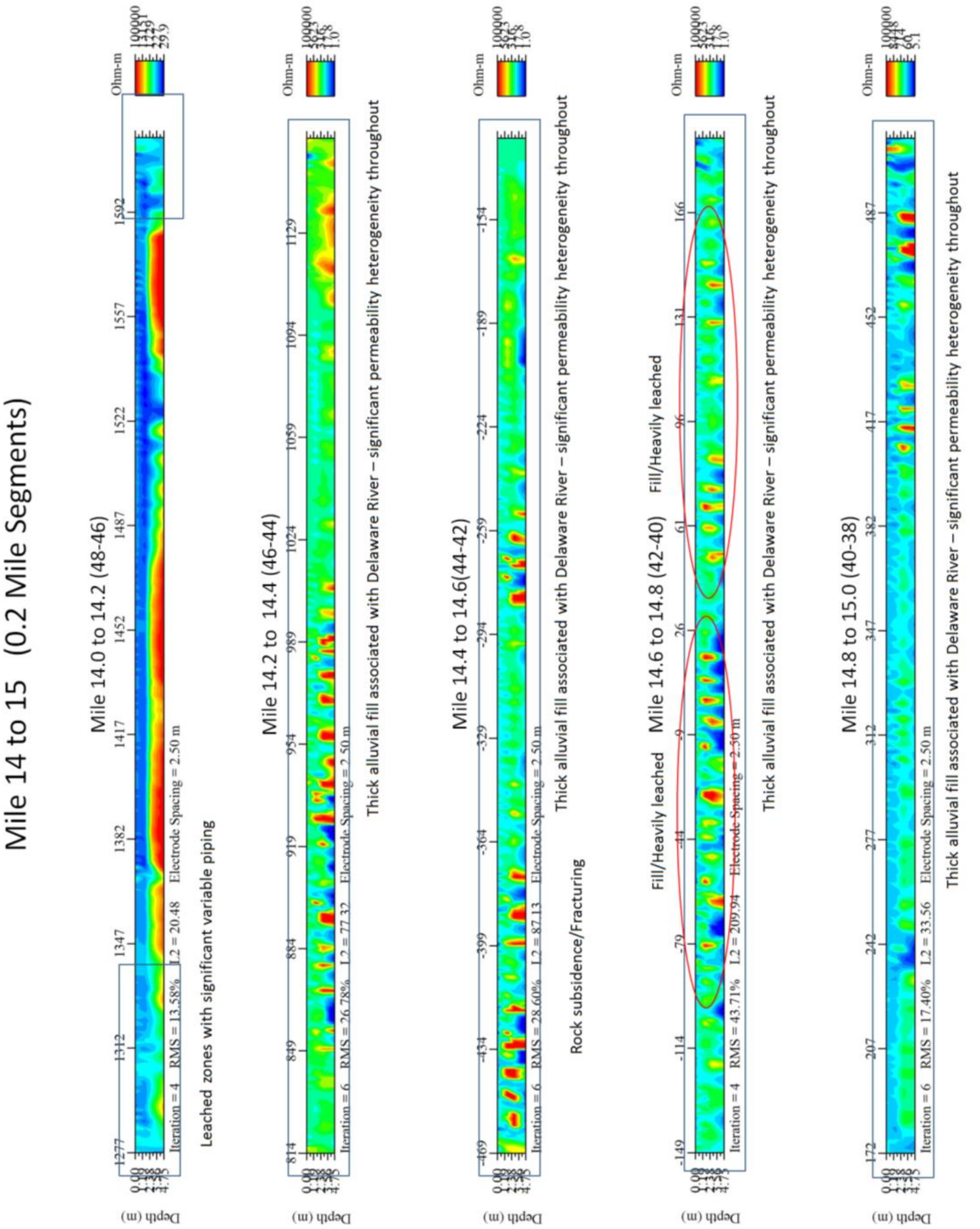

Figure C30. *Resistivity profiles of Mile 14-15 with anomalies marked and interpreted.*

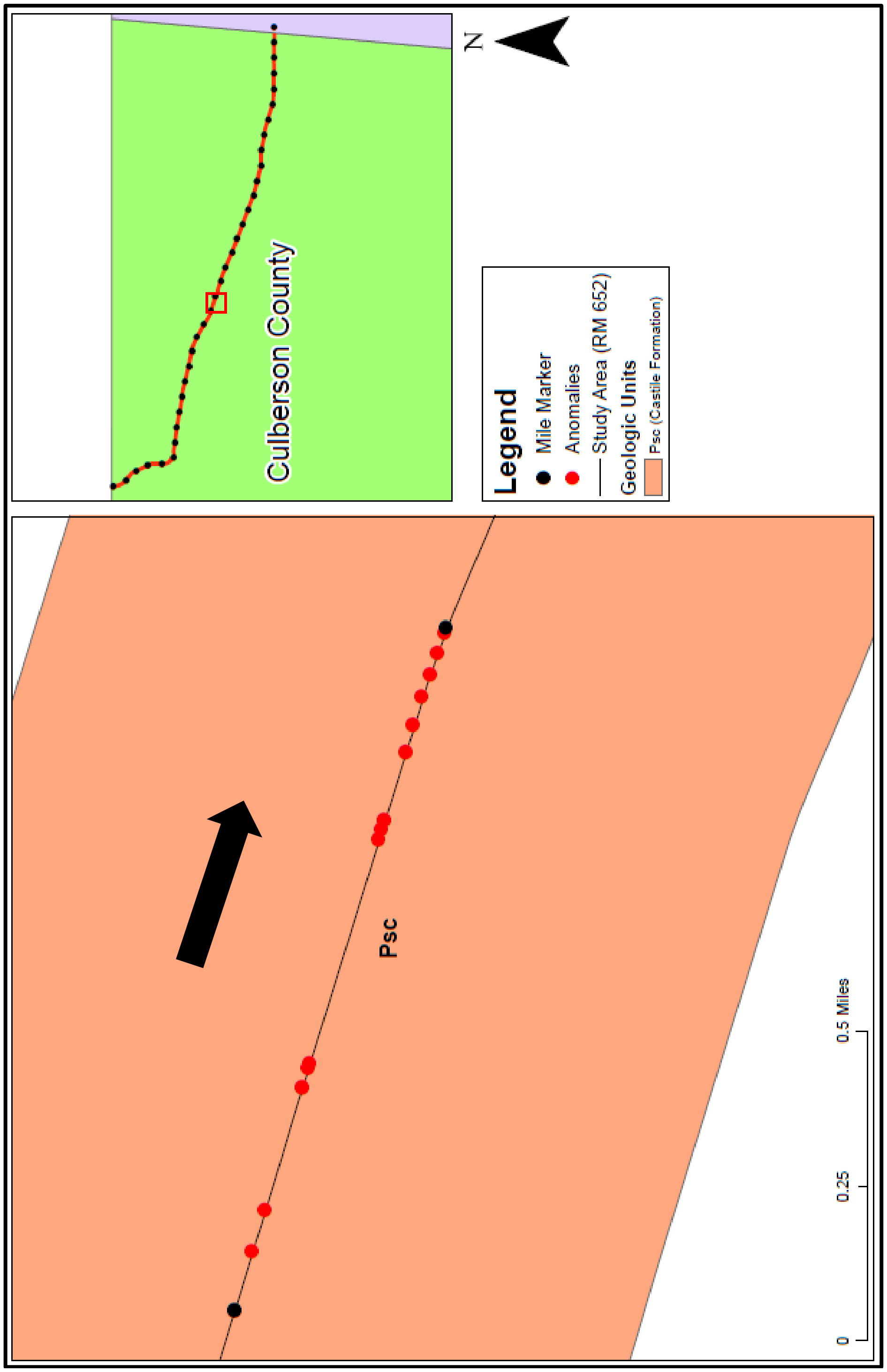

Figure C31. *Map indicating the location of Mile 15-16 resistivity profiles, along with anomalies. The black arrow indicates profile direction.*

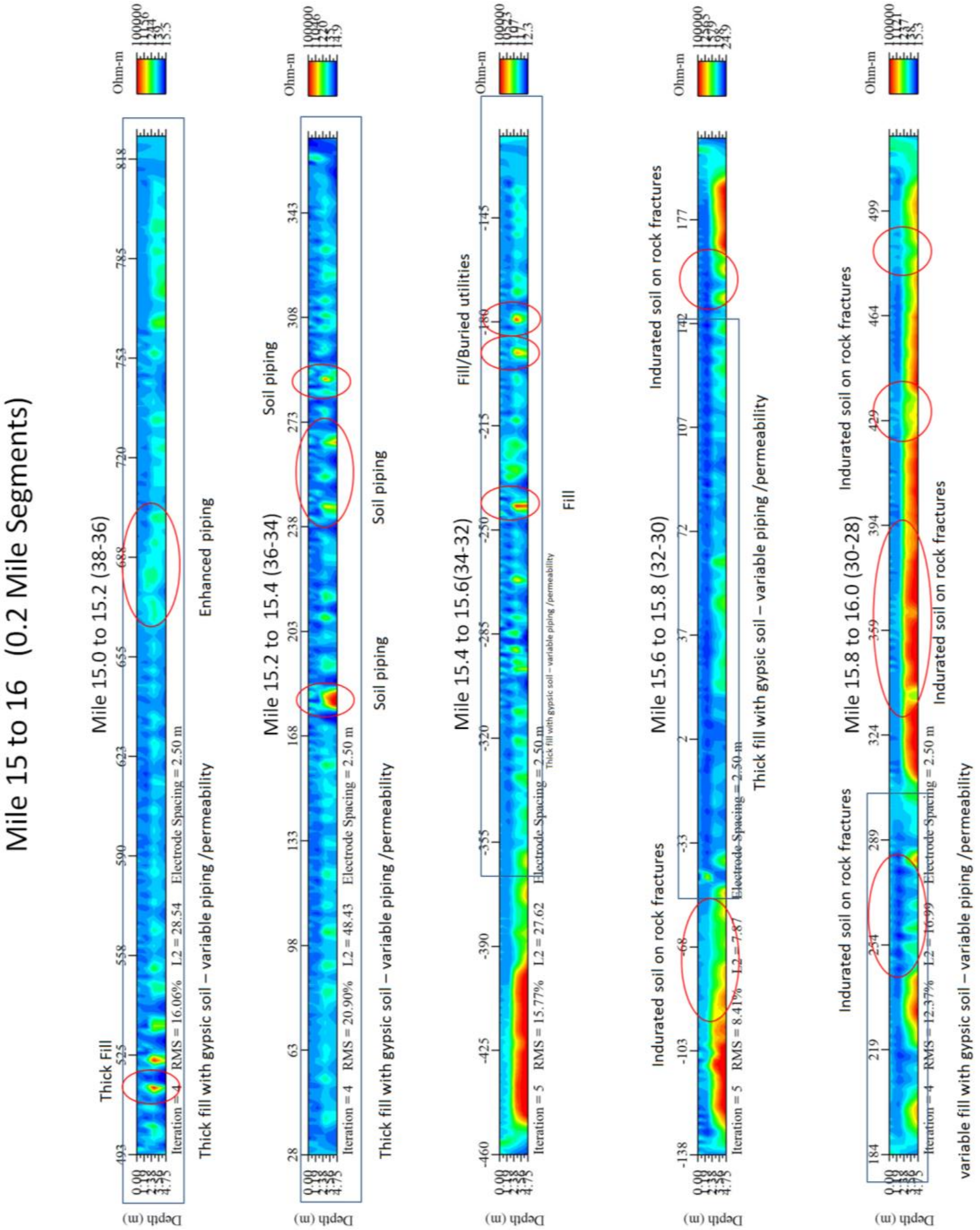

Figure C32. *Resistivity profiles of Mile 15-16 with anomalies marked and interpreted.*

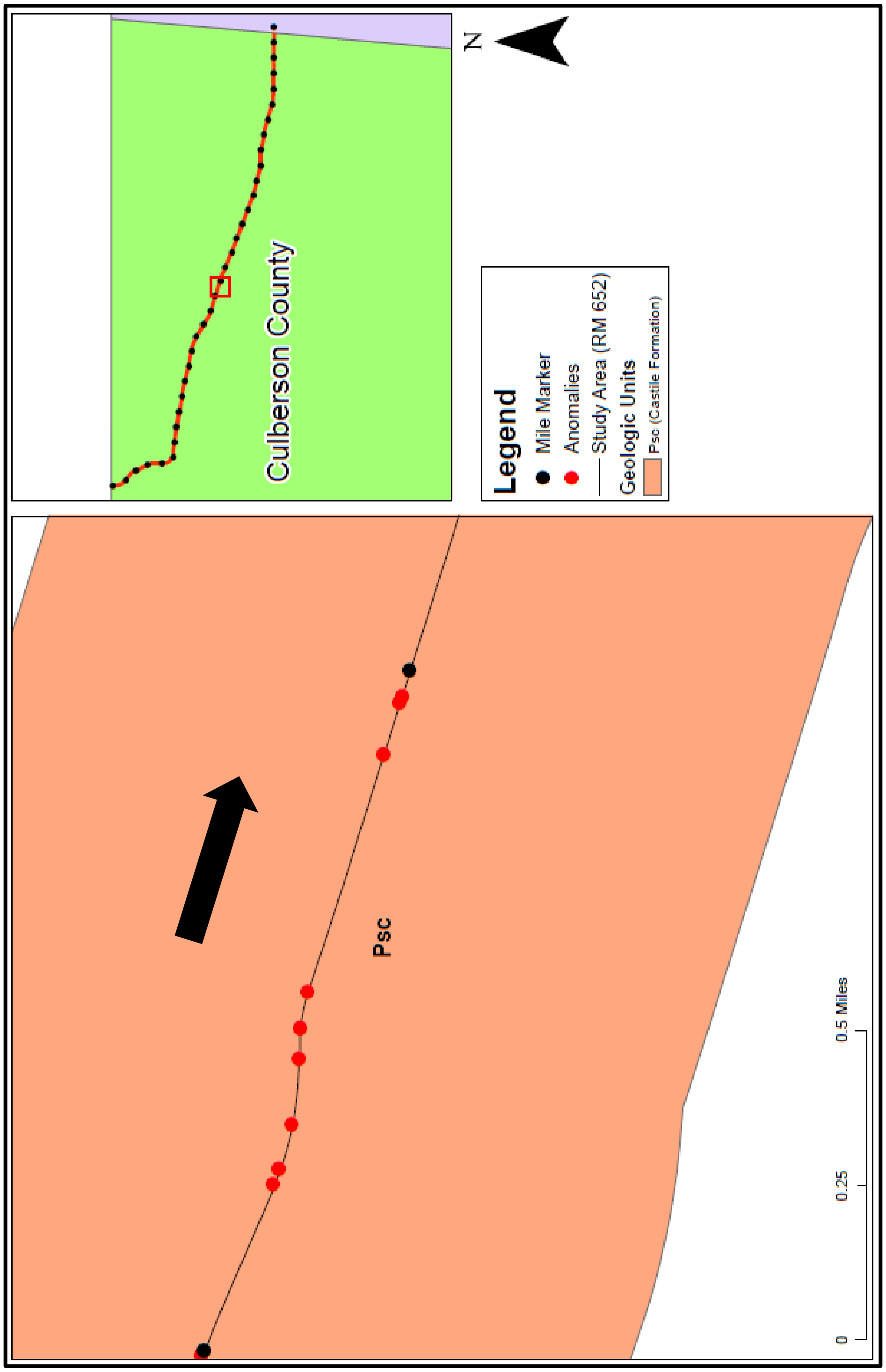

Figure C33. *Map indicating the location of Mile 16-17 resistivity profiles, along with anomalies. The black arrow indicates profile direction.*

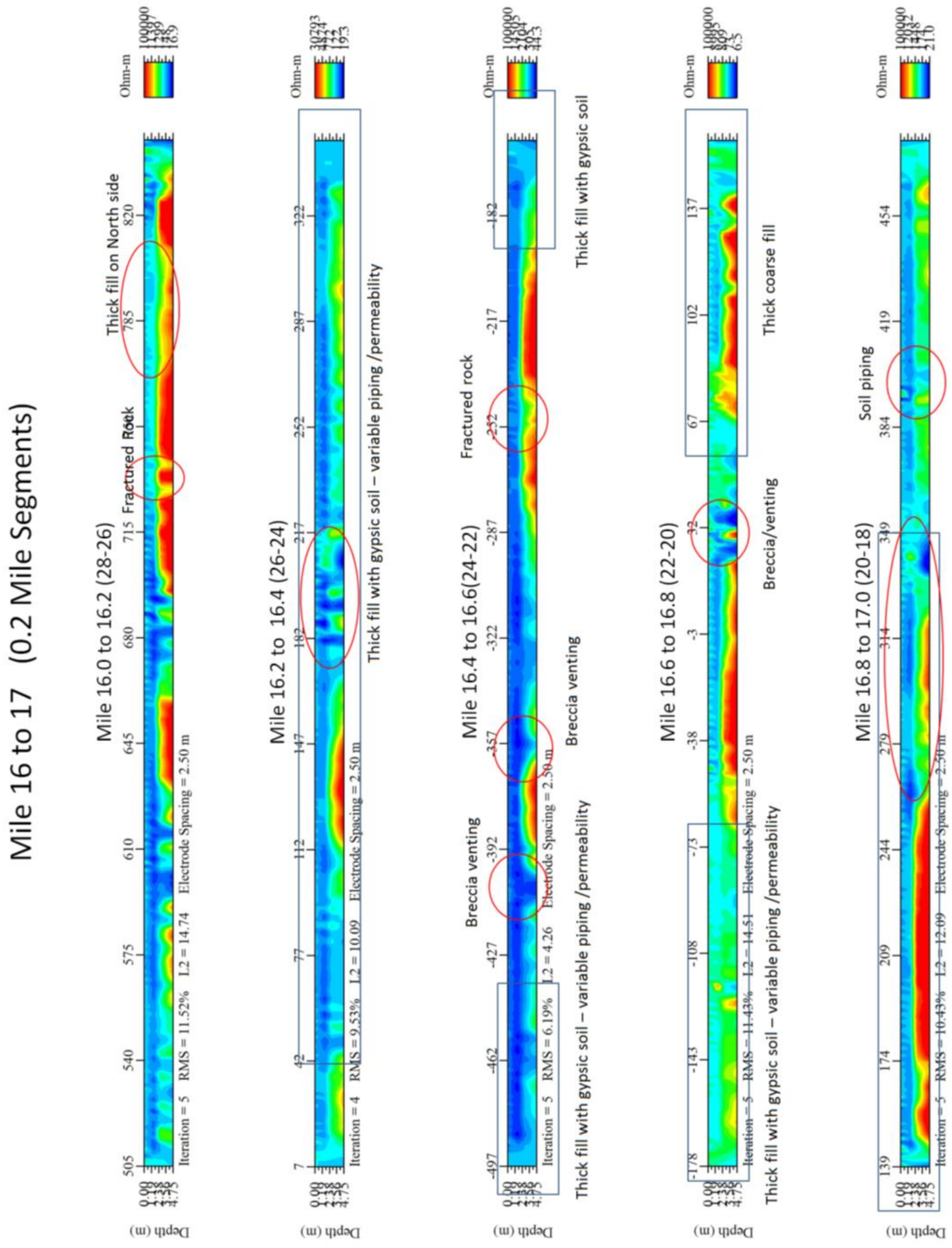

Figure C34. *Resistivity profiles of Mile 16-17 with anomalies marked and interpreted.*

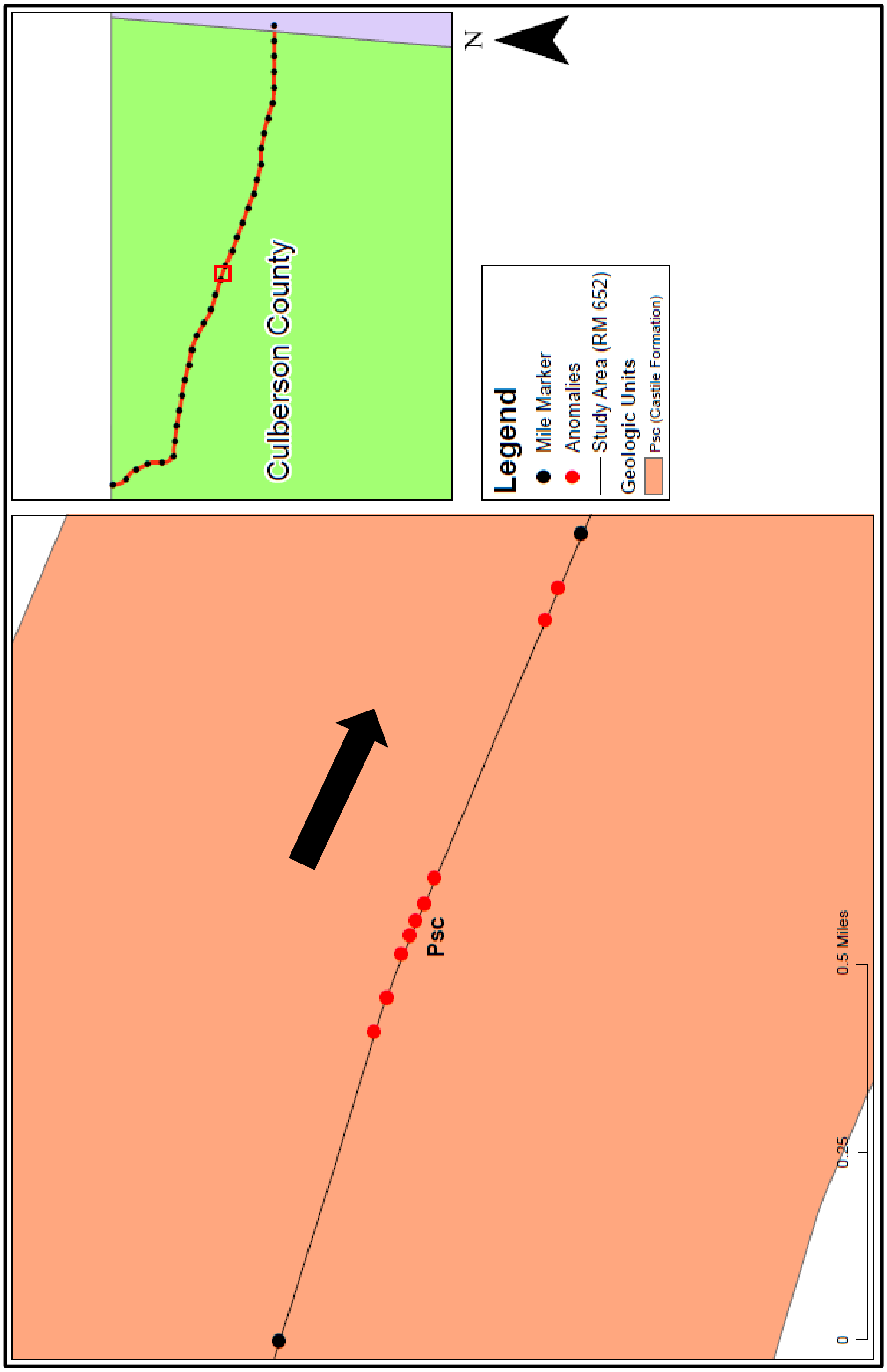

Figure C35. *Map indicating the location of Mile 17-18 resistivity profiles, along with anomalies. The black arrow indicates profile direction.*

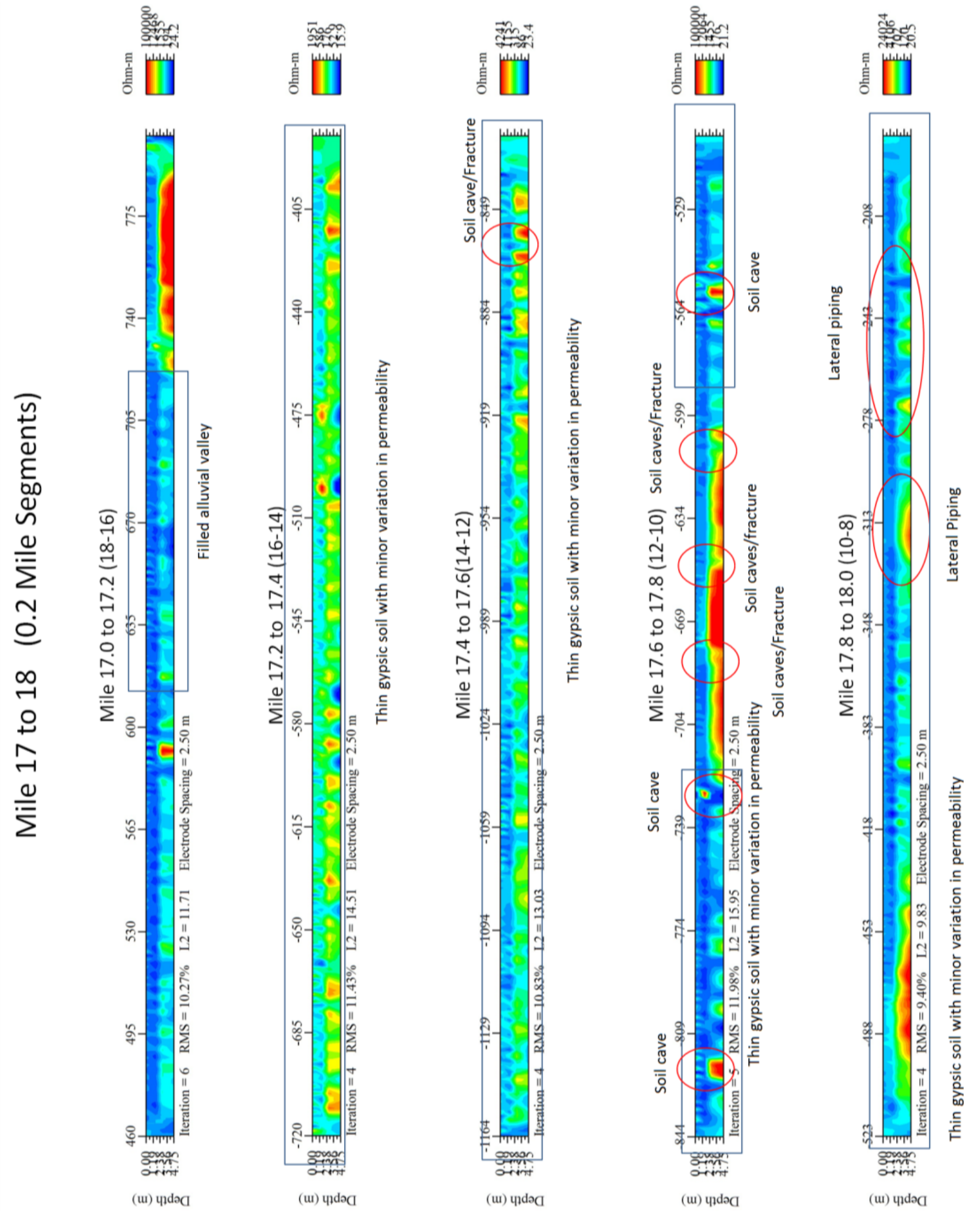

Figure C36. Resistivity profiles of Mile 17-18 with anomalies marked and interpreted.

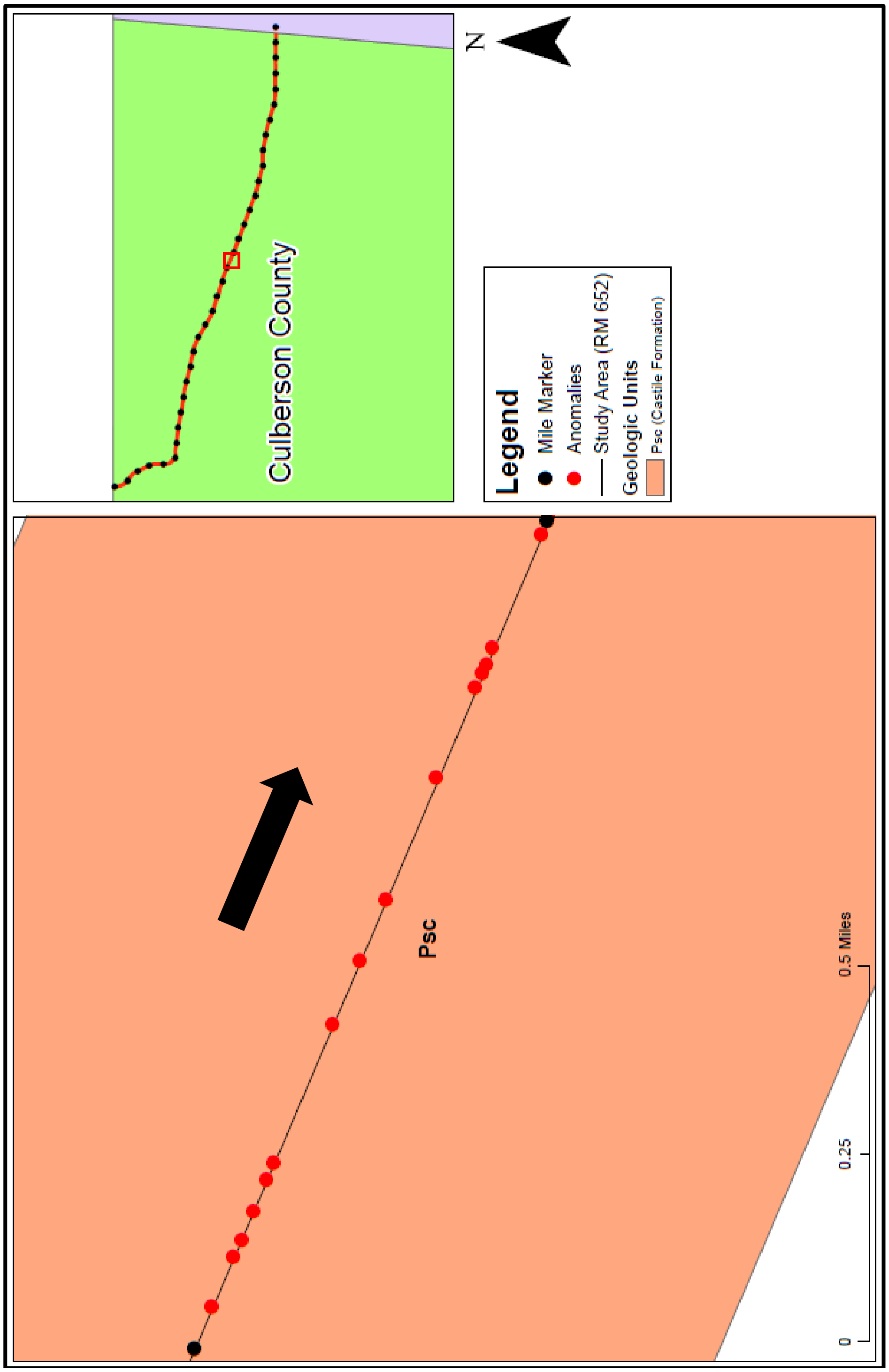

Figure C37. *Map indicating the location of Mile 18-19 resistivity profiles, along with anomalies. The black arrow indicates profile direction.*

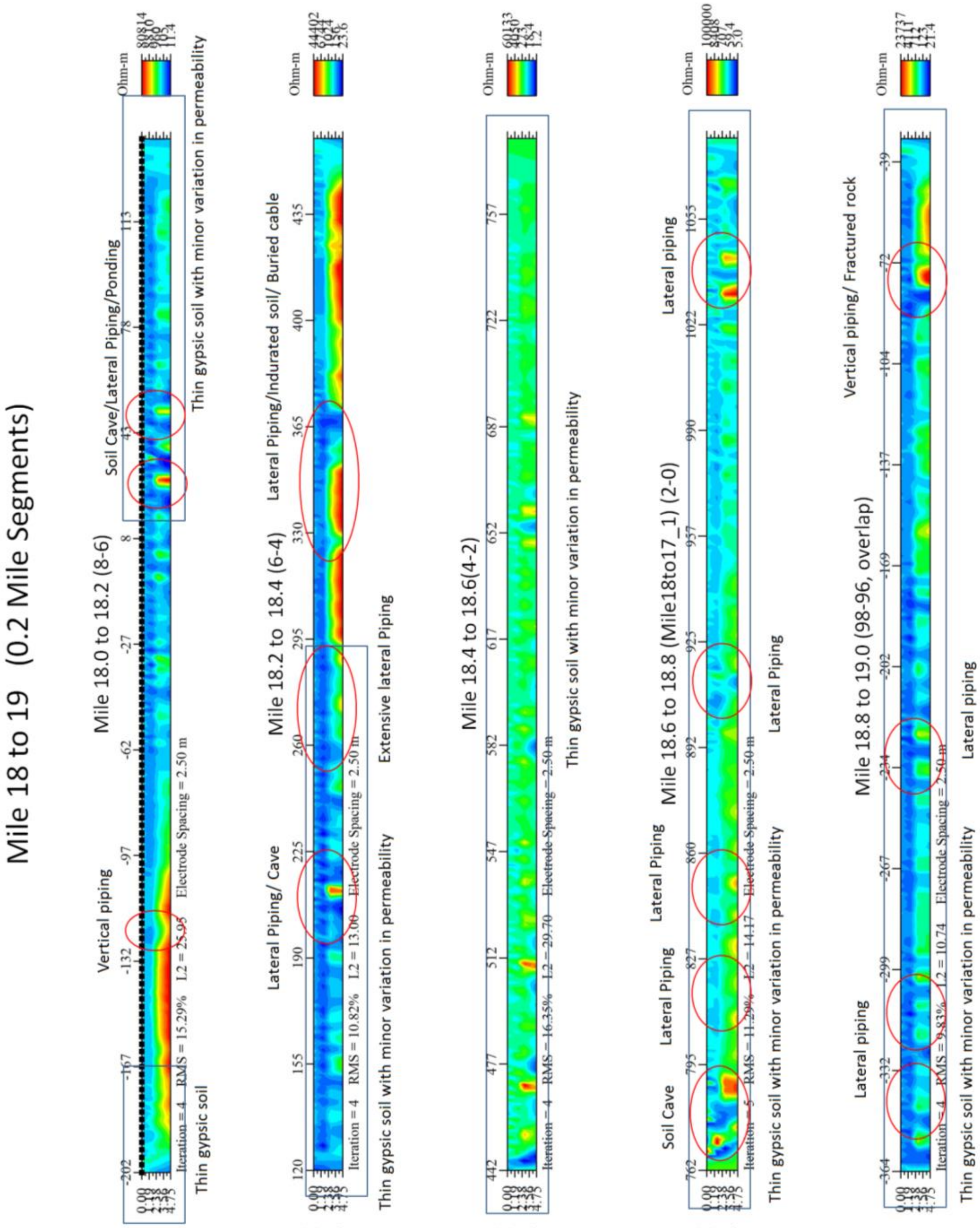

Figure C38. *Resistivity profiles of Mile 18-19 with anomalies marked and interpreted.*

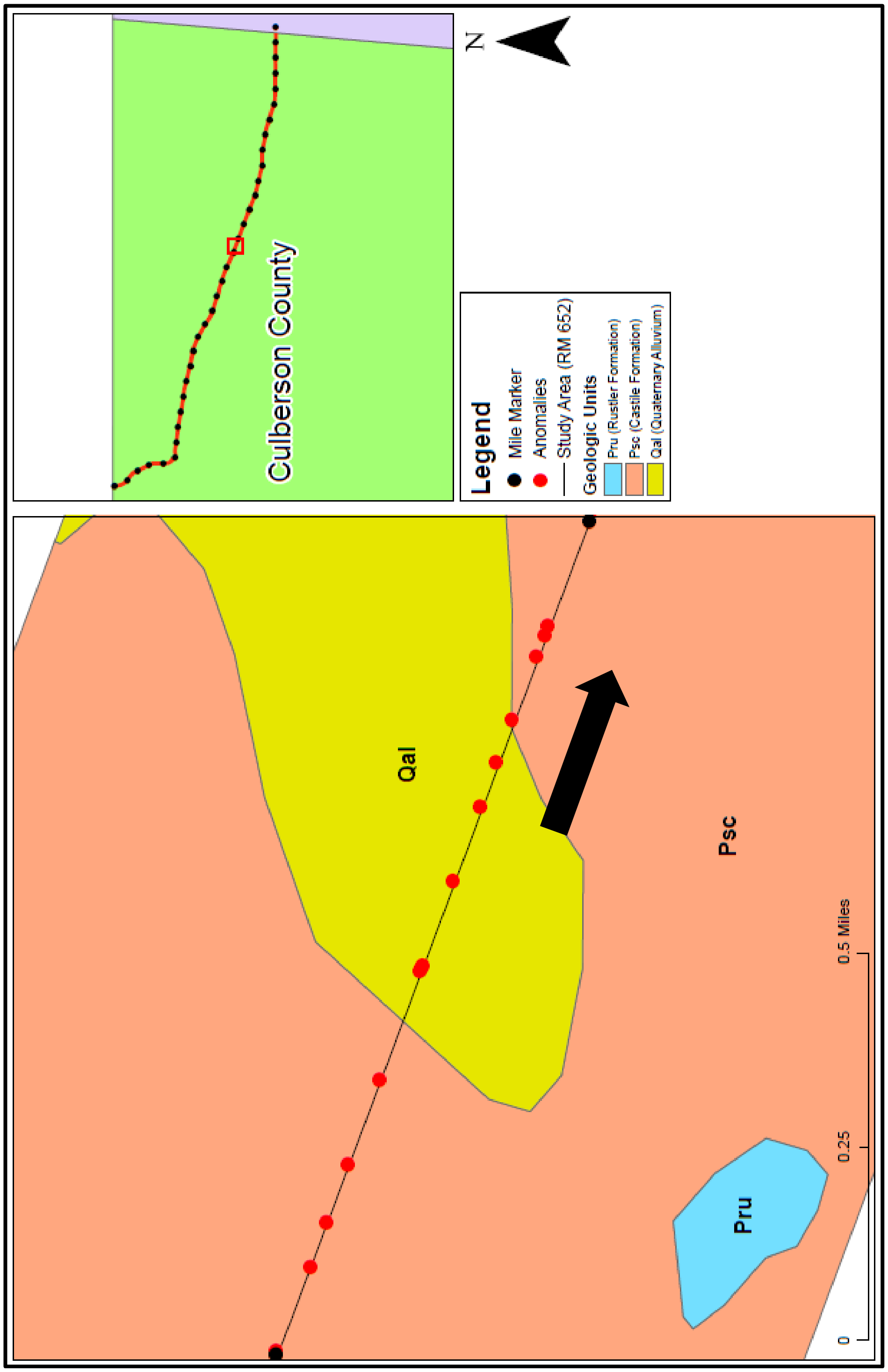

Figure C39. *Map indicating the location of Mile 19-20 resistivity profiles, along with anomalies. The black arrow indicates profile direction.*

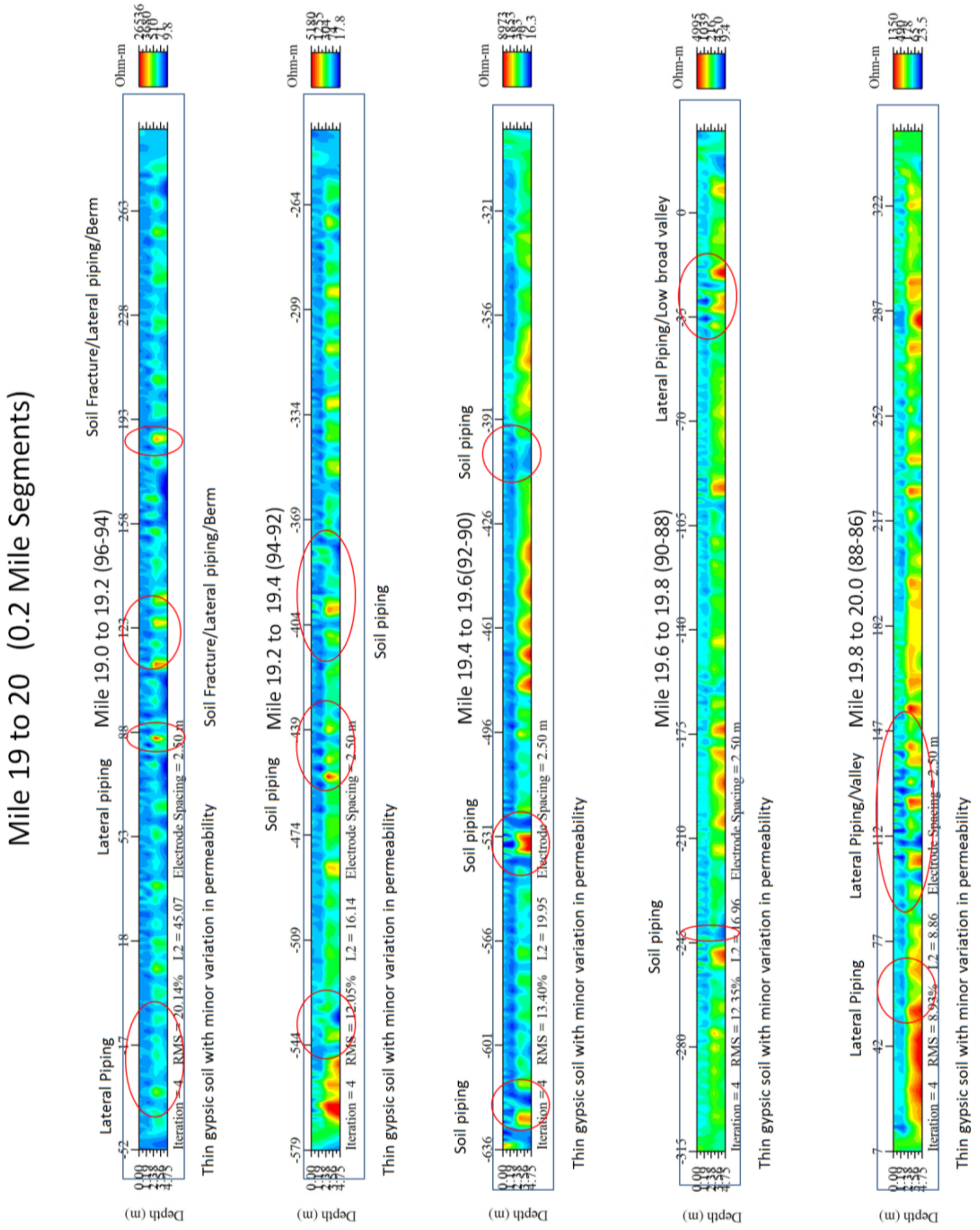

Figure C40. *Resistivity profiles of Mile 19-20 with anomalies marked and interpreted.*

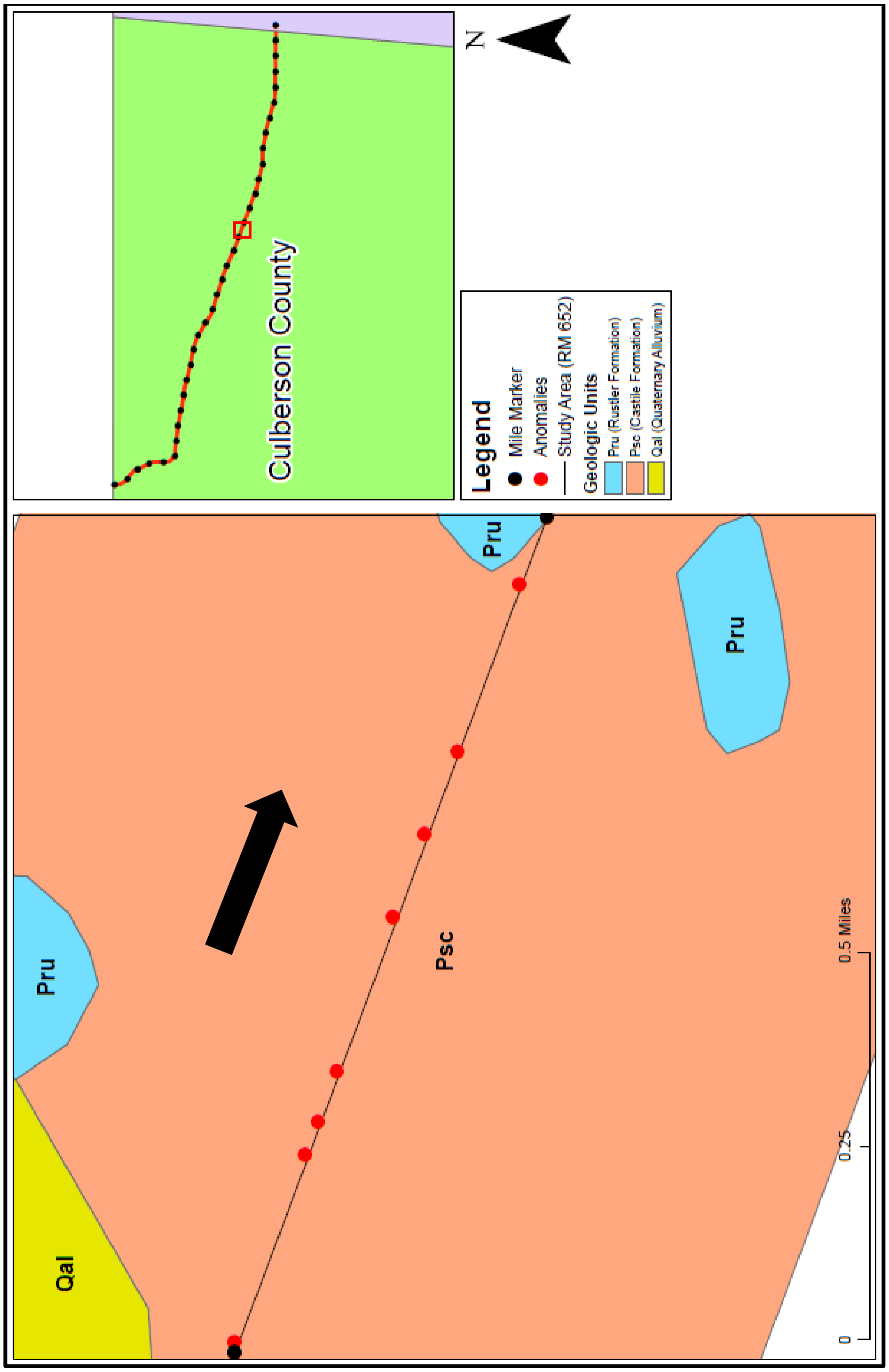

Figure C41. *Map indicating the location of Mile 20-21 resistivity profiles, along with anomalies. The black arrow indicates profile direction.*

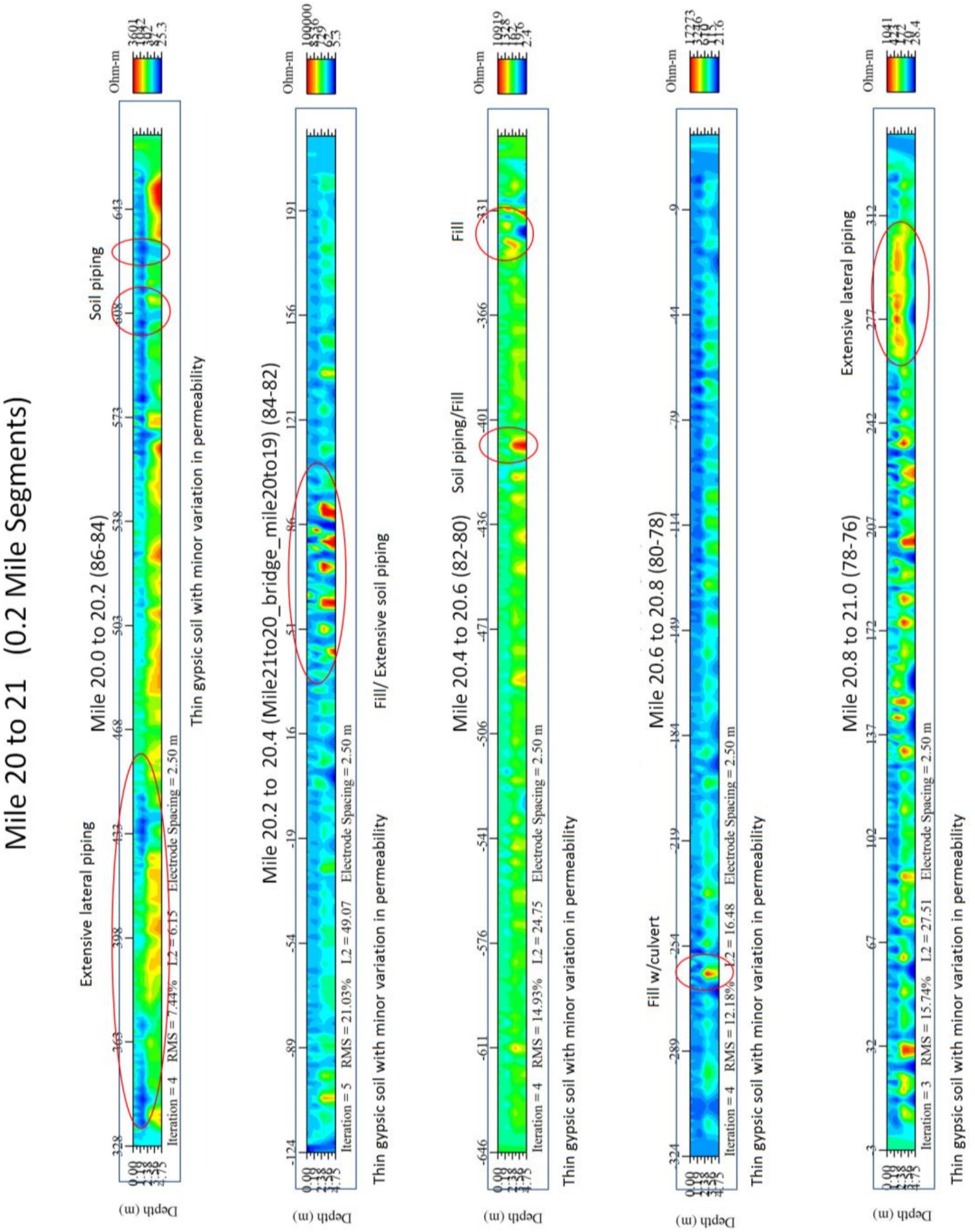

Figure C42. *Resistivity profiles of Mile 20-21 with anomalies marked and interpreted.*

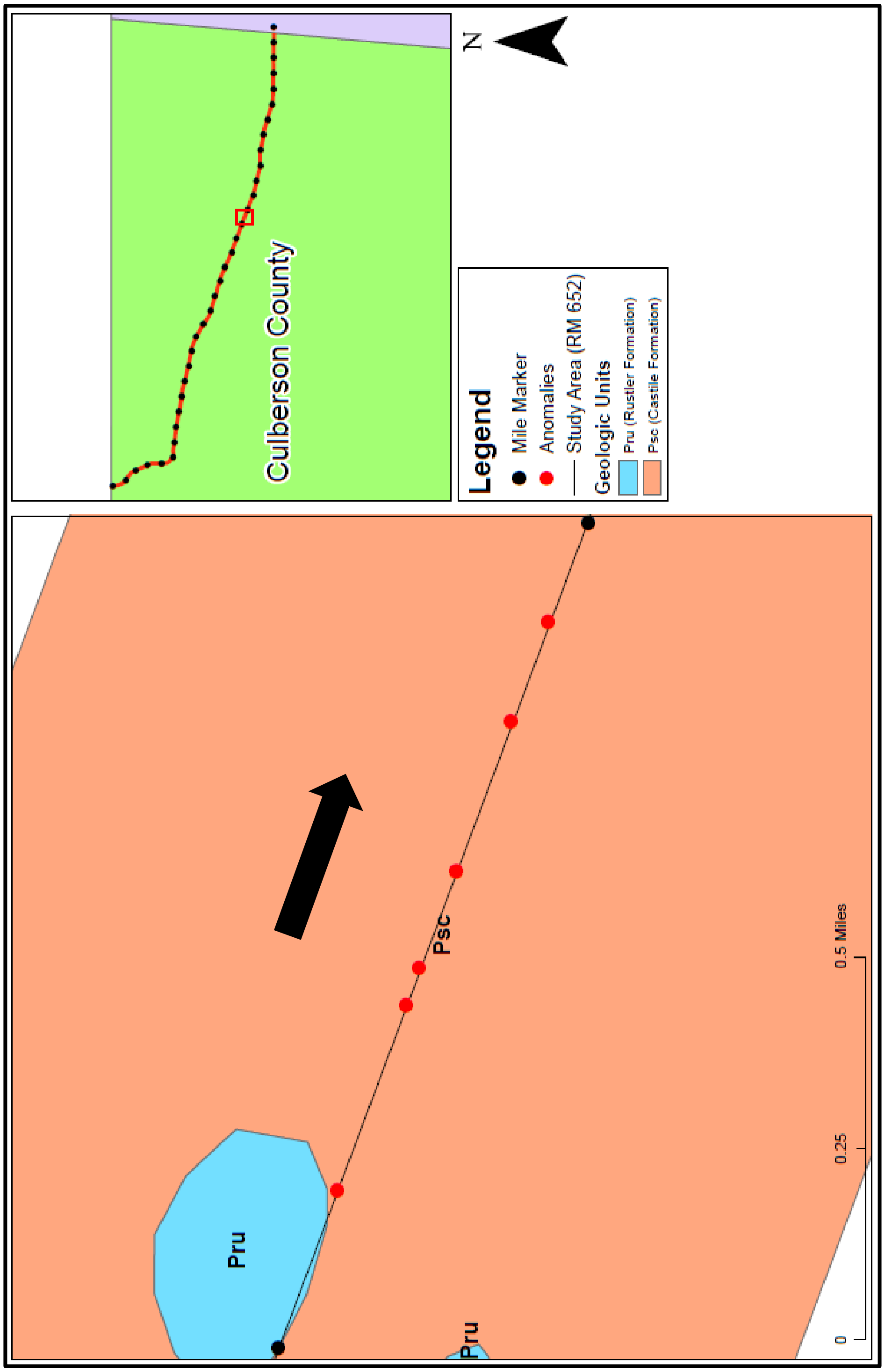

Figure C43. *Map indicating the location of Mile 21-22 resistivity profiles, along with anomalies. The black arrow indicates profile direction.*

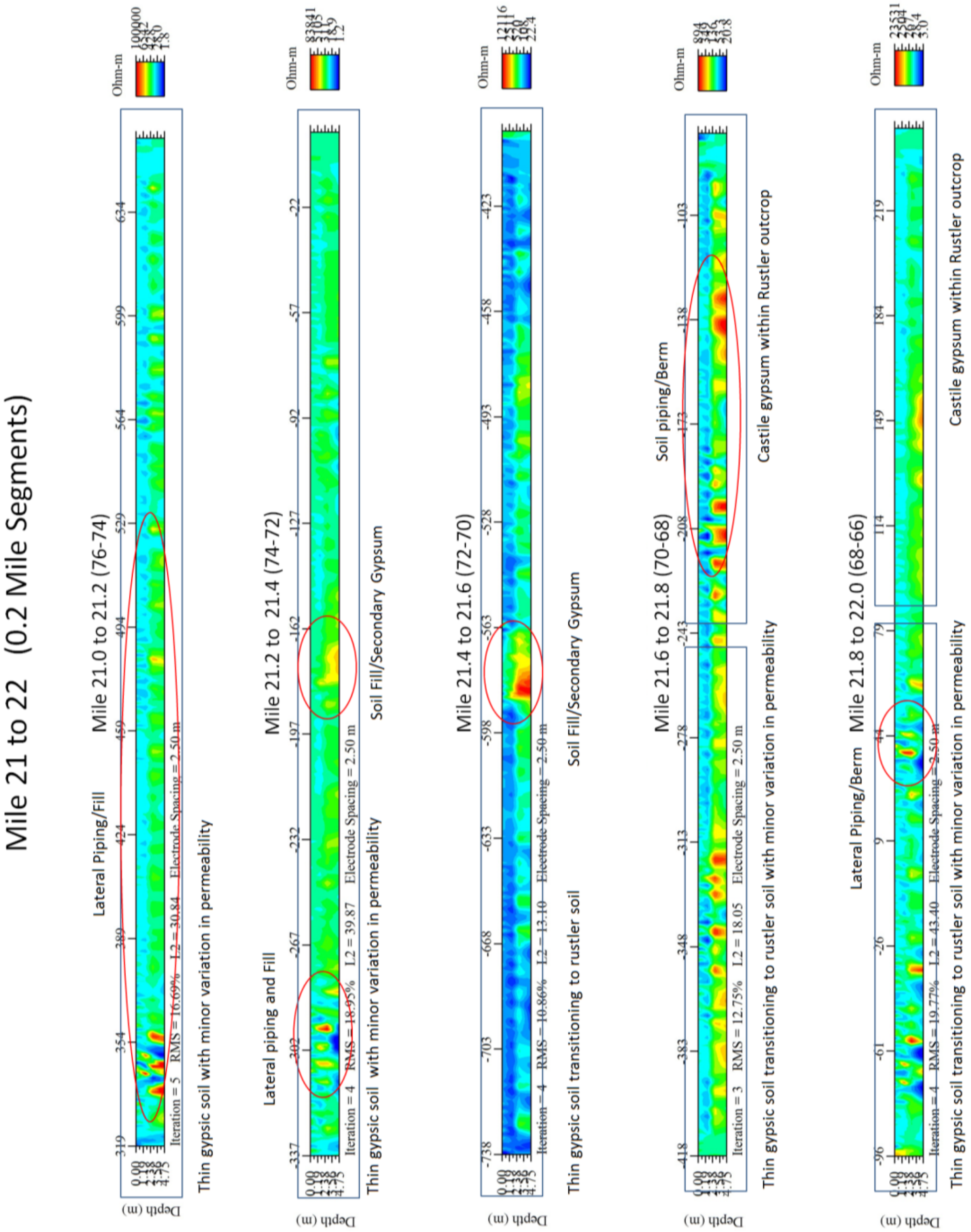

Figure C44. *Resistivity profiles of Mile 21-22 with anomalies marked and interpreted.*

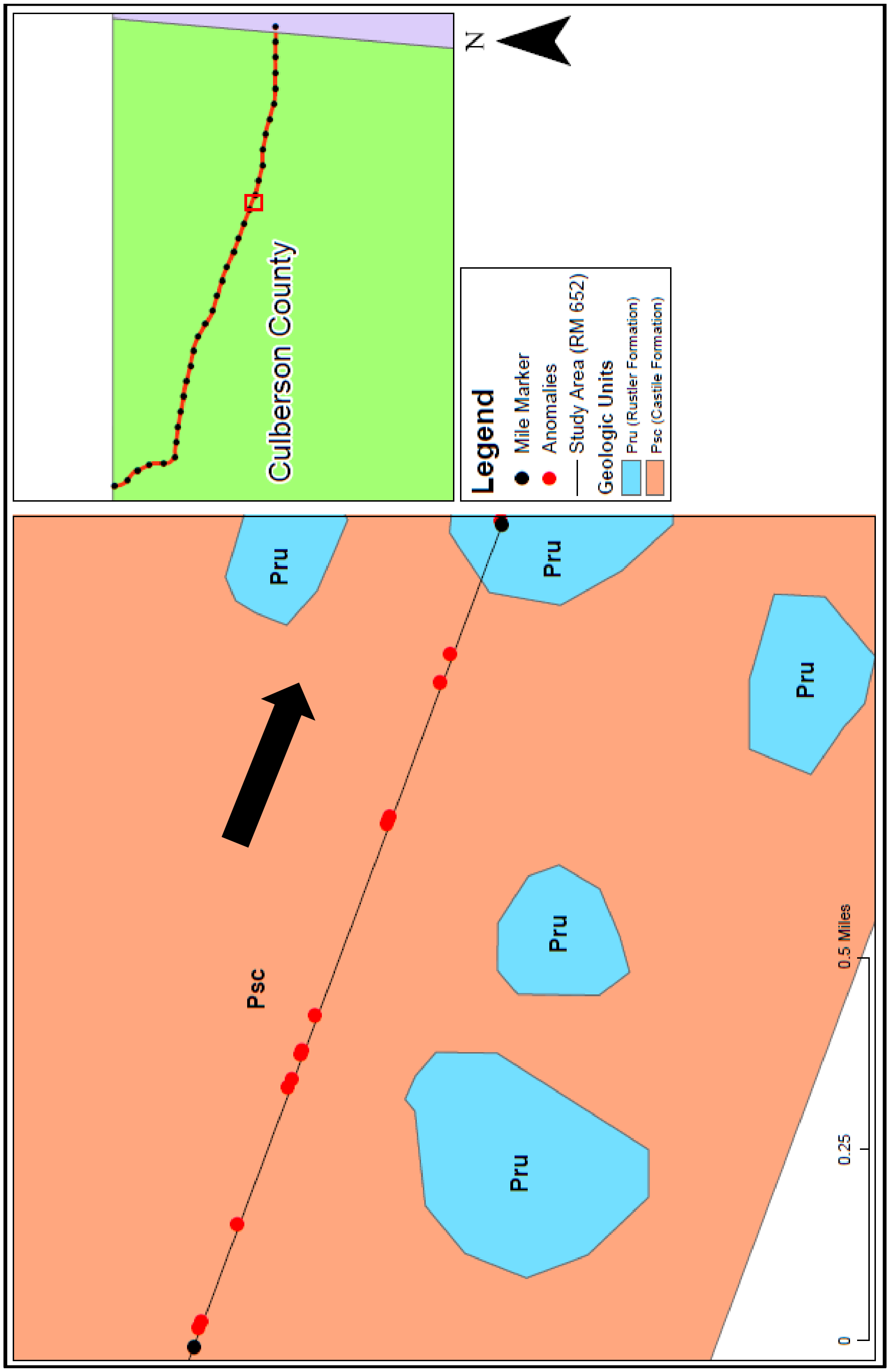

Figure C45. *Map indicating the location of Mile 22-23 resistivity profiles, along with anomalies. The black arrow indicates profile direction.*

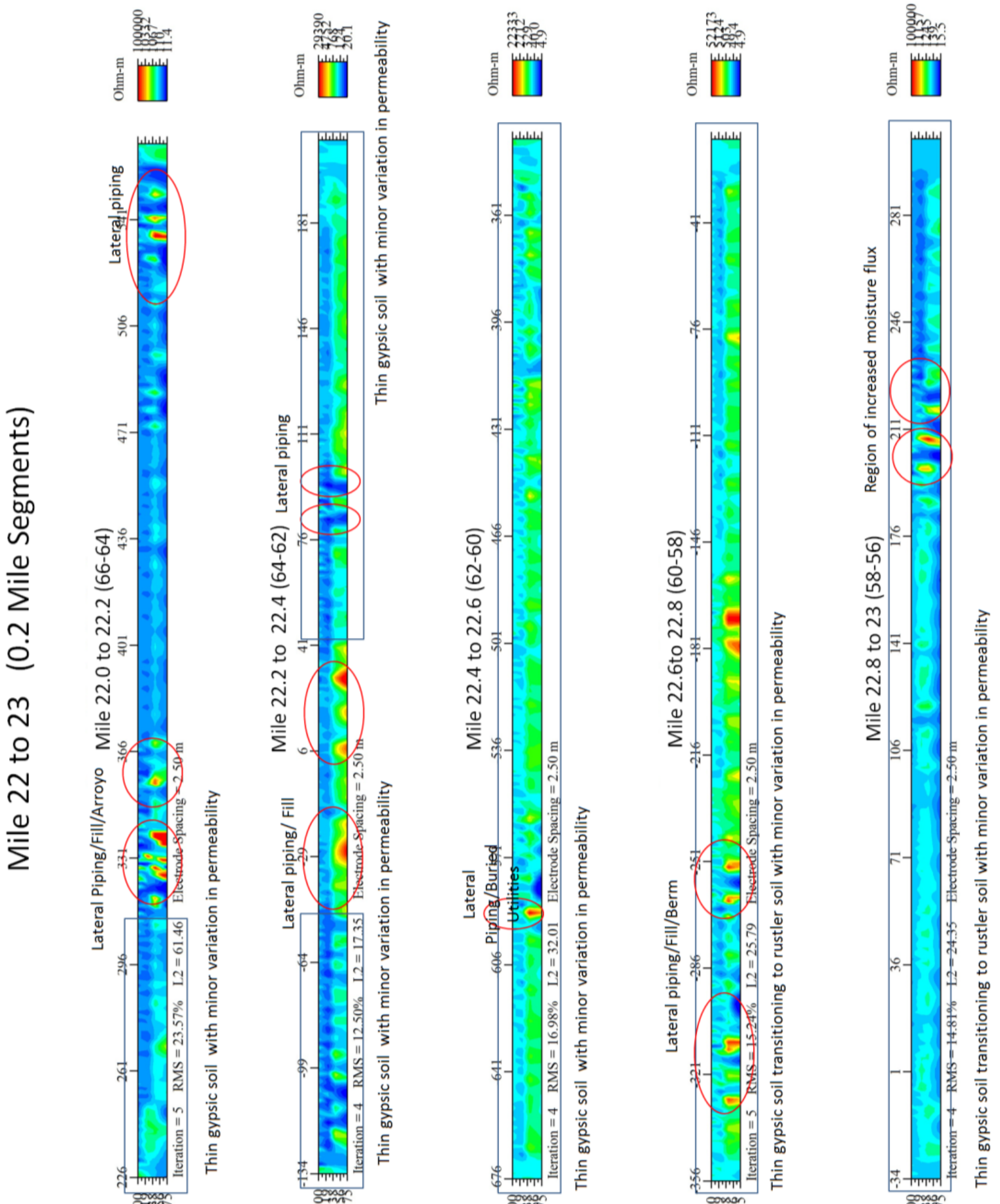

Figure C46. *Resistivity profiles of Mile 22-23 with anomalies marked and interpreted.*

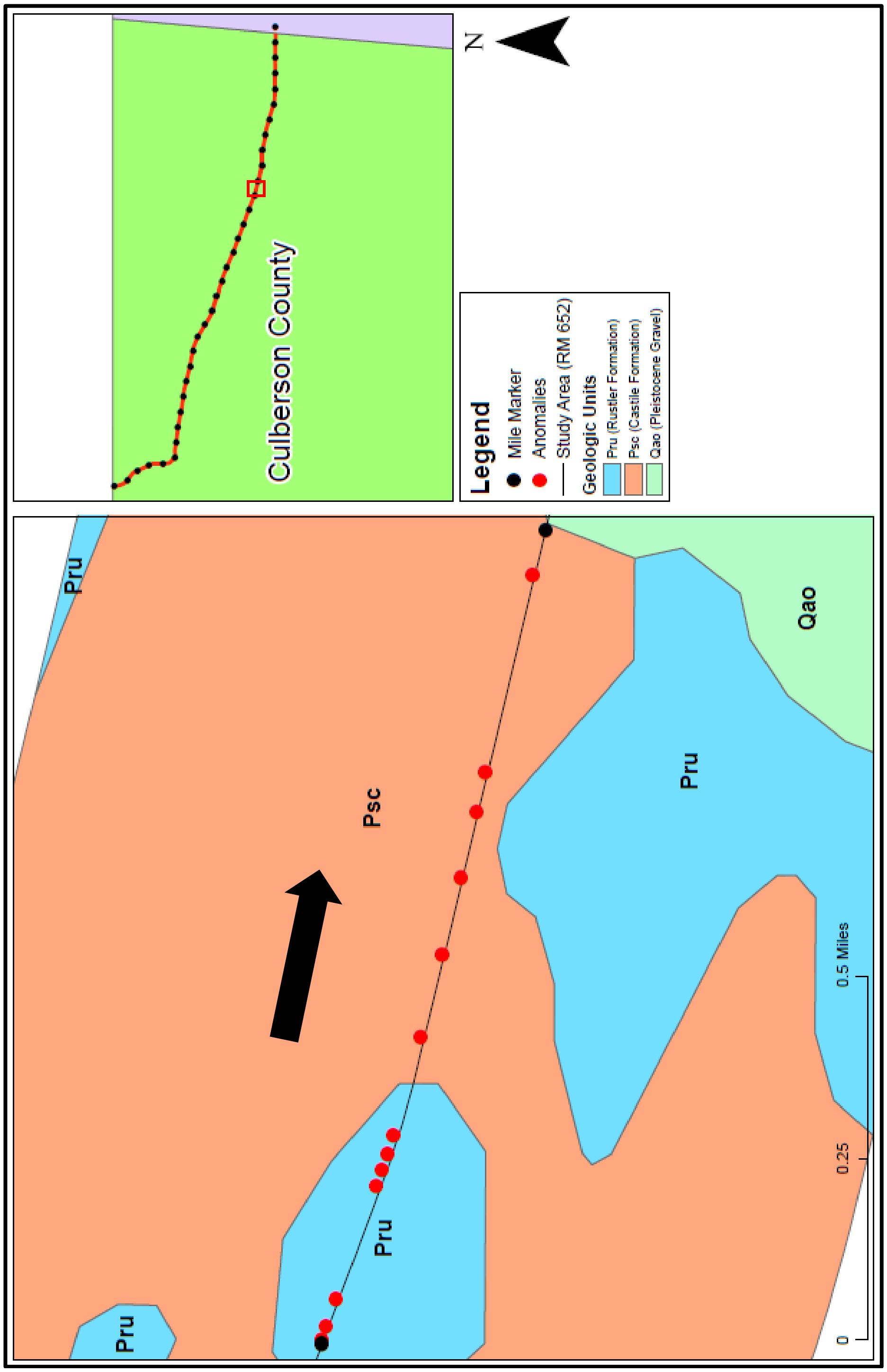

Figure C47. *Map indicating the location of Mile 23-24 resistivity profiles, along with anomalies. The black arrow indicates profile direction.*

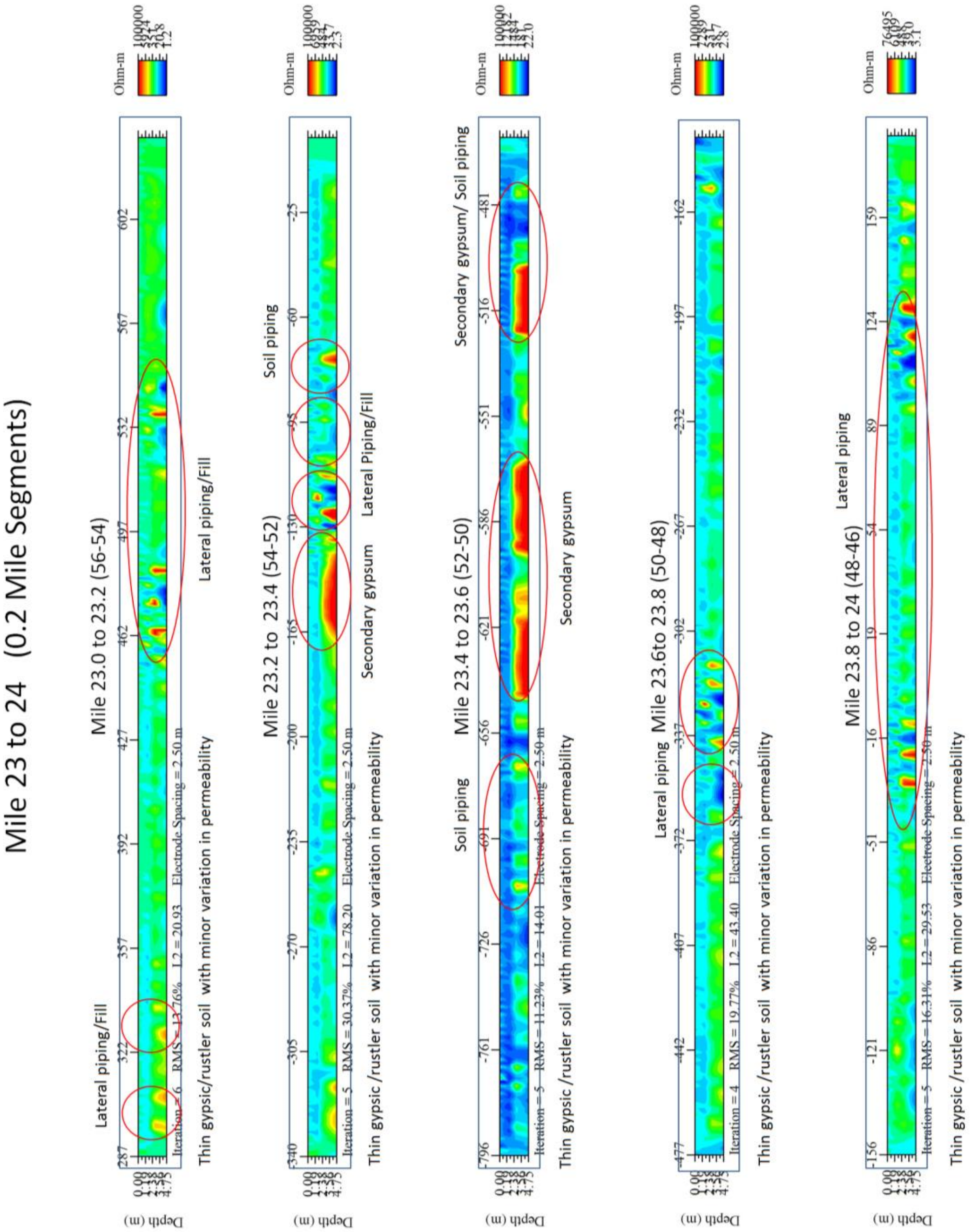

Figure C48. *Resistivity profiles of Mile 23-24 with anomalies marked and interpreted.*

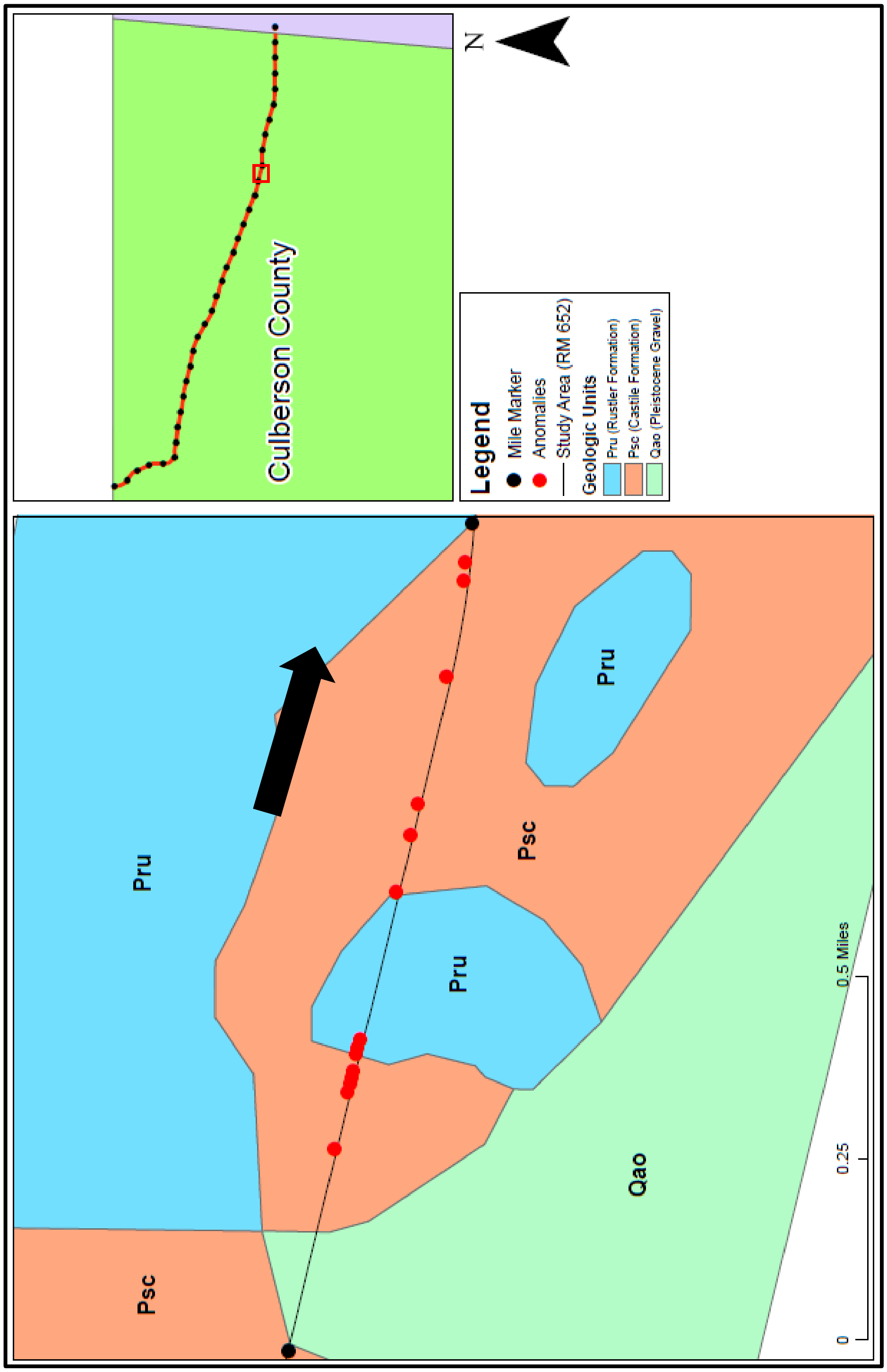

Figure C49. *Map indicating the location of Mile 24-25 resistivity profiles, along with anomalies. The black arrow indicates profile direction.*

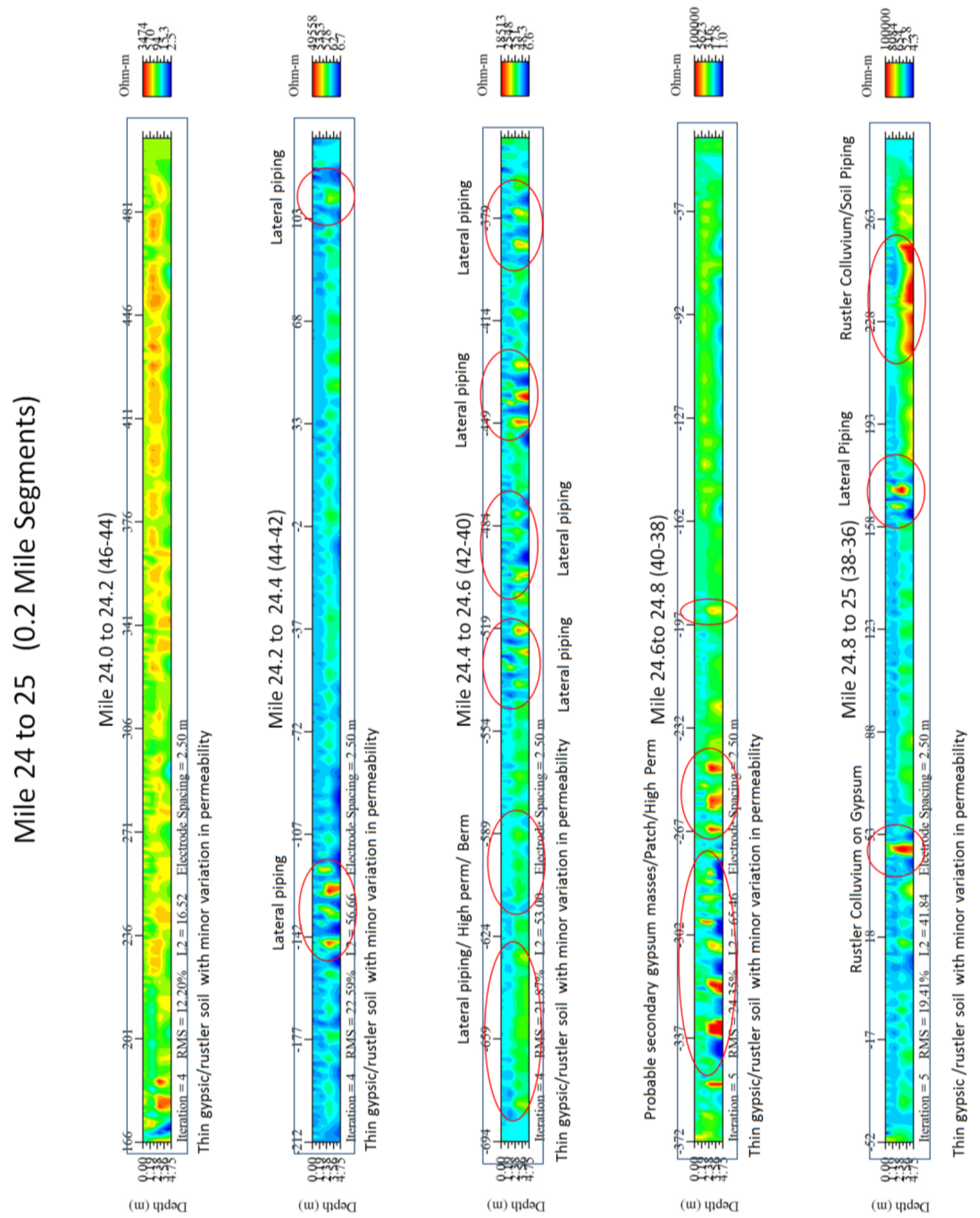

Figure C50. *Resistivity profiles of Mile 24-25 with anomalies marked and interpreted.*

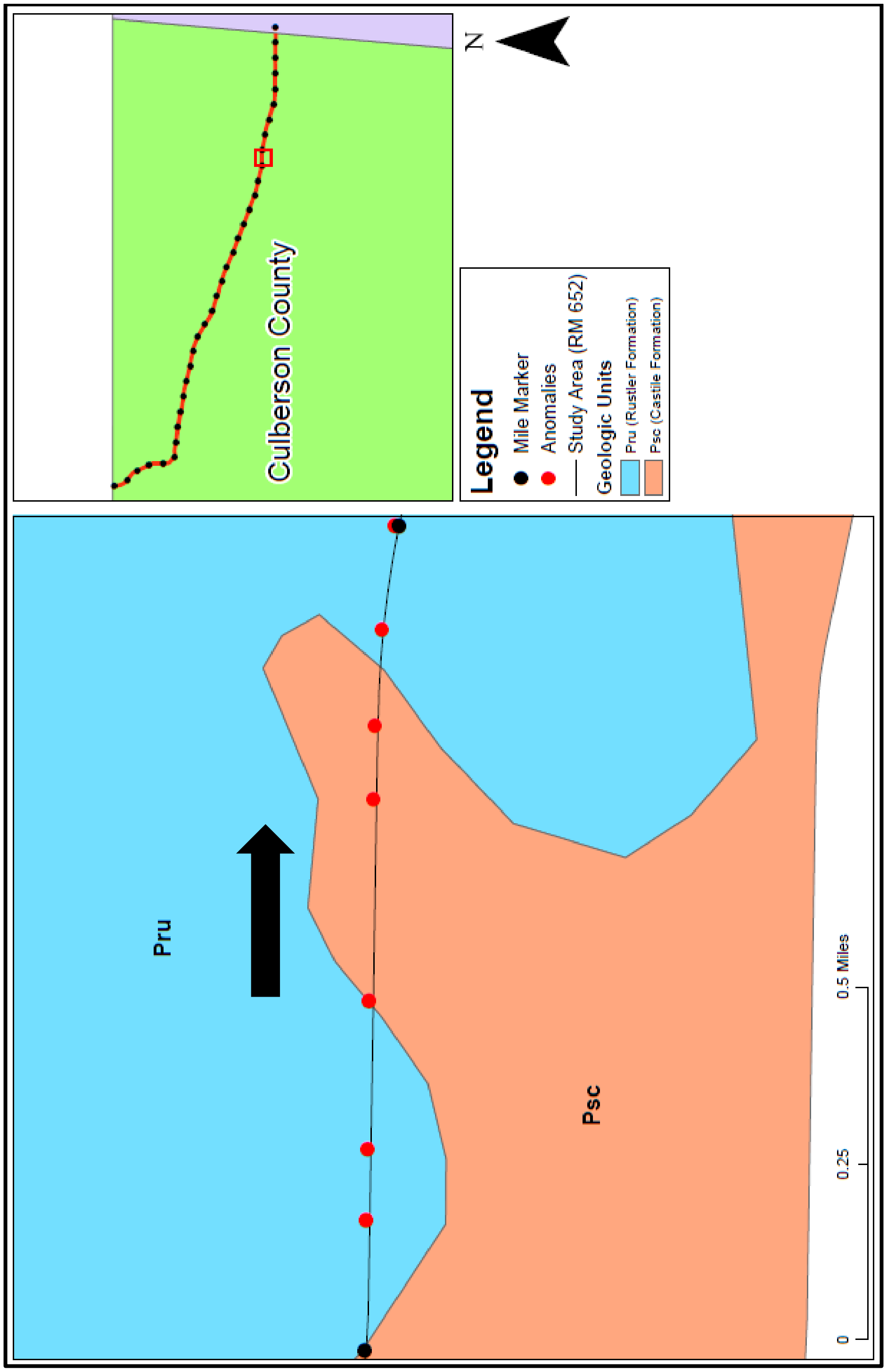

Figure C51. *Map indicating the location of Mile 25-26 resistivity profiles, along with anomalies. The black arrow indicates profile direction.*

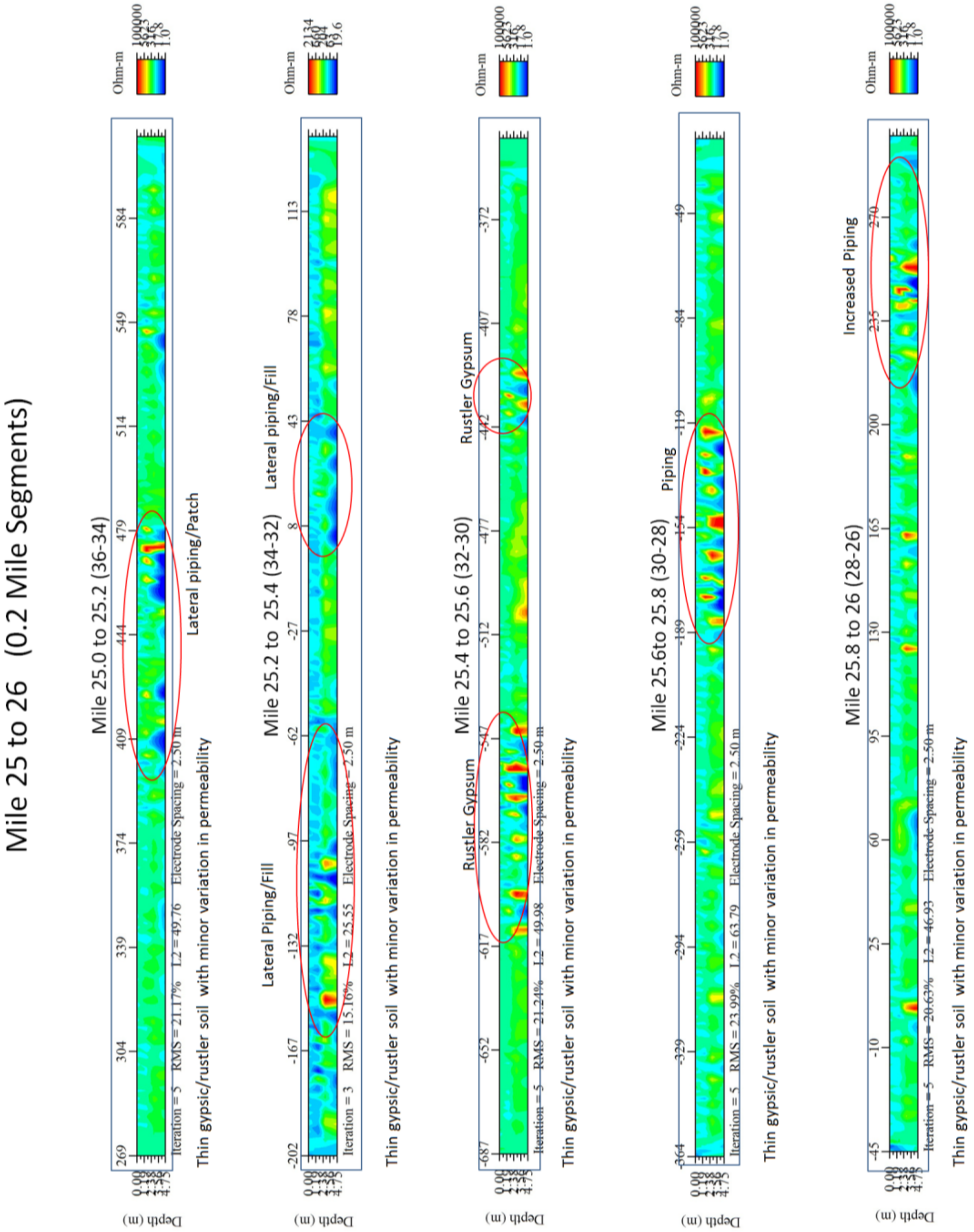

Figure C52. *Resistivity profiles of Mile 25-26 with anomalies marked and interpreted.*

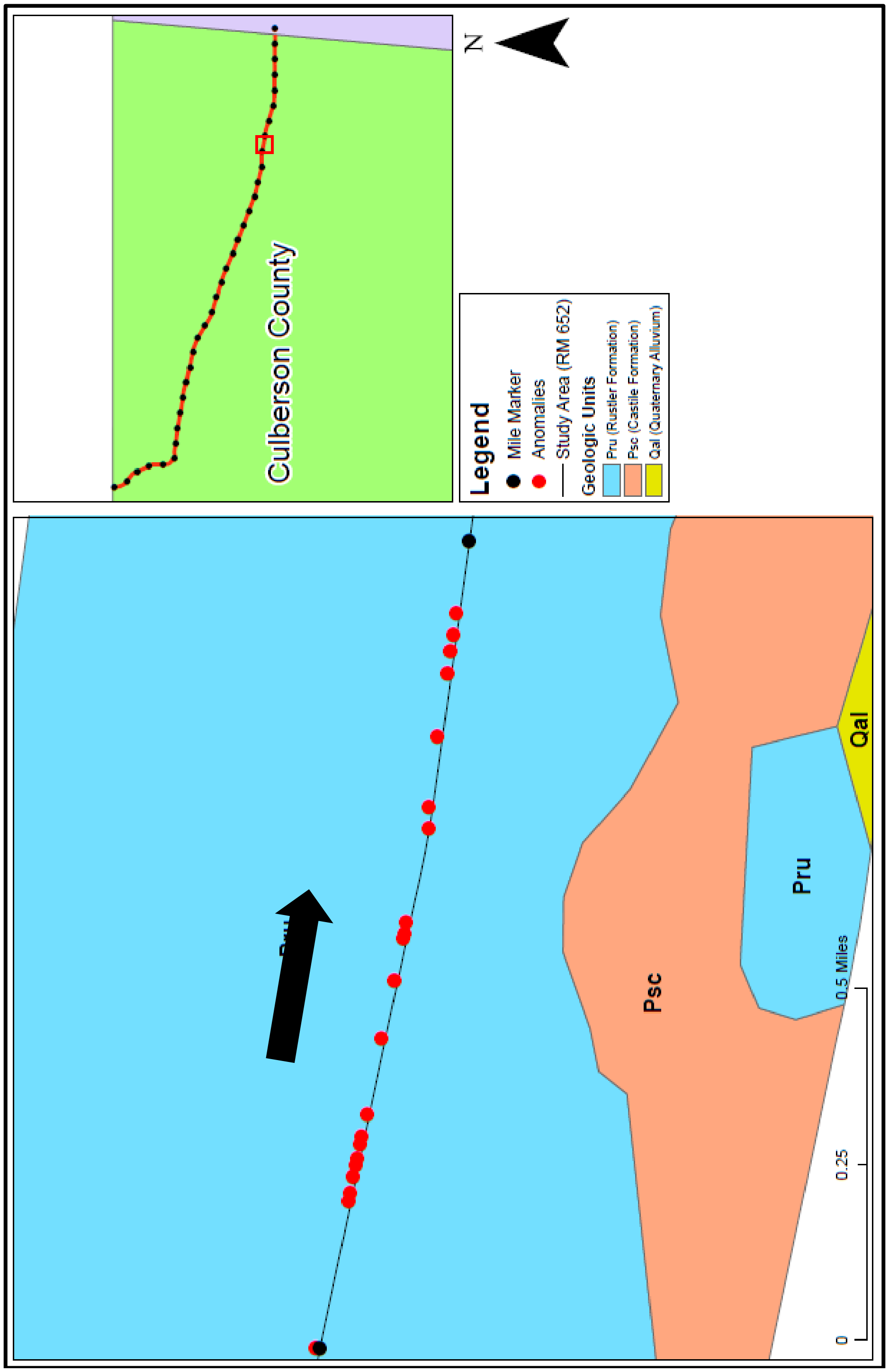

Figure C53. *Map indicating the location of Mile 26-27 resistivity profiles, along with anomalies. The black arrow indicates profile direction.*

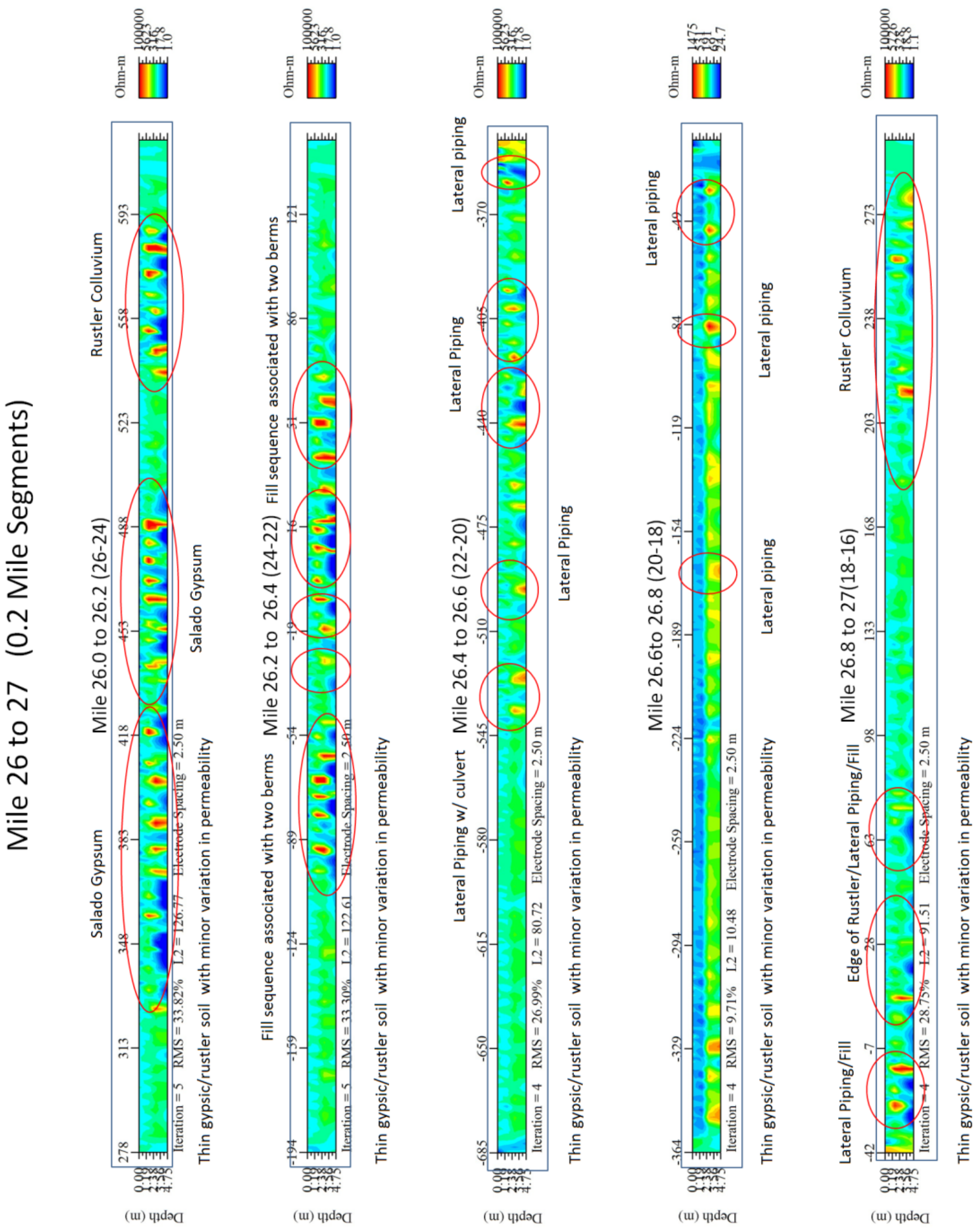

Figure C54. *Resistivity profiles of Mile 26-27 with anomalies marked and interpreted.*

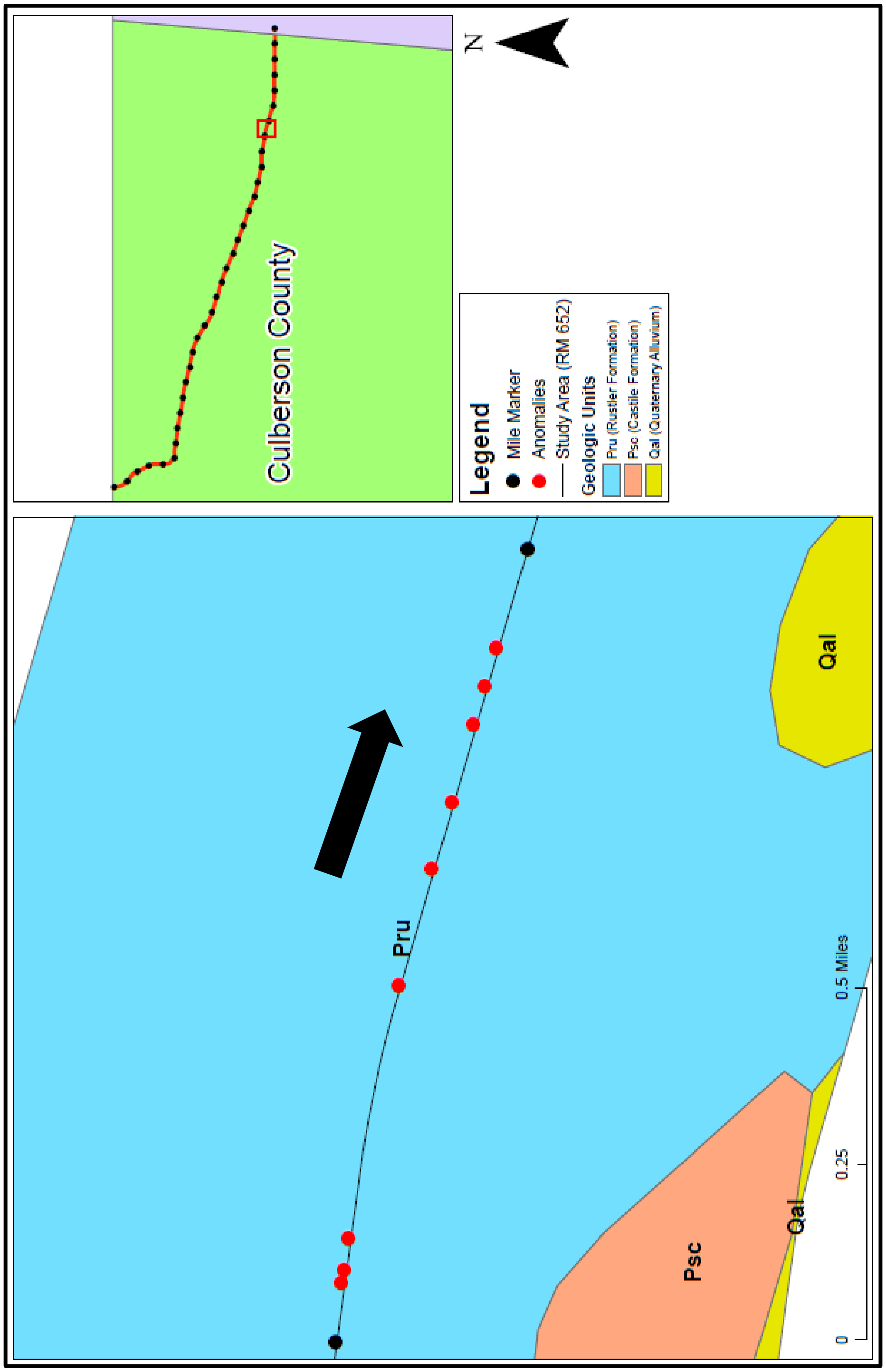

Figure C55. *Map indicating the location of Mile 27-28 resistivity profiles, along with anomalies. The black arrow indicates profile direction.*

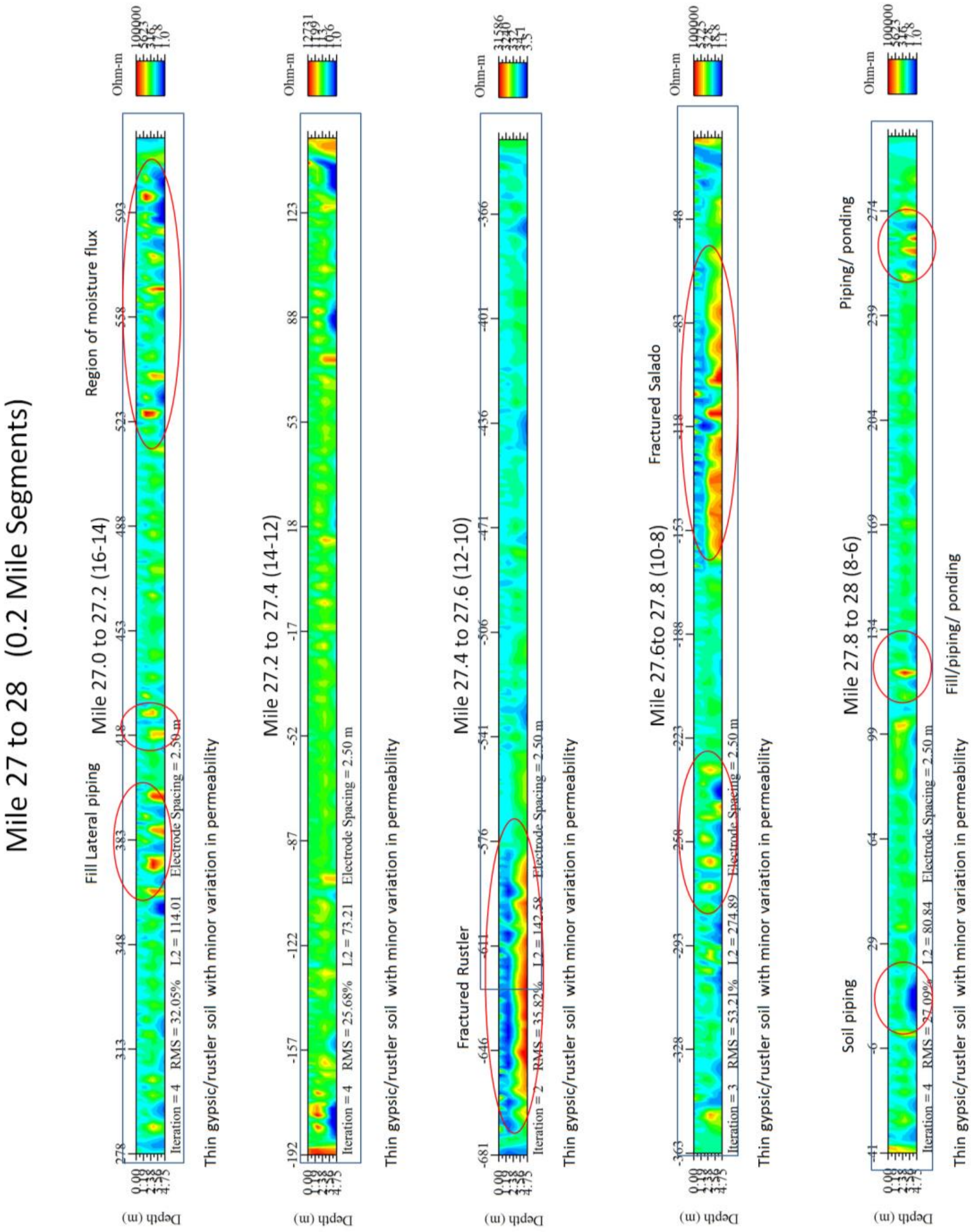

Figure C56. *Resistivity profiles of Mile 27-28 with anomalies marked and interpreted.*

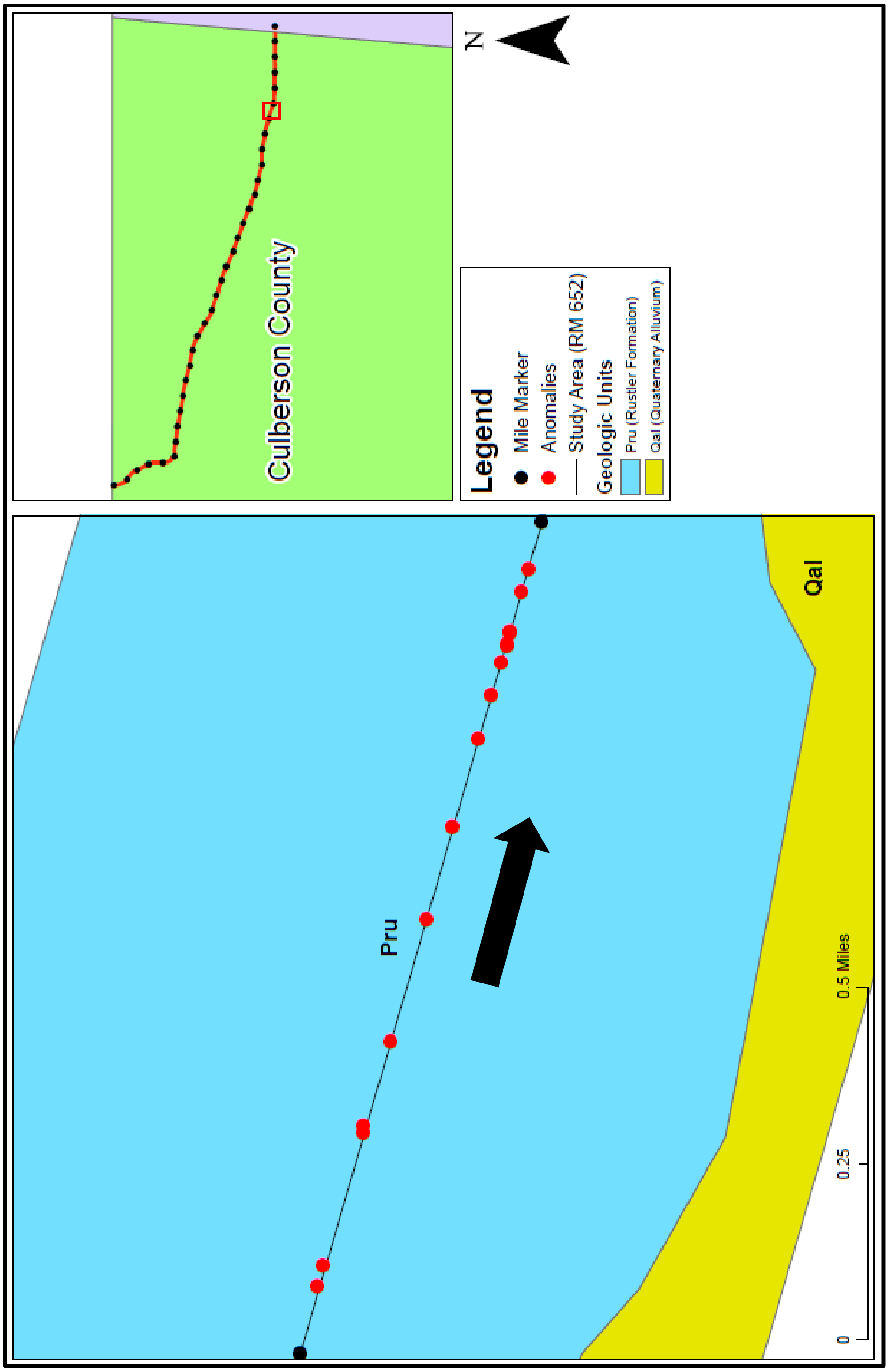

Figure C57. *Map indicating the location of Mile 28-29 resistivity profiles, along with anomalies. The black arrow indicates profile direction.*

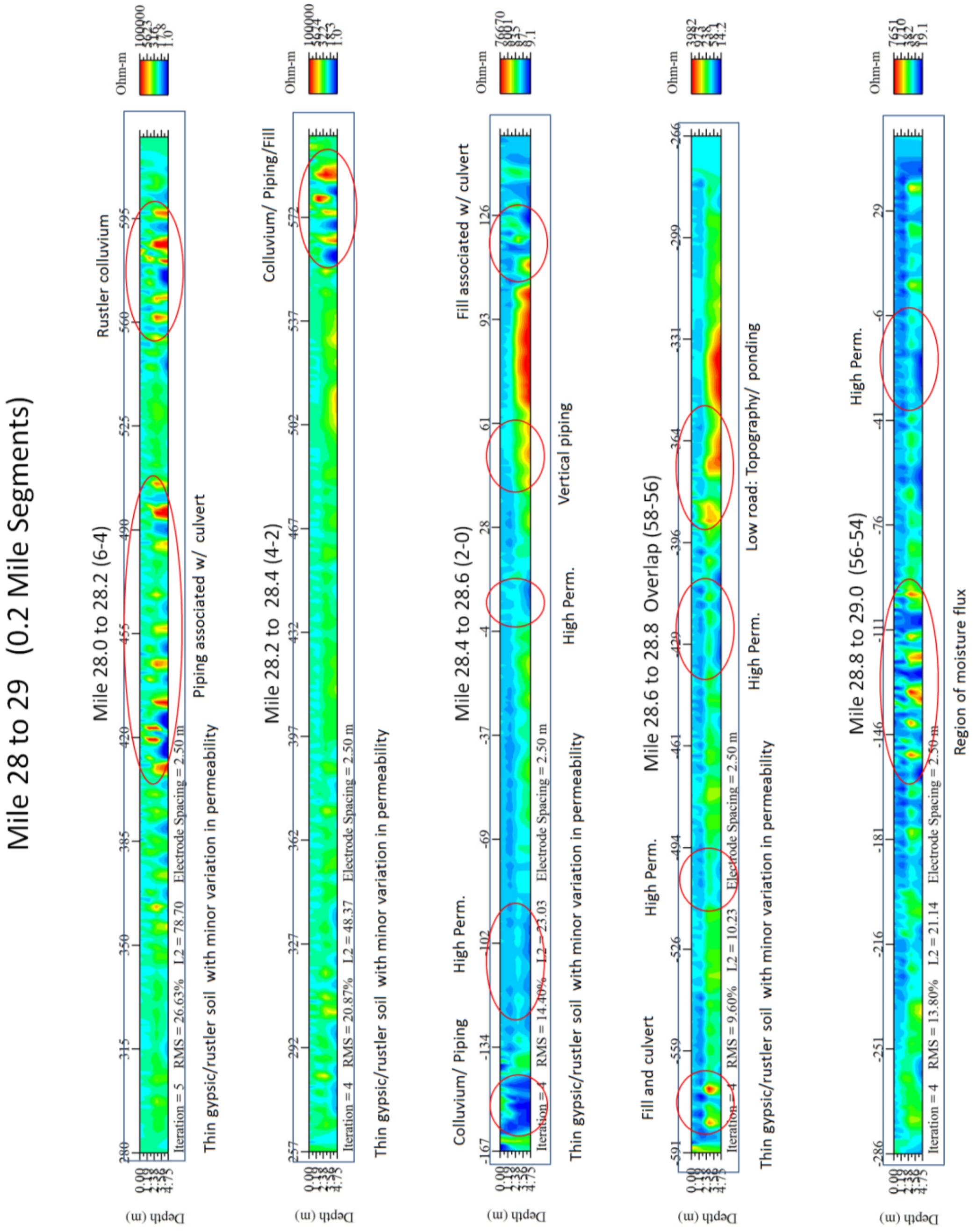

Figure C58. *Resistivity profiles of Mile 28-29 with anomalies marked and interpreted.*

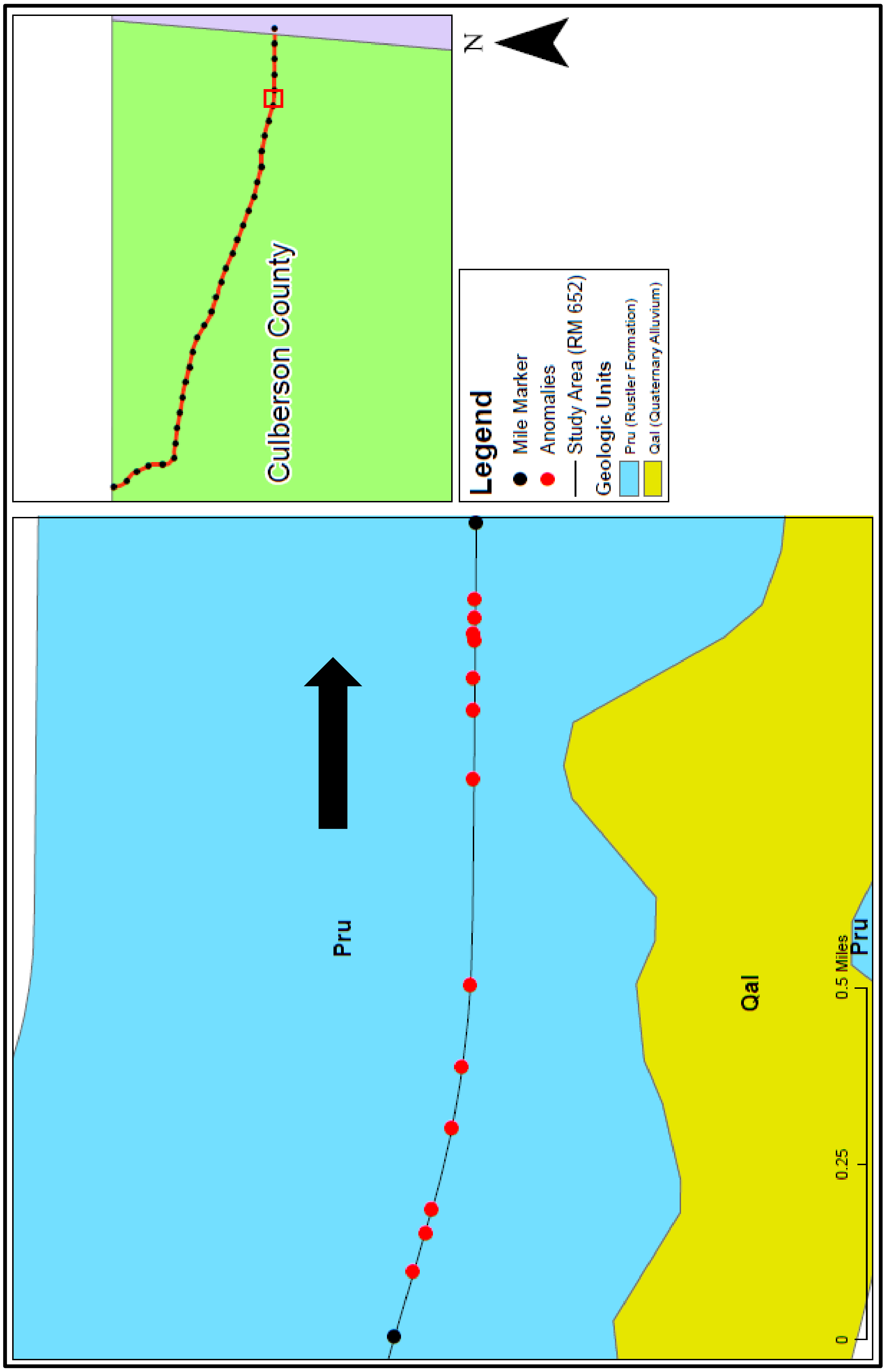

Figure C59. *Map indicating the location of Mile 29-30 resistivity profiles, along with anomalies. The black arrow indicates profile direction.*

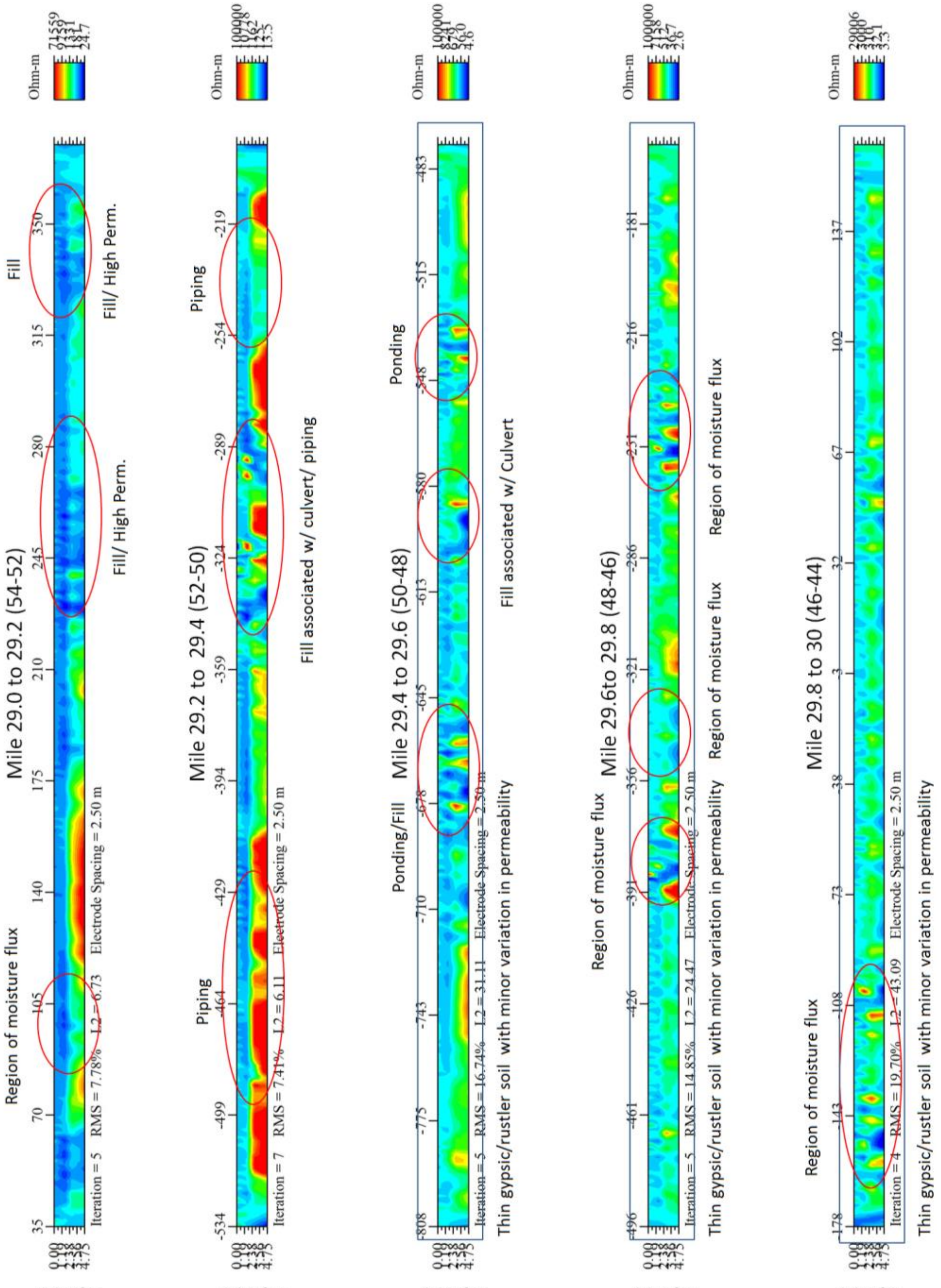

Figure C60. *Resistivity profiles of Mile 29-30 with anomalies marked and interpreted.*

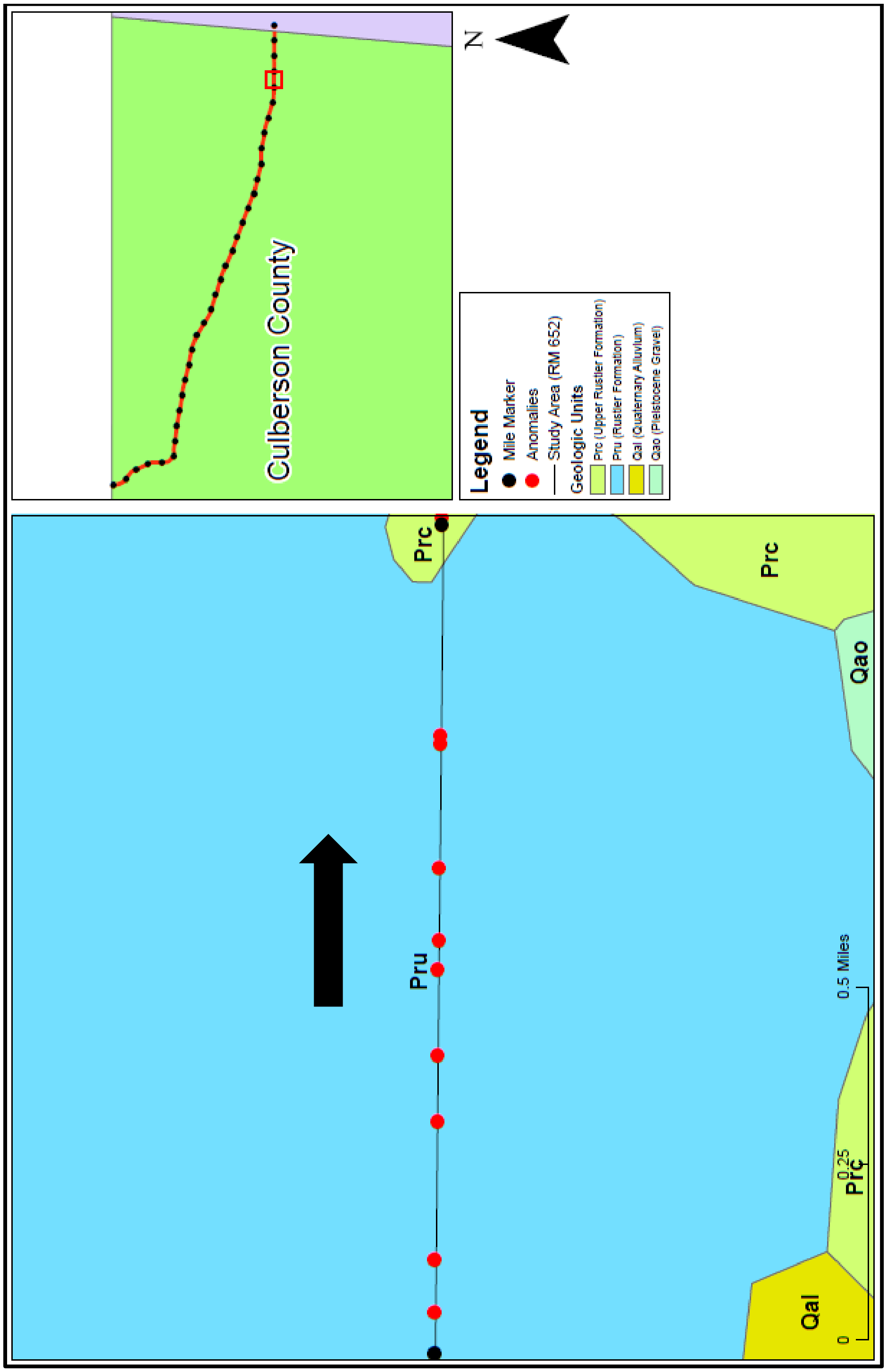

Figure C61. *Map indicating the location of Mile 30-31 resistivity profiles, along with anomalies. The black arrow indicates profile direction.*

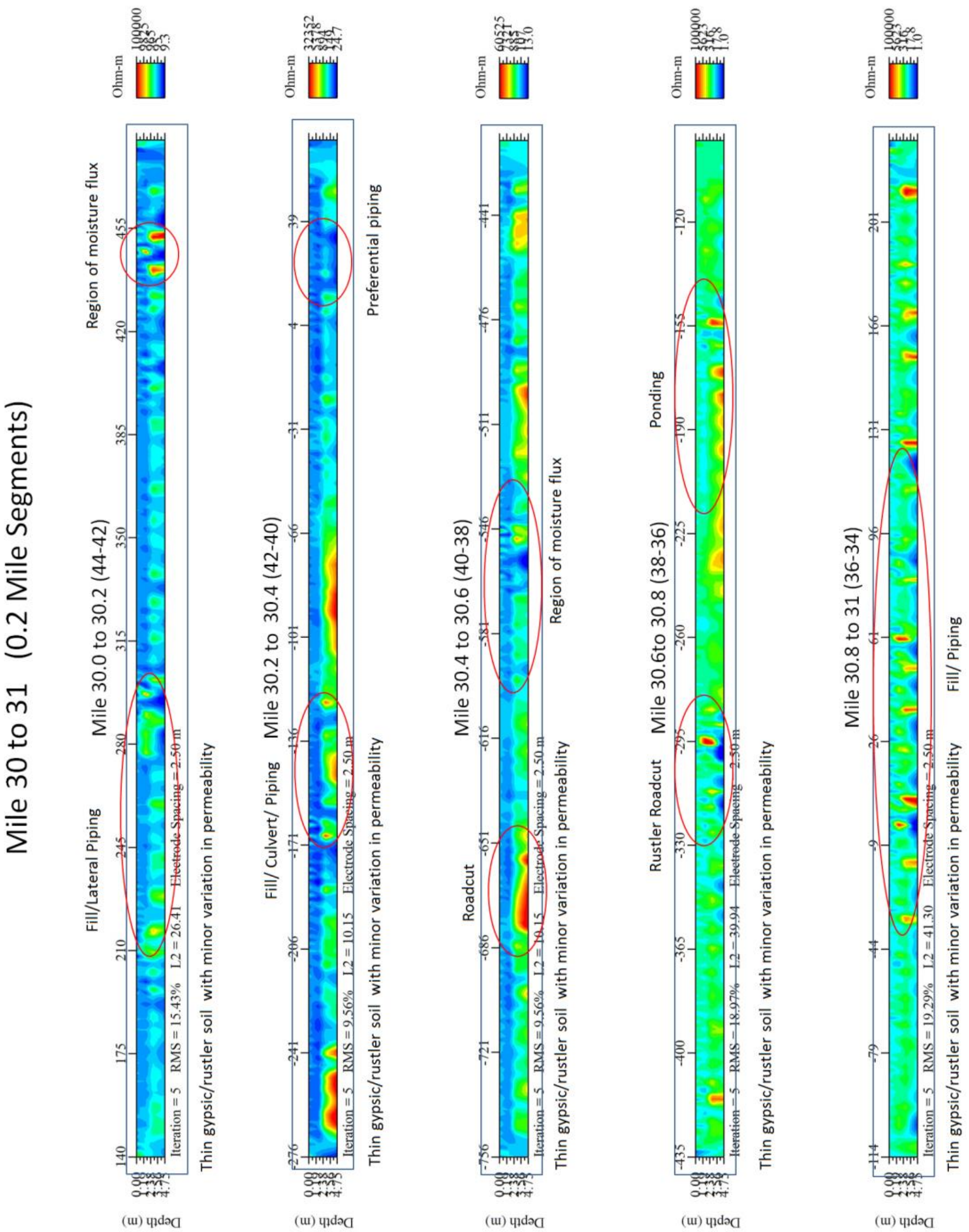

Figure C62. *Resistivity profiles of Mile 30-31 with anomalies marked and interpreted.*

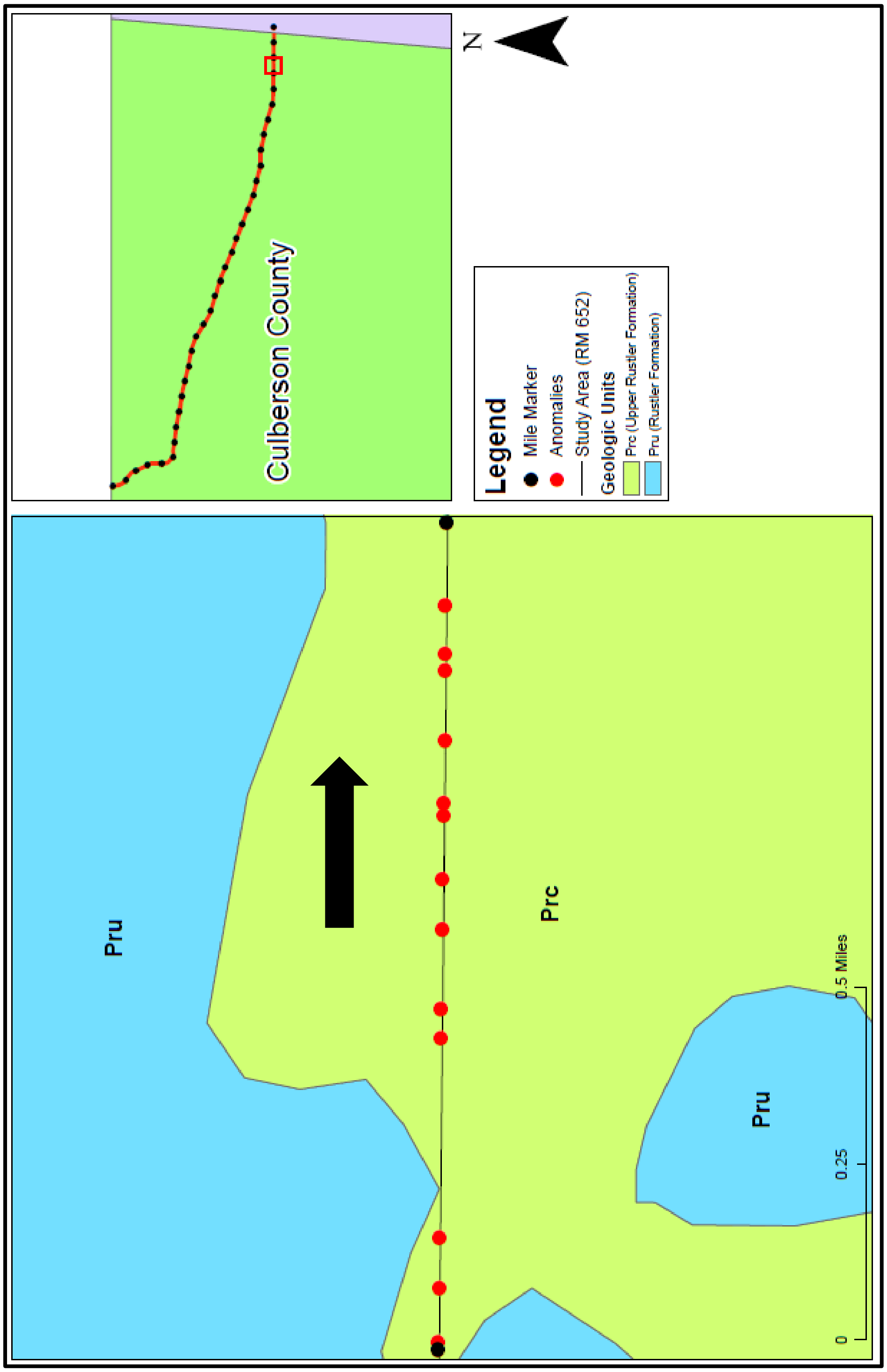

Figure C63. *Map indicating the location of Mile 31-32 resistivity profiles, along with anomalies. The black arrow indicates profile direction.*

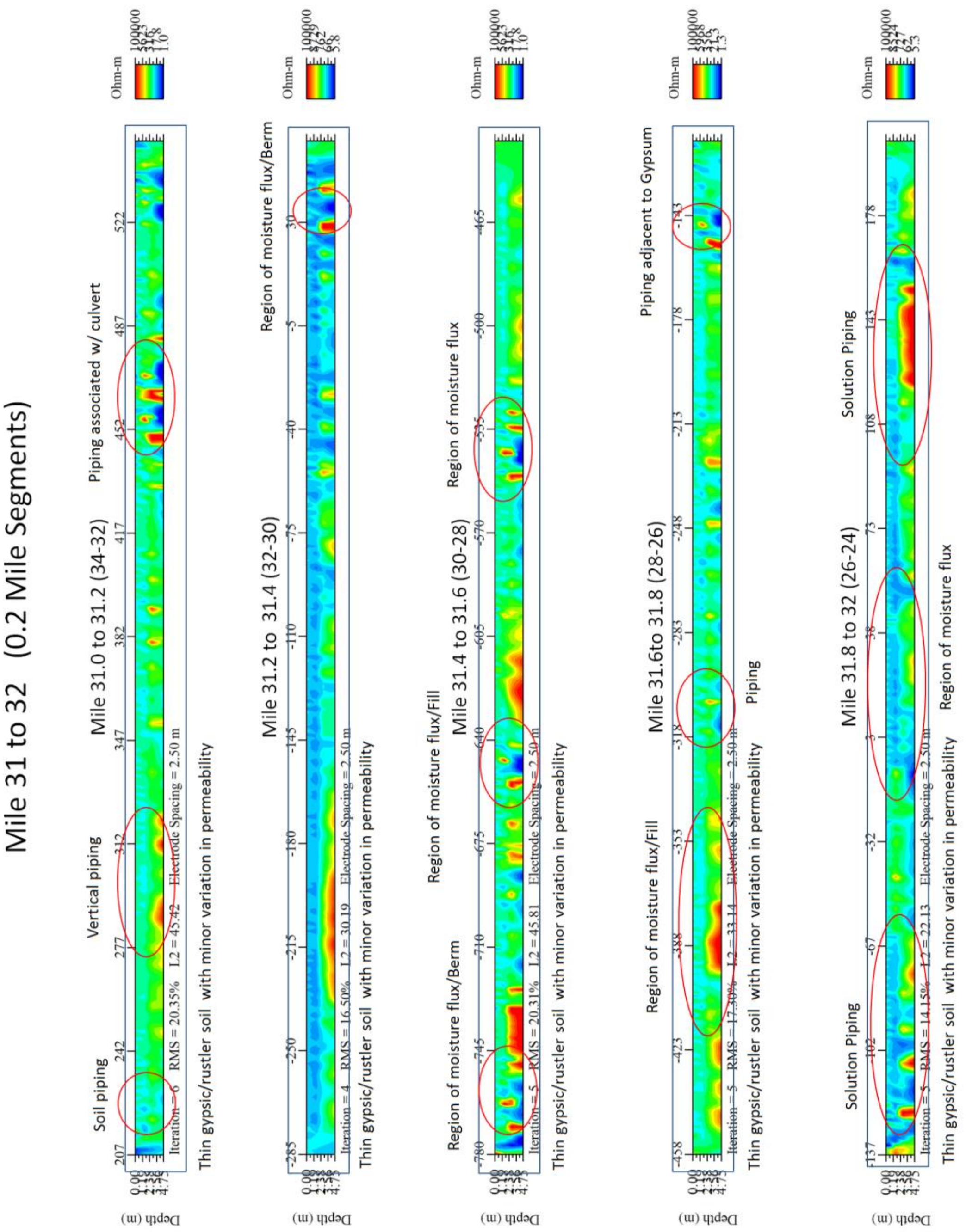

Figure C64. *Resistivity profiles of Mile 31-32 with anomalies marked and interpreted.*

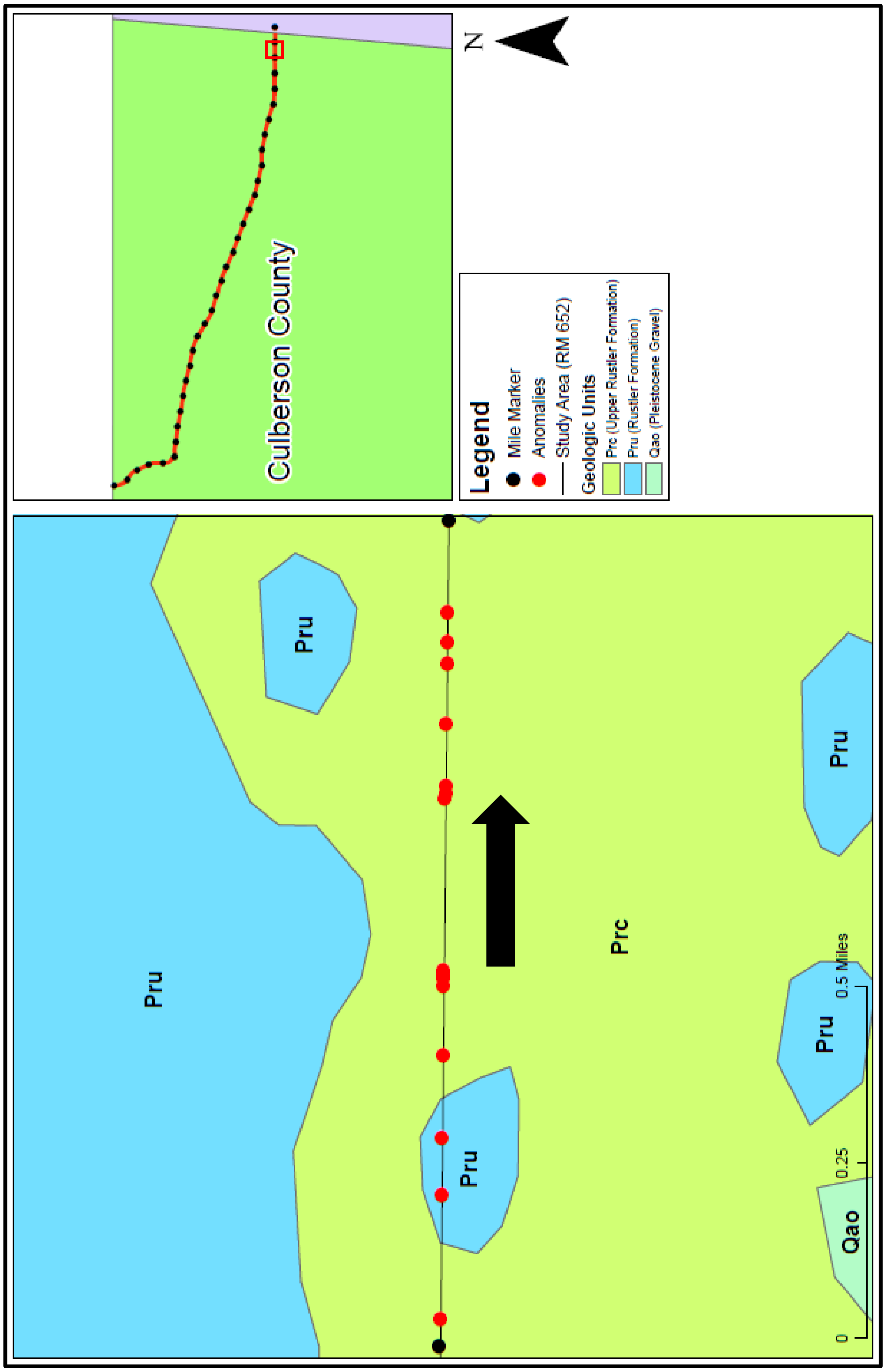

Figure C65. *Map indicating the location of Mile 32-33 resistivity profiles, along with anomalies. The black arrow indicates profile direction.*

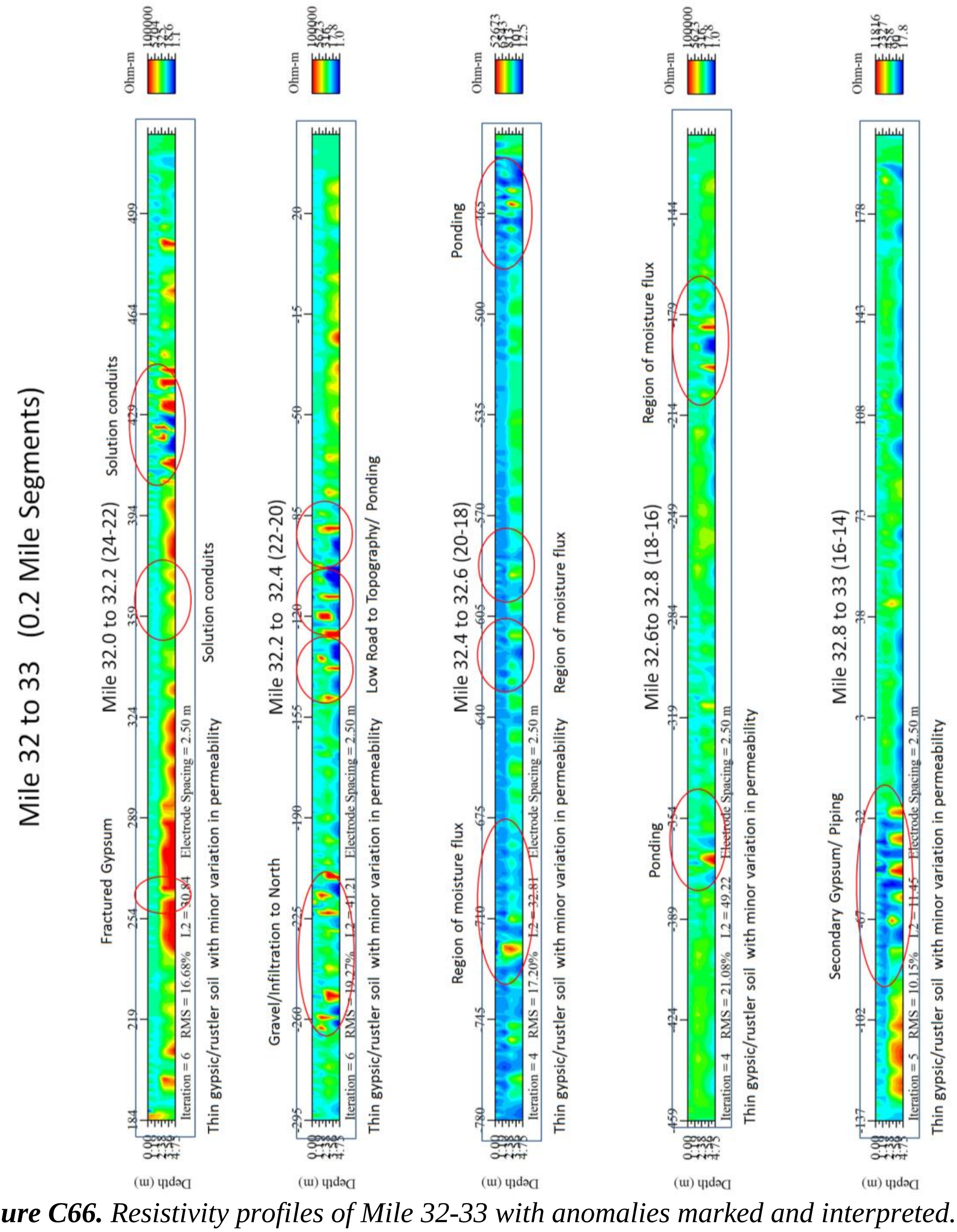

Figure C66. *Resistivity profiles of Mile 32-33 with anomalies marked and interpreted.*

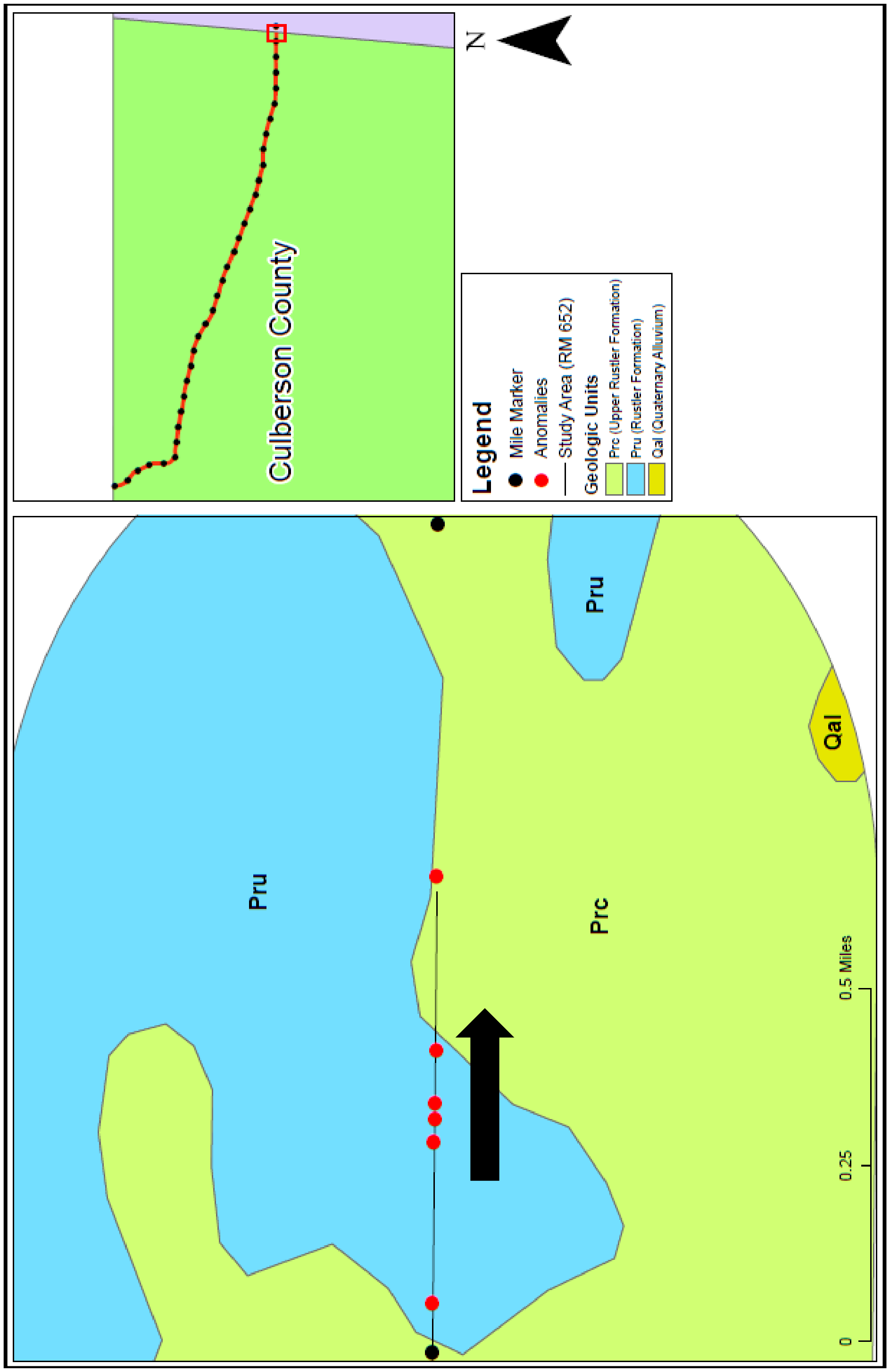

Figure C67. *Map indicating the location of Mile 33-34 resistivity profiles, along with anomalies. The black arrow indicates profile direction.*

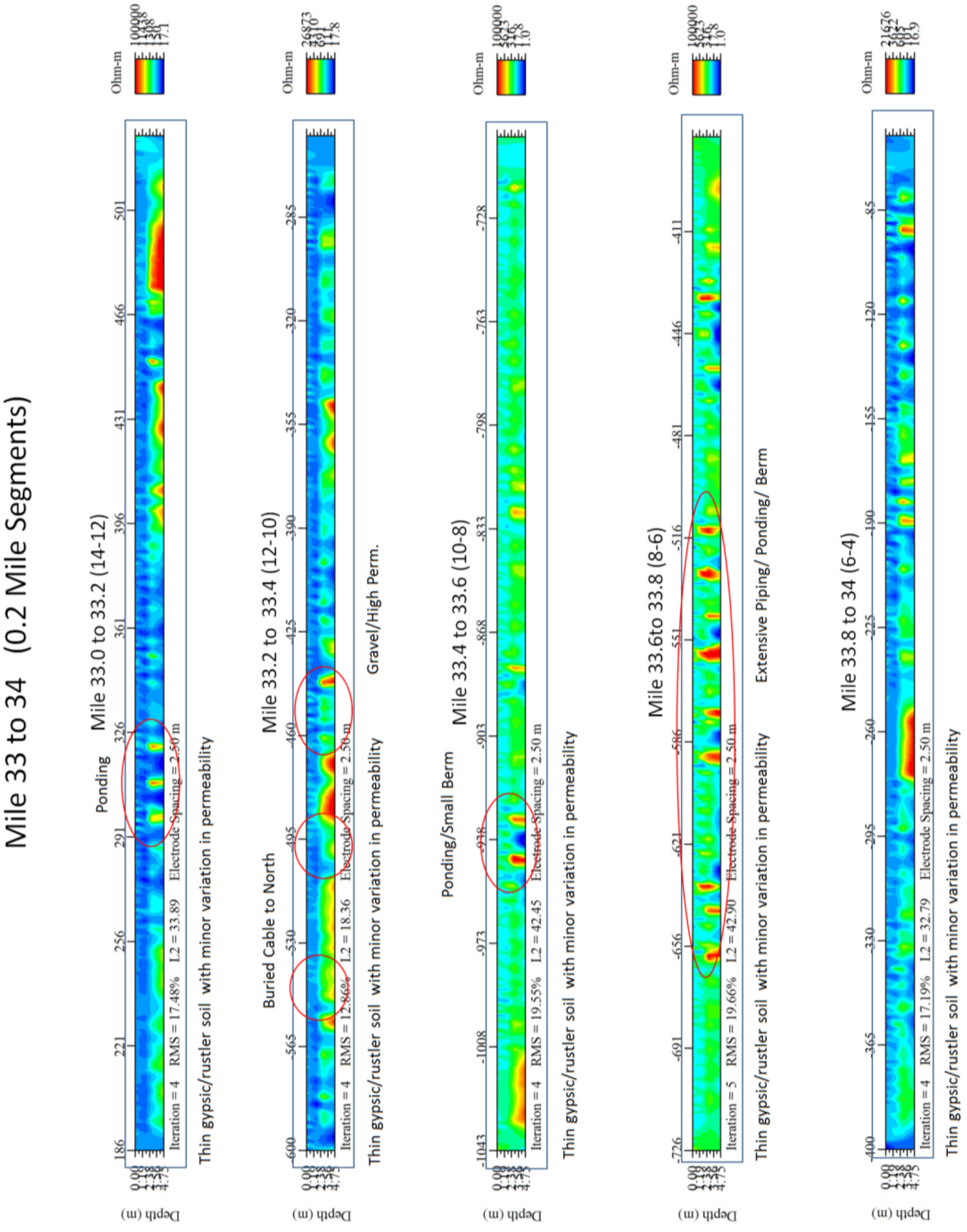

Figure C68. *Resistivity profiles of Mile 33-34 with anomalies marked and interpreted.*

CONCLUSION

Subsidence, dissolution, anthropogenic engineering, and suffosion processes greatly impact the soluble Castile Formation, and to a lesser degree the Rustler Formation, along Rm 652 within the Delaware Basin. Resistivity profiles showed a higher amount of individual anomalous signatures within the Castile Formation than were seen within the Rustler Formation (Figure C69). The effect that these anomalies have within the study area is greater within the Castile Formation than within the Rustler Formation. The extensive nature of karst features along RM 652 is more pronounced in the western portion of the study area within the Castile Formation (Figure C70).

The soluble nature of evaporites that make up the Castile Formation is highly responsible for the amount of anomalies and the broad impact they have per anomaly along the study area. Natural hypergenic and hypogenic processes exploit these susceptible rocks allowing for further degradation. Surficial drainage patterns will continue to incise the soluble evaporites directing runoff into the already existing karst within the subsurface, while pressurized hypogenic fluids continue to dissolve rock, forming voids that will possibly lead to a collapse. These two natural, karst development regimes work simultaneously to evolve the Gypsum Plain and further deteriorate roadway conditions along RM 652 within the Castile and Rustler formations.

However, current anthropogenic methods also contribute, correlating well with anomaly intensity. Berms and toe-walls that were originally emplaced to the preserve roadway integrity seem to enhance the occurrence of individual features along with aiding in their development by creating a specific flow path that runoff follows. Resistivity profiles that contain a thicker amount of gypsic soil roadbase show distinct resistivity contrasts, which seems to indicate increase soil piping. These preferential piping features will cause road failure and are in large part due to the soluble properties of the original roadbase used to engineer RM 652. Along with natural processes, current anthropogenic features will continue to evolve the Gypsum Plain, forming more extensive features that will connect in the subsurface and form complex networks of passageways.

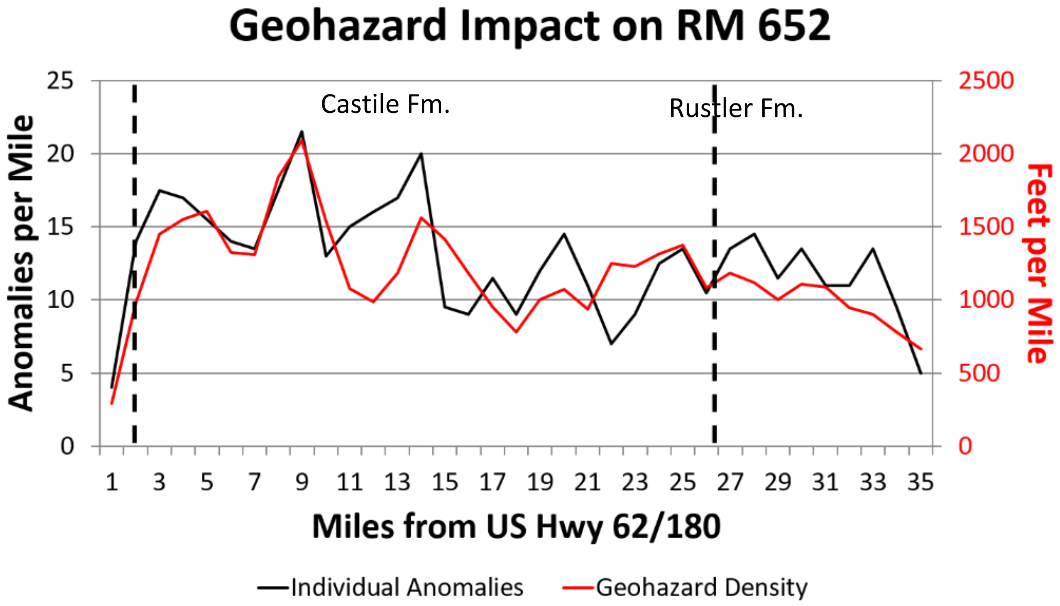

Figure C69. *Rolling average of individual anomalies (black line) and the density impact of geohazards (red line) that occur in each mile along RM 652. The first black dashed line indicates when the Castile Formation outcrops and the second black dashed line indicates when the Rustler Formation outcrops within the study area.*

VITA

Jonathan David Woodard graduated from Blum High School in 2005. He attended Hill Junior College and worked various jobs before he enlisted in the United States Air Force in 2008. After a few years, he left active service and joined the United States Air Force Reserves in order to return to school full time in July of 2011, and remained in the reserves until April of 2016 while simultaneously completing his undergraduate and graduate education. Upon returning to Hill Junior College for the 2011-2012 school year, Jonathan decided on majoring in a degree of geoscience. At the beginning of the 2012 school year he enrolled at Tarleton State University where he earned a Bachelor of Science in Geoscience in May of 2015. During his tenure at Tarleton State University, Jonathan served as a Lab Instructor from the beginning of 2014 until he graduated. In the fall of 2015 he was accepted into the graduate program at Stephen F. Austin State University where he continued to serve as a graduate teaching assistant until May of 2017. Jonathan completed his Master of Science in Geoscience in December of 2017.

Permanent Address: 916 FM 934
Blum, TX 76627

Style manual designation: Geological Society of America

This thesis was typed by Jonathan D. Woodard